The Microwave Response of Metasurfaces

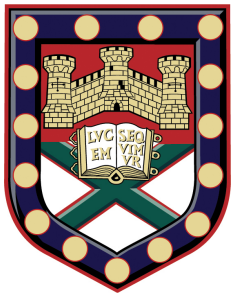

Benjamin James Tremain

School of Physics

University of Exeter

A thesis submitted for the degree of

Doctor of Philosophy

August 2016

The Microwave Response of Metasurfaces

Submitted by Benjamin James Tremain to the University of Exeter as a thesis for the degree of Doctor of Philosophy in Physics
2016

I certify that all material in this thesis which is not my own work has been identified and that no material has previously been submitted and approved for the award of a degree by this or any other University.

Benjamin James Tremain
2016

For Denis, Barbara, James and Mavis.

Abstract

This thesis details original experimental investigations of surface modes supported by thin metasurfaces in the microwave regime. The structures studied comprise sub-wavelength-sized periodic structuring in two dimensions, and are extremely subwavelength in thickness in the third dimension.

To begin with, three layer metal-dielectric-metal structures are studied with the aim of manipulating the polarisation state of impinging radiation. A bianisotropic polarisation-converting mirror is first considered in order to switch the plane of polarisation by 90° to its orthogonal state when the incident radiation is polarised at 45° to the array vectors. Optimisation of material parameters and geometry minimise absorption loss, resulting in a 2.5 GHz band of frequencies over which 98% of incident power is converted to the orthogonal polarisation, representing a marked performance improvement on similar studies in the literature. Secondly, a chiral geometry is investigated comprising two stacked arrays of cross-shaped elements twisted with respect to one another. Recent investigations into similar structures have shown a broad frequency band of dispersionless rotation of the polarisation as it transmits through the structure. The present study provides further understanding of this phenomenon by studying the resonant conditions which lead to the polarisation rotation, as well as determining the dependence of spacing between the two layers. A multi-layered structure is proposed in order to enhance the transmission bandwidth.

The remainder of the work studies single metallic layer structures, supported on a dielectric substrate. Initially, bound surface waves supported by checkerboard square hole arrays are investigated. Surface modes supported by a compound square hole array (the unit cell of which contains two different sized holes laterally shifted with respect to each other) is compared to those of a single array of holes. A sharp feature in transmission is observed due to the lack of radiative losses of the surface mode supported at normal incidence. A study of the trapped modes supported by the surface shows that the compound array provides improved isotropy of in-plane surface wave propagation compared to the ordinary checkerboard. A second

study of metallic checkerboard arrays introduces disorder into the periodic array, by applying a random rotation to each square individually according to a Gaussian distribution. The aim of this work is to suppress the resonant feature in the transmission spectrum of the ordered checkerboard array, producing a broadband beamsplitter at microwave frequencies. The result shows that the transmission spectrum inverts as the disorder changes the electrical conductivity of the array. As much as 40% of incident power is shown to scatter away from the specular beam when half of the metallic squares are isolated from their neighbours. Finally, a bound mode is investigated that is confined to the zig-zag edge of the checkerboard and distinct from that which propagates on the surface. Modes supported on adjacent edges are shown to couple together forming a symmetric/antisymmetric pair.

The next experimental study focusses on surface modes with negative mode index, i.e. with group and phase velocities in the opposite direction. One-dimensional planar waveguides are designed to support a mode where the phase fronts propagate *backwards* towards the power source. All-angle negative mode index is experimentally demonstrated using an array of four-armed spiral-shaped holes in a metallic sheet, demonstrating the structure's potential for use as a surface wave superlens. Finally, a preliminary investigation into quasiperiodic metasurfaces is presented where surface wave propagation on a metallic quasiperiodic diamond tiling and Penrose tiling is characterised experimentally.

Contents

Contents **i**

List of Figures **v**

1 Introduction **1**
1.1 Aim of Research 1
1.2 Outline 1

2 Theory **5**
2.1 Introduction and Historical Background 5
2.2 Drude Model 6
2.3 Surface Waveguides 7
2.3.1 Planar Interface 8
2.3.2 Impedance Description of Surfaces 13
2.3.3 Corrugated Surface 14
2.4 Coupling to Surface Modes 17
2.4.1 Brillouin Zone 19
2.4.2 Phase and Group Velocities 20
2.4.3 Band Gaps 21
2.5 Surface Waves on Metasurfaces 22
2.5.1 Band Gaps 22
2.5.2 Coupled Surface Modes 24
2.5.3 Transverse Electric Modes 26
2.6 Glide Symmetry 26
2.7 Conclusion 32

3 Methods **33**
3.1 Introduction 33
3.2 Sample Fabrication 33
3.2.1 Photolithography 33

3.2.2 Print and Etch . . . 34
3.3 Experimental Equipment . . . 36
3.3.1 Network Analysers . . . 36
3.3.2 Horn Antennas . . . 37
3.3.3 Absorbing Material . . . 39
3.4 Radiative Experiments . . . 40
3.4.1 Transmission Setup . . . 42
3.4.2 Reflection Setup . . . 44
3.5 Non-radiative Experiments . . . 45
3.5.1 Near Field Probes . . . 45
3.5.2 XYZ Stage . . . 47
3.5.3 Reciprocal Space . . . 48
3.6 Data Analysis . . . 49
3.7 Numerical Simulations . . . 50
3.7.1 Finite Element Method . . . 50
3.7.2 Field Solver . . . 51
3.7.3 Boundary Conditions and Excitations . . . 51
3.7.4 Meshing and Convergence . . . 53
3.7.5 Conclusion . . . 53

4 Polarisation Conversion from Microcavity Arrays 55
4.1 Introduction . . . 55
4.2 Background . . . 55
4.3 Results and Discussion . . . 59
4.3.1 Monograting . . . 59
4.3.2 Bigrating . . . 63
4.3.3 Slit Width . . . 65
4.3.4 Incident Angle . . . 66
4.3.5 Polarisation Angle . . . 66
4.3.6 Linear to Circular Conversion . . . 68
4.4 Conclusion . . . 68

5 Twisted-Cross Chiral Metamaterial 71
5.1 Background . . . 71
5.2 Results and Discussion . . . 74
5.2.1 D-cross Structure . . . 74
5.2.2 C-cross Structure . . . 79
5.2.3 Experimental Results . . . 83

5.2.4 Varying Dielectric Thickness . . . 85
5.2.5 Multilayer . . . 86
5.3 Conclusions . . . 87

6 Compound Checkerboard Array 89
6.1 Background . . . 89
6.2 Band Structure Simulation . . . 92
6.3 Non-Radiative Measurements . . . 93
6.3.1 Ordinary Checkerboard Array ($L_2 = 0$) . . . 93
6.3.2 Compound Checkerboard Array ($L_2 \neq 0$) . . . 95
6.4 Radiative Measurements . . . 99
6.4.1 Compound Checkerboard Array . . . 99
6.5 Conclusion . . . 101

7 Non-Periodic Checkerboard Arrays 103
7.1 Rotational Disorder . . . 103
7.1.1 Background . . . 103
7.1.2 Transmission Measurements . . . 107
7.1.3 Scatter Measurements . . . 111
7.2 Fibonacci Checkerboard . . . 114
7.2.1 Background . . . 114
7.2.2 Surface Modes . . . 117
7.3 Conclusion . . . 118

8 Edge Waves on Checkerboard Arrays 121
8.1 Background . . . 121
8.2 Results and Discussion . . . 122
8.2.1 Single Edge . . . 123
8.2.2 Coupled Edges . . . 127
8.2.3 Surface to Edge Conversion . . . 129
8.3 Conclusion . . . 131

9 Planar Metallic Waveguides with Negative Mode Index 133
9.1 Background . . . 133
9.2 One-Dimensional Planar Waveguides . . . 137
9.2.1 Coupled Domino Waveguide . . . 138
9.2.2 Planar Hook Waveguide . . . 142
9.2.3 Split Ring Resonator Waveguide . . . 149
9.3 Two-Dimensional Planar Waveguide . . . 154

9.3.1 2D Quadrafilar Spiral Array 154
9.4 Conclusions 158

10 Future Work: Non-periodic Metasurfaces **161**
10.1 Generation of Non-periodic Tilings 162
10.2 Experimental Results 166
10.2.1 Quasiperiodic Diamond 166
10.2.2 Penrose Tiling 167
10.3 Conclusion 167
10.4 Other Future Work 167

11 Conclusions **169**

12 Publications and Conferences **171**
12.1 Publications 171
12.2 Conference Presentations 171
12.2.1 Oral Presentations 171
12.2.2 Poster Presentations 172

References **173**

List of Figures

2.1 The schematic illustration of the dispersion curve (blue line) of a surface wave that asymptotes to frequency, ω_0 (grey dotted line), which corresponds to the resonant frequency of oscillating electrons for a planar metallic interface or the resonance of a single subwavelength element in the periodic surface case. At lower frequencies (orange region), the mode is best described as a surface current; loosely bound to the interface and propagating close to the speed of light, c. The phase velocity of the surface mode is given by the ratio of ω to k_{x} and defines the mode index, $n = c/v_{\mathrm{p}}$. The group velocity is defined by the gradient of dispersion (dashed blue line) and falls to zero at ω_0. The light line (black line) represents the dispersion of grazing plane wave radiation, where $v_{\mathrm{p}} = v_{\mathrm{g}} = c$. 7

2.2 a) The complex relative permittivity as a function of frequency for silver. The real part is magnified by 5×10^3 (green dot-dashed line) to show the frequency at which it passes though zero . This is based on a plasma frequency $\omega_{\mathrm{p}} = 1.2 \times 10^{16}$ rad/s and mean free time $\tau = 6.9 \times 10^{-14}$ s[1]. b) The propagation length (black line), and penetration depths of a wave guided by a planar interface between silver (red dashed) and air (blue dot-dashed) as a function of frequency, ω, according to equations 2.20 and 2.22. 8

2.3 a) A planar metallic surface with dielectric overlayer b) A corrugated perfect electrical conducting surface. Both support a bound surface wave at microwave frequencies. 9

2.4 a) A ray picture of a wave incident on the interface between two dissimilar media, with transverse magnetic (TM) polarisation. b) The penetration depth of electric field into a metal and dielectric (air) for visible and microwave frequencies. This is caused by the change in permittivity of metals as a function of frequency (Drude model, Sec. 2.2) and as a result a tightly bound surface mode is supported by a planar metallic interface at higher frequencies, whereas surface currents (loosely bound) exist in the microwave regime. 10

2.5 a) A corrugated perfect electrical conducting surface with periodicity, a, and a cavity depth of d. 15

2.6 Schematic representation of the dispersion of TM and TE surface modes supported by a corrugated surface. The surface impedance is defined by a lumped LC circuit. The asymptotic frequency, ω_0, coincides with a cavity depth, d, equal to a quarter of the wavelength. 16

2.7 The dispersion of a bound surface mode on a planar interface (black line). Radiation incident on the interface at angle θ to the surface normal cannot have in-plane wavevector greater than that of grazing radiation ($\theta = 90°$, also known as the light line) and therefore can not couple to the mode with wavevector k_{sw}. b) The in-plane wavevector is related to the angle of incidence by $k_{\mathrm{x}} = k_0 \cos(\theta)$ where $k_0 = \omega/c$. c) With a periodic perturbation to the surface with periodicity a, additional modes are created with wavevector $k_{\mathrm{x}} + 2N\pi/a$. d) As a result, the momentum k'_{sw} of a diffracted surface mode is matched by the in-plane momentum of incident radiation with $\theta = 50°$. 18

2.8 A zoomed in view of the dispersion diagram showing just the zeroth and first order scattered surface wave modes. The edge of the first Brillouin zone (BZ) is marked by the blue dashed lines. Within the Brillouin zone there are three regions; non-radiative (blue), radiative with specular radiation only (green) and radiative with specular and first order diffracted modes (purple). The surface modes split causing band gaps to appear (grey regions), with the upper and lower band edges corresponding to standing wave solutions. 20

2.9 Schematic of the band-split modes supported by a sinusoidal grating at $k_{\mathrm{x}} = 0$. a) The lower frequency solution b) The higher frequency solution. c-d) The equivalent modes for a case of a discontinuous surface. 21

2.10 a) The standing wave solution for the symmetric mode of the circular hole array at the lower band edge at $k_x = \pi/a$, on the xz plane. Colour: electric field magnitude. Arrows: electric field vector. b) The magnetic field on the yz plane, with the vector field advanced by 90°. c) The electric field in the xy plane on the top face of the hole. d-f) The same plots for the antisymmetric mode. 23

2.11 a) The standing wave solution for the symmetric mode of the circular hole array at the upper band edge at $k_x = \pi/a$, on the xz plane. Colour: electric field magnitude. Arrows: electric field vector. b) The magnetic field on the yz plane between the holes, with the vector field advanced by 90°. c) The electric field in the xy plane on the top face of the hole. d-f) The same plots for the antisymmetric mode. The z axis in a,b,d,e is scaled by 1/7. 25

2.12 A glide symmetric waveguide (inset) consists of a parallel plate waveguide with periodic inclusions on each plate, shifted by half of the periodicity with respect to each other. The dispersion diagram of supported modes show a degenerate pair of modes at the first Brillouin zone boundary ($\beta d = \pi$). 27

2.13 The field configurations of the two lowest order transverse magnetic (TM) modes of a parallel plate waveguide. The plates are positioned on the top and bottom edges of the field plots. a) the TEM mode with 'even' transverse magnetic field with respect to the central plane (dashed line). b) the TM_1 mode with 'odd' transverse magnetic field. Mode propagation is from left to right. 28

2.14 a) The dispersion of modes supported by a parallel plate waveguide. Blue: even H_z modes, Green: odd H_z, Thin: planar PEC walls, Thick: with periodic inclusions (inset). b) The dispersion when the inclusions on the bottom plate are shifted by $a/2$ with respect to those on the top plate, forming a glide-symmetric waveguide. The modes are neither purely odd or even in H_z. 29

2.15 The field configurations of the two lowest order transverse magnetic (TM) modes of a parallel plate waveguide with periodic protrusions obeying the translation operator, T. The plates are positioned on the top and bottom edges of the field plots. a) the TEM mode with 'even' transverse magnetic field with respect to the central plane (dashed line). b) the TM_1 mode with 'odd' transverse magnetic field. Mode propagation is from left to right. 30

2.16 The field configurations of the two lowest order transverse magnetic (TM) modes of a parallel plate waveguide with periodic protrusions obeying the glide operator, G. The plates are positioned on the top and bottom edges of the field plots. Mode propagation is from left to right. 31

3.1 The stages of the photolithography process from the initial copper laminate in (a) to the finished patterned sample in (g). Photoresist is marked as green, hardened resist in blue and the photomask in black. 34

3.2 The stages of the print and etch process from the initial copper laminate in (a) to the finished patterned sample in (d). Grey regions denote Solid Ink which is printed directly onto the laminate. 35

3.3 A schematic demonstrating the principles of S-parameters and how they relate to the transmission and reflection measurement of a system between two ports. 36

3.4 a) A horn antenna connected to a coax to waveguide adapter. The orange arrow indicates the electric field polarisation of the emitted radiation. b) The coax to waveguide adapter, modelled using COMSOL. The vertical plane shows variation of the instantaneous x component of electric field within the coax and surrounding the exposed pin. The horizontal plane shows the y component within the waveguide. Both are normalised to unity. c) The directivity of the horn antenna in the xz plane (blue dashed line) and the yz plane (red solid line). d) A slice of the horn antenna in the xz plane showing the variation of E_{y}. Only one half of the cross-section is shown, with the orange line acting as a mirror plane. 38

3.5 A photograph of a pyramidal absorbing panel. 99% of radiation incident from above is absorbed up to an incident angle of 60°. 39

3.6 A schematic of the scalar (a) and vector (b) network analyser measurements for radiative experiments. The signal, A, that has passed through the system under test is reference to a signal that has not, R. 40

3.7 A typical transmission spectrum for a metallic checkerboard array obtained experimentally. The linear transmission coefficient (black, left axis) is contrasted with the same data represented on a logarithmic scale (grey, right axis). 41

3.8 The radiative experimental setup, shown in the normal incidence transmission configuration. A spherical mirror of focal length ($f = 1$ m) collimates microwave radiation from a horn antenna and directs it to the sample (blue dashed line). The transmitted beam (dashed red line) is focussed by a second mirror on to a detecting horn antenna. A computer-controlled rotating table allows transmission at various angle of incidence to be determined. 42

3.9 The experimental setup in reflection configuration. The incident and reflected beams are represented as blue and red dashed lines respectively. A rotating arm allows reflection to be determined at a range of incident angles, θ, between 10° to 60°. 43

3.10 The normal incidence reflection setup. The same mirror is used to both collimate and re-focus the microwave beam. The incident and reflected beams are represented as blue and red dashed lines respectively. 44

3.11 Finite Element Method simulation of a stripped coaxial antenna placed normal to a metallic sheet, driven at a frequency of 10 GHz. The colour scale shows the electric field magnitude and the arrows demonstrate the instantaneous electric field vector at a phase corresponding to maximum field strength. Metallic regions are shaded black. 45

3.12 A schematic of the near field scanning experiment. A stripped coaxial antenna is placed approximately 1 mm away from and perpendicular to the sample plane. A second probing antenna is scanned across the opposite side of the sample using an XYZ stage. 46

3.13 An example field plot produced using the near-field scanner with antennas oriented normal to the surface. The magnitude of the electric field (a) is combined with the phase measurement (b) to produce the instantaneous field image (c). The excitation is at the image centre. . . 47

3.14 The 2D spatial Fourier transform of the instantaneous field (a) produces the isofrequency contour (b). Combining this data for a range of frequencies results in the dispersion curve (c). The black horizontal line shows the frequency at which (a) and (b) are shown and the blue and orange lines represent the zeroth order and diffracted light lines respectively. . . 48

3.15 a) A tetrahedral mesh element, with arrows representing the field components evaluated at each vertex. b) A typical unit cell for the checkerboard array. c) The mesh around the metallic patch shown on a plane through the patch centre (blue area in (b)). 50

3.16 The boundary conditions for the checkerboard unit cell for a) a driven model with Floquet ports and b) an eigenmode model with perfectly matched layers. 52

3.17 A convergence plot showing how a given S-parameter converges on a solution as the mesh density increases with each consecutive pass. Inset: The initial mesh (a) and the refined mesh after the convergence condition is met (b). 53

4.1 Some schematics showing the structures utilised for polarisation conversion by other authors. Each comprises a metallic ground plane and a dielectric substrate supporting a periodic arrangement of anisotropic conductive elements. Images are taken from the original papers and labelled with the citation number. 56

4.2 Sample geometry and coordinate system for a) the monograting cavity array with period λ_g and slit width w_s and b) the bigrating cavity array with periodicity λ_{gx} and λ_{gy} in the x and y-directions respectively. . . . 57

4.3 A cross-section of a single unit cell of a typical monograting structure perpendicular to the slit at the fundamental resonant frequency. The metallic sections are shown as bordered white regions. a) Resonant time-averaged electric field magnitude where black to white represents increasing field strength. b) Resonant electric field vector at a phase corresponding to maximum field enhancement, showing the reversal of the field beneath the metallic strip. 58

4.4 a) Normal incidence reflectivity as a function of frequency for the monograting sample. Co-polarised reflectivity for polarisation angles of 0° (blue squares), 90° (purple triangles) and 45° (red circles) and cross-polarised reflectivity at $\phi = 45°$ (hollow yellow circles). Black line indicates estimated reflectivity by fitting to resonant frequency and width. b) Relative phase of detected radiation as a function of frequency, normalised to the phase of reflection from a planar metallic mirror. c) Ellipticity of reflected radiation, where negative and positive values indicate left and right handed respectively. Results from numerical modelling are shown as dotted lines. 60

4.5 Schematic diagram showing the incident and reflected polarisation states at the resonant frequency of 11.2 GHz when the electric field is polarised at 45° to the grating slits. 61

4.6 a) Co-polarised (filled red circles) and cross-polarised (hollow yellow circles) reflectivity for normal incidence radiation at $\phi = 45°$. b) Relative phase of co-polarised detected radiation as a function of frequency, normalised to the phase of reflection from a planar metallic mirror, for 0° (blue squares), 90° (purple triangles) and their difference (green circles) c) Ellipticity of reflected radiation, where negative and positive values indicate left and right handed respectively. Results from numerical modelling are shown as dotted lines. 64

4.7 The bandwidth (grey squares) and central frequency (black circles) of the 95% polarisation converting band for various slit widths w_s. The values corresponding to the bigrating sample are shown as triangles. . . 65

4.8 Simulation: Cross-polarised reflectivity of the bigrating sample with incident polarisation angle $\phi = 45°$, as a function of both frequency and incident angle θ. 66

4.9 Experiment: Cross-polarised reflectivity of the bigrating sample with incident polarisation angle $\phi = 45°$, as a function of both frequency and incident angle θ. 67

4.10 Cross-polarised reflectivity of the bigrating sample at normal incidence, as a function of both frequency and polarisation angle ϕ. The data is obtained via numerical modelling. The sinusoidal variation with changing ϕ is demonstrated inset. 67

4.11 Normal incidence numerical modelling results for the linear to circular polarisation converting bigrating structure. a) Co-polarised (solid line) and cross-polarised (long dashed line) reflectivity for $\phi = 45°$. b) Relative phase of reflected radiation as a function of frequency, normalised to the phase of reflection from a planar metallic mirror, along the x-direction (dot-dash), y-direction (dashed) and their difference (dotted). c) Ellipticity of reflected radiation, where negative and positive values indicate left and right handed respectively. 69

5.1 Unit cells of the two chiral metamaterials studied. a) the 'D-cross' geometry consisting of two layers of metallic crosses, separated by a dielectric layer and with one cross rotated with respect to the other. b) the 'C-cross' structure; the second layer is replaced with cross shaped holes in a continuous metal film. 72

5.2 The linear (a) and circular (b) polarised transmission coefficients for the D-cross structure overs a frequency band from 14 to 22 GHz. The transmission is represented on a logarithmic (dB) scale. c) The optical rotation, ϕ (black points), calculated from the phase of RCP (red line) and LCP (blue line) transmitted radiation, according to equation 5.3. d) The ellipticity, η of transmitted radiation calculated from the magnitude of circularly polarised transmitted radiation in (b), according to equation 5.4. Two resonant frequencies are highlighted by grey dashed lines. The frequency band of interest, where non-zero optical rotation is accompanied by negligible ellipticity, is shaded grey. 75

5.3 A polarisation ellipse. The electric field vector of elliptically polarised radiation traces the ellipse as the phase of the field advances. The ellipse is defined by its major (A) and minor (B) axes and orientation ϕ with respect to the x-axis. 76

5.4 Direction of current flow (arrows) and surface current density (colour) in the upper and lower elements of one unit cell of the D-cross structure at (a) $f = 17.5$ GHz and (b) $f = 20.0$ GHz, corresponding to resonant dips in transmission. Inset: electric dipole orientation (purple arrows) and magnetic dipoles (blue arrows) in a cross-section through the dielectric in the mid-rotation plane, marked by the dashed red line. Displacement currents (dashed purple lines) link electric dipoles. 77

5.5 Schematic of the currents (red arrows) in a two-rod (i.e. stacked cut-wire pair) structure with rotation ϕ between them. a) symmetric currents b) antisymmetric currents. The upper and lower rod are indicated by darker and lighter colour rendering. Displacement currents (dashed red lines) link the rods and result in magnetic fields (blue arrows) due to current loops. The net electric (magenta arrows) and magnetic (cyan arrows) dipole moments for the symmetric (c) and antisymmetric (d) modes are shown to be aligned. 78

5.6 The linear (a) and circular (b) polarised transmission coefficients for the C-cross structure across a frequency band of 5 to 40 GHz. The transmission is represented on a logarithmic (dB) scale. c) The optical rotation, ϕ (black points), calculated from the phase of RCP (red line) and LCP (blue line) transmitted radiation, according to equation 5.3. d) The ellipticity, η, of transmitted radiation calculated from the magnitude of circularly polarised transmitted radiation in (b), according to equation 5.4. Two resonant frequencies are highlighted by grey dashed lines. The frequency band of interest, where non-zero optical rotation is accompanied by negligible ellipticity, is shaded grey. 80

5.7 One unit cell of the C-cross structure showing the direction and magnitude of surface current density in the cross layer (red arrows) where the magnitude is proportional to the arrow size and is normalised for each plot. This cross, aligned along x and y, is closest to the source of radiation, and is marked by a black outline. The surface current density on the complementary cross layer beneath is illustrated by black arrows (direction) and colour scale (magnitude). (a) $f = 8.4$ GHz (b) $f = 14.8$ GHz (c) $f = 26.6$ GHz and (d) $f = 35.4$ GHz. (a) and (c) correspond to transmission maxima whereas (b) and (d) result in transmission minima due to dipolar and quadrapolar modes of the vertical arm of the cross element. Normally-incident electric field is polarised vertically. 81

5.8 Experimental measurements of transmission through the C-cross sample. a) The RCP (pink circles) and LCP (blue cross) transmission amplitudes, $\tau_{R/L}$, on a logarithmic (dB) scale. b) The optical rotation, ϕ (red circles). Results from numerical modelling are overlaid as black lines. c) The modelled ellipticity of transmitted radiation. 82

5.9 The experimentally obtained, linearly polarised transmission coefficient, t_{xx} as a function of in-plane wavevector (incident angle). Left-hand-side: transverse electric (TE) radiation, right-hand-side: transverse magnetic (TM). Quadrapolar cross modes are seen away from normal incidence. Inset: The charge configurations on the cross layer (black) and out of plane magnetic field direction within the hole (blue) for modes marked 1-3. 84

5.10 Simulated demonstration of the change in optical rotation on increasing the separation, t, between upper and lower layers. (a) Modelled optical rotation for (a) D-cross structure and (b) C-cross structure with dielectric thicknesses of 100 μm to 500 μm. (c) Upper and lower resonant frequencies (where $\phi = \pm\pi/2$) for the D-cross (unfilled) and C-cross (filled) structures for a range of separations; (d) Optical rotation midway between the two resonances. Simulations were carried out by Lauren Barr. 86

5.11 Experimental measurements of transmission through the Double-C-cross sample. a) The RCP (pink circles) and LCP (blue cross) transmission amplitudes, $\tau_{R/L}$, on a logarithmic (dB) scale. The simulated result for LCP is shown as a solid black line, with negligible difference for RCP radiation on this scale. 87

6.1 Sample illustration for a) the connected ordinary checkerboard array (CA) with square hole size L_1 b) the compound checkerboard array (CCA) with two different sized square holes per unit cell, L_1 and L_2. The CA is the CCA with $L_2 = 0$. The samples consist of a patterned metallic layer above a 25 μm Mylar substrate. 90

6.2 Modelled band structure for an ordinary (black points) and compound (red points) checkerboard array, representing the mode propagation around the irreducible Brillouin zone (see inset). Eigenfrequencies are obtained via COMSOL Multiphysics. Solid black lines represent light lines (grazing radiation). 92

6.3 Experimental band structure for the ordinary checkerboard array (CA), obtained via near field excitation and detection of surface modes. The points a-d correspond to standing wave solutions of lower and upper band edges at the X and M points. Light lines are represented as dashed lines and eigenmode positions from numerical modelling are shown as blue circles. 93

6.4 FEM predictions of electric field profiles of the CA standing wave eigenmode at the points a-d in Fig. 6.3, shown in the x-y plane at a height corresponding to the top-plane of the metallic layer. Within the holes the electric field magnitude is plotted as a colour scale (arb. units), with the instantaneous electric vector as white arrows. On the metal surface, the charge density is shown as a greyscale (arb. units), and corresponding charges labelled. The current density is plotted as orange arrows. Overlaid is an approximation to the charge modulation across the surface (black/white lines). 95

6.5 Experimental band structure for the compound checkerboard array, obtained via near field excitation and detection of surface modes. The points e-h correspond to standing wave solutions of lower and upper band edges at the X and M points. Light lines are represented as dashed lines and eigenmode positions from numerical modelling are shown as blue circles. The source antenna is positioned above (a) the larger square hole and (b) the smaller square hole. 96

6.6 Electric field profiles of the CCA standing wave eigenmode at the points e-h in Fig. 6.6, shown in the x-y plane at a height corresponding to the top-plane of the metallic layer. Within the holes the electric field magnitude is plotted as a colour scale (arb. units), with the instantaneous electric vector as white arrows. On the metal surface, the charge density is shown as a colour scale (arb. units), and corresponding charges labelled. The current density is plotted as orange arrows. Overlaid is an approximation to the charge modulation across the surface (black/white lines). 98

6.7 Experimentally obtained isofrequency contours demonstrating the in-plane wavevector of a surface wave on the regular checkerboard (a) and the compound checkerboard (b) at the same reduced frequency, $a/\lambda = 0.416$. The first Brillouin zone boundary is shown as a dashed blue line, and light circles as red and black dotted lines. The mode positions along ΓX and ΓM according to eigenmode modelling are shown as white points, and their difference in wavevector from the light line (δk_{M} and δk_{X}) is labelled 99

6.8 Experimental dispersion of radiative modes on the CCA structure for TE (left hand side) and TM (right hand side) incident polarization. The colour scale represents the transmission coefficient obtained for incident angles up to 60° and light lines are plotted as solid black lines. 100

6.9 Normal incidence transmission coefficient (logarithmic scale) as a function of frequency for the CCA structure. Experimental data is shown as a black line for L_2 =3.744 mm. Simulated transmission spectra are shown for a variety of square hole sizes, L_2. The data is terminated at the onset of diffracted orders at a normalised frequency of 1. 102

7.1 Illustration of square metallic patches of side length L rotated at 45° to a square lattice of pitch $a = 5.95$ mm. Orientation of the incident electric field vector E is also illustrated. a) disconnected patches, where metallic occupancy X = 40% b) threshold connection, X = 50% c) connected patches, X = 60% 104

7.2 50% metal occupancy arrays with increasing rotational disorder in square orientation defined by an increase in the standard deviation (σ) of a Gaussian distributed rotation: a) $\sigma = 0°$ b) $\sigma = 6°$ c) $\sigma = 10°$ d) uniform distribution corresponding to $\sigma = 26.5°$ 106

7.3 Normal incidence microwave transmission of an aluminium square checkerboard array of periodicity $a = 5.95$ mm, with increasing standard deviation, σ, in square orientation. i.e. $\sigma = 0$ corresponds to an ordered checkerboard array, with every square rotated by 45° with respect to the square lattice. a) 40% patch array b) 40% hole array c) 51% patch array d) 51% hole array e) 60% patch array f) 60% hole array. Data obtained with Chris Durrant (PhD student, Exeter). 108

7.4 Percentage of patches that are connected to at least one neighbouring square as a function of standard deviation of the rotation for both 51% and 60% patch arrays, based on a 20 × 20 array. There is a limiting standard deviation of approximately 26.5°, which corresponds to the standard deviation of the uniformly distributed sample. 110

7.5 Schematics representing the difference in connectivity of the 51% patch arrays with a standard deviation of a) 2° and b) 6°. Rather than the squares themselves, connections between them are depicted as lines between the lattice points. Disconnected squares are shown as dots. At 2° disorder ≈ 30% of squares are isolated, whereas at 6°, ≈ 70% are isolated. 111

7.6 Reflected intensity (red triangles), transmitted intensity (blue squares) and their sum (black circles) for 51% occupancy copper patch arrays with standard deviations of a) 0° b) 4° and c) 18°. The transmission in b) is an average of 6 measurements with the standard deviation represented by the grey region. 113

7.7 Schematics representing the difference in connectivity of the 51% patch arrays with a standard deviation of a) 4° and b) 18°. Connections between patches are depicted as lines between the lattice points. Disconnected squares are shown as dots. 114

7.8 a) A section of the Fibonacci checkerboard array (black corresponds to metallic regions) comprising two periods a_1 and a_2. b) A fast fourier transform of a larger sample image. 115

7.9 The dispersion of modes supported by the 'Fibonacci Checkerboard' array, represented along the irreducible Brillouin zone in reciprocal space. 117

7.10 Isofrequency contours showing the Fourier transform of experimentally obtained electric field maps at various frequencies. Zeroth order and diffracted light circles associated with the average pitch, a_{m}, are shown as red dashed lines. Additional light circles due to the quasi-periodicity are shown in purple. 119

8.1 a) The edge of a metallic checkerboard array. The array supports a mode bound to its surface, as discussed in previous chapters, and also a mode on its edge. This edge mode decays into the y and z directions and only propagates in the x direction, along the edge. b) The unit cell used in eigenmode modelling with COMSOL. The boundaries are periodic in the x direction and PEC in the y and z directions. 122

8.2 Experimentally obtained map of the z-component of electric field, recorded using a pair of stripped coaxial antennas. The source is positioned at the edge, on the left of the image. In the lower half-space a surface wave is excited on the checkerboard structure, whereas in the upper half-space, free-space radiation is observed with weaker amplitude. Along the edge a mode is supported that propagates from left to right and decays in the y-direction. 123

8.3 The dispersion of modes obtained via a Fast Fourier Transform of the image in Fig. 8.2 for a range of frequencies. The x-axis corresponds to the wavevector component in the x-direction. The dispersion of the edge mode is clear, with large Fourier amplitude due to strong coupling to the mode in the experiment. A surface mode is also supported with weaker Fourier amplitude and smaller k_{x} for all frequencies. Eigenmode positions according to numerical simulations are overlaid for both the surface (red squares) and edge (blue circles) modes. 124

8.4 a) The electric field magnitude (colour plot), vector (red arrows) and current density (white arrows) for the standing wave solution at $k_x = \pi/a$. Like the surface wave, the edge wave has transverse magnetic polarisation. Additional unit cells either side are shown as a guide. b) The edge mode frequency at the edge of the Brillouin zone ($k_x = \pi/a$) for increasing rows of checkerboard holes in a metallic sheet. The unit cell for each is shown inset. 125

8.5 Schematic of the coupled edge samples with separation of a) 3 mm and b) 1 mm. Orange asterix represents the position of near field antenna. . 127

8.6 The dispersion of modes supported on the coupled edge sample with edge separation $s = 3$ mm, with results from eigenmode modelling overlaid. Two modes are excited, corresponding to antisymmetric (green circles) and symmetric (yellow squares) E_z field with respect to a line midway between the two edges. The frequency splitting of the standing wave solutions at the Brillouin zone is ≈ 1 GHz. 128

8.7 The dispersion of modes supported on the coupled-edge sample with edge separation $s = 1$ mm, with results from eigenmode modelling overlaid. Two modes are excited, corresponding to antisymmetric (green circles) and symmetric (yellow squares) E_z field with respect to a line midway between the two edges. The frequency splitting of the standing wave solutions at the Brillouin zone is ≈ 3 GHz. 129

8.8 The E_z field (out of plane component) measured at 12 GHz and separation $s = 1$ mm. The source is positioned on the left hand edge of the image. The field shows that the E_z field of the lower frequency mode has asymmetric character. 130

8.9 The E_z field (out of plane component) measured at 19.1 GHz and separation $s = 1$ mm. The source is positioned on the left hand edge of the image. The field shows that the E_z field of the higher frequency mode has symmetric character. 131

8.10 a) The proposed modified geometry for conversion between surface and edge modes. The depth of the zigzag groove is reduced to $a\tan(30)/2$ in order to increase the frequency of the edge mode. b) Preliminary modelling results showing a surface wave impinging on the boundary to free space. An edge wave is seen propagating from left to right. 132

9.1 a) Direction of group velocity (red arrows) and phase velocity (blue arrows) as a wave passes from a positive index material (PIM) into a negative index material (NIM). Negative refraction occurs and the transmitted ray appears on the same side of the normal as the incident ray. Inside the NIM, group and phase velocities are in opposite directions. b) A NIM acting as a superlens. Rays emitted from an object focus within the NIM and again on the opposite side, forming an image. 135

9.2 Figure published in [2]. a) A section of the Sievenpiper mushroom array b) The simulated dispersion curve covering the irreducible Brillouin zone. ΓX and ΓM correspond to propagation along the x direction and 45° in-plane direction respectively. Both of these sections of the dispersion contain a region of negative mode index. 136

9.3 Sections of the three metallic waveguides studied. A) the coupled domino waveguide B) the hook or 'J' waveguide and C) the rectangular split ring resonator chain. The experimental samples (B and C) were attached to a Mylar substrate and the chains contained approximately 100 and 200 unit cells respectively. 137

9.4 a) Schematic demonstrating the glide operation on a coupled domino waveguide. Colours are used to highlight different regions of the geometry and do not correspond to any physical quantity. b-c) The two degenerate field solutions at the Brillouin zone of the waveguide's dispersion diagram, where the wavelength $\lambda = 2a$. The colour plot and black arrows represent the z component of the electric field and the Poynting vector, S, respectively. The two modes have the same energy (and frequency) but propagate in opposite directions. 138

9.5 The simulated dispersion diagram for the glide domino structure in Fig. 9.3A which supports two coupled bound modes. Points indicate eigenmode solutions according to COMSOL. The wavevector axis spans from zero to the edge of the first Brillouin zone. Inset: The x component of time-averaged power flow 0.5 mm above the metal surface (colour scale) and the Poynting vector (arrows) for the two eigenmodes at a normalised in-plane wavevector of 0.8 (marked (1) and (2)). The modes have opposing power flow and hence opposite group velocity (also evident by the gradient of the dispersion curve). The light line is shown in red. The origin of this dispersion relation is discussed in Sec. 2.6 and Fig. 2.14 in particular. 139

9.6 The x component of the power flow, integrated over the entire unit cell volume, S_x, as a function of normalised in-plane wavevector. These values are obtained from eigenmode simulations using COMSOL for each of the one-dimensional waveguides studied: lower frequency mode of the glide domino (hollow green circles/solid line), higher frequency mode of the glide domino (filled green circles/dashed line), the hook waveguide (blue squares) and the split ring resonator waveguide (red triangles). The negative region of the y axis (grey area) has been scaled by a factor of 10 for clarity. The S_x values at $k_x a/\pi = 1$ have been interpolated (black lines) from the preceding points due to the inability to distinguish degenerate modes at the Brillouin zone boundary using the eigenmode model. 141

9.7 The z component of magnetic field, H_z, 1 mm above the glide domino structure. Power propagation is from right to left, as is the direction of group velocity, v_g. Each successive image shows an advance in phase by 45°. Along the central plane of the waveguide (white line), the phase fronts appear to flow forwards (dashed magenta line), i.e. phase velocity in the same direction to group velocity. However on the outside of the guide (black line), where the mode decays in the ± y direction, the phase fronts advance backwards (dashed cyan line), suggesting v_p, v_g are in the opposite direction. This is a typical shortcoming of defining phase velocity in a photonic crystal, where the structuring is not significantly subwavelength in size. Despite this, such materials are often deemed to have 'negative index'. 143

9.8 a) The normalised electric field magnitude on the top face of the waveguide for $k_x a/\pi = 1$ (edge of first BZ). Arrows represent instantaneous electric field magnitude and direction. The source antenna (see Fig. 3.11) is positioned in order to couple to the mode where the electric field strength is largest. b) The normalised instantaneous normal (z) component of the magnetic field and the current density on the metal surface (arrows). Both have the phase advanced by $\pi/2$ relative to (a). c) The normalised time averaged power flow (colour scale) in the x direction at $k_x a/\pi = 0.8$, along with the Poynting vector (arrows) 0.4 mm above the top face of the waveguide for . White regions represent metal in a) and b).144

9.9 Experimentally obtained dispersion curve for the planar hook waveguide (shown inset). Eigenmodes of the system according to numerical modelling are shown as red circles, and the light line as a solid red line. The greyscale signifies the amplitude of Fourier components present in the measured instantaneous field image. The dispersion is obtained via a Fourier Transform of the instantaneous electric field profile across the surface of the sample, an example of which is shown above for a frequency of 6.4 GHz (blue line). The E_z scale has arbitrary units and is normalised to unity. 146

9.10 The time averaged power flow (given by the Poynting vector) in the direction of mode propagation (S_x) on three orthogonal planes about the unit cell centre. a) S_x in the plane of the waveguide (xy) integrated over the z direction. b) S_x in the yz plane integrated over the x direction. c) S_x in the xz plane integrated over the y direction. The position of the waveguide is shown as solid black lines. 147

9.11 The numerically modelled z-component of magnetic field, H_z, 1 mm above the 'hook' waveguide structure. Power propagation along the guide is negative: from right to left, as is the direction of group velocity, v_g. Each successive image shows an advance in phase by 45°. Phase fronts move forwards both along the central plane of the waveguide (white line) outside of the guide (black line), where the mode decays in the ± y direction. The propagation of phase fronts in the same direction everywhere on the guide suggests that the guide is acting as an effective medium, with negative v_g and positive v_p and therefore negative mode index. 148

9.12 The experimentally obtained dispersion curve for the lowest order mode supported by the split-ring resonator chain. The x-axis spans from zero to the edge of the first Brillouin zone at $k_x a/\pi = 1$. The results from eigenmode modelling are shown as red circles and the light line is marked in red. For in-plane wavevector with magnitude above 0.26, the mode supported has counterpropagating group and phase velocities, and hence negative mode index. 150

9.13 a) The normalised electric field magnitude on the top face of the waveguide for $k_x a/\pi = 1$ (edge of first BZ). Arrows represent instantaneous electric field. b) The normalised instantaneous normal (z) component of the magnetic field and the current density on the metal surface (arrows). Both with the phase advanced by $\pi/2$ relative to (a). c) The normalised time averaged power flow in the x-direction at $k_x a/\pi = 0.9$, along with the Poynting vector 0.4 mm above the top face of the waveguide. 151

9.14 The experimentally measured z-component of the instantaneous electric field, on a plane 1 mm above the split-ring resonator waveguide. Each successive plot is advanced in phase by 60° and the phase fronts traced to observe the direction of phase velocity. A positive v_p wave can be seen by tracing the minimum in E_z along a line at $y = 10$ mm and a negative v_p wave (green line) along $y = 3$ mm, both with positive v_g. 152

9.15 The equivalent circuit (A) and dispersion curves (B) for a transmission line that is right handed (a), left handed (b) and composite right/left handed (c) 153

9.16 The quadrafilar spiral geometry. The unit cell (inset) consists of a single four-armed spiral shaped hole in a metal sheet. Each arm undergoes five 90° bends creating a square quadrafilar spiral with periodicity $a = 2.8$ mm. The arms have width $w = 200$ μm and the gap between them $g = 200$ μm. 155

9.17 The 2D dispersion of the spiral array, covering the irreducible Brillouin zone defined by the points Γ, X and M in reciprocal space. Eigenmode positions according to numerical modelling are shown as red circles. The red dashed lines correspond to frequencies at which isofrequency contours are plotted in Fig. 9.18. 156

9.18 Isofrequency contours at a) 9.46 GHz b) 9.7 GHz (marked as red dashed lines in Fig. 9.17). In a) the direction of group velocity (power flow) is represented as arrows (Blue: v_g positive. Red: v_g negative) 157

10.1 a) The substitution method for generating a segment of the aperiodic Penrose tiling shown in b). The tiling is composed of narrow (36°, blue) and wide (72°, red) rhombs and has 5-fold rotational symmetry about its centre. 162

10.2 a) The substitution method for generating the quasiperiodic diamond tiling shown in b). Each diamond (red) is divided into 8 smaller diamonds in the shape of an arrow (blue). These are then divided again (green). 163

10.3 A section of the Penrose (a), quasiperiodic diamond (c) and box diamond (e) tilings. Black lines represent copper traces on the sample of width 0.5 mm. Each rhomb has side length $L = 5$ mm. The corresponding Fourier spectra for the images in a,c,e are shown in b,d,f. 164
10.4 a) The normal component of the instantaneous electric field, measured on a plane 1 mm above the quasiperiodic diamond sample at 25.9 GHz. The source is positioned in the centre of the image. b) The FFT of the image in (a). Peaks in the Fourier amplitude map out the isofrequency contours of modes supported by the metasurface. 165
10.5 a) The normal component of the instantaneous electric field, measured on a plane 1 mm above the Penrose tiling sample at 26.2 GHz. The source is positioned in the centre of the image. b) The FFT of the image in (a). Peaks in the Fourier amplitude map out the isofrequency contours of modes supported by the metasurface. 166

Chapter 1

Introduction

1.1 Aim of Research

Since the development of radar in the middle of the 20th century, the design of structured metallic surfaces to manipulate the propagation of long-wavelength radiation has been of utmost importance to the defence and telecommunications industries; from filters which can be configured to transmit or reflect specific frequency bands (known as frequency-selective-screens), to absorbing materials and polarisation converters. Despite the wealth of studies over the years, many challenges remain in this research area where more compact, flexible and broadband structures are always desirable. The emergence of the field of metamaterials since the turn of the century has led many to focus on the microwave regime, where subwavelength structure can be easily fabricated and manufactured, and concepts tested for future applications at higher frequencies. Significant advances in fabrication techniques such as 3D printing have led to the development of metamaterials with an array of properties. The work presented in this thesis concerns the investigation of some of these properties including polarisation manipulation, surface mode isotropy, edge localisation of modes and negative mode index.

1.2 Outline

The aim of this thesis is to investigate surface waves supported on a variety of metallic metasurfaces at microwave frequencies. The goal is to characterise the propagation of these surface waves in the plane of the structure and in some cases study how their presence gives rise to features in the scattering parameters of radiation incident on the metasurface.

In the following chapter, a historical background is presented along with a review of relevant theory on the broad topic of metasurfaces and waves bound to interfaces. Chap-

ter 3 goes on to explain specific experimental and numerical methods used throughout the work presented in this thesis. In addition, fabrication methods and data analysis tools are outlined, providing a basis to follow the proceeding experimental chapters.

Chapters 4 and 5 investigate polarisation manipulation using 3-layer metasurfaces. In Chapter 4, a reflecting anisotropic microcavity array is designed to convert linearly polarised incident radiation to its orthogonal polarisation state upon reflection. Absorption in the resonant cavities is minimised, resulting in 98% reflected intensity with converted polarisation over a 2.5 GHz band centred at 10 GHz. A modification of the geometry is shown to provide linear to circular conversion over a similar bandwidth. In Chapter 5, a chiral metasurface is used to provide a rotation of linearly polarised radiation upon transmission through the structure. This is possible due to circular birefringence; a differential phase change for left and right handed polarisation. The structure contains two metallic layers patterned with cross-shaped elements in a square array, with those of the bottom layer rotated by 22.5° with respect to the upper layer. The origin of optical rotation in such chiral metasurfaces is explained as a resonant effect. At frequencies between two resonances, a dispersionless band of non-zero rotation is observed. The sensitivity of both the bandwidth and degree of rotation to changes in the layer separation is shown to depend on the electrical connectivity of each of the two metallic layers and a multilayer system is proposed in order to enhance the bandwidth of transmission.

Chapters 6 and 7 focus on variations of a single layer metallic checkerboard metasurface. In Chapter 6, a compound checkerboard geometry is studied, which consists of two arrays of different sized square holes offset from one another in both in-plane directions. Surface waves propagating in the plane of the metasurface are shown to have greater isotropy than in the ordinary checkerboard case. Further, the structure is shown to exhibit a sharp resonance in its transmission spectrum, the width of which is controlled by the ratio of square sizes. Chapter 7 presents two non-periodic variations. First, disorder is gradually introduced by rotating each patch about its lattice point. This perturbative approach allows the transition from an electrically connected (inductive) structure to a disconnected (capacitive) structure to be studied. An inversion of the transmission spectrum is observed as this transition occurs. The effect of disorder in the geometry is maximised when half of the metallic squares are isolated from their neighbours. At this level of disorder scatter loss is maximised, with only 60% of incident power detected in the speculation reflection and transmission paths.

In Chapter 8, modes localised at the edge of the metallic checkerboard samples are investigated. These modes exponentially decay in both transverse directions and propagate along the edge. They are distinct from the well-studied topologically-protected edge modes that occur in the band gap of bulk states; instead they exist as surface

states supported on an extremely narrow region at the sample's edge. Much like surface waves, the edge waves are shown to couple together creating a symmetric/anti symmetric pair. Finally, the prospect of mode conversion between the surface and edge waves is discussed.

Chapter 9 focuses on the phenomenon of negative mode index. First, one dimensional planar metallic waveguides that support a mode with negative mode index, i.e. opposite signs of group and phase velocity, are studied. To achieve this, current loops that provide the waveguide with a magnetic polarisability are required within each subwavelength element. The much-studied split-ring resonator is shown experimentally to support such a mode, the asymptotic frequency of which is reduced by lengthening the current loop in the transverse direction. The concept is extended to a two-dimensional surface mode that has negative mode index in all propagation directions in the plane of the structure. This is achieved using a four-armed spiral shape geometry and is experimentally verified. This presents the first observation of a surface wave with all-angle negative mode index supported on a single patterned metallic layer.

Finally, Chapter 10 presents a study of surface wave propagation on non-periodic rhombic tiling arrays. The metasurfaces studied consist of rhombic-shaped holes arranged in two tilings; the Penrose tiling and a quasiperiodic diamond tiling, both of which are deterministic, yet non-periodic. Despite this, their Fourier spectra contain peaks corresponding to scattering planes of the structure, allowing surface waves to be supported. The isofrequency contours of these surface waves reveal the underlying symmetry of the array. This demonstrates the advantage of quasicrystalline surfaces; they can have symmetries that periodic geometries can not. For instance, the Penrose tiling supports a mode that, at a certain frequency, directs the majority of power into ten beams (due to five-fold rotational symmetry).

Chapter 2

Theory

2.1 Introduction and Historical Background

Bound surface modes can be supported by metallic surfaces at microwave frequencies despite the high conductivity of metals. This may be achieved by adding subwavelength-scale surface texture that changes the boundary condition and allows electromagnetic fields to penetrate the effective surface, something which is not possible with planar near-perfect conductors at low frequencies. In this chapter, the origin of modes supported at an interface between two dissimilar media across the entire electromagnetic spectrum is discussed. This covers studies in the early 20th century at radio frequencies of planar and corrugated surfaces, the surface impedance description of interfaces, and waves supported by periodic surfaces. Since the turn of the century, the field of metamaterials has emerged; materials composed of subwavelength 'meta-atoms' which can be designed to provide the structure with macroscopic properties vastly different from its constituent materials. Examples of such phenomena include negative refractive index, polarisation rotation, large effective permittivity or permeability, electromagnetic absorption and anisotropic propagation of waves. Many of these concepts will be investigated throughout this thesis.

One of the earliest studies of waves localised at the interface between two media was performed by Zenneck in 1907[3], who found a solution to Maxwell's equations for a wave at an interface between air and salt (which has non-zero conductivity). Later, Sommerfeld studied the guiding of radio waves around the surface of the Earth[4] and further studies followed in the middle of the 20th century as a result of radar development[5][6][7]. Research on periodic surfaces continued into the 1970s, with Cutler[8] employing grooves in a metallic surface in order to enhance localisation of radio waves to the exterior of aircraft, and Ulrich and Tacke[9] studying surface waves supported by a metallic mesh. An overview of the field of surface waves is covered by

many electromagnetic textbooks[10], with that of Collin[11] providing the basis for the background theory presented in this chapter.

In parallel with the surface wave research path discussed above, in 1941 Fano conducted a theoretical study of total internal reflection within a glass layer above a metal sheet at optical frequencies[12]. When characterising the propagation of waves within the glass with varying thickness, he discovered a single solution to Maxwell's equations as the thickness tended to zero. This solution is now known as a surface plasmon polariton (SPP), a trapped mode at the interface between a metal and a dielectric which decays exponentially into both media either side.

Bound surface waves are normally dispersive, meaning the energy (frequency) and momentum (wavevector) of the wave do not have a linear relationship. An example of a surface wave dispersion is illustrated in Fig. 2.1. The mode becomes more tightly bound to the surface and propagates at a slower speed as the frequency increases. The mode propagation halts entirely at the asymptotic frequency, ω_0. For the SPP this asymptotic frequency corresponds to the surface plasma frequency; the natural frequency of oscillating electrons on the surface of a metal. For a structured surface, ω_0 corresponds to the structural resonance associated with each subwavelength element. At lower frequencies (orange region) where the dispersion follows closely to the light line, a mode guided by an interface is more appropriately called a 'surface current', as the surface acts to guide the wave rather than bind it. The remainder of this chapter begins with a brief description of the Drude model for a free-electron gas, followed by the derivation of a guided wave on a planar interface. From there, the structuring of the surface, which results in the trapping of the wave at microwave frequencies, is discussed.

2.2 Drude Model

The frequency dependence of the complex permittivity, ε of metals is described using the Drude model for a free-electron gas[13], which states that

$$\varepsilon(\omega) = 1 - \frac{\omega_\mathrm{p}^2}{\omega^2 + i\omega/\tau} \tag{2.1}$$

where i is the imaginary unit, ω_p is the 'plasma frequency'; the natural frequency of conducting electrons in the bulk of the material which typically occurs at ultraviolet (UV) frequencies and above which the metal becomes transparent, and τ is the mean free time between collisions for an electron within the material[1]. Fig. 2.2a plots the real and imaginary parts of the permittivity for silver as a function of frequency, highlighting the difference between the microwave and visible/UV regimes.

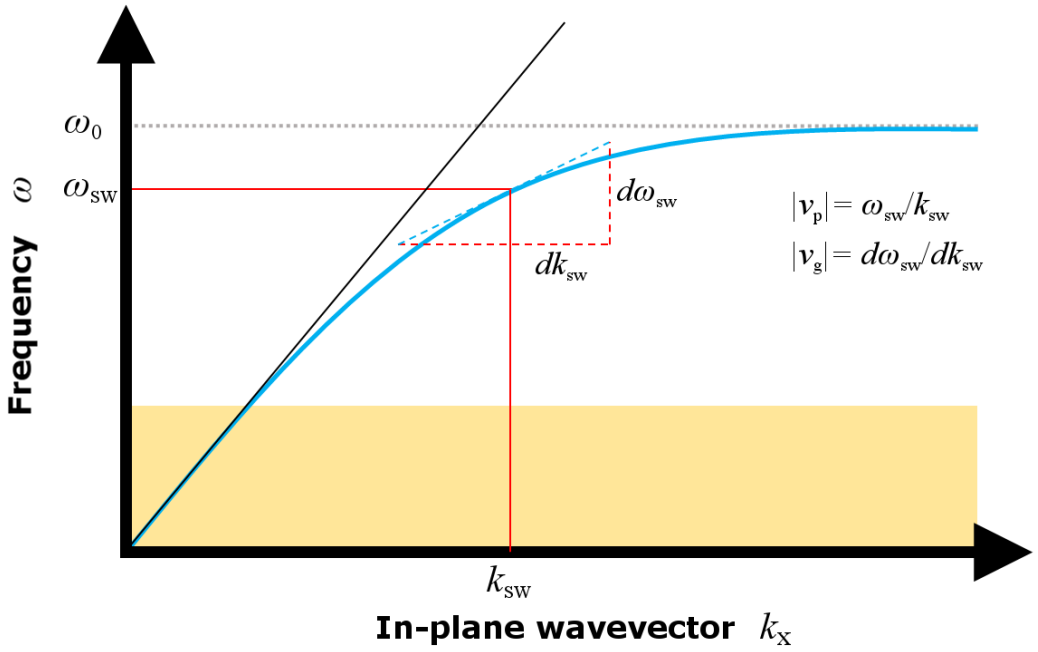

Figure 2.1: The schematic illustration of the dispersion curve (blue line) of a surface wave that asymptotes to frequency, ω_0 (grey dotted line), which corresponds to the resonant frequency of oscillating electrons for a planar metallic interface or the resonance of a single subwavelength element in the periodic surface case. At lower frequencies (orange region), the mode is best described as a surface current; loosely bound to the interface and propagating close to the speed of light, c. The phase velocity of the surface mode is given by the ratio of ω to k_x and defines the mode index, $n = c/v_p$. The group velocity is defined by the gradient of dispersion (dashed blue line) and falls to zero at ω_0. The light line (black line) represents the dispersion of grazing plane wave radiation, where $v_p = v_g = c$.

The frequency dependence of permittivity demonstrates that the polarisation within a material is not an immediate response to the applied field. The permittivity is complex, and the real and imaginary parts correspond to energy stored within the material and energy lost, respectively. The real part is large and negative for microwave frequencies, whereas the imaginary part is positive and large compared to visible/UV regimes. It is these properties that allow one to assume that a metal is a perfect electrical conductor (PEC) with no field penetration into the metal, at microwave frequencies, as shown in Fig. 2.4b.

2.3 Surface Waveguides

A surface waveguide is an open-boundary structure that supports a mode that is bound to its surface and propagates along it according to the wavefunction $\exp(ik_x x)$. The

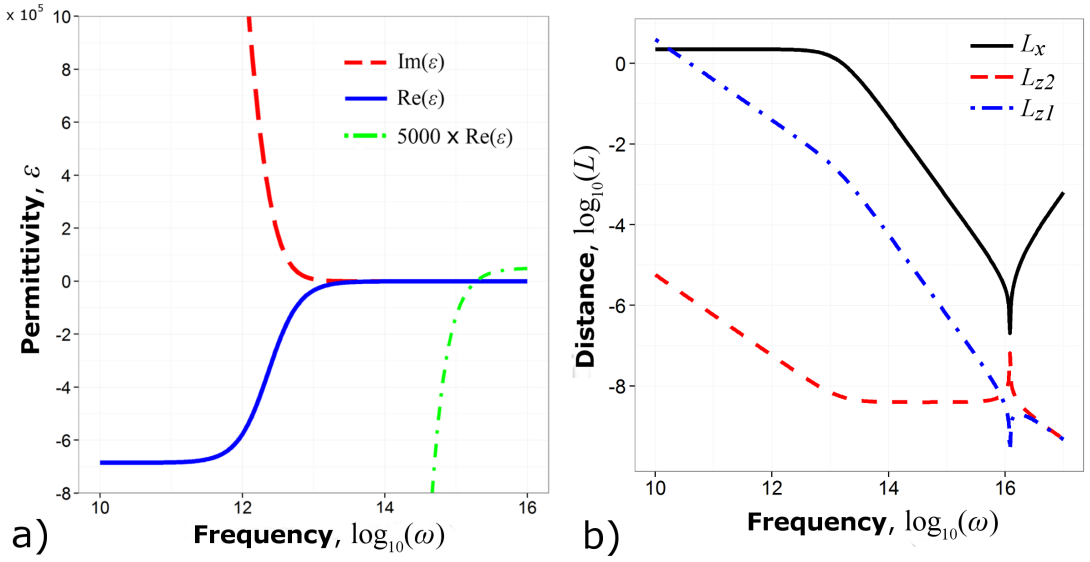

Figure 2.2: a) The complex relative permittivity as a function of frequency for silver. The real part is magnified by 5×10^3 (green dot-dashed line) to show the frequency at which it passes though zero . This is based on a plasma frequency $\omega_p = 1.2 \times 10^{16}$ rad/s and mean free time $\tau = 6.9 \times 10^{-14}$ s. b) The propagation length (black line), and penetration depths of a wave guided by a planar interface between silver (red dashed) and air (blue dot-dashed) as a function of frequency, ω, according to equations 2.20 and 2.22.

fields of the mode exponentially decay away from the surface in the z direction and hence k_z is purely imaginary. Two structures that can support such a mode at microwave frequencies are shown in Fig. 2.3, one is a planar PEC surface coated with a dielectric layer (a), the other a corrugated PEC surface (b). In this section, the properties of these surface waves are investigated.

2.3.1 Planar Interface

First consider an interface between two dissimilar, non-magnetic, dielectric media. Such an interface can guide plane waves; a phenomenon first studied in the early 20th century by Zenneck[3], after whom the waves are commonly known. Fig. 2.4a shows a transverse magnetic (TM) polarised plane wave propagating in free-space (medium 1, with permittivity $\varepsilon_1 = \varepsilon_0$) and impinging on the interface at an angle θ_i to the surface normal. In general, both a reflected and transmitted wave exist for $x > 0$. The transmitted wave refracts into medium 2 (permittivity $\varepsilon_2 = \epsilon_r \varepsilon_0$) at angle θ_r to the surface normal. The relative permittivity ϵ_r of the medium is, in general, a complex parameter with a real (ϵ_r') and imaginary part (ϵ_r'').

The derivation of a bound mode requires a reflectionless interface (i.e. the surface

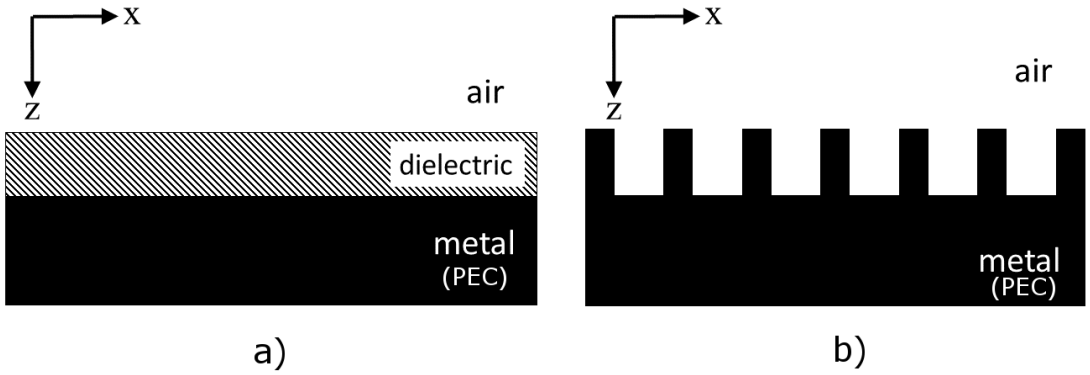

Figure 2.3: a) A planar metallic surface with dielectric overlayer b) A corrugated perfect electrical conducting surface. Both support a bound surface wave at microwave frequencies.

mode does not require incident radiation), which for the case of a lossless medium ($\epsilon'' = 0$), is satisfied for a particular angle of incidence, θ_0, known as the Brewster angle. When losses are introduced into medium 2 there is no *real* incident angle corresponding to a reflection-less interface, however there exists a solution for an inhomogeneous TM plane wave with a *complex* angle of incidence, which is derived below.

The ray picture shown in the schematic in Fig. 2.4a shows that at the interface, TM incident radiation with wavenumber and electric field magnitude given by k_0, E_0 is either reflected into medium 1 (white) or transmitted into medium 2 (grey). The wave contains only x and z components of its wavevector, with $k_\mathrm{y} = 0$. For this TM case, the electric $\mathbf{E_m}$ and magnetic $\mathbf{H_m}$ fields in each medium can be expressed as,

$$\mathbf{E}_m = [E_{\mathrm{x}_m}, 0, E_{\mathrm{z}_m}] \exp(i(\mathbf{k}_m \cdot \mathbf{x} + \mathbf{k}_m \cdot \mathbf{z})) \exp(-i\omega t) \tag{2.2}$$

$$\mathbf{H}_m = [0, H_{\mathrm{y}_m}, 0] \exp(i(\mathbf{k}_m \cdot \mathbf{x} + \mathbf{k}_m \cdot \mathbf{z})) \exp(-i\omega t) \tag{2.3}$$

where the vectors E and H (square brackets) represent the polarisation state, i.e. the magnetic field has only a y component, whereas the electric field is in the xz plane. The first exponential term is a spatially-dependent component defining the wavevector (i.e the direction of propagation and the wavelength) and the second exponential is the time-dependent oscillatory component related to the angular frequency ω.

A trapped surface wave requires no incident field and hence $\mathbf{E}_0$ and $\mathbf{H}_0$ are set to zero, leaving expressions for the electric and magnetic fields in media 1 and 2 as,

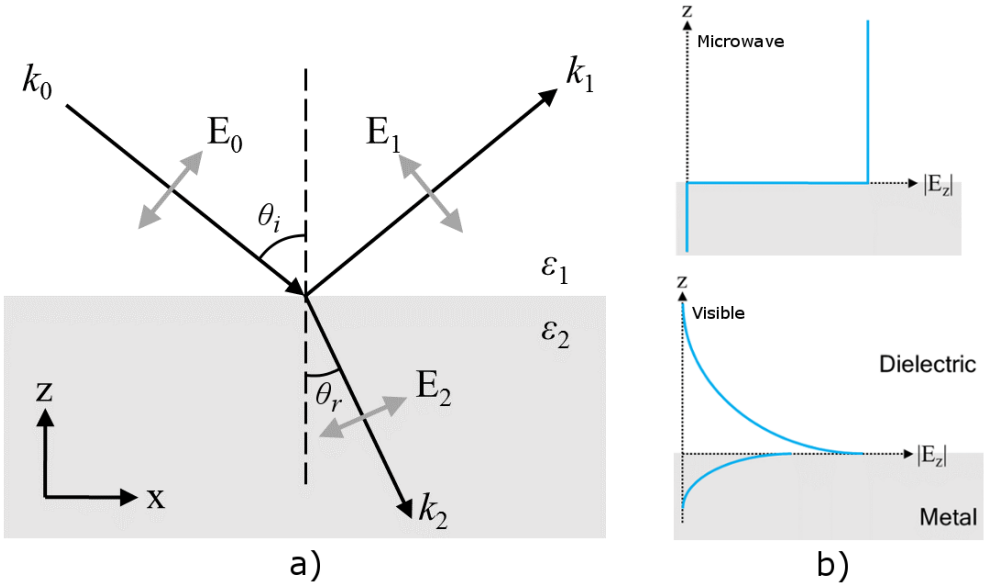

Figure 2.4: a) A ray picture of a wave incident on the interface between two dissimilar media, with transverse magnetic (TM) polarisation. b) The penetration depth of electric field into a metal and dielectric (air) for visible and microwave frequencies. This is caused by the change in permittivity of metals as a function of frequency (Drude model, Sec. 2.2) and as a result a tightly bound surface mode is supported by a planar metallic interface at higher frequencies, whereas surface currents (loosely bound) exist in the microwave regime.

$$\mathbf{E}_1 = [E_{\mathrm{x}_1}, 0, E_{\mathrm{z}_1}] \exp(i(k_{\mathrm{x}_1} x + k_{\mathrm{z}_1} z)) \exp(-i\omega t) \tag{2.4}$$

$$\mathbf{H}_1 = [0, H_{\mathrm{y}_1}, 0] \exp(i(k_{\mathrm{x}_1} x + k_{\mathrm{z}_1} z)) \exp(-i\omega t) \tag{2.5}$$

$$\mathbf{E}_2 = [E_{\mathrm{x}_2}, 0, E_{\mathrm{z}_2}] \exp(i(k_{\mathrm{x}_2} x - k_{\mathrm{z}_2} z)) \exp(-i\omega t) \tag{2.6}$$

$$\mathbf{H}_2 = [0, H_{\mathrm{y}_2}, 0] \exp(i(k_{\mathrm{x}_2} x - k_{\mathrm{z}_2} z)) \exp(-i\omega t) \tag{2.7}$$

where k_{x_m} and k_{z_m} are the *complex* wavevector components in medium m. Boundary conditions at the interface link the field components above and below it as follows,

$$E_{\mathrm{x}_1} = E_{\mathrm{x}_2} \tag{2.8}$$

$$H_{\mathrm{y}_1} = H_{\mathrm{y}_2} \tag{2.9}$$

$$\varepsilon_1 E_{\mathrm{z}_1} = \varepsilon_2 E_{\mathrm{z}_2}. \tag{2.10}$$

The first and second of these ensure that E_{x} and H_{y} are continuous across the

boundary, whereas the third is the continuity of electric displacement field D.

Ampere's Law links the curl of the magnetic field to the time derivative of the electric field in each medium

$$\nabla \times \mathbf{H}_m = \varepsilon_m \frac{\partial \mathbf{E}_m}{\partial t}, \tag{2.11}$$

which for this TM case can be reduced to two equations linking the electric and magnetic fields in each medium via the permittivity of the medium ε_m by substituting in equations 2.4 - 2.7,

$$k_{\mathrm{z}_1} H_{\mathrm{y}_1} = \omega \varepsilon_1 E_{\mathrm{x}_1} \tag{2.12}$$

$$k_{\mathrm{z}_2} H_{\mathrm{y}_2} = -\omega \varepsilon_2 E_{\mathrm{x}_2} \tag{2.13}$$

These can be combined using the continuity of tangential electric field (equation 2.8) to give,

$$\frac{k_{\mathrm{z}_1}}{\varepsilon_1} H_{\mathrm{y}_1} + \frac{k_{\mathrm{z}_2}}{\varepsilon_2} H_{\mathrm{y}_2} = 0. \tag{2.14}$$

and subsequently the continuity of transverse magnetic field (equation 2.9) gives,

$$\frac{k_{\mathrm{z}_1}}{\varepsilon_1} + \frac{k_{\mathrm{z}_2}}{\varepsilon_2} = 0 \tag{2.15}$$

From this point onwards ε_{m} is taken to be the *relative* permittivity in each medium. The conservation of total momentum, $\varepsilon_m k_0^2 = k_{\mathrm{x}_m}^2 + k_{\mathrm{z}_m}^2$, combined with the conservation of tangential momentum $k_{\mathrm{x}_1} = k_{\mathrm{x}_2} = k_{\mathrm{x}}$ gives

$$k_{\mathrm{x}}^2 + k_{\mathrm{z}_m}^2 = \varepsilon_m \left(\frac{\omega}{c}\right)^2 \tag{2.16}$$

where $k_0 = \omega/c$. When substituted into equation 2.15, this yields the dispersion relation for a bound mode on the planar interface linking the angular frequency ω to the complex in-plane wavevector k_{x},

$$k_{\mathrm{x}} = \frac{\omega}{c} \sqrt{\frac{\varepsilon_1 \varepsilon_2(\omega)}{\varepsilon_1 + \varepsilon_2(\omega)}}. \tag{2.17}$$

where the square root term is known as the mode index. By definition, the fields of a bound surface wave decay exponentially into the surrounding media, i.e. k_{z_m} is purely imaginary. The penetration of field into each medium m is given by the penetration (or skin) depth, L_{z}, defined as the distance at which the amplitude of field has dropped

to $1/e$ of its value at the interface. Substituting the dispersion relation (equation 2.17) into equation 2.16 reveals an expression for k_{z_m},

$$\mathrm{Im}(k_{z_m}) = \pm k_0 \sqrt{\frac{\varepsilon_m^2}{\varepsilon_1 + \varepsilon_2}} \tag{2.18}$$

Consider that medium 1 is a dielectric with $\mathrm{Re}(\varepsilon_1) > 0$ and $\mathrm{Im}(\varepsilon_1) = 0$ (does not absorb), and medium 2 is a realistic metal with $\mathrm{Re}(\varepsilon_2) < 0$ and $\mathrm{Im}(\varepsilon_2) > 0$. Further, using the valid assumptions at microwave frequencies that $\mathrm{Re}(\varepsilon_2) << -1$ and $|\mathrm{Re}(\varepsilon_2)| >> |\mathrm{Im}(\varepsilon_2)|$, the expression for k_z can be reduced to,

$$k_{z_m} = \pm k_0 \sqrt{\frac{|\mathrm{Re}(\varepsilon_m)^2|}{|\mathrm{Re}(\varepsilon_2)|}} \tag{2.19}$$

which corresponds to a penetration depth of,

$$L_{z_m} = \frac{1}{k_{z_m}} = \frac{\lambda_0}{2\pi} \sqrt{\frac{\mathrm{Re}(\varepsilon_2)}{\mathrm{Re}(\varepsilon_m)^2}}. \tag{2.20}$$

For a typical silver/air interface this corresponds to $L_{z_2} = 6$ μm in the silver and $L_{z_1} = 4$ m in the air for a frequency of 10 GHz ($\lambda_0 = 3$ cm). The ratio of the decay into the two regions is much closer to unity for radiation in the visible spectrum than for microwaves, with $L_{z_2} = 25$ nm and $L_{z_1} = 240$ nm for red light ($\lambda_0 = 440$ nm). This difference in penetration depth between the two regimes is shown schematically in Fig. 2.4b. At visible frequencies, this mode is known as a surface-plasmon-polariton; an electromagnetic wave coupled to a longitudinal charge oscillation on the surface of the metal. At microwave frequencies it is more accurately described as a surface current, with the planar interface acting to guide the loosely-bound wave rather than bind it. In a later section, it will be shown that the penetration into the interface of a material can be effectively increased by adding subwavelength-scale surface structure.

The imaginary part of the in-plane wavevector, k_x, describes the spatial decay of the mode along the interface, also known as the propagation length. Rearranging the dispersion relation (equation 2.17) into a sum of its real and imaginary parts gives

$$\mathrm{Im}(k_x) = \frac{k_0 \mathrm{Im}(\varepsilon_2)}{2\mathrm{Re}(\varepsilon_2)^2} \left(\frac{\varepsilon_1 \mathrm{Re}(\varepsilon_2)}{\varepsilon_1 + \mathrm{Re}(\varepsilon_2)} \right)^{3/2} \tag{2.21}$$

and the reciprocal of this value is the propagation length, L_x

$$L_x = \lambda_0 \frac{\mathrm{Re}(\varepsilon_2)^2}{2\pi \mathrm{Im}(\varepsilon_2)} \left(\frac{\varepsilon_1 + \mathrm{Re}(\varepsilon_2)}{\varepsilon_1 \mathrm{Re}(\varepsilon_2)} \right)^{3/2} \tag{2.22}$$

Again using the silver/air example the mode has a propagation length of $L_x = 14$ m

at microwave frequencies (10 GHz) and $L_x \approx 30$ μm for red light. Fig. 2.2b shows the variation in propagation length as a function of frequency for silver (solid black line), using the Drude model[13] to describe permittivity, as outlined above.

2.3.2 Impedance Description of Surfaces

As mentioned before, a corrugated PEC surface can support a bound surface mode at microwave frequencies. Such non-planar surfaces are often described by a surface impedance, $Z_s = R_s + iX_s$, a complex parameter consisting of a resistive (R) and reactive (X) term that together define the characteristics of any modes supported. A TM mode requires the reactive part of Z_s to be inductive (a simple planar metallic surface below ω_p is an example), whereas for TE mode propagation the reactive part must be capacitive. In this section, the dispersion relation is again derived, this time in terms of surface impedance.

A TM surface wave has a single magnetic field component, with spatial variation given by

$$H_y = H_0 \exp(-i(k_x x + k_z z))) \tag{2.23}$$

where H_0 is the constant field amplitude and $k_x^2 + k_z^2 = k_0^2$. Maxwell's equations link H_y to the two electric field components (E_x and E_z) via the following

$$i\omega\varepsilon_0 E_x = \frac{\partial H_y}{\partial z} \tag{2.24}$$

$$i\omega\varepsilon_0 E_z = -\frac{\partial H_y}{\partial x}. \tag{2.25}$$

The surface impedance is given by the ratio of the electric to the magnetic field, of which there is only one component at the interface ($z = 0$) for a TM mode, H_y and E_x. The surface impedance is therefore given by

$$Z_s(\mathrm{TM}) = \frac{E_x}{H_y} = \frac{k_z}{\omega\varepsilon_0} = \frac{k_z}{k_0} Z_0 \tag{2.26}$$

where Z_0 is the impedance of free space, and k_z/k_0 is the normalised surface impedance Z_S. Note that, as k_z of the assumed surface wave is purely imaginary, the surface impedance must be defined as having an positive (inductive) surface reactance, X_S in order to support a TM surface wave. Combining this equation with

$k_x^2 + k_z^2 = k_0^2$ gives

$$k_x = \sqrt{k_0^2 - k_0^2 Z_S^2} = k_0 \sqrt{1 + X_S^2 - R_S^2 - 2iR_S X_S} \tag{2.27}$$

Assuming that the reactance term is positive as mentioned above and the resistive term (corresponding to electromagnetic losses) is negligible (which is valid for metals at microwave frequencies), this becomes

$$k_x = \frac{\omega}{c} \sqrt{1 + X_S^2} \tag{2.28}$$

where $\sqrt{1 + X_S^2}$ defines the mode index, n, of the surface wave, which is the ratio of the speed of light in vacuum to the phase velocity v_p of the mode. This is the same dispersion relation as equation 2.17, derived again using the surface impedance description.

In this section it has been shown how the surface impedance description of surface waves reveals that the condition for a TM surface mode is an inductive reactance term. It can also be demonstrated that a capacitive (negative) term is required for a TE surface mode given by

$$Z_s(\mathrm{TE}) = -\frac{\omega \mu_0}{k_z} \tag{2.29}$$

using a similar derivation[11] with roles of electric and magnetic field switched. Earlier it was shown that a planar conducting interface can guide a TM plane wave, however the mode is very loosely bound to the surface at microwave frequencies. In order to increase the confinement of the mode the inductive surface reactance must be increased. This can be achieved using a dielectric overlayer or by surface corrugation, the latter of which is most relevant to this work.

2.3.3 Corrugated Surface

In this section the surface impedance of a corrugated surface (such as that shown in Fig. 2.5) will be derived. This begins by defining a standing wave formed by waves propagating within the cavities of the structure (z-direction) and reflecting at the lower ($z = 0$) and upper ($z = d$) interfaces. The electric and magnetic fields of this standing wave have the following form

$$E(z) = E_+ \exp(-ik_z z) + E_- \exp(ik_z z) \tag{2.30}$$

$$H(z) = H_+ \exp(-ik_z z) + H_- \exp(ik_z z) \tag{2.31}$$

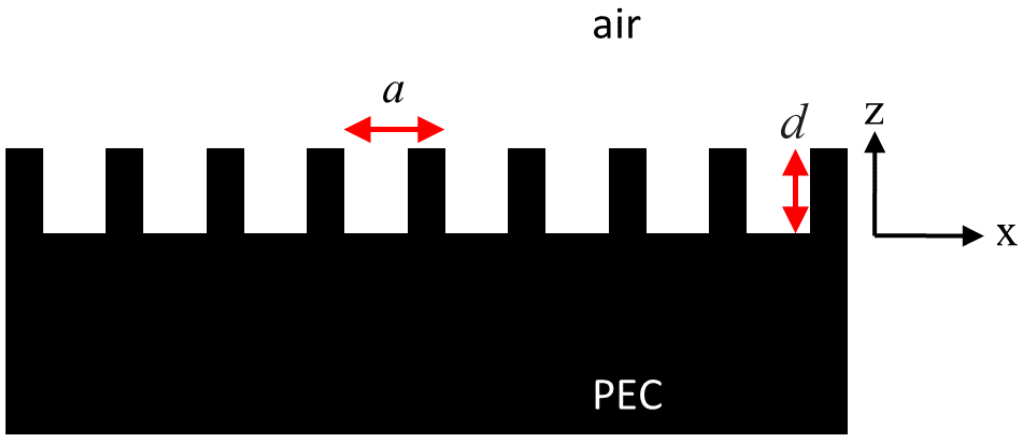

Figure 2.5: a) A corrugated perfect electrical conducting surface with periodicity, a, and a cavity depth of d.

where the subscripts + and − signify forward and backward propagating waves in the z-direction respectively. As before, the surface impedance is defined as the ratio of electric and magnetic fields at the surface as follows

$$Z_{\mathrm{s}} = -\frac{E(z=d)}{H(z=d)} \tag{2.32}$$

The impedance within the cavities, η, can be similarly defined as

$$\eta(z) = \left|\frac{E_{+}(z)}{H_{+}(z)}\right| = \left|\frac{E_{-}(z)}{H_{-}(z)}\right| \tag{2.33}$$

The bottom interface ($z = 0$) acts as a short ($\eta(0) = 0$), i.e. field goes to zero, and therefore the standing wave fields must reverse upon reflection, linking E_{+} and E_{-} as follows

$$E_{-}(z=0) = -E_{+}(z=0) \tag{2.34}$$

By combining this equation with those of the standing wave fields (equations 2.30-2.31), the surface impedance as a function of depth, d, from the short ($z = 0$) is found

$$Z(d) = \frac{E(d)}{H(d)} = \frac{E_{+}\exp(ik_{\mathrm{z}}d) - E_{+}\exp(-ik_{\mathrm{z}}d)}{H_{+}\exp(ik_{\mathrm{z}}d) + H_{+}\exp(-ik_{\mathrm{z}}d)} \tag{2.35}$$

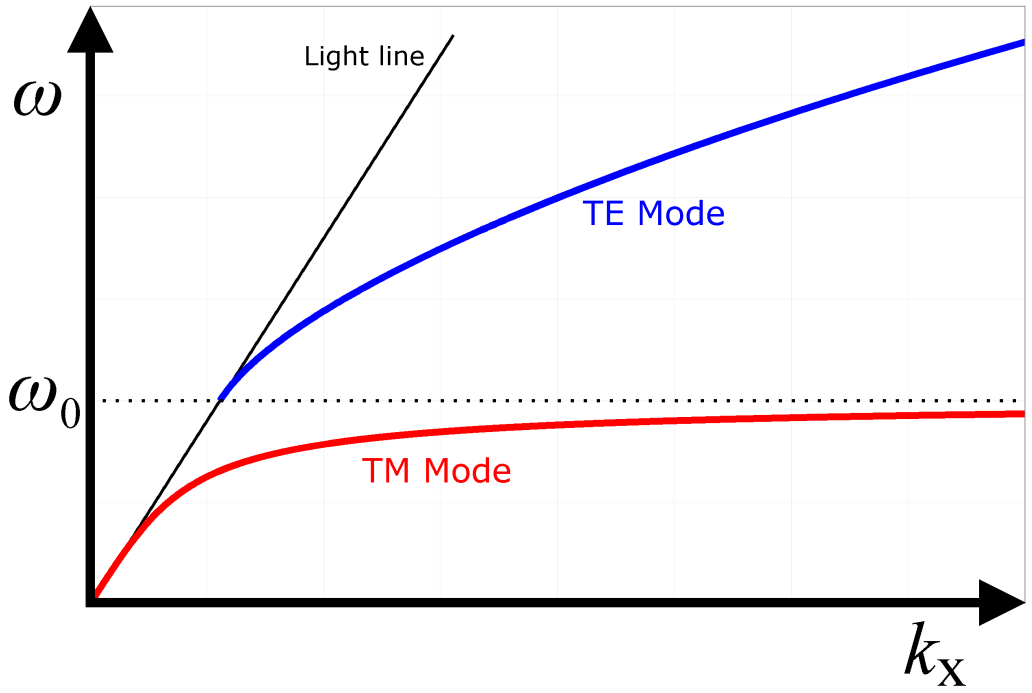

Figure 2.6: Schematic representation of the dispersion of TM and TE surface modes supported by a corrugated surface. The surface impedance is defined by a lumped LC circuit. The asymptotic frequency, ω_0, coincides with a cavity depth, d, equal to a quarter of the wavelength.

which, using the definition of complex exponentials reduces to

$$Z(d) = i\eta \tan(k_z d) \tag{2.36}$$

For $d > \lambda/4$, the tangent term is negative, leading to a negative impedance and therefore a capacitive surface. When $d < \lambda/4$, the opposite is true, with the surface being inductive and allowing the propagation of TM surface waves. This impedance is maximum as d approaches $\lambda/4$. An equivalent circuit model[14][15] is often used to describe the surface impedance as having an inductance, L, and capacitance, C as follows

$$Z_s = \frac{i\omega L}{1 - \omega^2 LC} \tag{2.37}$$

where L and C define a resonant frequency given by $\omega_0 = (LC)^{-1/2}$, at which equation 2.37 has a pole and hence the impedance is infinite. The dispersion of modes on a general corrugated surface can derived in a similar way as that of the planar interface above. A transverse magnetic (TM) and transverse electric (TE) surface

modes can be shown to disperse according to

$$k_{\mathrm{x,TM}} = \frac{\omega}{c}\sqrt{1 - \frac{Z^2}{Z_0^2}} \tag{2.38}$$

$$k_{\mathrm{x,TE}} = \frac{\omega}{c}\sqrt{1 - \frac{Z_0^2}{Z^2}} \tag{2.39}$$

Below the resonant frequency ω_0, only a TM mode exists, supported by the inductive surface. Above ω_0, a TE mode is supported. The dispersion relationship is shown in Fig. 2.6. Again, these are another form of the dispersion relation (equation 2.17), written in terms of surface impedance.

Surface features have resonant conditions that define the frequencies, ω_0, to which modes are asymptotic, such as that in Fig. 2.6. Resonances associated with the macroscopic but not microscopic structure can give rise to surface-plasmon polariton-like behaviour at microwave frequencies. Hence, the term 'spoof surface plasmons' was coined to describe surface waves on periodic structures[16][17] and the structural resonant frequency is often referred to as the 'spoof surface plasmon frequency'.

2.4 Coupling to Surface Modes

At all frequencies, bound surface modes have greater in plane momentum $\hbar k_{\mathrm{x}}$ than that available to incident radiation. Fig. 2.7a shows the dispersion curve (black line) of a typical bound mode, with the grey region within the light line (red) representing momenta available to an incident wave. Each diagonal line from the origin corresponds to an angle of incidence θ that is related to k_{x} via the following trigonometric equation,

$$k_{\mathrm{x}} = k_0 \sin(\theta) = \frac{\omega}{c}\sin(\theta) \tag{2.40}$$

This analysis assumes that $k_{\mathrm{y}} = 0$ and hence the only in-plane component to the wavevector is the x-component, with the mode exponentially decaying in the z-direction. Fig. 2.7b shows how the projection of a number of such lines for $\theta = 5, 50, 90^\circ$ onto the $k_{\mathrm{x}}, k_{\mathrm{z}}$ plane at a particular frequency corresponds to this incident angle upon a horizontal interface. Grazing radiation (red arrow, light line) has maximum in-plane wavevector but is short of the required k_{sw} to excite a surface wave.

There are conventionally two ways to overcome this mismatch in momentum. The first is to use a dielectric prism with $\mathrm{Re}(\varepsilon_r) > 1$ above the surface, which replaces the light line as the limit of in-plane momentum with a dielectric line with shallower gradient (known as Otto coupling[18]). The second method is to introduce some surface

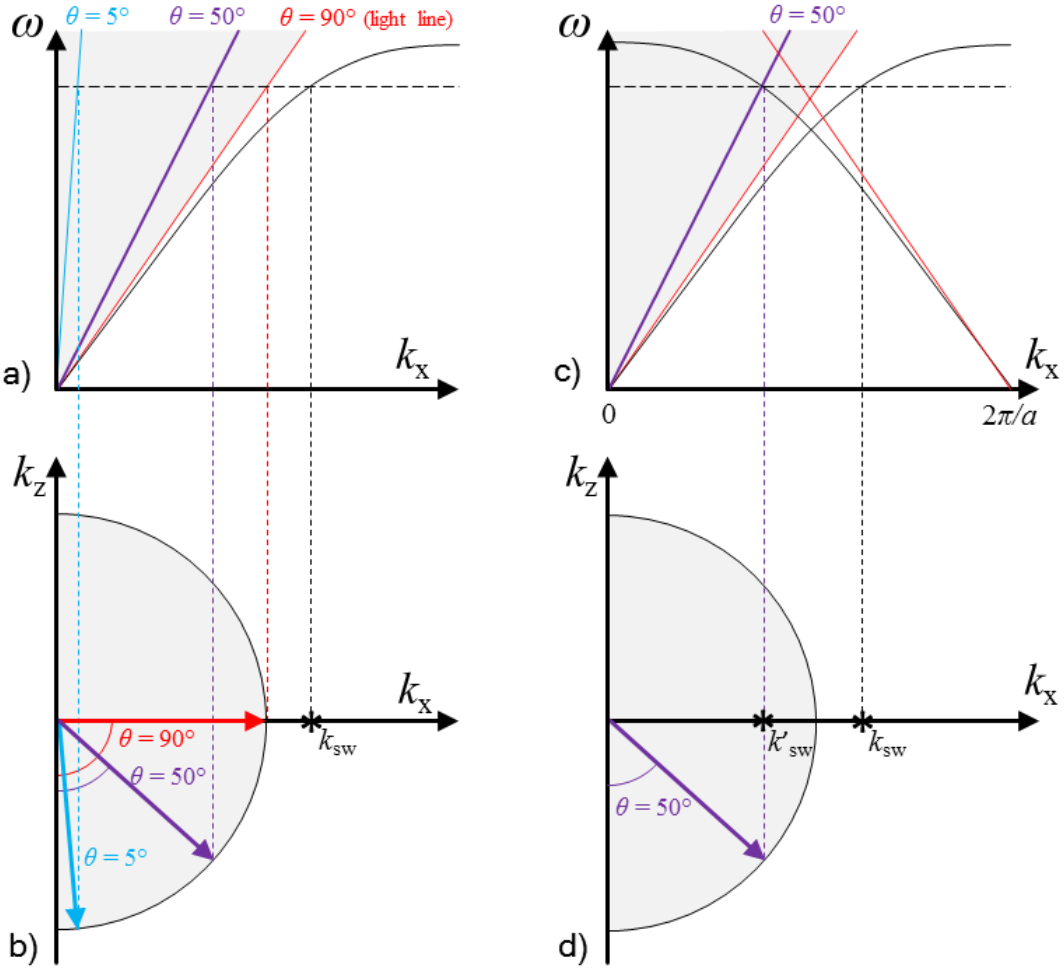

Figure 2.7: The dispersion of a bound surface mode on a planar interface (black line). Radiation incident on the interface at angle θ to the surface normal cannot have in-plane wavevector greater than that of grazing radiation ($\theta = 90°$, also known as the light line) and therefore can not couple to the mode with wavevector k_{sw}. b) The in-plane wavevector is related to the angle of incidence by $k_x = k_0 \cos(\theta)$ where $k_0 = \omega/c$. c) With a periodic perturbation to the surface with periodicity a, additional modes are created with wavevector $k_x + 2N\pi/a$. d) As a result, the momentum k'_{sw} of a diffracted surface mode is matched by the in-plane momentum of incident radiation with $\theta = 50°$.

structure such that the momentum can be enhanced via scattering off features on the surface. It is this method that is of interest in this work and to the topic of microwave metamaterials in general.

A periodically varying surface, such as the corrugated plane discussed in the previous section, or a sinusoidal grating, enhances the in-plane momentum by multiples of the grating (or periodic) wavevector $k_a = 2\pi/a$, where a is the distance of one period

of the structure, so that

$$k_{\mathrm{x}} = k_0 \sin(\theta) \pm N k_a \tag{2.41}$$

where N is an integer. As a result the dispersion curve becomes periodic in k_a along the k_{x} axis, and scattered surface modes can exist within the light line centred at $k_{\mathrm{x}} = 0$. In Fig. 2.7c only the first scattered mode $N = 1$ is considered and the projection onto the $k_{\mathrm{x}}, k_{\mathrm{z}}$ plane in Fig. 2.7d shows how at the chosen frequency (dashed black line) an impinging wave at incident angle $\theta = 50°$ has in-plane momentum that matches the scattered surface mode (k'_{sw}). It is important to note that this mode may also 're-radiate' into free-space as readily as it is excited by free-space radiation.

2.4.1 Brillouin Zone

Fig. 2.8 demonstrates the first Brillouin zone of a dispersion diagram for a medium that is periodic in the x-direction[19]. The Brillouin zone (BZ) exists for $-\pi/a \geq k_{\mathrm{x}} \geq \pi/a$ and is bound by dashed blue lines in the figure. As shown above the dispersion is also periodic, and the BZ contains all information regarding modes supported by the structure. The BZ is divided into regions bound by the non-diffracted and diffracted light lines (red lines).

Modes supported by the structure within the blue region are bound to the surface and despite the periodic nature of the system, cannot be excited by incident plane wave radiation and cannot radiate. These trapped modes are of real interest for this work, and the following chapter will describe how these can be excited on a surface using near field sources of electromagnetic radiation (Sec. 3.5). This region is referred to as 'non-radiative'. Within the green region (radiative) incident radiation can couple to the surface mode. The coupling efficiency is increased by matching the field of the incident wave to that of the mode (often known as maximising field overlap). This is sometimes as trivial as choosing the correct polarisation (transverse electric or magnetic) of an incident plane wave. These modes can re-radiate back into the specular (not diffracted) beam from which they were excited, causing features to appear in the far-field transmission and reflection spectra due to constructive or destructive interference. Finally, the purple region corresponds to modes above the onset of diffraction, where specular radiation that transmits through or reflects off the surface is accompanied by diffracted radiation due to the periodicity. At the interface between the radiative (green) and diffracted (purple) regions a sharp discontinuity is often seen in the reflection/transmission spectra. This is due to the abrupt redistribution of power into the first diffracted order. It is referred to in this work as the 'diffraction edge' and is also commonly referred to as one of Wood's anomalies, as interpreted by Rayleigh[20].

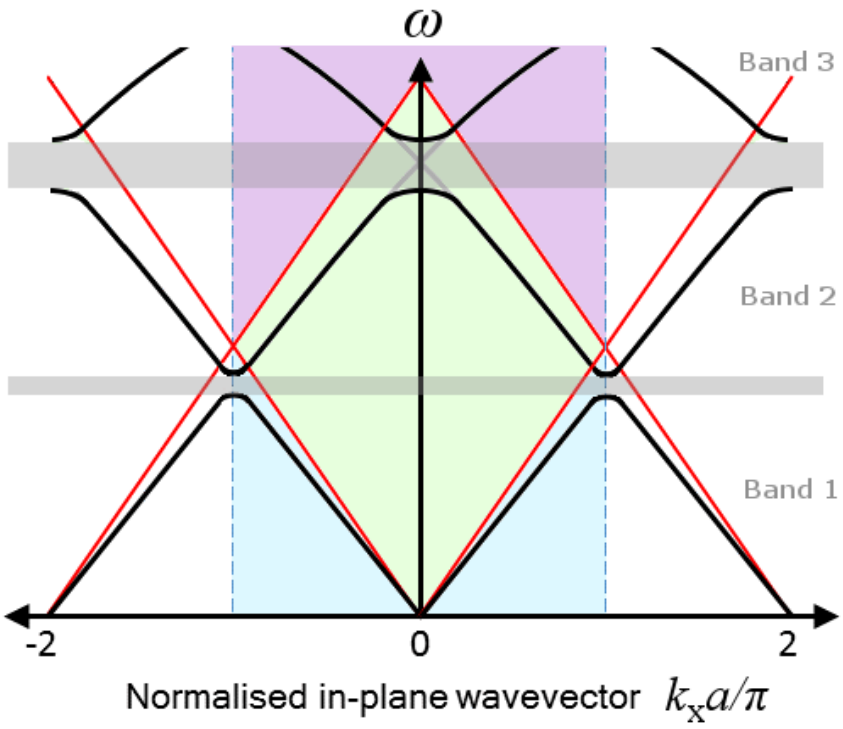

Figure 2.8: A zoomed in view of the dispersion diagram showing just the zeroth and first order scattered surface wave modes. The edge of the first Brillouin zone (BZ) is marked by the blue dashed lines. Within the Brillouin zone there are three regions; non-radiative (blue), radiative with specular radiation only (green) and radiative with specular and first order diffracted modes (purple). The surface modes split causing band gaps to appear (grey regions), with the upper and lower band edges corresponding to standing wave solutions.

2.4.2 Phase and Group Velocities

The dispersion curve reveals how a mode's energy and momentum are related by its velocity. However two velocities are defined for a dispersive wave such as the surface wave supported by a corrugated surface in Fig. 2.6. The first, called the phase velocity ($\mathbf{v}_\mathrm{p}$) is given by the ratio of angular frequency ω to wavevector, $\mathbf{k}_\mathrm{ip} = k_\mathrm{x}\hat{\mathbf{x}} + k_\mathrm{y}\hat{\mathbf{y}}$, where the subscript is used to denote in-plane wavevector (the z-direction is normal to the surface). This is the speed at which phase fronts of the wave advance and is also that which defines the mode index $n = c/|\mathbf{v}_\mathrm{p}|$. The group velocity, $\mathbf{v}_\mathrm{g}$, is defined as the first derivative of ω with respect to $\mathbf{k}_\mathrm{ip}$,

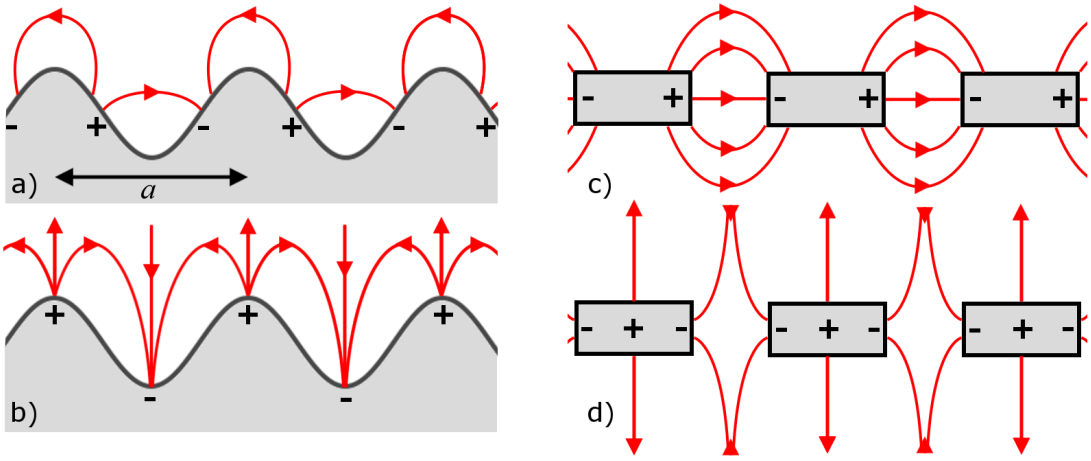

Figure 2.9: Schematic of the band-split modes supported by a sinusoidal grating at $k_x = 0$. a) The lower frequency solution b) The higher frequency solution. c-d) The equivalent modes for a case of a discontinuous surface.

$$\mathbf{v}_g = \nabla_{\mathbf{k}_{ip}} \omega \tag{2.42}$$

$$\mathbf{v}_p = \omega / k_{ip} \tag{2.43}$$

These relationships are illustrated in Fig. 2.1. The group velocity is the speed at which a wave can transmit information and hence has an upper limit of c; the speed of light in a vacuum. Note that the phase velocity has no such limitation. The direction of group velocity indicates the direction of power flow and energy transfer and can be in a different direction to the phase velocity. Recently, negative index metamaterials that have phase and group velocity in *opposite* directions have been subject to extensive research[21], and will be the topic of Chapter 9 of this thesis. Although the wavevector and group/phase velocities are vectors (there are two in-plane components) often propagation in a particular direction is of interest (x-direction has been used so far). Hence, scalar notation is used throughout the remainder of this thesis, i.e. $|v_p| = \omega / k_x$ and $|v_g| = d\omega / dk_x$

2.4.3 Band Gaps

The surface mode dispersion of a periodically structured surface depicted in Fig. 2.8 shows that rather than crossing each other at $k_x = 0, \pm N\pi/a$, the modes split, resulting in band gaps (grey regions); frequency ranges over which no modes are supported by the structure. Band gaps are a common phenomenon of photonic crystals[22] and electron

band structures in semiconductors[23]. Two modes exist within the radiative region, corresponding to $k_x = \pm(k_{sw} - k_a)$ (i.e. scattered by $\pm k_a$). At $k_x = 0$ the two modes both have a wavelength $\lambda_{sw} = 2\pi/k_{sw} = a$ and are counterpropagating. This results in two standing wave solutions (and also at $k_x = \pm\pi/a$, where the wavelength is $2a$). The two solutions both have zero group velocity (gradient is zero, no net power flow) and differ by an offset of charge in x of $\lambda_{sw}/4$, as shown in Fig. 2.9a-b. These standing wave solutions have the same wavelength (same k_x, same in-plane momentum), but differ in energy (and hence frequency). The result is a gap in frequency between these two modes that are known as the lower and upper band edge. Fig. 2.9a shows the lower energy solution, corresponding to charges positioned at mid-height of the sinusoidal corrugations. For the higher energy mode (Fig. 2.9b), charges are positioned in the peaks and valleys of the surface. The energy stored in the system depends upon both the charge and field configurations. The standing wave with charges at the peaks and troughs represents the higher energy state, as the field lines are distorted more by the increased separation of charge. The size of the energy gap depends on the surface geometry and the contrast between the parameters of the two materials. These band gaps are present in all structures where the underlying symmetry of the surface is represented by a translation operator. It will be shown in a later section that under certain symmetry conditions band gaps do not appear.

2.5 Surface Waves on Metasurfaces

In this section, the principles outlined previously are discussed in the context of thin structures with two interfaces typically separated by much less than a wavelength. An example of such a metasurface is a thin metallic sheet perforated with a 2D array of cylindrical holes with period $a = 4$ mm. This is an example of a surface defined by an inductive impedance, and hence supports a TM surface wave. For holes with radius $r = 1.5$ mm, the effective surface plasma frequency can be approximated as the cut off for the first order mode of a circular waveguide[10], given by

$$\omega_0 = \frac{1.8412c}{2\pi r} = 58.6 \text{ GHz} \tag{2.44}$$

where the value 1.8412 is the first root of the derivative of the Bessel function; J_1' and the hole is assumed to be air-filled.

2.5.1 Band Gaps

The band gaps that appear at integer multiples of $k_x a/\pi$ in the dispersion curve as discussed in Sec. 2.4.3 are, in general, significantly different for discontinuous surfaces

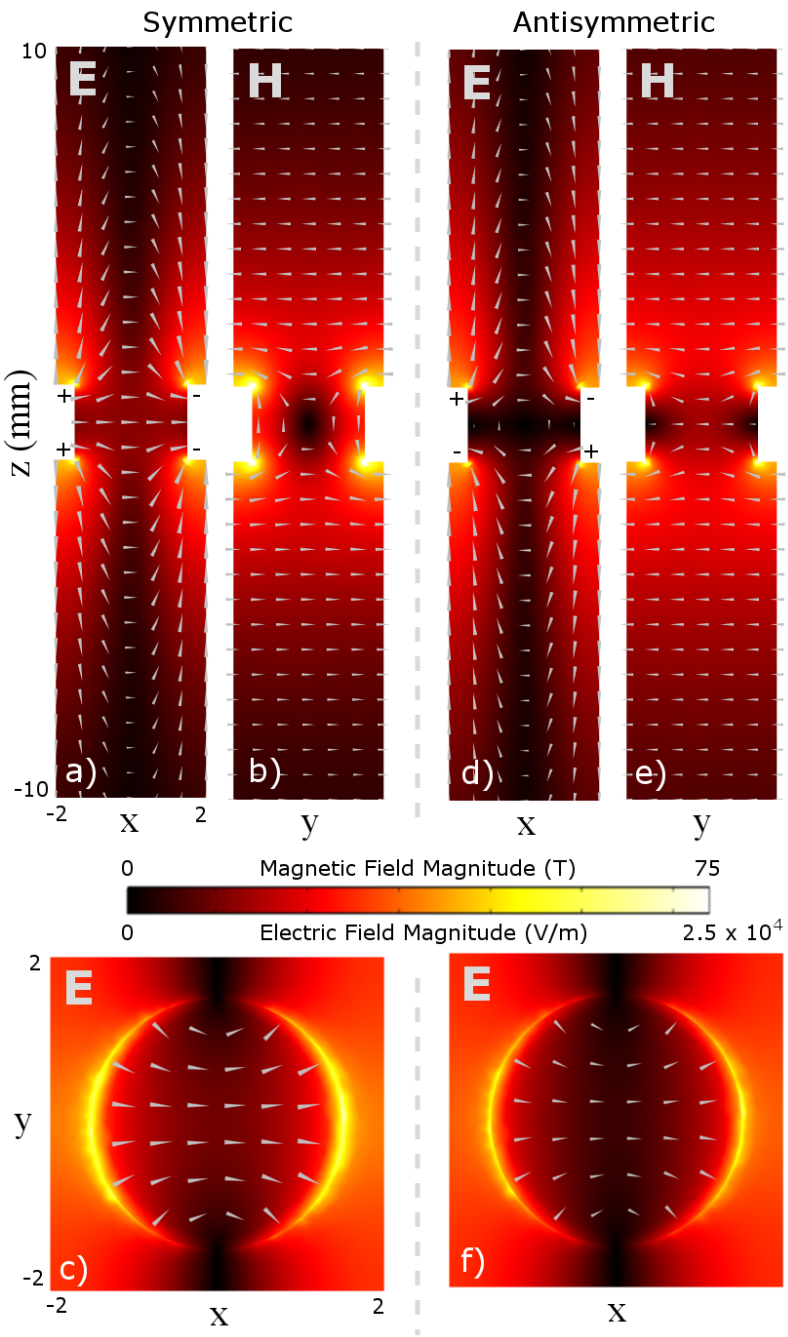

Figure 2.10: a) The standing wave solution for the symmetric mode of the circular hole array at the lower band edge at $k_x = \pi/a$, on the xz plane. Colour: electric field magnitude. Arrows: electric field vector. b) The magnetic field on the yz plane, with the vector field advanced by 90°. c) The electric field in the xy plane on the top face of the hole. d-f) The same plots for the antisymmetric mode.

(i.e. holey surfaces). Previously it was shown that for a continuous, sinusoidal grating the lower and upper band edges correspond to a $\lambda_{sw}/4$ shift in the standing wave position, and therefore a shift in the position of charge accumulation on the surface (see Fig. 2.9a). For discontinuous surfaces, there are regions of the surface that can not hold charges. The result is that the upper band edge is a high energy solution and the mode is not strongly bound to the interface, i.e. the penetration depth of the mode into the air region is much larger than for the lower band edge. Fig. 2.9c-d illustrates the field lines associated with the two band edges at $k_x = 0$, in comparison with the sinusoidal grating in Fig. 2.9a-b.

Fig. 2.10a-c shows the field configuration for the lower band edge mode supported by the array of circular holes of radius $r = 1.5$ mm, periodicity $a = 4$ mm and metal thickness, $t = 1$ mm, at the edge of the Brillouin zone ($k_x = \pi/a$). The top two plots represent the electric field magnitude and vector in the xz plane (a), and the magnetic field magnitude and vector in the yz plane (b). Both of these planes pass through the centre of the circle. The bottom plot shows the electric field in an xy plane across the top of the circular hole (c). The magnetic field vector plot (arrows in b) shows that, as for all hole arrays, the surface mode has transverse magnetic (TM) polarisation. In other words, the magnetic field is in the transverse directions (y and z) whilst the electric field loops in the plane of propagation (xz). The standing wave solution corresponds to a node in the centre of the unit cell (centre of the hole) and antinodes either side. This is best seen in the electric field magnitude variation (colour plot) of Fig. 2.10c. The excitation of the dipolar mode of the circle-shaped element confines the wave to the surface.

The corresponding upper band edge is shown in Fig. 2.11a-c. This standing wave mode has an antinode in the circle centre, and nodes either side. Charge cannot sit in the hole, instead it surrounds the hole, which does not act to localise the field to the surface. As seen in a-b, this significantly reduces the confinement of the mode (note the change in scale of the y axis). The electric and magnetic field vectors resemble that of grazing radiation, and the distortion of these field lines at the centre of the hole explain the increase in energy.

As a result of having voids within the structure where charges cannot sit, the surface mode band gap at the Brillouin zone is asymmetric in frequency, with the upper band edge sitting just below the light lines.

2.5.2 Coupled Surface Modes

Two surface waves supported on parallel interfaces will couple together resulting in two modes supported by the system as a whole. The strength of this coupling increases as

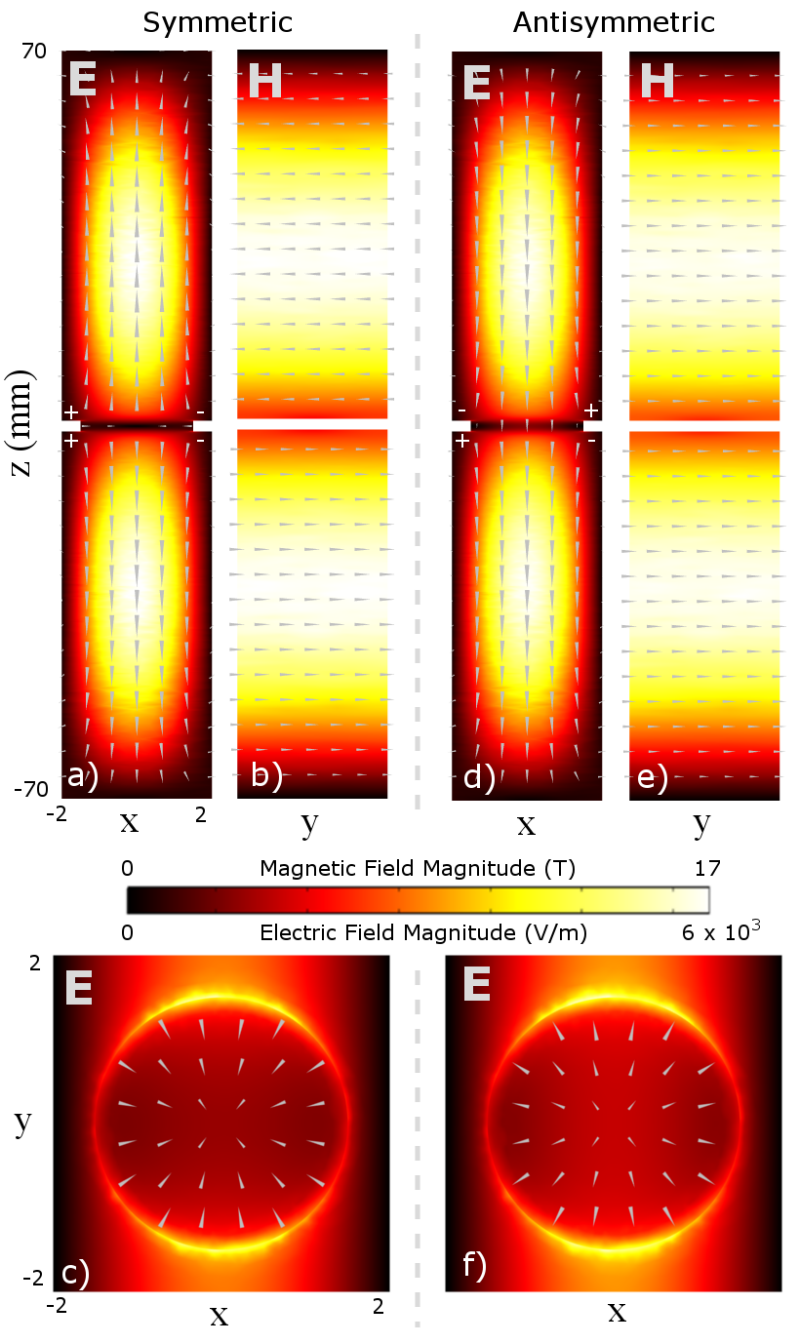

Figure 2.11: a) The standing wave solution for the symmetric mode of the circular hole array at the upper band edge at $k_x = \pi/a$, on the xz plane. Colour: electric field magnitude. Arrows: electric field vector. b) The magnetic field on the yz plane between the holes, with the vector field advanced by 90°. c) The electric field in the xy plane on the top face of the hole. d-f) The same plots for the antisymmetric mode. The z axis in a,b,d,e is scaled by 1/7.

the interfaces are brought closer together and the field overlap of their single-interface modes increases. Much like modes at the upper and lower band edge in a band gap discussed above, the separation in energy of the two coupled surface modes depends on the field configuration. Two identical surfaces that are parallel and aligned support modes that are distinguishable by the symmetry of electric or magnetic field components about the central plane between the interfaces. As a result the two modes are commonly referred to as a symmetric/antisymmetric pair. To avoid confusion, the symmetry of charges within the metallic regions is used to define them here.

For the case of the circular hole array this means that there are in fact four standing wave solutions at the Brillouin zone. Fig. 2.10d-f and Fig.2.11d-f show the lower and upper band edge configurations for the antisymmetric charge mode, respectively. The characteristics of the two solutions are similar to those of the symmetric modes, however there is a separation of charges between the top and bottom interfaces (see charge symbols in a and d). The antisymmetric mode exists at higher energy than the symmetric mode due to the reversal of field within the hole resulting in enhanced distortion of the field lines.

For thin metasurfaces (where the two interfaces may be separated by less than 20 μm) the entire antisymmetric band follows the light line. Therefore it is typical for these thin holey structures for only one of four standing wave solutions to be distinguishable and exist with greater momentum than incident radiation (the symmetric mode lower band edge), with the other three effectively propagating as grazing radiation.

2.5.3 Transverse Electric Modes

For the complementary structure of that presented in the previous section; an array of disconnected circular patches, the surface mode supported has a transverse electric (TE) polarisation, and the surface impedance is capacitive, as discussed in Sec. 2.3.3. In this system, neighbouring patches couple together via displacement currents, and charge separation occurs in the transverse direction. As a result, the magnetic field instead forms loops in the propagation plane (xz).

2.6 Glide Symmetry

Band gaps in the dispersion diagram for modes on periodic structures appear due to the difference in energy of the two standing wave solutions when the wavevector is an integer multiple of π/a where a is the periodicity (see Fig. 2.8). The nodes (and antinodes) of the two standing waves are shifted by $\lambda_{sw}/4$ with respect to each other. This raises the question of what happens in a system where this $\lambda_{sw}/4$ shift results in

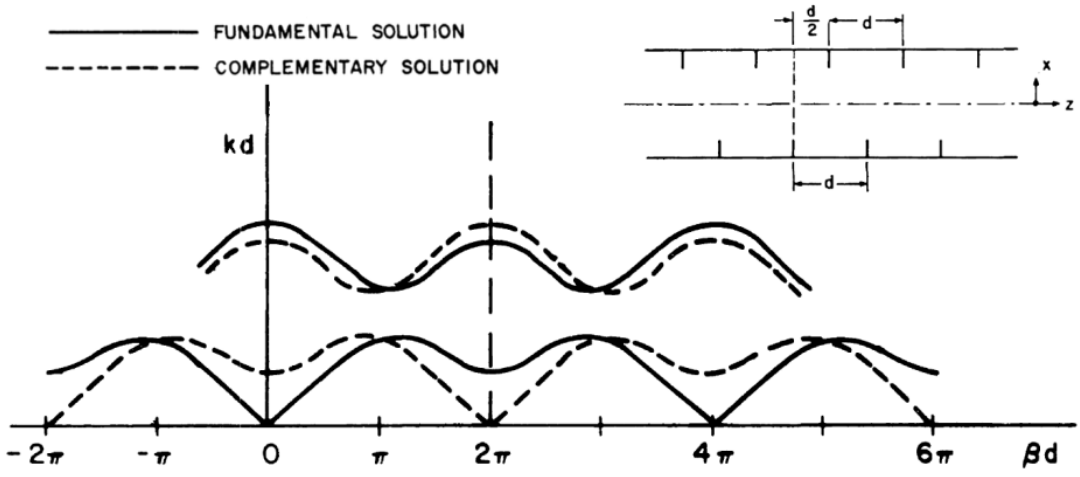

Figure 2.12: Figure taken from [24]. A glide symmetric waveguide (inset) consists of a parallel plate waveguide with periodic inclusions on each plate, shifted by half of the periodicity with respect to each other. The dispersion diagram of supported modes show a degenerate pair of modes at the first Brillouin zone boundary ($\beta d = \pi$).

the same field configuration and therefore the same energy for the two solutions? Such a system can be described as having *glide* symmetry, as outlined below.

A structure that possesses glide symmetry is invariant under a mirror inversion in the y direction and a translation by half of its periodicity a in the x direction. The mirror plane in the xz orientation is known as the glide plane. The glide operator, G, is written as follows,

$$G \equiv \begin{cases} x & \to x + a/2 \\ y & \to -y \\ z & \to z \end{cases} \tag{2.45}$$

A zigzag is a good example of a shape that is glide symmetric, and surface modes that are gapless at the edge of the Brillouin zone have indeed been studied on zigzag diffraction gratings[25]. Fig. 2.12 shows a glide symmetric geometry (inset) corresponding to a parallel plate waveguide with periodic inclusions along with its predicted band structure. There are two degenerate modes at the Brillouin zone boundary ($\beta d = \pi$ in the figure notation) that have non-zero group velocity. This figure is extracted from the theory of Hessel and Oliner[24][26], as is the analysis of the system given below.

To understand the interaction of modes in a glide-symmetric system, first consider a parallel plate waveguide[11]. The lowest order mode supported by this waveguide is a transverse electromagnetic (TEM) wave with no low frequency cutoff. This mode

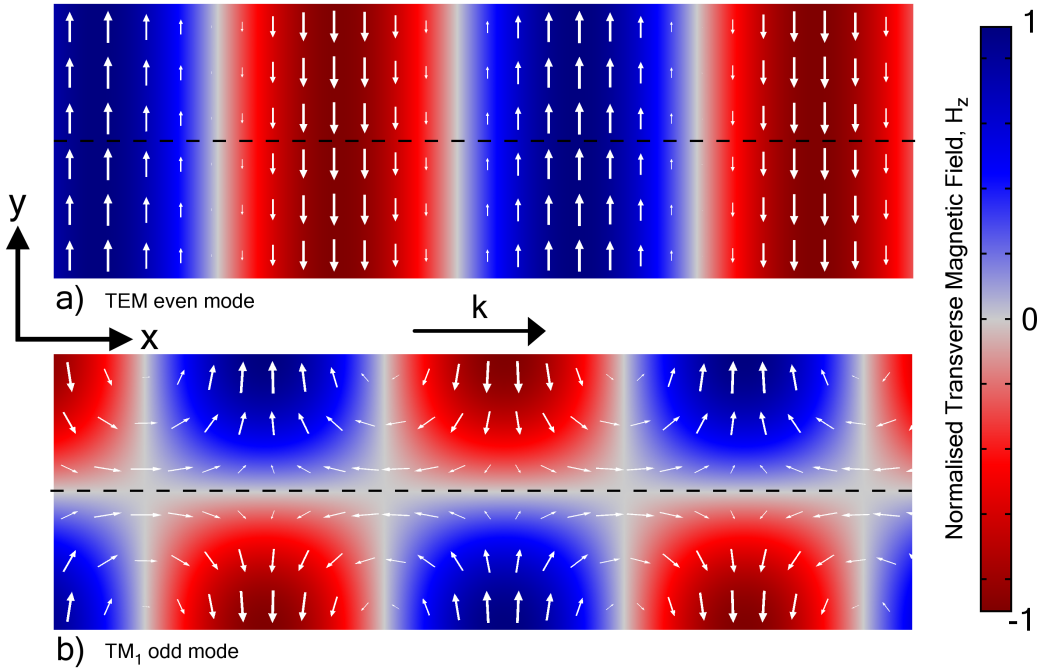

Figure 2.13: The field configurations of the two lowest order transverse magnetic (TM) modes of a parallel plate waveguide. The plates are positioned on the top and bottom edges of the field plots. a) the TEM mode with 'even' transverse magnetic field with respect to the central plane (dashed line). b) the TM_1 mode with 'odd' transverse magnetic field. Mode propagation is from left to right.

propagates at speed c, assuming a vacuum filled waveguide with no losses, and exists on the light line in the dispersion curve (see thin blue line in Fig. 2.14a). The field profile of this mode is shown in Fig. 2.13a and the magnetic field in the transverse direction, H_z, is an even function with respect to the central plane shown as a black dashed line (i.e. the field is symmetric). This plane corresponds to an electric wall (PEC). The first order transverse magnetic mode, TM_1, has a cutoff frequency at $k_x = 0$ dictated by the plate separation, d, and disperses towards the light line according to the dispersion relation

$$\omega^2 = k_x^2 + \left(\frac{\pi}{d}\right)^2 \tag{2.46}$$

This mode is shown as a thin green line in Fig. 2.14a, and the field profile shown in Fig. 2.13b. For both modes, there is no variation in z and the problem can be considered as a two-dimensional one. In contrast to the fundamental TEM mode, the transverse magnetic field for the TM_1 mode is an odd function about the central plane that acts as a perfect magnetic conductor (PMC). There is also a transverse electric

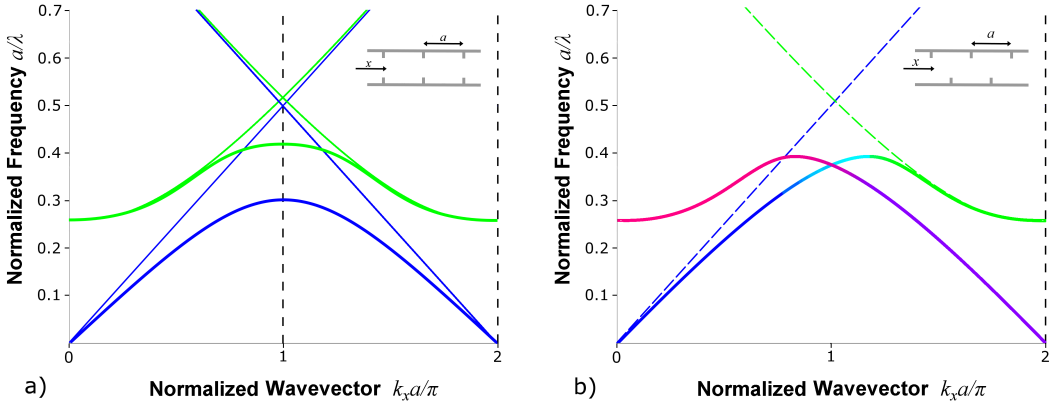

Figure 2.14: a) The dispersion of modes supported by a parallel plate waveguide. Blue: even H_z modes, Green: odd H_z, Thin: planar PEC walls, Thick: with periodic inclusions (inset). b) The dispersion when the inclusions on the bottom plate are shifted by $a/2$ with respect to those on the top plate, forming a glide-symmetric waveguide. The modes are neither purely odd or even in H_z.

TE_1 mode, which is degenerate with the TM_1 for a planar parallel plate waveguide, however this discussion focusses on the TM modes only.

Introducing periodic small protrusions without glide symmetry (inset of Fig. 2.14a) creates scattered versions of these modes from $k_x a/\pi = 2$, as seen in Fig. 2.14a. Modes of even symmetry in H_z (thin blue lines) interact forming a band gap at the Brillouin zone boundary. The lowest band of this mode is shown as a thick blue line. Similarly modes of odd symmetry interact resulting in the thick green dispersion curve. The field configurations of these two TM modes of the structured waveguide at $k_x a/\pi = 1$ are shown in Fig. 2.15. The transverse magnetic field, H_z, is given by the eigenfunctions ψ_T of the translation operator T

$$\begin{aligned} \psi_{T1} &= \sum_{n=-\infty}^{\infty} A_n \sin(k_{y,n} y) \exp(-i k_{x,n} x) \\ \psi_{T2} &= \sum_{n=-\infty}^{\infty} B_n \cos(k_{y,n} y) \exp(-i k_{x,n} x) \end{aligned} \tag{2.47}$$

for the odd (green) and even (blue) modes respectively. A and B are weighting factors and the subscript n defines the diffracted order of the modes ($n = 1$ refers to modes originating from $k_x a/\pi = 2$). The corresponding eigenvalue of the translation operator is

$$t = \exp(i k_x a) \tag{2.48}$$

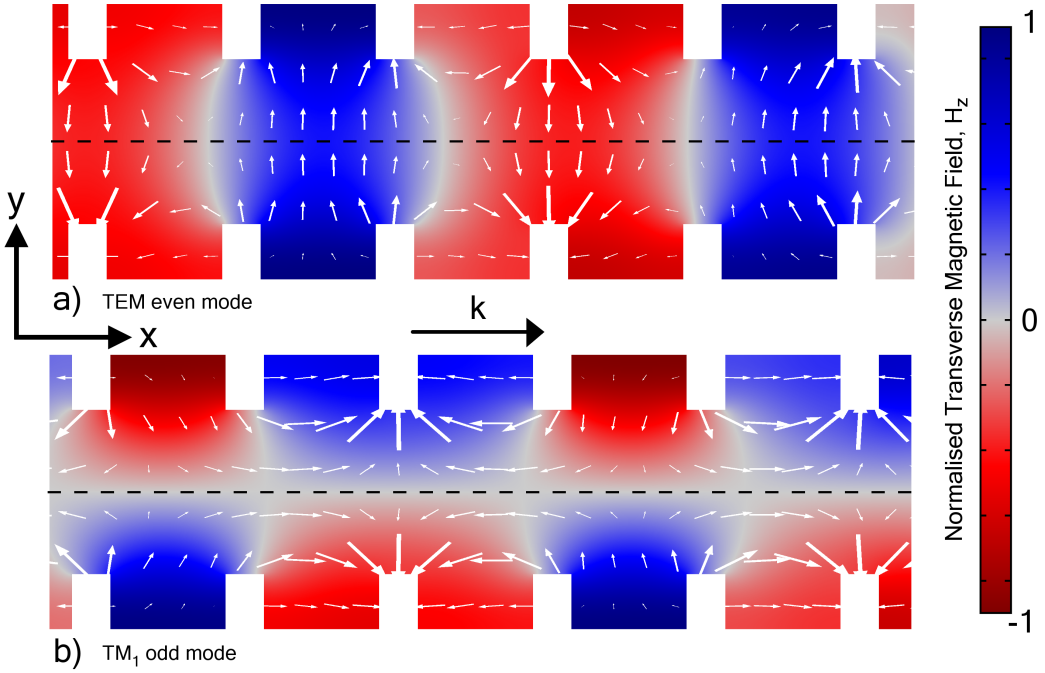

Figure 2.15: The field configurations of the two lowest order transverse magnetic (TM) modes of a parallel plate waveguide with periodic protrusions obeying the translation operator, T. The plates are positioned on the top and bottom edges of the field plots. a) the TEM mode with 'even' transverse magnetic field with respect to the central plane (dashed line). b) the TM_1 mode with 'odd' transverse magnetic field. Mode propagation is from left to right.

which accords with the Bloch theorem[27] that the band structure is periodic in $2\pi/a$.

Upon shifting the protrusions on one plate with respect to the other (inset of Fig. 2.14b), the H_z field can no longer be described as purely odd or even function in y but rather as a mixture of the two. The glide operation, G, and its eigenvalues, g are given by

$$\begin{aligned} G\psi(x,y) &= \psi(x+a/2,-y) \\ g &= \pm e^{-ik_x\frac{a}{2}} \end{aligned} \tag{2.49}$$

These eigenvalues are the two square roots of the translation eigenvalues, due to the fact that applying the glide operator twice is equivalent to applying the translation operator once, $GG \equiv T$. This implies that the corresponding eigenvectors result in a

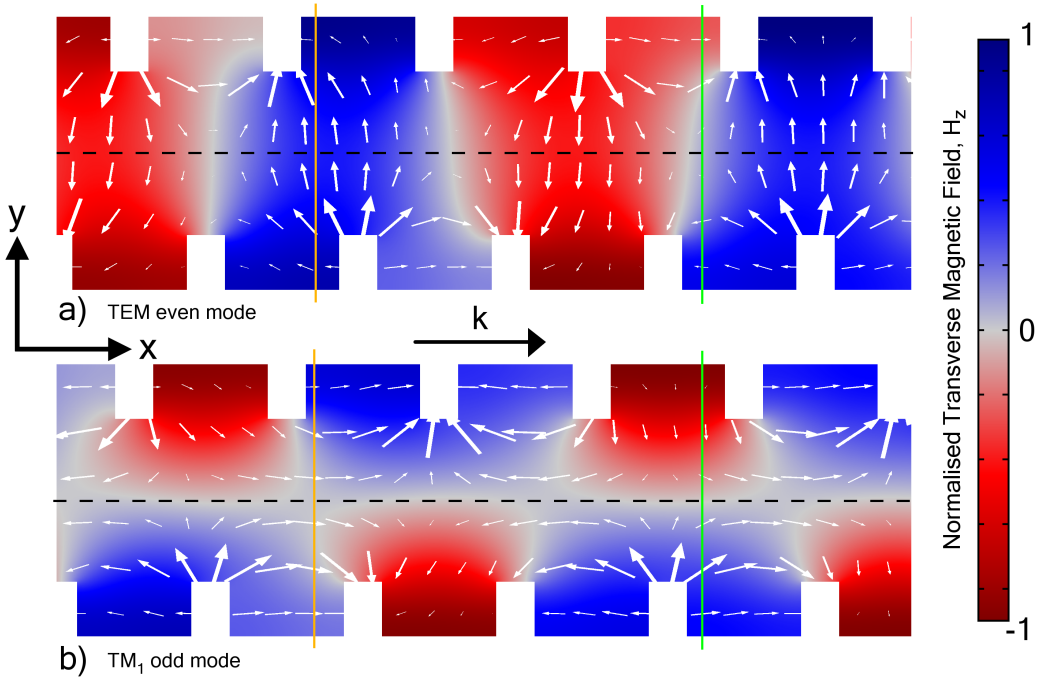

Figure 2.16: The field configurations of the two lowest order transverse magnetic (TM) modes of a parallel plate waveguide with periodic protrusions obeying the glide operator, G. The plates are positioned on the top and bottom edges of the field plots. Mode propagation is from left to right.

band structure periodic in $k_{\mathrm{x}} = 4\pi/a$. These eigenvectors are

$$\psi_{G1} = \sum_{n=-\infty}^{\infty} A_{2n+1}\sin(k_{\mathrm{y},2n+1}y)\exp(-ik_{\mathrm{x},2n+1}x) + \sum_{n=-\infty}^{\infty} B_{2n}\cos(k_{\mathrm{y},2n}y)\exp(-ik_{\mathrm{x},2n}x)$$
$$\psi_{G2} = \sum_{n=-\infty}^{\infty} A_{2n}\sin(k_{\mathrm{y},2n}y)\exp(-ik_{\mathrm{x},2n}x) + \sum_{n=-\infty}^{\infty} B_{2n+1}\cos(k_{\mathrm{y},2n+1}y)\exp(-ik_{\mathrm{x},2n+1}x) \tag{2.50}$$

The first eigenvector has a mixture of odd and even terms in y, specifically even (TEM) modes with even n, and odd (TM_1) modes with odd n. These are highlighted by the thin dashed green and blue lines in Fig. 2.14b. The interaction of these results in the thick blue/green line, which is periodic in $k_{\mathrm{x}} = 4\pi/a$. The field profile, shown in Fig. 2.16a, has both even (orange line) and odd (green line) character. In contrast, the second eigenvector combines even (TEM) modes with *odd* n, and odd (TM_1) modes with *even* n, resulting in the thick purple/pink line. The fields are shown in Fig. 2.16b. It can be seen from Fig. 2.14b that the overall dispersion is periodic in $k_{\mathrm{x}} = 2\pi/a$,

satisfying the Bloch condition for periodic structures. However, unusually there is no band gap formed at the Brillouin zone boundary, instead this happens at some k_x either side of $k_x = \pi/a$ where the group velocity (gradient of the dispersion curve) falls to zero. Only the lower bands are depicted in the figure.

Glide symmetric waveguides have a band structure that is gapless at the Brillouin zone boundary. This is because the half-period shift in position of periodic inclusions either side of the glide plane acts to mix the odd and even modes. At the Brillouin zone boundary, two degenerate modes exists with non-zero group velocity.

2.7 Conclusion

In this chapter, the properties of surface modes supported by planar and structured interfaces were discussed. Periodic variation of the surface was shown to allow coupling to these modes via diffraction and also allows surface-plasmon-polariton-like behaviour at microwave frequencies by providing the system with a low frequency resonant condition. The dispersion of modes supported by a thin, discontinuous surface was discussed as well as concepts such as band gaps and coupled surface modes. Finally, the dispersion of modes supported by a glide symmetric structure was shown to be gapless at the edge of the first Brillouin zone. The following chapter outlines the experimental and numerical methods used throughout the thesis.

Chapter 3

Methods

3.1 Introduction

This chapter outlines the processes and techniques used to produce the results presented in the following chapters. This includes both numerical simulations and experimental methods. A metallic checkerboard array is used as an example throughout.

3.2 Sample Fabrication

The samples used in this thesis all comprise a dielectric film clad, on one side or both, with a patterned metallic layer. These laminates are produced using either an electrodeposition or annealing process, or a combination of the two, and are conventionally used as flexible printed circuit boards. The laminates used are provided by Rogers PCB or GTS Flexible and vary in thickness and materials.

Larger and double-sided laminates are patterned using photolithographic techniques, whereas smaller (A3 size), one-sided laminates can be made using a 'print and etch' method. In both cases, the patterning of the metallic layers is performed using a mask to protect metallic regions and then chemically removing the unwanted void regions using an etchant. Where possible, these processes are carried out 'in house' however for higher resolution patterning or larger (>A3), thicker (>0.1 mm) panels the patterning is outsourced to local printed circuit board manufacturers, Graphic PLC and Eurotech.

3.2.1 Photolithography

The photolithographic process of patterning metallic laminates is described below and depicted in Fig. 3.1.

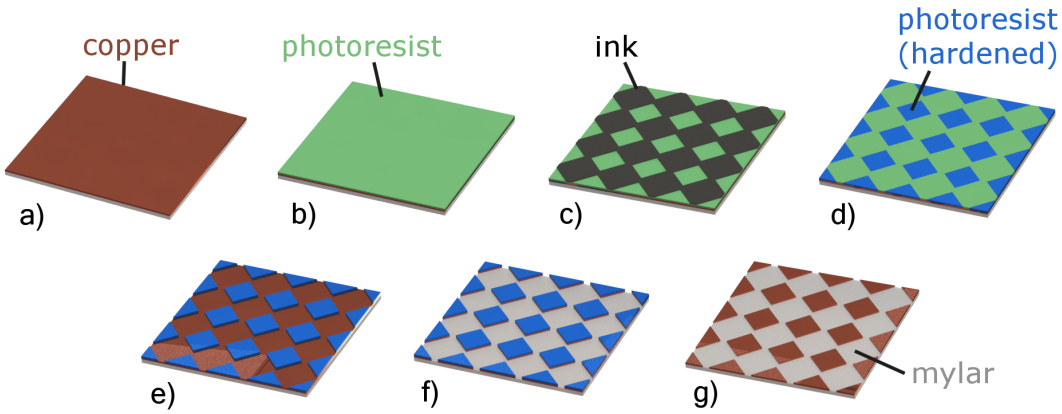

Figure 3.1: The stages of the photolithography process from the initial copper laminate in (a) to the finished patterned sample in (g). Photoresist is marked as green, hardened resist in blue and the photomask in black.

Initially, a negative of the required design is printed onto white paper as a black and white binary image with inked regions representing the holes in the metallic film, and white regions the metallic regions of the final sample. A Repromaster 2200 camera is used to transfer this design onto a photosensitive transparency film by front-illumination of the paper in a dark-room. During this process the black and white regions of the image are inverted. This transparency film is 'developed' using standard photo developing and fixing chemical, creating a positive mask.

The laminate (a) is coated in an ultra-violet (UV) sensitive photoresist film using heated rollers (b). The mask is placed on top of the photoresist and illuminated with UV radiation (c). The UV hardens the exposed areas of the photoresist (shown as blue in (d)). The unhardened regions of photoresist are chemically removed using a solvent, revealing the copper below (e).

The sample is then placed in a heated bath of Ferric Chloride etchant which removes the unwanted metallic regions (f). Finally, the hardened photoresist is removed using acetone solvent (g).

3.2.2 Print and Etch

The 'print and etch' method is a simplified version of the photolithography process described above which reduces time and cost but is limited by the printer specifications

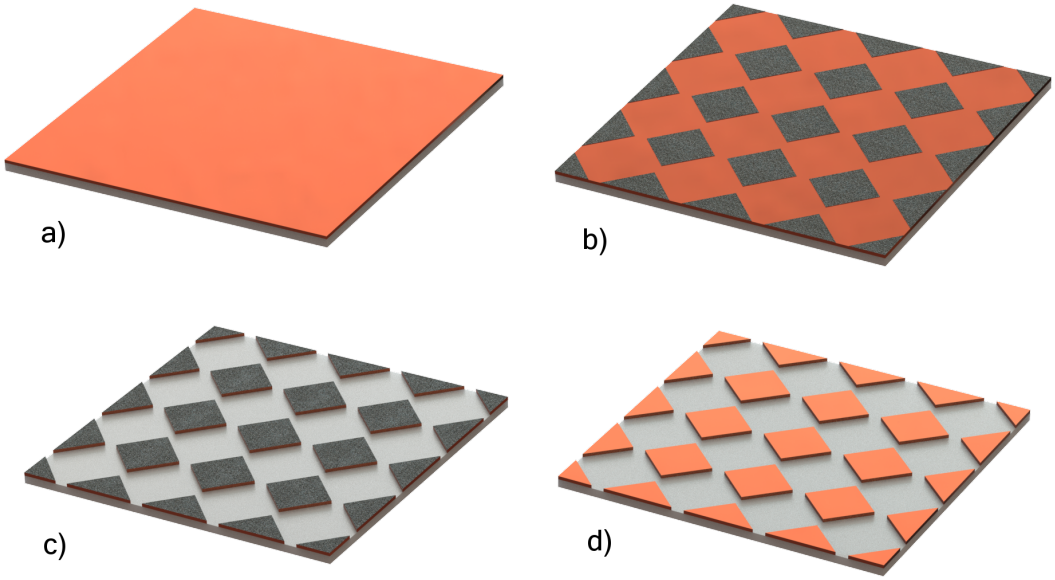

Figure 3.2: The stages of the print and etch process from the initial copper laminate in (a) to the finished patterned sample in (d). Grey regions denote Solid Ink which is printed directly onto the laminate.

to single sided laminates up to a maximum size of 410 × 295 mm. Fig. 3.2 shows the sample at various stages throughout the process, beginning with an unpatterned laminate (a).

A positive (black corresponding to metallic regions) image is designed and printed directly onto the laminate using a Xerox ColorQube printer (b). This printer uses 'Solid Ink' which is similar to wax and bonds well with the metallic surface of the laminate. The ink acts as a direct etching mask when the laminate is submerged in Ferric Chloride solution to remove the unwanted metal (c). Due to the mechanism of the printing process, the laminates are limited in thickness to no greater than 18 μm metal on 50 μm of dielectric. For the majority of cases throughout this thesis the laminate used is GTS 5510 consisting of 18 μm copper on 25 μm Mylar. The ink can be removed abrasively or using a solvent such as acetone, however in the majority of cases the presence of the ink has little effect on the electromagnetic response of the structure.

3.3 Experimental Equipment

3.3.1 Network Analysers

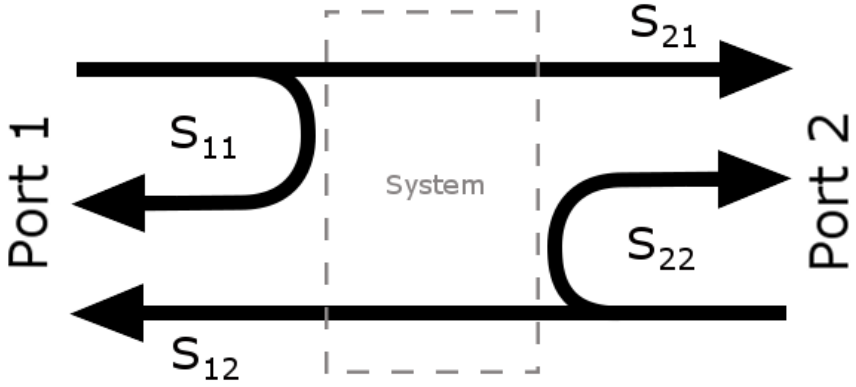

Figure 3.3: A schematic demonstrating the principles of S-parameters and how they relate to the transmission and reflection measurement of a system between two ports.

A Vector Network Analyser (VNA) is used throughout the work in this thesis to measure the microwave response of various systems, in both the radiative and non-radiative regimes (Sec. 2.4.1). The VNA (Anritsu VectorStar MS4647) is a two-port instrument that simultaneously measures the ratio of incoming to outgoing signal for all four possible signal paths between the two ports, which are connected via the device or system under test. These measurements are known as S-parameters and are denoted as S_{mn} where m and n are the receiving and emitting ports respectively. For example, S_{12} is the transmitted signal from port 2 to port 1, and S_{11} is the reflected signal at port 1. A schematic of these S-parameters is shown in Fig. 3.3. Each S-parameter is a complex value representing the magnitude and phase of the incoming signal, referenced to the outgoing signal and the VNA uses an auto-reversing feature that captures all four parameters near simultaneously. The MS4647 VNA uses a step-sweep of frequencies within a range from 100 kHz to 70 GHz to produce the frequency dependent S-parameters, represented most commonly in the form of linear magnitude and phase.

The VNA combines a source signal (produced from a crystal) with a local oscillator (in this case a voltage controlled oscillator) which are mixed to create the desired frequency. Phase-locking loops are used to maintain this precise frequency over time before it passes through the system under test. Finally, the detected signal is down-converted to a lower frequency at which signal processing is possible. A more in-depth discussion on the VNA's operation can be found in [28].

The system under test is connected to the VNA via coaxial cables. These cables

(Gore Phaseflex) are both amplitude and phase stable, meaning that moving or bending the cable does not significantly affect the signal. Signal response associated with the cable itself such as losses and impedance mismatches at the cable ends, can be removed from the measured signal via a short-open-load-through (SOLT) calibration process[29].

In some cases, where phase information is not required, a Scalar Network Analyser (Agilent 8757A)(SNA) is used instead. In this scalar set up the source of radiation to the system under test is a signal generator. The SNA measures the strength of an electrical signal through three input channels in decibel-milliwatts (dBm), the magnitude of the signal compared to 1 mW. Typically, two inputs are used, simultaneously measuring the signal before and after it passes through the system under test, allowing a normalised measurement to be obtained. This scalar set up is only used for radiative experiments.

3.3.2 Horn Antennas

Horn antennas (Fig. 3.4a) are a means of converting a guided wave into free-space radiation. Coaxial cables (coax) feed into a waveguide adapter in which the central pin of the coax acts as a dipole and excites the fundamental mode of a rectangular waveguide, as shown in Fig. 3.4b. The vertical plane depicts the instantaneous E_x field on a plane through the coax diameter. The horizontal plane shows the E_y component within the waveguide and the arrows represent the electric field vector on a cross-section of the waveguide. A transverse electric (TE) waveguide mode propagates down the rectangular channel and out of the horn (as in Fig. 3.3.2d), which is a tapered section of the waveguide designed to match the wave impedance in the guide to that of free-space ($Z_0 \approx 377\Omega$). The wave's impedance in the guide depends on its cutoff frequency f_c via the equation

$$Z = Z_0 \left(1 - \frac{f_c}{f}\right)^{-\frac{1}{2}}. \tag{3.1}$$

and the cut-off for the lowest order mode, the TE_{01}, corresponds to a half-wavelength quantisation across the longest width of the guide, a, and is therefore

$$f_c = \frac{c}{2a}. \tag{3.2}$$

The power output of the horn and its directivity vary with frequency due to this frequency-dependent impedance and separate narrowband standard gain horns are used to cover different frequency bands. These bands are industry standards and those most commonly used in this thesis are the Ku (12-18 GHz), K (18-27 GHz), Ka (27-40 GHz), and V (40-75 GHz) bands. For some experiments a broadband horn is used which operates between 5 and 40 GHz. Fig. 3.4c shows the directivity of a standard

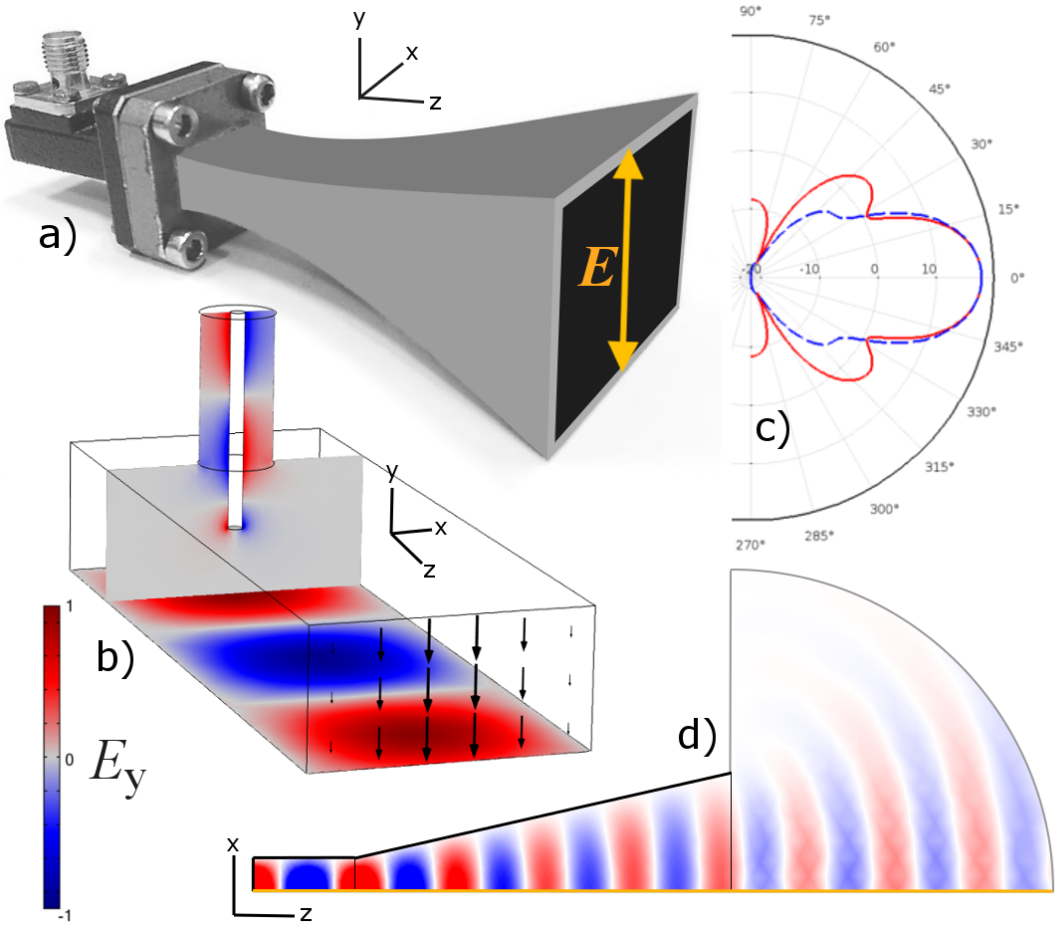

Figure 3.4: a) A horn antenna connected to a coax to waveguide adapter. The orange arrow indicates the electric field polarisation of the emitted radiation. b) The coax to waveguide adapter, modelled using COMSOL. The vertical plane shows variation of the instantaneous x component of electric field within the coax and surrounding the exposed pin. The horizontal plane shows the y component within the waveguide. Both are normalised to unity. c) The directivity of the horn antenna in the xz plane (blue dashed line) and the yz plane (red solid line). d) A slice of the horn antenna in the xz plane showing the variation of E_y. Only one half of the cross-section is shown, with the orange line acting as a mirror plane.

gain Ku band horn antenna, at its central frequency of 15 GHz. This represents the transmitted power (in decibels) as a function of angle, obtained at some distance r from the centre of the horn aperture and normalised to that of an isotropic point source. The solid red line shows the plane of electric field (yz) and the blue dashed line the plane of magnetic field (xz), where the z direction is along the waveguide axis. In both planes, the majority of power is in a $\approx 50°$ beam, centred around $0°$ and the beam diffracts into side lobes due to the termination of horn. Fig. 3.4d demonstrates the E_y component of the radiated beam over half of the magnetic field plane (xz), with the

orange line representing a mirror plane of the structure.

3.3.3 Absorbing Material

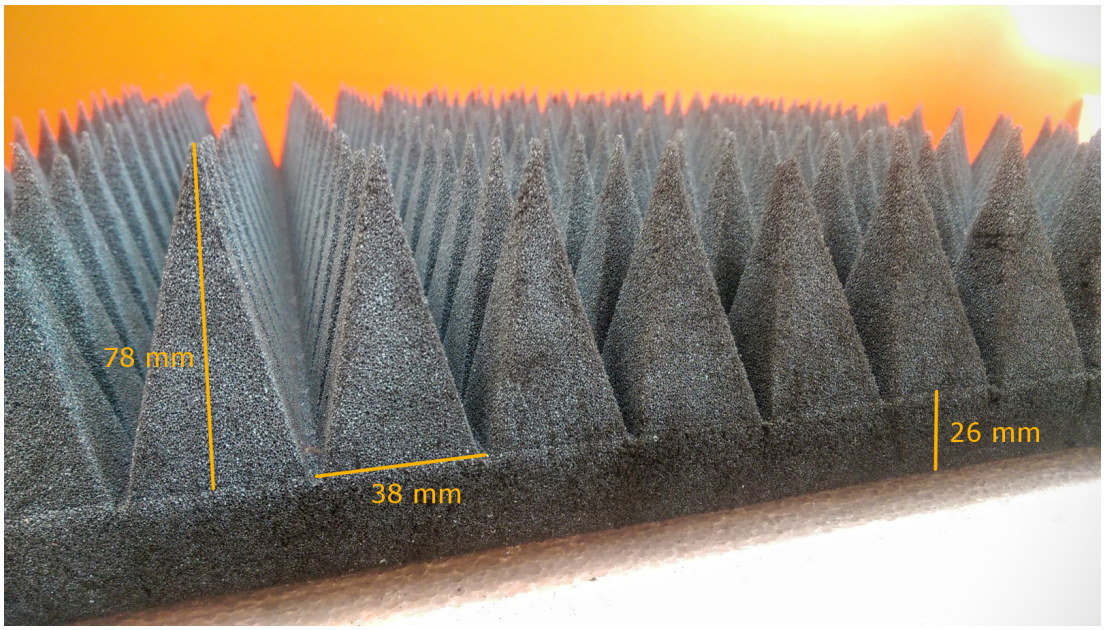

Figure 3.5: A photograph of a pyramidal absorbing panel. 99% of radiation incident from above is absorbed up to an incident angle of 60°.

Pyramidal and convoluted absorbing panels (Eccosorb CV and VHP respectively) are used to shield scattering objects in and around the experimental apparatus. They consist of a sheet of foam, loaded with an electromagnetically lossy powder. For Eccosorb CV (shown in Fig. 3.5) the side of the foam facing the incident radiation is tapered into multiple 'pyramids' that act to match the impedance of free-space to that of the absorber. For Eccosorb VHP, the surface is instead a convoluted 'egg box' shape. Both of these panels are broadband, absorbing over 99% of incident power at all frequencies considered in this thesis. This performance is maintained up to an incident angle of 60°[30][31].

In order to absorb surface waves, tapered sheets of graphite loaded elastomer are used. Combining flakes of graphite into the elastomer increases its dielectric loss tangent[32] and therefore surface waves are attenuated within the sheet. This prevents unwanted reflection of surface waves from the sample edge. In some cases, single strips of the pyramidal absorbing panels are laid on the surface instead.

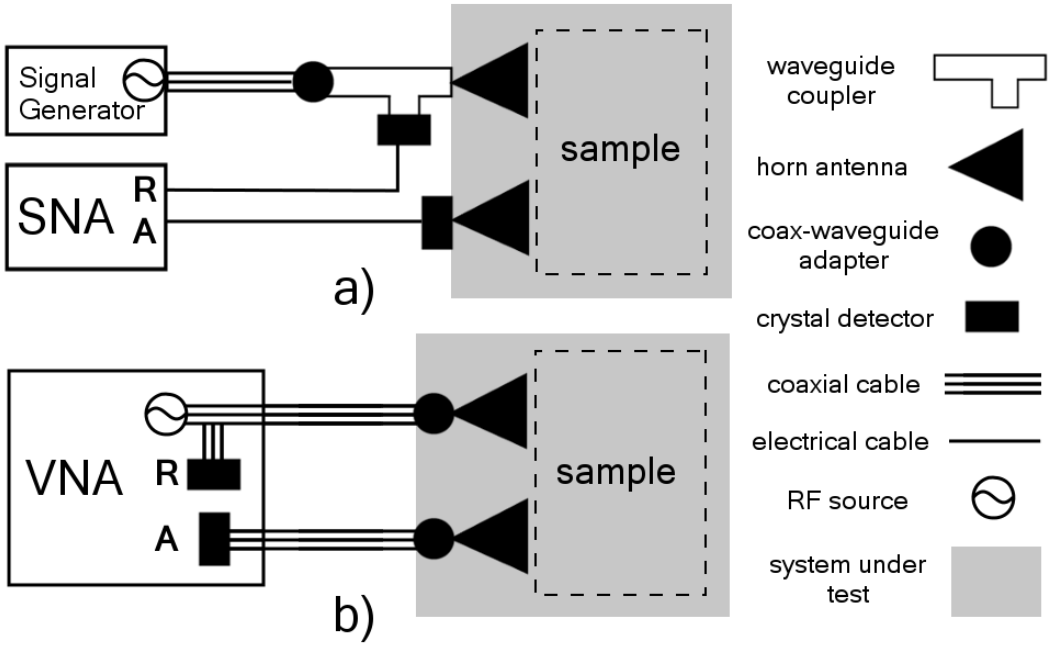

Figure 3.6: A schematic of the scalar (a) and vector (b) network analyser measurements for radiative experiments. The signal, A, that has passed through the system under test is reference to a signal that has not, R.

3.4 Radiative Experiments

Of particular interest regarding patterned metallic films is how they act as filters. In other words, how radiation reflects, transmits, scatters or absorbs when it impinges on the structure. This can be found experimentally by illumination with a planar microwave 'beam' which propagates through free-space. This is labelled a radiative experiment as it provides information of the structure's response within the radiative region of the energy-momentum dispersion diagram (Sec. 2.4.1 and Fig. 2.8). A description of the methods and instrumentation involved are outlined below.

Radiative measurements can be made using a scalar (which measures amplitude only) or a vector (amplitude and phase) network analyser. The two systems require different configurations of cables, antennas and other devices as shown in Fig. 3.6. In the scalar system (Fig. 3.6a), the radio frequency (RF) signal is supplied by a signal generator and fed through a coaxial cable. A coax to waveguide adapter (Sec. 3.3.2) excites the fundamental TE_{10} mode of a rectangular waveguide directional coupler, which divides the signal in two. One half enters a crystal detector which converts the signal into an electrical current which travels down a single conductor cable to the Scalar Network Analyser (SNA) where it is recorded as a reference signal, R. The other half is emitted from a horn antenna, interacts with the sample in some way, and is collected

by a second horn antenna. This signal is also converted using a crystal detector and fed into a second input, A, of the SNA. The grey shaded region in Fig. 3.6a shows the extent of the system under test (SUT), which includes the horn antennas and the free-space between them. Losses within the SUT that are not attributed to the sample cannot be accounted for by the reference measurement, R. Therefore, two measurements are required, one with the sample (denoted A) and one blank measurement, without the sample in the SUT (B).

A diagram of the principles behind the vector system is shown in Fig. 3.6b. The most notable difference is that the VNA is both a generator and detector of RF radiation. A reference signal, R, is recorded as radiation leaves the VNA, as mentioned in Sec. 3.3.1. Coaxial cables attach the input and output of the VNA to horn antennas via coax to waveguide adapters. The crystal detectors in this system are located within the VNA itself. Losses within the coaxial cables is accounted for by the calibration process (Sec. 3.3.1), however those of the horn antennas and adapters cannot be and hence they are included in the system under test (grey region). Again, this means two measurements, A and B are required in order to obtain a fully normalised signal through the sample.

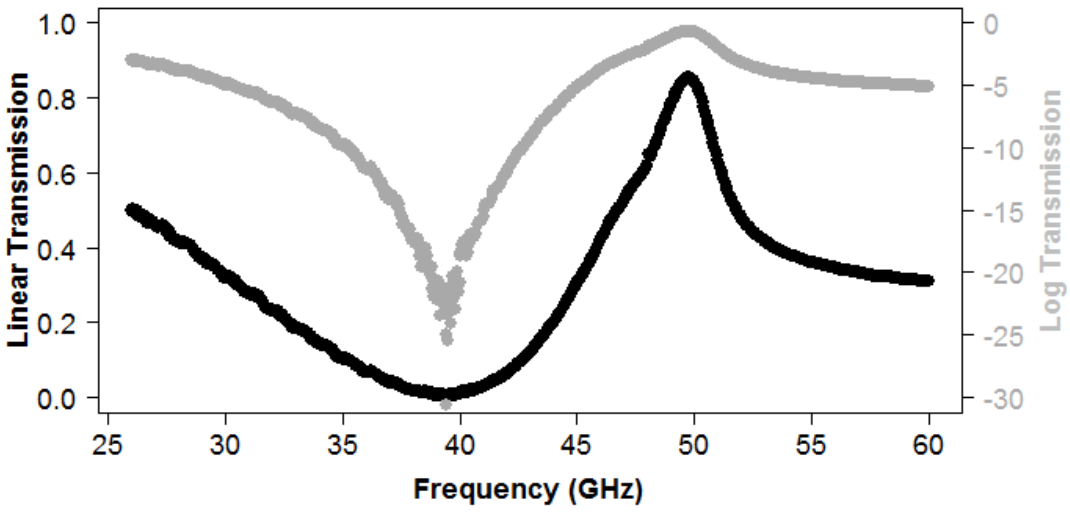

Figure 3.7: A typical transmission spectrum for a metallic checkerboard array obtained experimentally. The linear transmission coefficient (black, left axis) is contrasted with the same data represented on a logarithmic scale (grey, right axis).

This normalised signal can either be expressed on a linear or logarithmic scale. The latter is often useful as it emphasizes variations at small signal levels. Given that A and B are recorded in decibels (dB), they relate to the linear, S, and logarithmic, S_{dB}

normalised signal intensity by the following formulas

$$S = 10^{(A-B)/10} \tag{3.3}$$

$$S_{dB} = 10log_{10}(S) = A - B \tag{3.4}$$

Fig. 3.7 shows the difference between a linear (black points) and a logarithmic (grey points) representation of the signal passing through a checkerboard square array structure at normal incidence. The following sections will outline how radiation passes between the two horn antennas in Fig. 3.6.

3.4.1 Transmission Setup

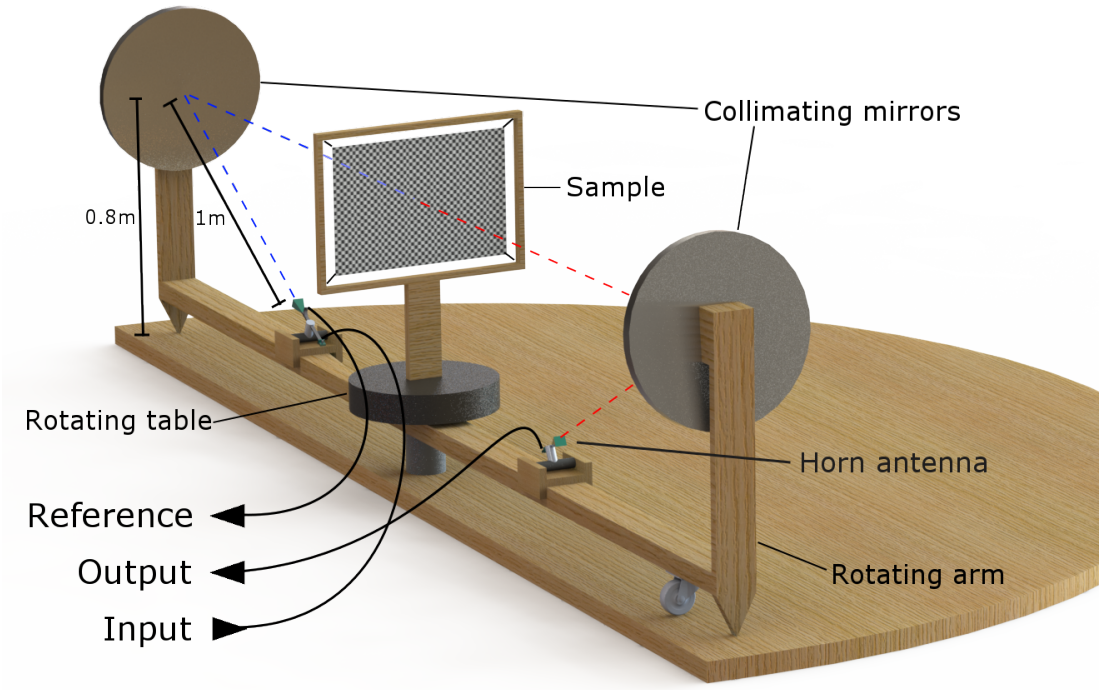

Figure 3.8: The radiative experimental setup, shown in the normal incidence transmission configuration. A spherical mirror of focal length (f = 1 m) collimates microwave radiation from a horn antenna and directs it to the sample (blue dashed line). The transmitted beam (dashed red line) is focussed by a second mirror on to a detecting horn antenna. A computer-controlled rotating table allows transmission at various angle of incidence to be determined.

Fig. 3.8 shows the experimental setup for measuring the transmission of microwave radiation through a structure. A horn antenna (as described in Section 3.3.2) is fed

via a coaxial cable attached to either the scalar or vector analysis system described above. Whilst the horn antenna is directive, there is considerable angle spread in the radiating lobe, as shown in Fig. 3.4b. Hence, before passing through the structure, the radiation is collimated using a spherically concave mirror with a one metre focal length. The outer regions of this mirror are covered with pyramidal absorbing material to reduce the effects of diffraction from the mirror edges, leaving a circular aperture at the mirror centre. The mirror reflects an approximately planar beam of diameter 200 mm that is directed at the sample. The transmitted signal is re-focussed by a second, identical mirror and collected using a second horn antenna, placed one metre away.

The sample is mounted to a wooden frame attached to a computer-controlled rotating table. This allows transmission measurements for a range of incident angles up to a maximum of 60°, a limitation due to finite sample size. Where possible, supports and mounts use wooden or perspex parts, to minimise unwanted interference arising from radiation scattering off them.

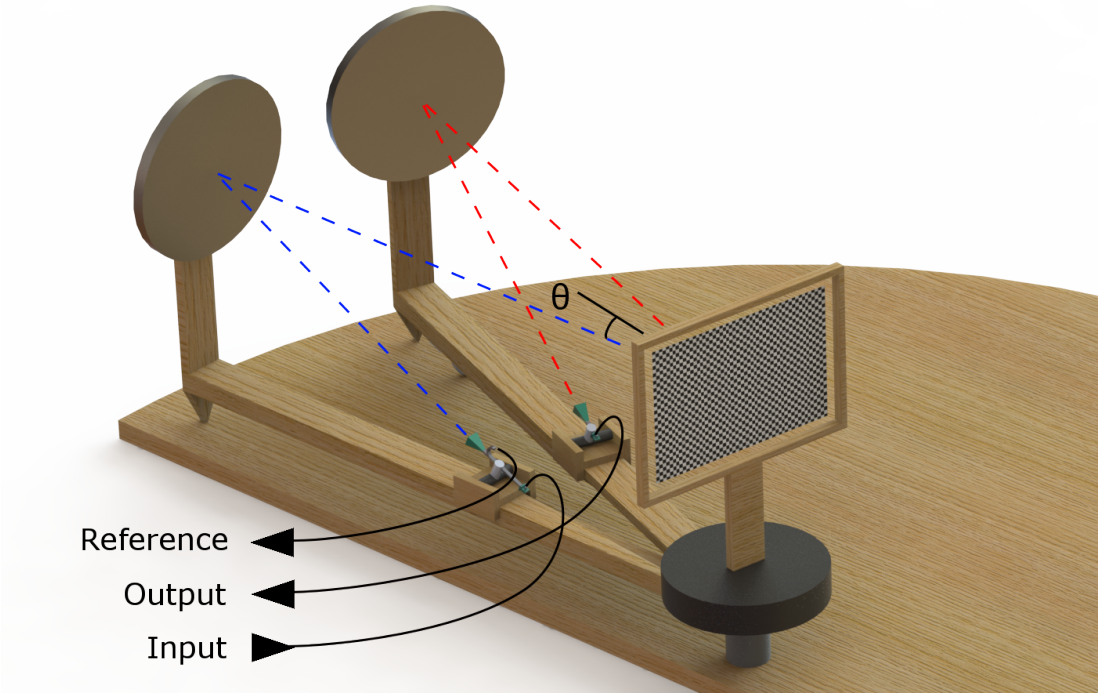

Figure 3.9: The experimental setup in reflection configuration. The incident and reflected beams are represented as blue and red dashed lines respectively. A rotating arm allows reflection to be determined at a range of incident angles, θ, between 10° to 60°.

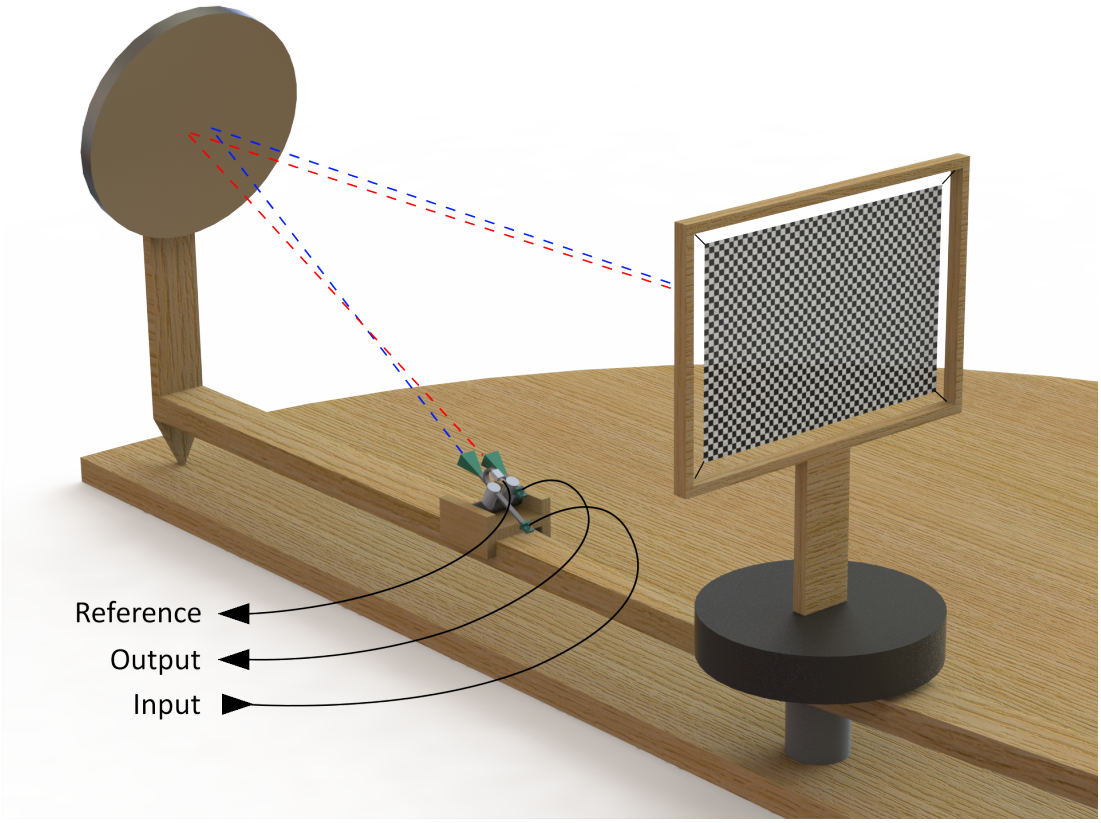

Figure 3.10: The normal incidence reflection setup. The same mirror is used to both collimate and re-focus the microwave beam. The incident and reflected beams are represented as blue and red dashed lines respectively.

3.4.2 Reflection Setup

Reflection measurements are taken using the same setup as for transmission as shown in Fig. 3.9. The second arm, holding the focussing mirror and receiving horn, can rotate to allow reflection at incident angles $10° \leq \theta \leq 60°$. As the arm rotates through an angle 2θ, the sample is rotated by θ, maintaining the specularly reflected beam's position in the centre of the second mirror. The incident and reflected beam paths are represented by blue and red dashed lines respectively.

For normal incidence reflection (see Fig. 3.10) only one collimating mirror is used, with both the emitting and receiving horn antenna placed at the focus, adjacent to each other. This offset from the focus means that the angle of incidence is in fact $\approx 2°$, as the incident (blue dashed line) and reflected (red dashed line) beam are slightly off-centred on the mirror. This is often a sufficient approximation to normal incidence. In all reflection measurements, pyramidal absorbing panels are placed directly behind the structure to absorb the transmitted signal.

3.5 Non-radiative Experiments

In addition to observing how surface waves in the radiative region can affect how microwaves transmit through and reflect from various structures, it is also possible to experimentally observe them in the non-radiative regime. Surface waves with momentum along the surface greater than that available from free-space radiation are bound to the interface between the surface and the air above. Exciting, detecting, and characterising these waves involves working in the near-field.

3.5.1 Near Field Probes

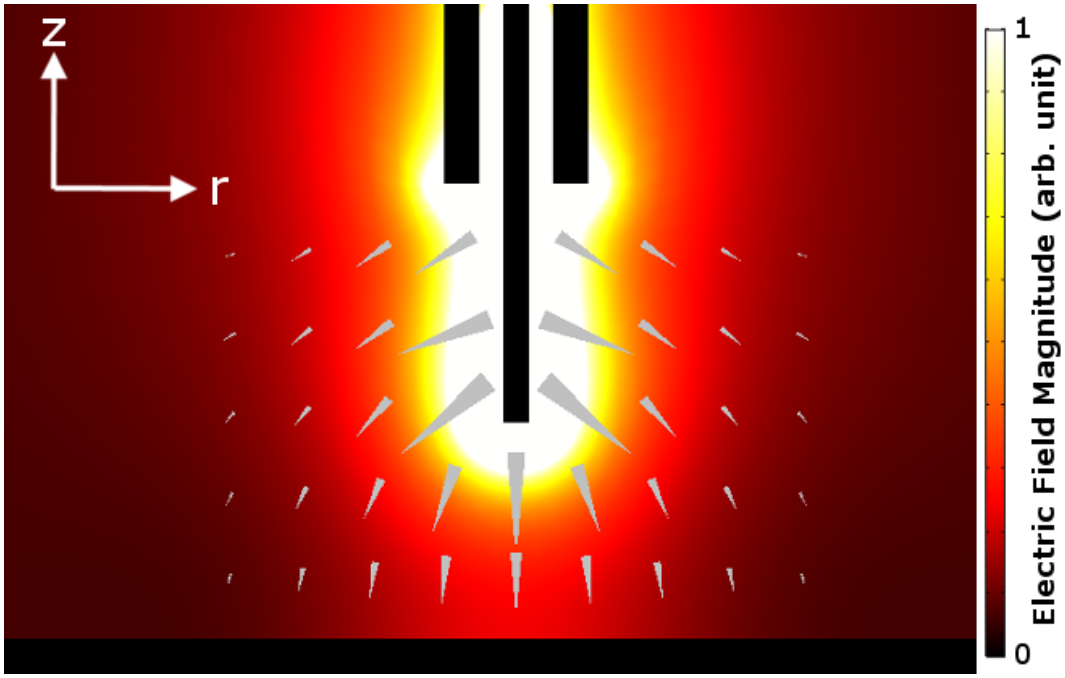

Figure 3.11: Finite Element Method simulation of a stripped coaxial antenna placed normal to a metallic sheet, driven at a frequency of 10 GHz. The colour scale shows the electric field magnitude and the arrows demonstrate the instantaneous electric field vector at a phase corresponding to maximum field strength. Metallic regions are shaded black.

To probe the near-field of a surface wave a pair of cut coaxial cables driven by a Vector Network Analyser (VNA) are used. A ≈ 1 mm section of the outer conductor and dielectric filler is stripped away from the cable leaving a length of the central conductor exposed. In contrast to horn antennas, these are not impedance matched to free space in their operating frequency band (up to 40 GHz). The radiating efficiency increases with frequency as the exposed wire increasingly resembles an electric dipole (which occurs at 150 GHz, where the exposed wire contains half a wavelength). Despite

power conversion from the coaxial mode to free space being poor, conversion to another guided wave (such as a surface wave) can be maximised. To achieve this, the antenna is placed in close proximity to the surface, oriented in such a way as to maximise coupling to the surface mode via evanescent near-fields containing a range of wavevectors. Fig. 3.11 shows the electric field magnitude (colour plot) and instantaneous electric field vector (arrows) in the vicinity of a stripped coax antenna oriented normal to a metallic ground sheet placed 1 mm away. The near field of the antenna contains both E_z and E_r components, and surface modes can be excited by either. However, below the exposed section of coax, the field is almost purely E_z. Orienting the antenna normal to the surface maximises the isotropy of any modes excited. A second, identical probe connected to the VNA can be used to measure the surface wave's magnitude and phase at any given point. Fig. 3.12 demonstrates a typical setup containing a metallic checkerboard array, with the source antenna placed over the centre of a metal patch, where E_z is largest (according to numerical modelling).

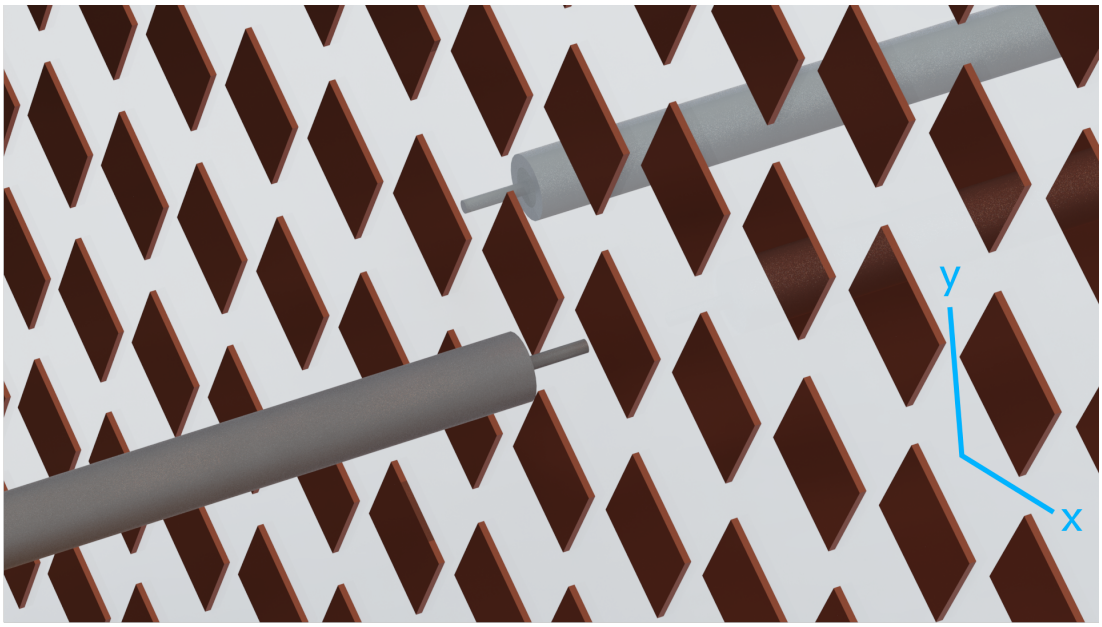

Figure 3.12: A schematic of the near field scanning experiment. A stripped coaxial antenna is placed approximately 1 mm away from and perpendicular to the sample plane. A second probing antenna is scanned across the opposite side of the sample using an XYZ stage.

Unlike propagating fields, whose in-plane momentum (i.e. wavevector) is limited to $|k| \leq \omega/c$ (within the light line), the exponentially decaying near field contains momenta much greater than that of free-space radiation. Hence it can excite surface waves radially that propagate on the surface until they are absorbed or scattered into a radiative mode from a defect or sample edge. The existence of the two antennas

themselves will perturb the surface wave they are coupling to, however providing the dipole dimensions are small compared to both the periodicity and wavelength this change is negligible.

3.5.2 XYZ Stage

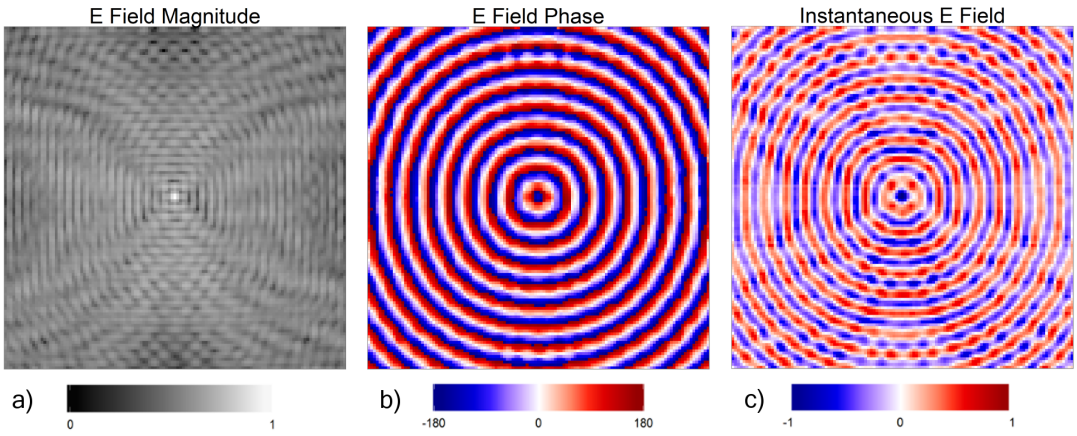

Figure 3.13: An example field plot produced using the near-field scanner with antennas oriented normal to the surface. The magnitude of the electric field (a) is combined with the phase measurement (b) to produce the instantaneous field image (c). The excitation is at the image centre.

The detecting probe is scanned over the surface of the sample using a motorised XYZ stage (provided by Aerotech and Hepco Motion). Both the stage and the VNA are controlled using Labview in order to automate the scanning process. The available scanning area is approximately a cube of side length 1 m, and the maximum resolution of steps in any direction is 200 μm. In the majority of cases a two-dimensional scan is required which, for flexible samples produced using the print and etch method in Section 3.2.2, is done in a vertical plane to avoid the sample bowing in the centre. The sample is mounted in a rectangular wooden frame, and the scanning probe is attached to the moving stage via a length of rigid perspex sheet. This ensures that no metallic components of the stage are in the vicinity of the sample, and reduces the likelihood of free-space radiation (not associated with the surface wave) scattering into the scanning area. Surface waves on thin samples (which support coupled waves on both sides of the film) can be excited on one side, and detected on the other. This not only allows for the scanning probe to pass over the excitation point, it also reduces the coupling between the two antennas via free-space radiation (which disperses along the light line).

An example field scan for the checkerboard array at a frequency of 20 GHz is demonstrated in Fig. 3.13. The source is positioned at the centre of the scan. The

magnitude of the probe signal, E_0 (shown in (a)) is combined with the phase, ϕ (shown in (b)) to produce the instantaneous electric field image (c) via the following equation

$$E_{\text{inst}} = \text{Re}(E_0 \exp(i\phi)) \tag{3.5}$$

As the probe is oriented along the surface normal, this can be considered the normal component (z-component) of the electric field, however the probe does inevitably pick up some of the in-plane components as well.

The magnitude of the field (Fig. 3.13a) is maximum at the source position and decays away from the source according to the mode's propagation length. For this example case the propagation length is much greater than the sample length and hence significant interference is present due to reflections from the sample edges. This can be overcome somewhat using absorbing materials. The phase measurement (Fig. 3.13b) reveals the phase fronts of the wave and Fig. 3.13c combines the two yielding the instantaneous field at a phase corresponding to maximum field strength.

3.5.3 Reciprocal Space

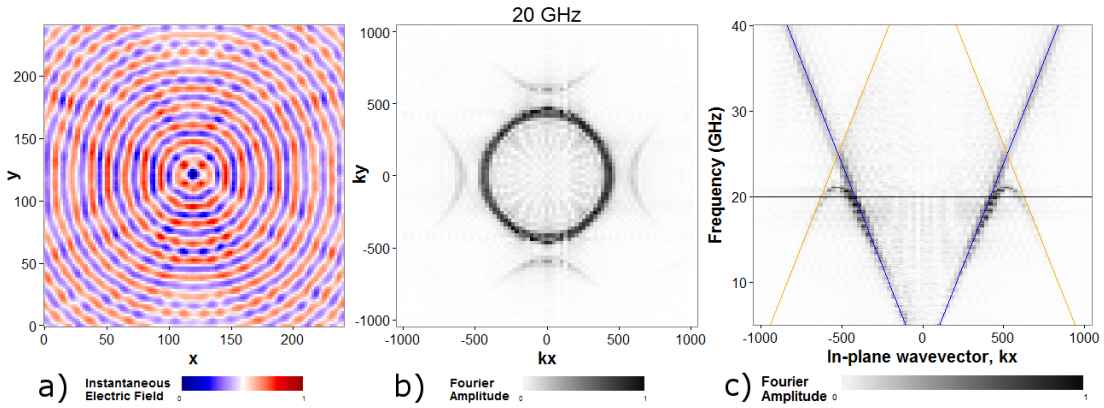

Figure 3.14: The 2D spatial Fourier transform of the instantaneous field (a) produces the isofrequency contour (b). Combining this data for a range of frequencies results in the dispersion curve (c). The black horizontal line shows the frequency at which (a) and (b) are shown and the blue and orange lines represent the zeroth order and diffracted light lines respectively.

Due to the presence of interference and the fact that multiple modes can be present in the instantaneous field image, it is difficult to extract information about the wave propagation directly from the plots in Fig. 3.13. A spatial Fourier transform of the instantaneous field shows the wavevectors (in both x and y directions) required to produce the image along with a corresponding weighting factor (known as Fourier

amplitude). For each frequency this Fourier analysis can convert the real space field image (Fig. 3.14a) into reciprocal space map illustrating the 'isofrequency contours' associated with the modes (Fig. 3.14b). Grazing radiation that exists on the light line of the dispersion curve appears as a circle in this reciprocal space plane, whilst bound surface modes exist outside of this circle, with greater momentum.

Repeating this process for a range of frequencies provides the full dispersion of modes in the form of Fourier amplitude, $\mathcal{F}$ (the weighting factor), as a function of frequency, f and in-plane wavevector $(k_{\mathrm{x}}, k_{\mathrm{y}})$. The dispersion can then be plotted through a particular plane of this data, as shown in Fig. 3.14c.

The chosen real space coordinates, in either x or y, are given by the sequence (of N values)

$$[0, \Delta x, ..., (N-1)\Delta x] \tag{3.6}$$

where Δx is the step size in the scan and $(N-1)\Delta x = L$ is the length of the scan.

This maps to the reciprocal space coordinates given by

$$[-k_{\max}, -k_{\max} + \Delta k, ..., 0, ..., k_{\max}] \text{ for even N} \tag{3.7}$$

$$[-(k_{\max} - \frac{\Delta k}{2}), -(k_{\max} - \frac{\Delta k}{2}) + \Delta k, ..., 0, ..., (k_{max} - \frac{\Delta k}{2})] \text{ for odd N} \tag{3.8}$$

where

$$k_{\max} = \frac{\pi}{\Delta x} \text{ and } \Delta k = \frac{2\pi}{L + \Delta x} \tag{3.9}$$

are the maximum wavevector and the resolution in wavevector of the resulting Fourier transform. Hence, the resolution in the real space scan alone dictates the maximum wavevector, whereas the wavevector resolution is determined primarily by the overall length of the scan. Hence, in order to maximise the resolution within the first Brillouin zone of the dispersion the scan should cover as many unit cells as possible. Obtaining two measurement points per unit cell such that $k_{\max} = 2\pi/a$, where a is the periodicity, ensures that the resulting dispersion spans both the first and second Brillouin zones.

3.6 Data Analysis

All data analysis and plotting is carried out via the statistical programming language R, using the RStudio software. This was chosen as it is open-source software and contains many packages for data analysis. Notable packages used are *ggplot2* for plotting data, *data.table* for management of large data sets, and *reshape2* for matrix representation

of data.

3.7 Numerical Simulations

Numerical simulations are initially utilised in order to predict experimental results. More importantly, however, they provide a greater understanding of electromagnetic phenomena by allowing the visualisation of electromagnetic fields. Two commercially available modelling packages, COMSOL and HFSS, are used throughout this thesis and both use the finite element method which is outlined below. The simulations conducted can be broadly split into 'driven' and 'eigenmode' categories. The radiative driven models require 'ports' through which radiation of any desired frequency (resonant or non-resonant) and field distribution can enter or exit the model. Conversely, eigenmode models require no ports as the software computes the resonant frequencies of the system. The basics of these procedures are outlined in this section. In general, driven simulations are carried out using HFSS and eigenmode simulations with COMSOL.

3.7.1 Finite Element Method

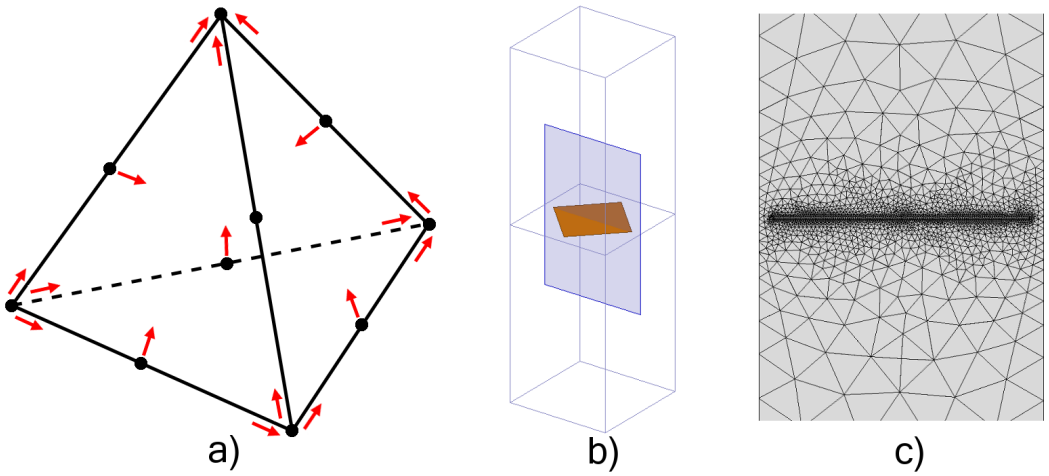

Figure 3.15: a) A tetrahedral mesh element, with arrows representing the field components evaluated at each vertex. b) A typical unit cell for the checkerboard array. c) The mesh around the metallic patch shown on a plane through the patch centre (blue area in (b)).

The finite element method of numerical simulation works by dividing the geometry of a structure into small, discrete elements (most commonly tetrahedra) collectively called a mesh, and solving Maxwell's equations at the boundaries between elements. Specifically, information regarding field components tangential to the tetrahedra's edges

are calculated at each vertex, while at the midpoints of the edges, the field component normal to the edge and parallel to each face is evaluated. This is illustrated schematically in Fig. 3.15a, along with the unit cell for a metallic checkerboard array (b) and an example of a mesh in the plane perpendicular to the patch (c). The spatial variation in field is interpolated based on these discrete mesh points.

3.7.2 Field Solver

The method of calculation varies depending on whether the model is 'driven' (i.e. it is given a source of field such as a rectangular port or coaxial cable) or whether it is an eigenmode model (which requires no source of excitation). In both cases, the software attempts to find a solution to the following wave equation, which is derived from Maxwell's equations. For a field quantity x;

$$Sx - {k_0}^2 Tx = b \tag{3.10}$$

where S and T are matrix quantities that depend on the geometry, mesh and materials, and k_0 is the free-space wavevector of radiation, related to frequency via $2\pi f = c/k_0$ where c is the speed of light in vacuum and b is a quantity related to the source of excitation for the model.

For driven models, b is determined by the chosen excitation (called ports) for the model, and the matrix equation above is solved for a desired frequency, providing the full field of the model geometry. This is converted into an S-matrix which contains radiative parameters such as the amount of reflection and transmission between different ports, which can be compared to experimental results.

For eigenmode models, the initial conditions are zero field everywhere and hence $b = 0$, and a set of eigenvectors and eigenfrequencies is calculated by solving equation 3.10, yielding one eigenfrequency for each unique field configuration. There are no S-parameters associated with eigenmode models, as no excitation is used. Eigenmode models are useful for finding resonant modes of the system that lie outside the light cone, such as surface modes. However the model only discovers if, and at what frequency, a mode exists and reveals nothing about the coupling strength to a particular source of radiation.

3.7.3 Boundary Conditions and Excitations

For both driven and eigenmode simulations periodic structures appropriate boundary conditions must be chosen. Periodic boundary conditions mean that the response of an infinite sample can be computed by simulating just a single unit cell of the structure,

with a given phase difference between the fields at opposite faces. External faces of the model that do not use periodic conditions and are not used for excitation need to be defined differently, for instance by a perfect electric or magnetic conductor (PEC/PMC, where the tangential component of the electric/magnetic field is zero).

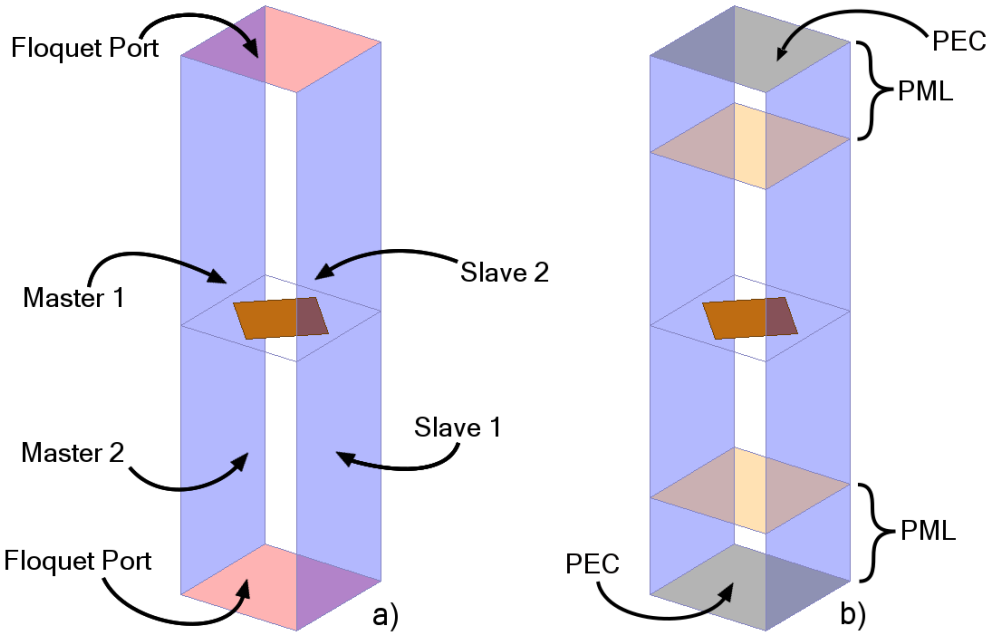

Figure 3.16: The boundary conditions for the checkerboard unit cell for a) a driven model with Floquet ports and b) an eigenmode model with perfectly matched layers.

A radiation absorbing boundary can be approximated using a perfectly matched layer (PML). A PML has a certain thickness over which radiation is gradually absorbed without reflecting, before the PML terminates, usually at a PEC or scattering boundary. This is most useful for approximating semi-infinite media, such as free-space above a conducting surface.

For most driven models used in this thesis, Floquet ports are used as an excitation. Placing a port on both sides of a structure allows the transmission and reflection to be determined. The Floquet port, along with the periodic boundary conditions, can inject a plane wave at any angle of incidence to the surface normal. A typical model geometry, complete with boundary conditions and excitations for the checkerboard array is shown in Fig.3.16. The driven model (a) contains Floquet ports through which radiation can enter and exit the model, whereas those same faces on the eigenmode model (b) are terminated with PMLs backed with PECs.

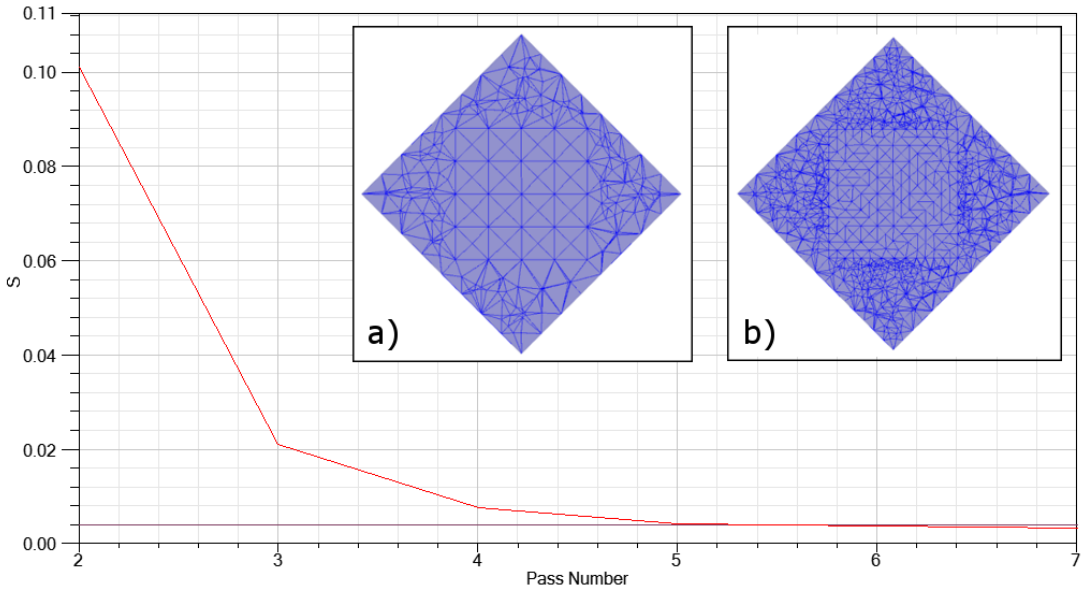

Figure 3.17: A convergence plot showing how a given S-parameter converges on a solution as the mesh density increases with each consecutive pass. Inset: The initial mesh (a) and the refined mesh after the convergence condition is met (b).

3.7.4 Meshing and Convergence

Convergence is a crucial procedure in finite element method modelling. Once the solver has computed the field distribution for a particular mesh it redefines the mesh, increasing the density of tetrahedra in regions of large gradient in the field strength. The field is computed once more and the solution compared to the previous one. This process is repeated, for multiple passes, until the difference in successive solutions is below a user-defined threshold. At this point the model is assumed to have converged on the correct solution, where the field at discrete mesh points can be considered a sufficient approximation to the continuous field distribution. Fig. 3.17 shows an example of a convergence plot of the difference in a chosen S-parameter, S, as the pass number increases, along with the difference between the initial mesh (a) and the converged mesh (b) on the plane of the metallic square, inset. During the convergence process, smaller mesh elements have been concentrated around the edges of the metallic patches, where electric field gradients are largest. The model used here is simplified in that the metallic patch is a two-dimensional PEC sheet floating in vacuum.

3.7.5 Conclusion

In this chapter, the methods and processes used during fabrication, experiment and simulation have been outlined. The experimental methods used in this thesis are either

radiative, where scattering parameters of patterned metallic sheets are studied, or non-radiative, where the propagation of bound surface waves are investigated using a near-field scanning technique. In simulation, finite element method modelling is performed in order to verify experimental measurements and study in detail the field components of a system. These methods are used throughout the work contained in the remainder of this thesis.

Chapter 4

Polarisation Conversion from Microcavity Arrays

4.1 Introduction

The ability to polarise and to manipulate the polarisation state of electromagnetic radiation has been an essential tool ever since the wave nature of light was first understood. One such manipulation is the ability to rotate the polarisation of linearly polarised radiation as it reflects from or transmits through a structure. This may be achieved via birefringence. Linear birefringence occurs in materials where orthogonal (x and y) components of electromagnetic radiation experience different refractive indices, in devices such as half- or quarter-waveplates that convert linearly polarised radiation into 90° rotated linear or circular polarisations respectively. Linearly birefringent structures possess anisotropy and hence their performance depends on their azimuthal orientation with respect to the incoming polarisation. In contrast, circularly birefringent materials possess different refractive indices for right (RCP) and left (LCP) circularly polarised radiation. This provides the potential to rotate linearly polarised radiation to any desired angle provided no circular dichroism, a differential absorption for LCP and RCP waves, is present. Chiral effects will be covered further in Chapter 5 of this thesis.

4.2 Background

Numerous structures have been used to achieve 90° polarisation conversion via linear birefringence. Diffraction gratings are capable of linear conversion upon reflection[33][34][35], and the bandwidth can be broadened by the excitation of bound surface modes[36][37].This has been experimentally demonstrated in both the microwave[38] and visible[39][40][41][42] domains of the electromagnetic spectrum. More recently, the field of metamaterials

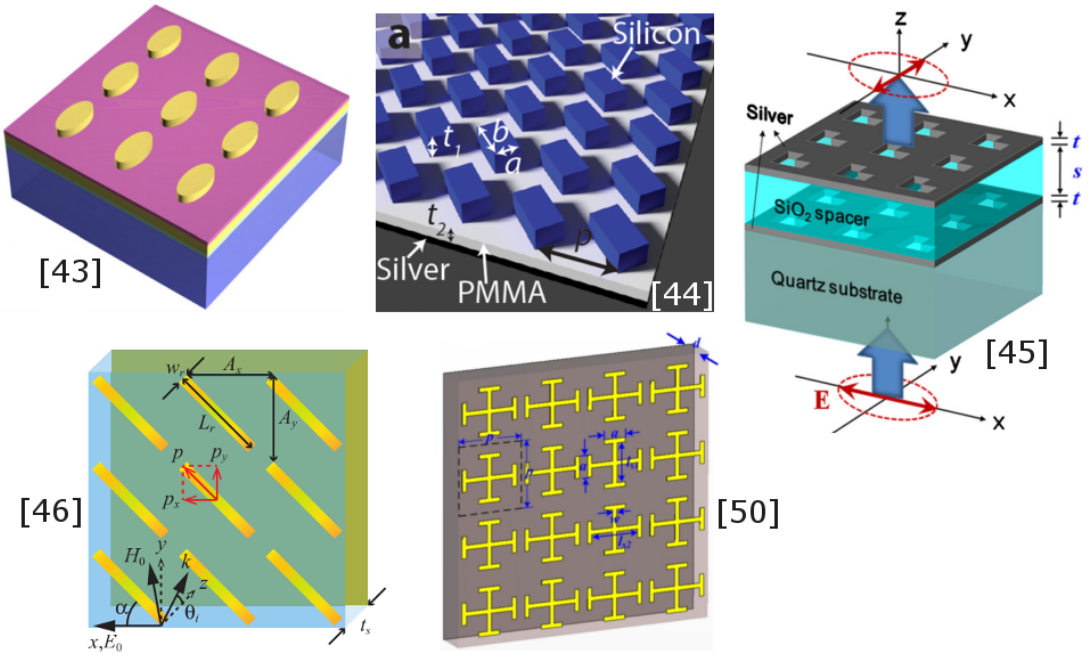

Figure 4.1: Some schematics showing the structures utilised for polarisation conversion by other authors. Each comprises a metallic ground plane and a dielectric substrate supporting a periodic arrangement of anisotropic conductive elements. Images are taken from the original papers and labelled with the citation number.

has led to a similar result; polarisation conversion upon reflection, using much thinner arrays of anisotropic metallic elements above a ground plane. These geometries include elliptical patches in the visible regime[43], dielectric cut-wire arrays[44] and 'L'-shaped holes[45] in the infra-red, metallic cut-wires at terahertz frequencies[46], and split-rings[47][48] and 'I' shaped wires[49][50] in the microwave regime. Many of the structures used in these studies are depicted in Fig. 4.1.

The underlying principle behind these structures, namely linear birefringence, is the same for the work presented in this chapter. However, we demonstrate that polarisation conversion can be realised using a much simpler structure consisting of two orthogonal arrays of narrow slits in a metal sheet separated from a ground plane by a dielectric layer. This design would be beneficial when scaled to higher frequency regimes where fabrication is more difficult. Unlike relief gratings, polarisation conversion from this array is a resonant effect associated with the dielectric cavity. Crucially, we use a very low-loss dielectric and optimise the geometry in order to minimise Joule heating resulting in less than 2% absorption. We design the structure so that the frequency of the cavity resonances results in a 3.1 GHz band across which 95% of incident radiation is polarisation converted. Finally, we study the effect of incident angle, polarisation

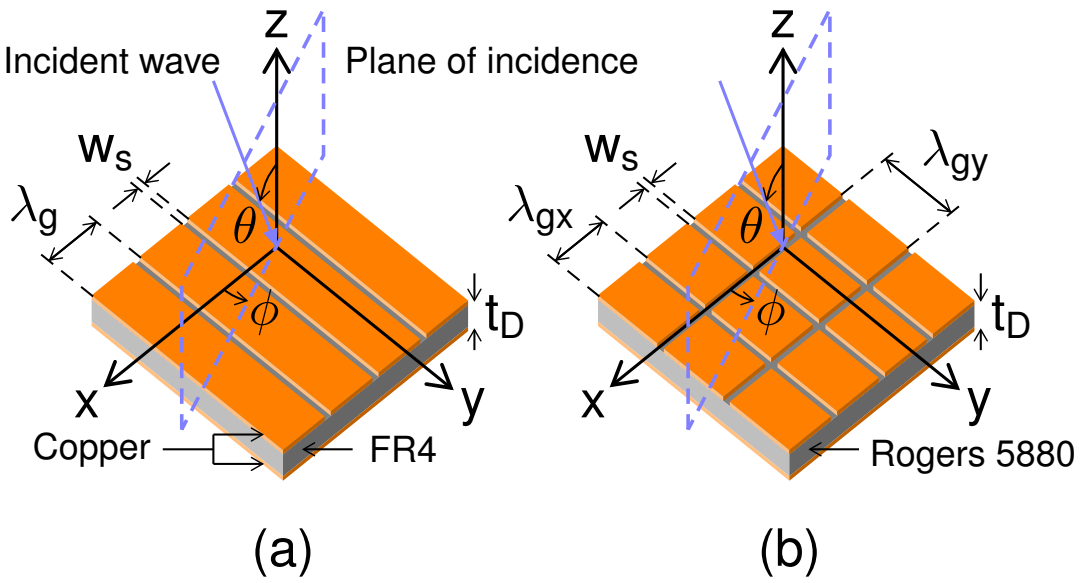

Figure 4.2: Sample geometry and coordinate system for a) the monograting cavity array with period λ_g and slit width w_s and b) the bigrating cavity array with periodicity λ_{gx} and λ_{gy} in the x and y-directions respectively.

angle and slit width on the polarisation conversion and study the polarisation state for all frequencies in the vicinity of the resonances.

The metamaterial studied in this chapter consists of a perforated metallic layer separated from a ground plane by a dielectric. Initially, the upper surface contains a single set of continuous, subwavelength, parallel slits (referred to here as a monograting) shown schematically in Fig. 4.2a. Resonant microwave absorption occurs because radiation polarised in a plane containing the grating vector has an electric field component which can excite lateral resonances within the dielectric cavities between adjacent slits[51][52]. At the fundamental resonant frequency the time-averaged electric field is maximum along the edge of the metallic strips due to a build up of charge. In the dielectric layer a standing wave is formed with field maxima at either side of the slit region and minima in the centre of each metallic strip and below the centre of the slit. This can be seen in Fig. 4.3 which shows, on resonance, the time-averaged electric field magnitude (a) and the electric field vector (b) of one unit cell of the structure across a plane perpendicular to the slit. Due to a rapid change of phase as the field diffracts through the slit, the structure resonates at a much lower frequency than expected given the unit cell size, as explained in Ref. [52]. Adding a second set of slits in the orthogonal direction, creating a bigrating (Fig. 4.2b), provides the structure with a second resonance. With normally incident radiation polarised at 45° to both sets of slits, the coupling efficiencies of the incident radiation to these resonances are equal. In this work

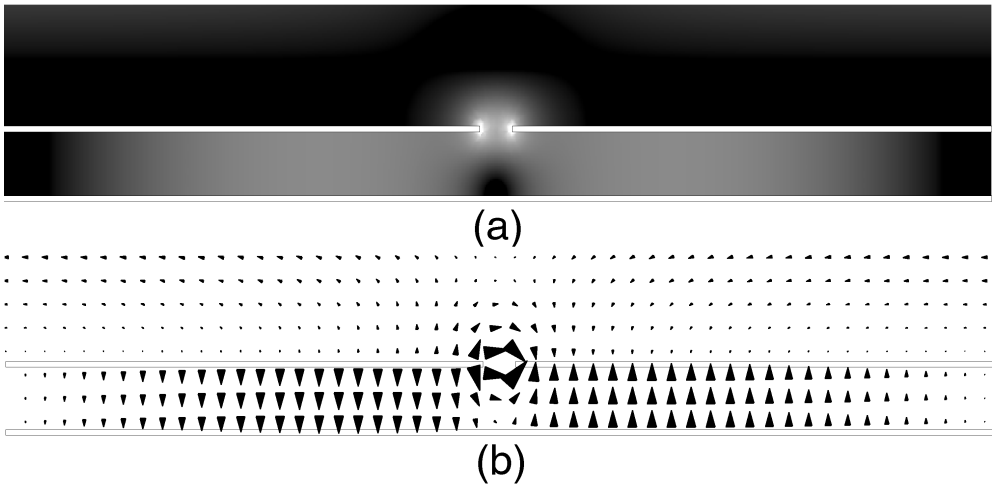

Figure 4.3: A cross-section of a single unit cell of a typical monograting structure perpendicular to the slit at the fundamental resonant frequency. The metallic sections are shown as bordered white regions. a) Resonant time-averaged electric field magnitude where black to white represents increasing field strength. b) Resonant electric field vector at a phase corresponding to maximum field enhancement, showing the reversal of the field beneath the metallic strip.

we show how the cavity structure can be used as a polarisation converting mirror. This is achieved by delaying the phase of one orthogonal component of the reflected electric field with respect to the other in much the same way as a half-wave plate. This phase delay is a frequency dependent quantity that is dictated by the cavity resonance(s).

Schematics of the two experimental structures studied are shown in Fig. 4.2. The samples have a dielectric thickness $t_{\mathrm{D}} = 0.787$ mm and metal thickness $t_{\mathrm{M}} = 0.018$ mm. This metal thickness is much greater than the penetration depth in copper at microwave frequencies and the metal may be considered to be a perfect electrical conductor. The upper layer of the monograting sample has a period of $\lambda_{\mathrm{g}} = 3.78$ mm and slit width $w_{\mathrm{s}} = 0.125$ mm and the dielectric, FR4, has complex relative permittivity $\varepsilon = 4.4 + i0.088$. The bigrating sample has a short period in the x-direction of $\lambda_{\mathrm{gx}} = 3.2$ mm and a long period in the y-direction of $\lambda_{\mathrm{gy}} = 4.7$ mm, with a slit width in both dimensions of $w_{\mathrm{s}} = 0.17$ mm. The dielectric used is Rogers RT/Duroid 5880 with $\varepsilon = 2.2 + i0.002$. This material is chosen as it has a small imaginary part to its permittivity and absorbs little power. The experimental samples are produced by Graphic PCB using standard lithographic techniques, outlined in Section 3.2.1.

4.3 Results and Discussion

Reflected intensity (reflectivity) spectra have been obtained for normal incident radiation with polarisation angles of $\phi = 0°, 45°, 90°$. For each of these incident polarisations both the polarisation conserved and converted responses have been measured. In addition, co-polarised phase measurements are shown for $\phi = 0°, 90°$ as well as the ellipticity, γ, and handedness of the reflected radiation as a function of frequency. Experimental results are obtained using the collimating beam set up (see Section 3.4.2), with narrow band horn antennas connected to a Vector Network Analyser. Linear magnitude and phase of the transmission signal (S_{21} parameter) between the horns is recorded. The results are compared to finite element method (FEM) modelling carried out using a driven model in Ansoft HFSS (Section 3.7).

4.3.1 Monograting

Fig. 4.4a shows the normal-incidence reflectivity spectra for the monograting sample. The first subscript represents the polarisation angle ϕ of the incident electric field and the second defines the respective orientation of the detecting antenna. The polarisation converted reflectivity along the mirror planes of the sample ($R_{0,90}$ and $R_{90,0}$) have been omitted as there is no polarisation conversion unless the symmetry of the surface is broken. Experimental data is obtained for the X band (8-12 GHz) and shows good agreement with numerical modelling. A 5-point moving average is used and the data is normalized to the reflection from a flat metal plate.

$R_{90,90}$ shows that when the electric field is polarised parallel to the slits and along the y-direction, no radiation couples into the cavity. Instead, all radiation within the frequency range is reflected as if from a mirror and no features are present. This is supported by Fig. 4.4b which shows the phase of reflected radiation, normalised to that of a planar mirror. $\Psi_{90,90}$ shows no difference between the responses from the structure and the mirror and it reflects with a phase change $\delta\Psi_{\mathrm{y}} = \pi$ at all frequencies within the range.

The co-polarised reflectivity when the electric field is polarised perpendicular to the slits (x-direction), $R_{0,0}$, shows a minimum at 11.2 GHz as the electric field diffracts through the slits and excites a lateral Fabry-Perot-like resonance in the dielectric cavity beneath, where $\sim$35% of the incident power is absorbed. The corresponding phase measurement displays the characteristic change in phase through the resonance when normalised to the reflected phase of a planar mirror. At the resonant frequency of 11.2 GHz, the phase of reflection from the monograting $\Psi_{0,0}$ is π out of phase with that from the mirror, indicating that at this frequency, the total change in phase upon reflection is $\delta\Psi_{\mathrm{x}} = 0, 2\pi$. Away from the resonance, beyond the limits of the figure, the phase of

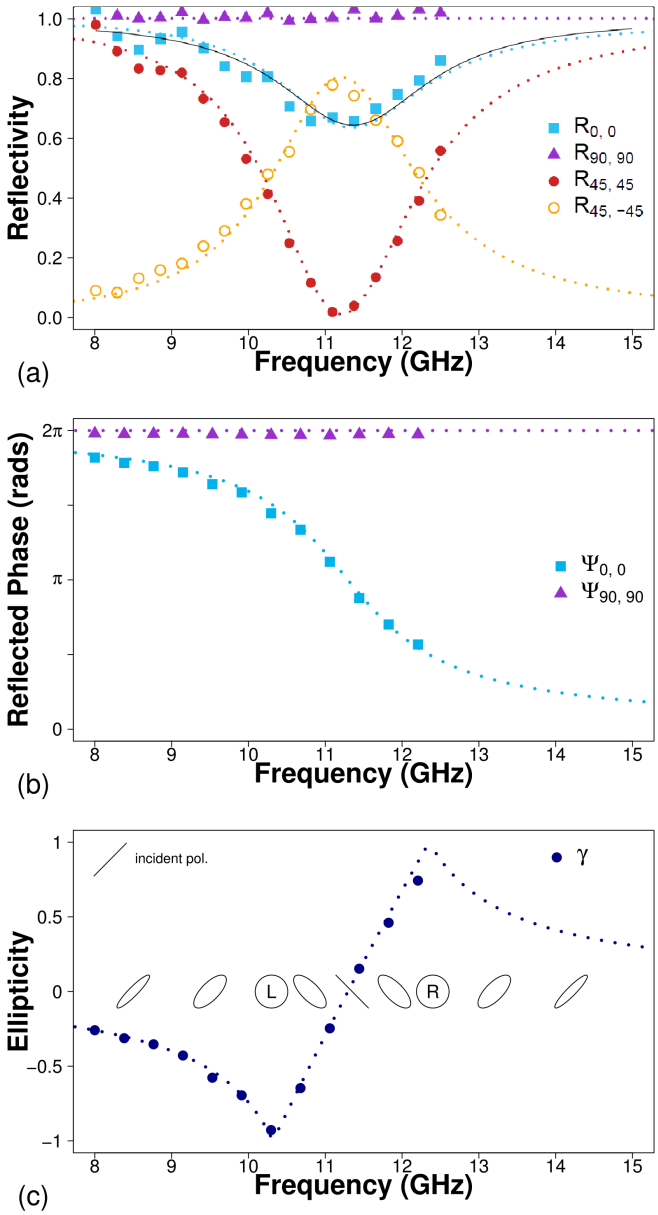

Figure 4.4: a) Normal incidence reflectivity as a function of frequency for the mono-grating sample. Co-polarised reflectivity for polarisation angles of 0° (blue squares), 90° (purple triangles) and 45° (red circles) and cross-polarised reflectivity at $\phi = 45°$ (hollow yellow circles). Black line indicates estimated reflectivity by fitting to resonant frequency and width. b) Relative phase of detected radiation as a function of frequency, normalised to the phase of reflection from a planar metallic mirror. c) Ellipticity of reflected radiation, where negative and positive values indicate left and right handed respectively. Results from numerical modelling are shown as dotted lines.

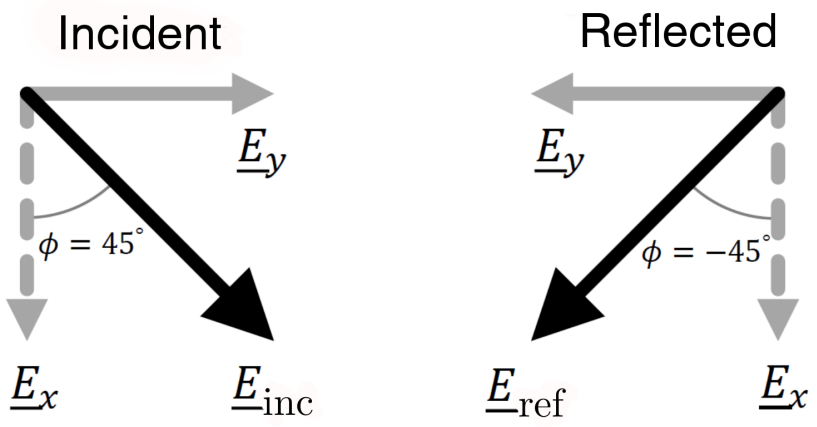

Figure 4.5: Schematic diagram showing the incident and reflected polarisation states at the resonant frequency of 11.2 GHz when the electric field is polarised at 45° to the grating slits.

reflected radiation returns to that of the mirror hence $\delta\Psi_x = \pm\pi$.

Absorption within the cavity can be maximised such that the array does not reflect at all on resonance[53][54]. Below the onset of diffraction (which occurs above the frequency range studied), power can only be absorbed in the array, or specularly reflected, i.e. $A + R = 1$, where A and R are the absorption coefficient and reflectivity. The amount of absorption by the array can be understood by considering the loss mechanisms from each cavity resonator; radiative loss (the cavity radiates on resonance and this radiation interferes with non-resonant reflection) and resistive loss (power lost to Joule heating of materials within the cavity). The rates of loss are denoted as δ_{rad} and δ_{res} respectively, and these are related to the impedance of the array, Z by

$$Z(f) = \frac{\delta_{rad}}{-i(f - f_0) + \delta_{res}} \tag{4.1}$$

where f is the frequency and f_0 the resonant frequency of the cavity. For total absorption on resonance, the array must be impedance-matched to free-space radiation; Z must equal 1, which is satisfied for $\delta_{rad} = \delta_{res}$, i.e. equal rates of radiative and resistive loss. The sum of δ_{rad} and δ_{res} dictates the spectral width of the resonance, and the reflectivity is given by

$$R(f) = \left|\frac{Z(f) - 1}{Z(f) + 1}\right|^2 \tag{4.2}$$

which is indeed equal to zero for $Z = 1$. By fitting this function to the experimental data it is possible to determine the ratio of δ_{res} to δ_{rad}. This function is shown in Fig.

4.4a as a solid black line. After fitting the resonant frequency and spectral width, it is found that the resistive loss is approximately 11% of the radiative loss. When radiative loss is greater than resistive loss the system is said to be overcoupled. Later, this overcoupling will be maximised for the bigrating structure.

When the incident radiation is polarised at $\phi = 45°$ to the slits, the electric field can be decomposed into equal components in the x and y-directions such that, assuming no losses,

$$\begin{aligned} \underline{E}_{\text{inc}} = &\frac{|\underline{E}|}{\sqrt{2}}\exp(i(kz - wt))\hat{x} \\ &+ \frac{|\underline{E}|}{\sqrt{2}}\exp(i(kz - wt))\hat{y} \end{aligned} \tag{4.3}$$

$$\begin{aligned} \underline{E}_{\text{ref}} = &\frac{|\underline{E}|}{\sqrt{2}}\exp(i(kz + wt + \delta\Psi_x))\hat{x} \\ &+ \frac{|\underline{E}|}{\sqrt{2}}\exp(i(kz + wt + \delta\Psi_y))\hat{y} \end{aligned} \tag{4.4}$$

where $\underline{E}_{\text{inc}}$ and $\underline{E}_{\text{ref}}$ are the incident and reflected electric field vectors, respectively. Hence, at 11.2 GHz, half of the incident power is reflected from the upper surface with a phase change $\delta\Psi_{\text{y}} = \pi$ and the other half diffracts into the resonant cavity mode which subsequently reradiates with a $\delta\Psi_x = 2\pi$ phase change. Due to the phase difference $\delta\Psi_{\text{x}} - \delta\Psi_{\text{y}} = \pi$ between these processes, the combined reflected field is polarised perpendicular to the incident field as portrayed in Fig. 4.5. The result of this is that a peak is observed in the cross-polarised reflectivity signal $R_{45,\text{-}45}$. This power is no longer detected in the co-polarised state and hence a minimum is observed in $R_{45,45}$. Due to loss in the dielectric, the peak in polarisation conversion cannot reach 100%. Selecting a dielectric material with a smaller imaginary part of its permittivity would minimise loss and maximise the polarisation conversion, hence the switch from FR4 to Rogers RT/Duroid 5880 for the bigrating sample discussed in the next section. The phase difference $\delta\Psi_{\text{x}} - \delta\Psi_{\text{y}}$ is frequency dependent and away from the resonance the reflected polarisation state is elliptically polarised. Fig. 4.4c shows the ellipticity, γ, of the reflected wave as a function of frequency, where the ellipticity is defined as the ratio of the semi-minor to semi-major axis of the polarisation ellipse. Positive and negative values indicate right and left handed polarisation respectively. Hence, at 10.3 GHz and 12.4 GHz, where $\delta\Psi_{\text{x}} - \delta\Psi_{\text{y}} = 3\pi/2, \pi/2$, the reflected radiation is circularly polarised, with left and right handedness respectively. This polarisation state assumes a linearly polarised incident beam with $\phi = 45°$. An incident polarisation of $\phi = -45°$

would cause the reflection to have the opposite handedness.

The response of the structure to circularly polarised incident light can be determined by decomposing the electric field into the x and y-directions. We can therefore infer the circular polarisation conversion (not shown) from the reflected amplitude and phase of linear polarisation. At the resonant frequency of the structure, circularly polarised light is reflected with the opposite handedness, where the handedness is defined in relation to the direction of propagation. Furthermore, at 10.3 GHz and 12.4 GHz, where $\delta\Psi_x - \delta\Psi_y = 3\pi/2, \pi/2$, the structure now acts as a circular to linear converter.

4.3.2 Bigrating

Now we consider the bigrating cavity array in order to broaden the frequency range over which polarisation conversion can be achieved. Fig. 4.6a shows the reflectivity as a function of frequency for the bigrating structure. The upper metal surface now contains periodic slits in both the x and y-directions and hence cavity resonances can be excited in both directions. It has been shown that when the pitches of these perpendicular slits are equal, $\lambda_{gx} = \lambda_{gy}$, a polarisation independent cavity resonance exists and there is no polarisation conversion due to the four-fold rotational symmetry of the structure[55]. If the pitches are not equal, the two orthogonal resonances separate in frequency and polarisation conversion is possible provided the electric field is not polarised along a mirror plane of the surface. The bigrating sample is designed to minimise absorption in the dielectric cavity such that the resonant dips in reflectivity cannot be clearly resolved. Hence, the reflectivity data $R_{0,0}$ and $R_{90,90}$ are omitted although the phase data in Fig. 4.6b shows two resonant features centred at 13.5 GHz and 17.4 GHz.

When the incident electric field is polarised at 45° to both sets of slits, two peaks in polarisation conversion arise, labelled with arrows in Fig. 4.6a. For this particular geometry, the two resonance frequencies are sufficiently separated such that the minimum between the two peaks is minimised in $R_{45,-45}$. There exists a 2.5 GHz frequency band where 98% of incident radiation is reflected with the orthogonal polarisation and the remaining 2% is absorbed. This bandwidth increases to 3.1 GHz over which 95% of the radiation is indicated by the grey region in Fig. 4.6. The phase and ellipticity data presented in Fig. 4.6b-c shows that the phase difference between the x and y components of the reflected electric field, $\Psi_{0,0} - \Psi_{90,90}$, is approximately equal to π over the same frequency range, causing linear polarisation conversion. As before, circularly polarised radiation would be reflected from this structure with the opposite handedness, where the handedness is defined in relation to the direction of propagation.

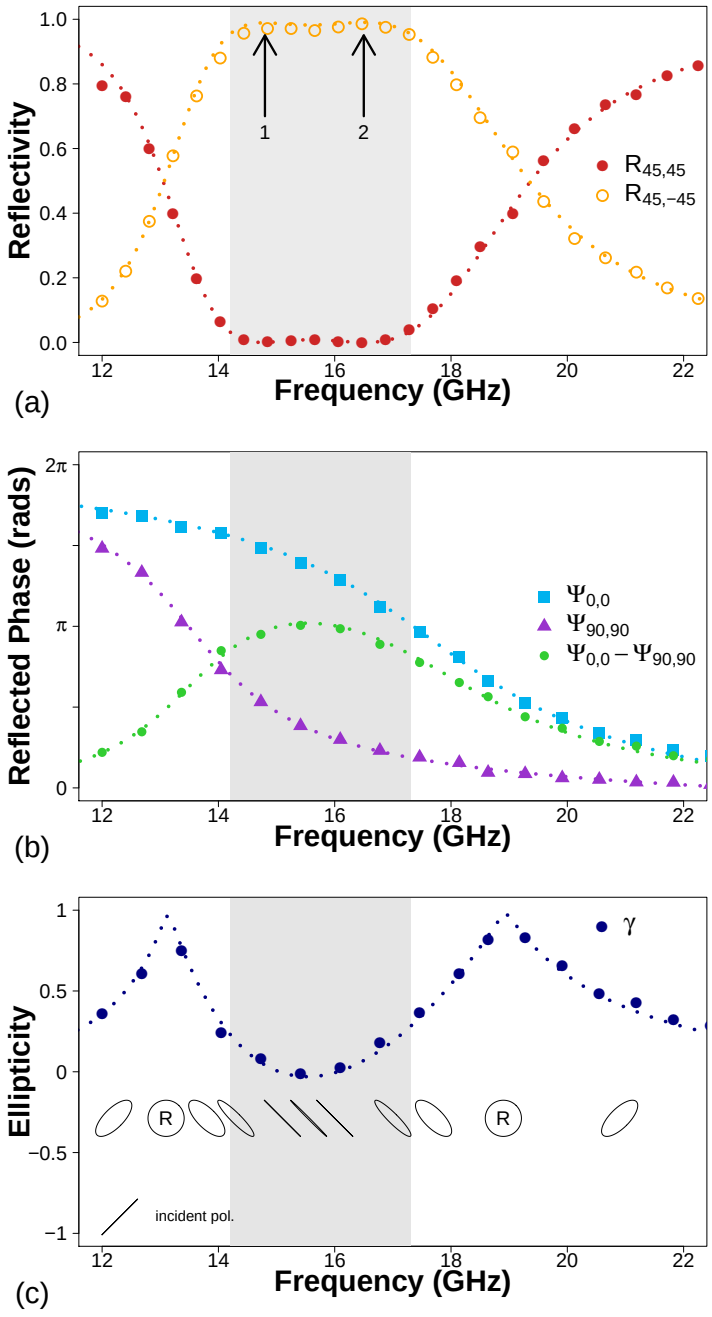

Figure 4.6: a) Co-polarised (filled red circles) and cross-polarised (hollow yellow circles) reflectivity for normal incidence radiation at $\phi = 45°$. b) Relative phase of co-polarised detected radiation as a function of frequency, normalised to the phase of reflection from a planar metallic mirror, for 0° (blue squares), 90° (purple triangles) and their difference (green circles) c) Ellipticity of reflected radiation, where negative and positive values indicate left and right handed respectively. Results from numerical modelling are shown as dotted lines.

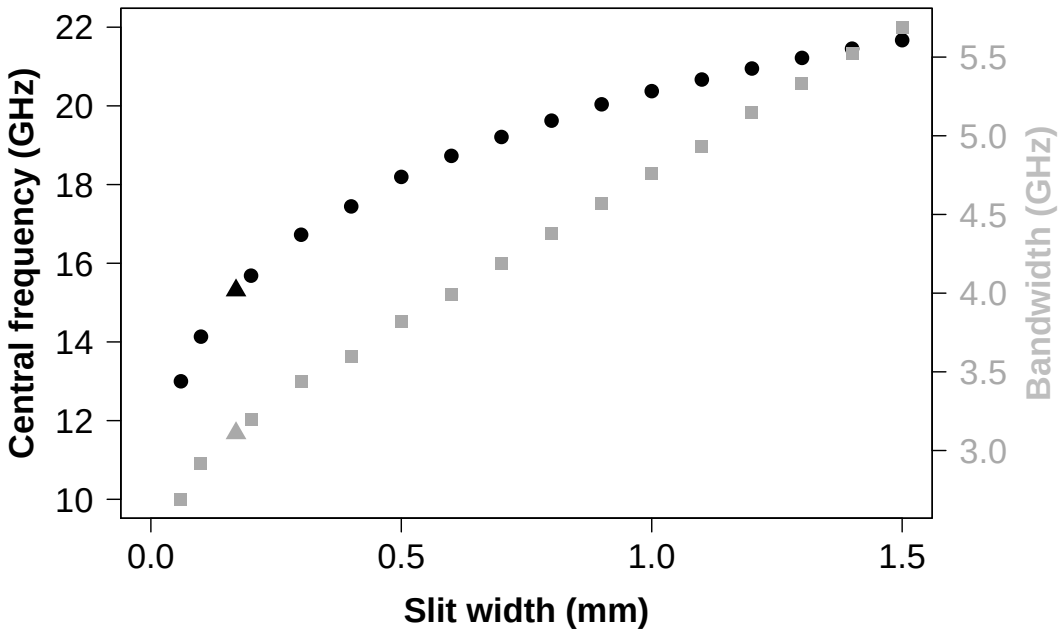

Figure 4.7: The bandwidth (grey squares) and central frequency (black circles) of the 95% polarisation converting band for various slit widths w_s. The values corresponding to the bigrating sample are shown as triangles.

4.3.3 Slit Width

Fig. 4.7 shows how the bandwidth and central frequency of the polarisation converting band for the bigrating structure varies with slit width w_s according to numerical modelling. Data points corresponding to the sample studied thus far are shown as triangles. The resonant frequency of each cavity depends not just on cavity volume but also on the separation between cavities. This is because a narrower slit results in a steeper field gradient beneath the slit as the incident field diffracts. The field undergoes a π phase change over a distance of the order of the slit width which leads to an effective lengthening of the cavity[52]. The central frequency data (black circles) shown in Fig. 4.7 show how the polarisation conversion band decreases in frequency as the slit is narrowed. This trend is very similar to that reported in Ref. [52] for the transmission resonance of a structured slit. The 95% conversion bandwidth (grey squares) also decreases with decreasing slit width. A range of slit widths between 0.06 and 1.5 mm were chosen as outside of this range the conversion is reduced below 95% at the central frequency. This data shows how the central frequency and the bandwidth of operation can be tailored by making a small variation to the design of the bigrating.

4.3.4 Incident Angle

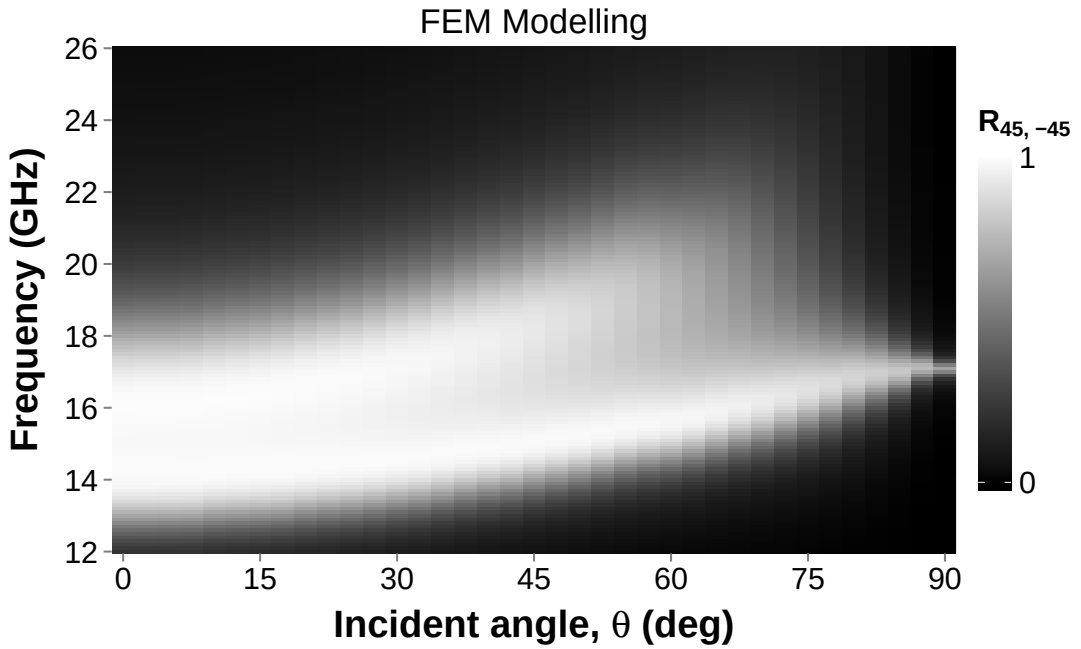

Figure 4.8: Simulation: Cross-polarised reflectivity of the bigrating sample with incident polarisation angle $\phi = 45°$, as a function of both frequency and incident angle θ.

In Fig. 4.8 the numerically modelled cross-polarised reflectivity is presented as a function of frequency and incident angle θ. The 95% conversion band remains up to an angle of 30°, where the bandwidth has increased to 3.55 GHz whilst the central frequency has shifted up to 15.9 GHz from 15.3 GHz. Beyond 30° incidence, the amplitudes of both conversion peaks reduces and they move further up in frequency. Fig. 4.9 shows the result from experiment (using the reflection setup outlined in Section 3.4.2), where the incident angle is limited to $10° \leq \theta \leq 60°$. There is a good qualitative agreement between the two, and the minimum at the centre of the polarisation conversion band is evident for angles greater than 30°. Small amplitude oscillations are present in the experimental data due to interference caused by mulitple reflections between the sample and the two mirrors.

4.3.5 Polarisation Angle

The polarisation conversion is maximum for a polarisation angle of $\phi = 45°$, when the cavity modes in both the x and y-directions are coupled to equally via the slits in the upper metallic surface. Fig. 4.10 shows the dependence of the polarisation

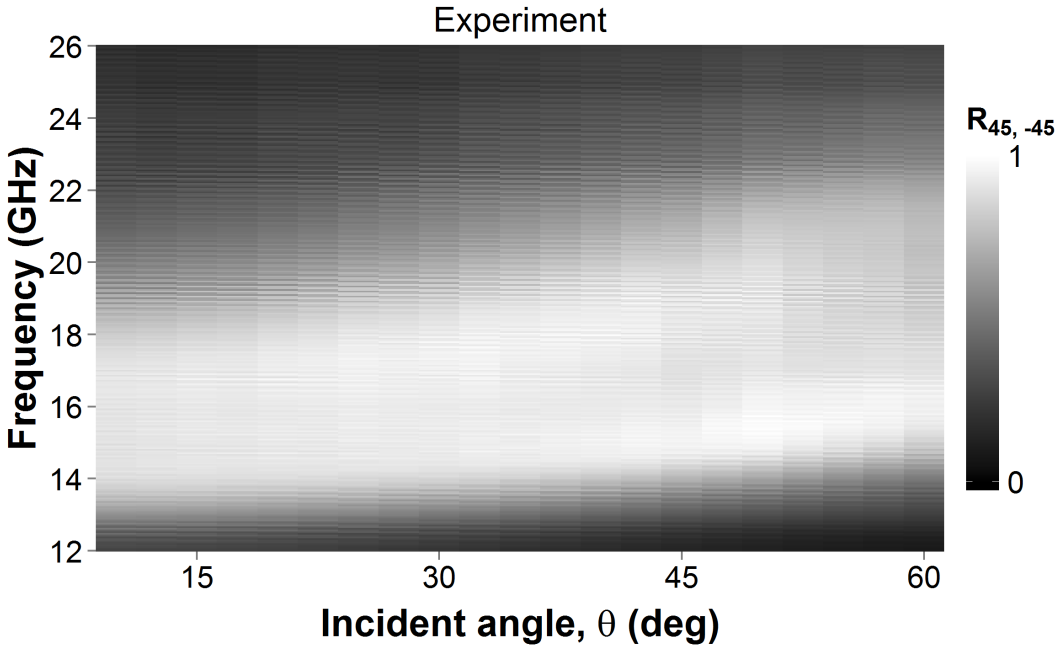

Figure 4.9: Experiment: Cross-polarised reflectivity of the bigrating sample with incident polarisation angle $\phi = 45°$, as a function of both frequency and incident angle θ.

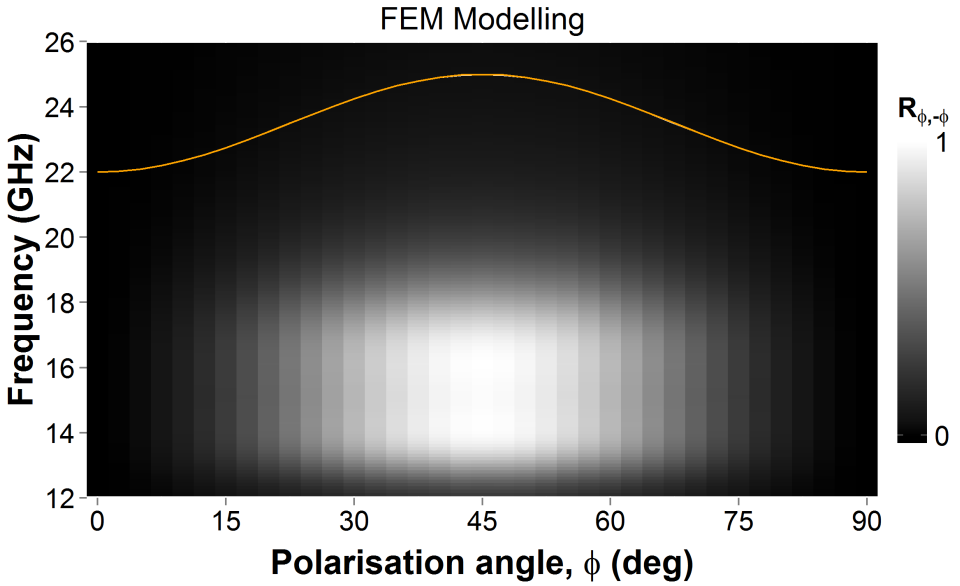

Figure 4.10: Cross-polarised reflectivity of the bigrating sample at normal incidence, as a function of both frequency and polarisation angle ϕ. The data is obtained via numerical modelling. The sinusoidal variation with changing ϕ is demonstrated inset.

converted reflectivity at normal incidence ($\theta = 0$) on the polarisation angle, ϕ. For angles less (greater) than 45°, there is a larger electric field component in the x (y)-direction corresponding to the higher (lower) frequency resonance. Despite this there is no asymmetry in the polarisation conversion with changing polarisation angle either side of $\phi = 45°$. The magnitude of the conversion $R_{\phi,-\phi}$ varies sinusoidally with changing polarisation angle according to

$$R_{\phi,-\phi} = \frac{R(\phi = 45°)}{2}(1 + \cos(4\phi + \pi)). \tag{4.5}$$

This means that at least 90% conversion is maintained for polarisation angles between 47° and 53°. This variation is shown inset (orange line), where the maximum corresponds to 98% conversion and the minimum is zero.

4.3.6 Linear to Circular Conversion

Just as this bigrating structure acts as a reflecting half-wave plate, it is also possible to achieve a reflecting quarter-wave plate (to convert between linear and circular polarisation) by separating the two resonant frequencies further. Numerical modelling for the bigrating array with a short period of $\lambda_{gx} = 5.4$ mm and a long period of $\lambda_{gy} = 2.05$ mm is shown in Fig. 4.11. Between 14.5 and 17 GHz, both the co-polarised, $R_{45,45}$, and the cross-polarised, $R_{45,-45}$, reflectivity is ∼0.5, hence the reflected signal must be circularly polarised. This is verified by the phase and ellipticity data in Fig. 4.11b-c. $\Psi_{0,0} - \Psi_{90,90}$ shows that the difference in phase between the reflected x and y components of the electric field is equal to $3\pi/2$. In Fig. 4.11c the ellipticity curve shows that whilst the magnitude of the ellipticity is not unity across this 2.5 GHz band, the polarisation state remains approximately circular, never falling below $|\gamma| = 0.8$.

4.4 Conclusion

In this chapter, a metamaterial consisting of a slotted metal grating separated from a ground plane by a low-loss dielectric has been experimentally optimised for polarisation conversion in reflection. The result is a 95% polarisation converting mirror for normally incident microwave radiation with its electric field polarised at 45° to the two orthogonal gratings. Using a rectangular bigrating as the upper surface of the array allows an increase of the operating bandwidth to 3.1 GHz centred at 15.3 GHz. This structure benefits from an uncomplicated geometry which could be scaled to higher frequency regimes. It is very thin ($\lambda/25$) and the unit cell size is also subwavelength ($\lambda/4$). Most importantly, the absorption is very small (2%) meaning less incident power is lost upon reflection than previous designs[43][44][45][46][47][49][50]. Numerical modelling

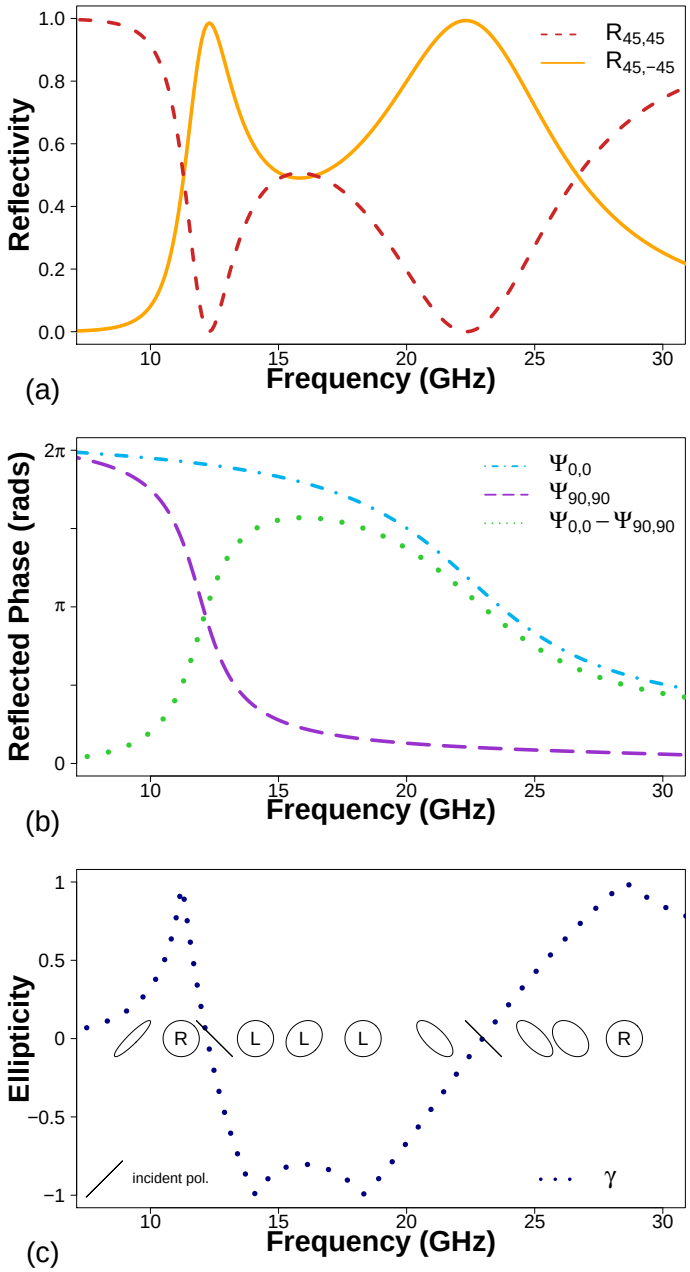

Figure 4.11: Normal incidence numerical modelling results for the linear to circular polarisation converting bigrating structure. a) Co-polarised (solid line) and cross-polarised (long dashed line) reflectivity for $\phi = 45°$. b) Relative phase of reflected radiation as a function of frequency, normalised to the phase of reflection from a planar metallic mirror, along the x-direction (dot-dash), y-direction (dashed) and their difference (dotted). c) Ellipticity of reflected radiation, where negative and positive values indicate left and right handed respectively.

has shown that the polarisation conversion performance is maintained for incident angles up to 30° and polarisation angles between 47° and 53°. The central frequency and bandwidth of operation can be varied by changing the slit width. Further modelling shows that by changing the dimensions of the cavity array it can also function as a linear to circular polarisation converter across the same frequency range.

Chapter 5

Twisted-Cross Chiral Metamaterial

In this chapter, the topic of polarisation manipulation will be extended to chiral metamaterials (CMMs). These metamaterials exhibit optical activity; a rotation of the plane of polarisation as linearly polarised radiation transmits through the structure. Circular birefringence and dichroism are two manifestations of optical activity, defined respectively as the differential refractive index and absorption for left and right circularly polarised radiation. Both of these effects will be studied in the context of a bilayer CMM consisting of square arrays of twisted cross-shaped elements.

5.1 Background

A chiral object is described as one that can not be superimposed onto its mirror image by rotation or translation. A good example is the human hand; the left and right hand are distinguishable by their chirality. In electromagnetism, chiral objects may respond differently to left and right circularly polarised incidence radiation, and linear polarisation can be rotated by them. Such chiral objects are often described as being 'optically active'.

Circular birefringence (refractive index) and dichroism (absorption) are manifestations of optical activity exhibited by natural chiral media such as a sugar solution. They are commonly determined by measuring the optical rotation, ϕ, and ellipticity, η, of radiation that passes through the media respectively. However, the degree of polarisation rotation attainable through these naturally occurring structures is typically small and hence research in artificial chiral metamaterials[56][57][58], arrays of subwavelength chiral 'meta-molecules' that offer a much stronger response, has received substantial interest. Collections of 3D (e.g. helical) elements have yielded circular polarisers and

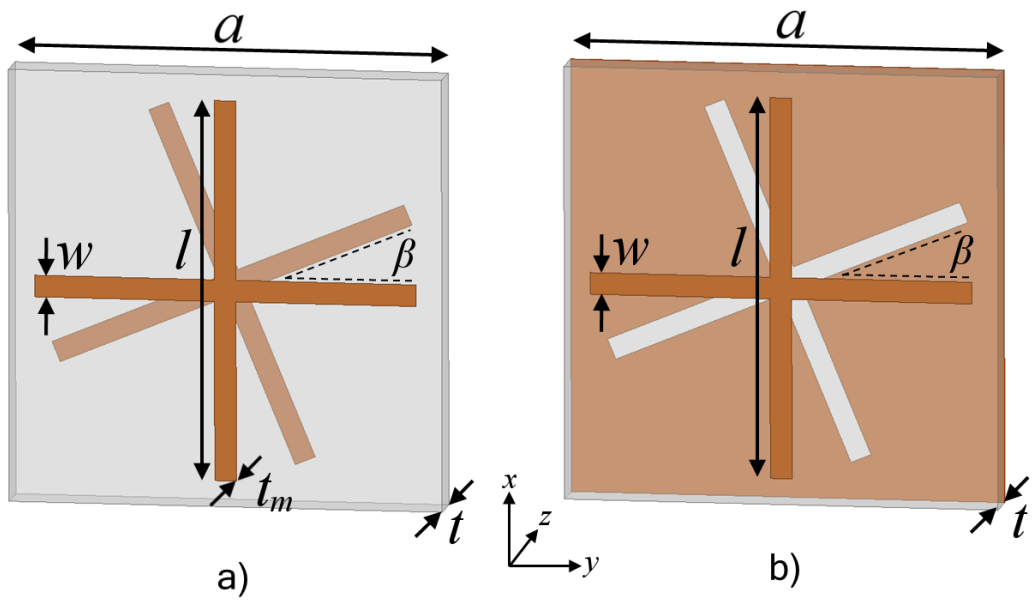

Figure 5.1: Unit cells of the two chiral metamaterials studied. a) the 'D-cross' geometry consisting of two layers of metallic crosses, separated by a dielectric layer and with one cross rotated with respect to the other. b) the 'C-cross' structure; the second layer is replaced with cross shaped holes in a continuous metal film.

linear polarisation rotators in transmission[59][60][61]. Planar 2D CMMs[62], mounted onto a substrate, have been shown to rotate linear polarisation[63][64][65][66] despite being extremely subwavelength in thicknesses. This rotation effect has been enhanced by using bilayers of chiral metamolecules[67][68][69][70][71][72], layers of nonchiral metamolecules rotated with respect to each other[73][74][75][76][77][78], or via oblique incidence illumination of a nonchiral anisotropic planar metamaterial[79]. The response of a chiral metasurface has recently been described by effective parameters, extracted from S-parameters[80]. In the dipole approximation, optical rotation ϕ in chiral media arises when electric μ_{e} and magnetic μ_{m} dipole moments of a resonator are parallel and out of phase, according to

$$\phi \propto \mathrm{Im}(\vec{\mu_{\mathrm{e}}} \cdot \vec{\mu_{\mathrm{m}}}) \tag{5.1}$$

In this study, the twisted-cross CMM (illustrated in Fig. 5.1) is investigated. Individually, the two layers of the structure are non-chiral, however when the elements ('meta-atoms') of one layer are rotated with respect to the other, the composite 'metamolecule' is chiral. The rotation allows magnetic and electric dipoles induced by incident radiation to be partially aligned.

Fig. 5.1 depicts the two twisted-cross CMMs studied in this chapter. Both comprise

two patterned metallic sheets (18 μm thick) separated by a dielectric layer of thickness t. The first, (Fig. 5.1a) consists of an upper layer of cross shaped metallic elements in a square array of period a, aligned with the lattice vectors (x and y axes). The crosses are defined by their arm length l and width w. The lower array is identical except that each cross is rotated about its centre by an angle β. In the second structure (Fig. 5.1b), the lower layer has been replaced with its complement, i.e. a cross-shaped hole twisted by β. The two structures are referred to as double cross 'D-cross' and complementary cross, 'C-cross', respectively.

The chiral response of these structures has previously been investigated by other authors. The 'D-cross' geometry was shown to exhibit a band of dispersionless (i.e. non-varying with frequency) optical rotation between two resonant features in transmission[73]. This result is reproduced in the following section. The magnitude of optical rotation in the sample studied was 4°, corresponding to a differential refractive index for circularly polarized rotation of $n_{\mathrm{RCP}} - n_{\mathrm{LCP}} \approx 0.35$. Importantly, this rotation is 'pure', meaning that the ellipticity of transmitted radiation is close to zero, maintaining the linearity of polarization. A shortcoming of the D-cross geometry in rotating linear polarization as it transmits through the structure, is that the transmitted intensity in the centre of the frequency band of interest is only $\approx 50\%$, with the remainder either absorbed or reflected. The C-cross structure was introduced by Hannam et al. in order to enhance this transmission[77]. The complementary pair of metallic sheets satisfies an impedance matching condition at the centre of the band, whilst maintaining the pure, dispersionless, optical rotation. The result is a peak in transmission of $\approx 80\%$.

Despite the success of recent work on twisted-cross CMMs highlighted above, some insight into the resonances leading to the band of dispersionless optical rotation is missing in the literature. In this chapter, the optical rotation band is shown to arise due to two resonances in the transmission spectrum, each providing an opposing twist to the polarization. The nature of these two resonances is different for the D-cross and C-cross structures, allowing predictions about their response to changes in geometry to be made and tested. Finally, a multilayer stack of the C-cross is shown to enhance the transmission bandwidth, whilst sacrificing transmitted intensity.

The response of each structure is modelled numerically using a driven modal simulation in Ansoft HFSS (Sec. 3.7). Four complex (magnitude and phase) transmission S-parameters, S_{12}, are calculated, where ports 1 and 2 correspond to the two Floquet ports encasing the unit cell above and below the structure. Subscripts are assigned depending on the polarisation orientation at each port. The four transmission parameters are therefore, t_{xx}, t_{yy}, t_{yx}, t_{xy}, where the first pair correspond to the polarisation *conserved* transmission and the second pair are polarisation *converted* transmission. The circular transmission parameters, τ_R and τ_L are obtained from these via the following

equation

$$\tau_{\mathrm{R/L}} = \frac{t_{\mathrm{xx}} + t_{\mathrm{yy}} \pm i(t_{\mathrm{xy}} - t_{\mathrm{yx}})}{2} \tag{5.2}$$

where the left and right handed response corresponds to the + and - sign respectively. The relative phase of these circular transmission parameters yields the optical activity, ϕ, whereas their difference in magnitude dictates the ellipticity, η, according to

$$\phi = \frac{\arg(\tau_{\mathrm{R}}) - \arg(\tau_{\mathrm{L}})}{2} \tag{5.3}$$

$$\eta = \mathrm{atan}\frac{|\tau_{\mathrm{R}}|^2 - |\tau_{\mathrm{L}}|^2}{|\tau_{\mathrm{R}}|^2 + |\tau_{\mathrm{L}}|^2} \tag{5.4}$$

Each of these parameters will be discussed and compared for the two structures shown in Fig. 5.1.

5.2 Results and Discussion

The transmission through both structures is determined using a driven modal simulation in Ansoft HFSS, across a range of frequencies (5-40 GHz). The geometrical parameters are $a = 7.5$ mm, $l = 6.6$ mm, $w = 0.375$ mm, $t = 0.2$ mm and $\beta = 22.5°$. These parameters are chosen so that the operating frequency band lies within the limits of the Vector Network Analyser (Sec. 3.3.1). The rotation β is in an anticlockwise direction, viewed from the incident side. The dielectric layer has a complex relative permittivity of $\epsilon = 3.02(1 + 0.002i)$ in order to match the experimental printed circuit board sample discussed in the next section. Metallic layers are approximated as idealised perfect electric conductor (PEC) sheets of zero thickness.

5.2.1 D-cross Structure

Fig. 5.2a-b show the linear and circular transmission coefficients for the D-cross structure (shown inset) on a logarithmic scale in order to identify the position of transmission minima. Due to the lack of mirror symmetry, the linear polarisation transmission (Fig. 5.2a) varies significantly with polarisation angle, here set along the y-axis. Two resonances are seen in the co-polarised transmission coefficients ($t_{\mathrm{xx}}, t_{\mathrm{yy}}$); a transmission minimum at 17.5 GHz and a much sharper 'Fano' resonance (a sharp change in transmission between a peak and a minimum, typically resulting from the interference between resonant and non-resonant transmission) at 20.0 GHz. These are highlighted by grey dashed lines in the figure. The latter also corresponds to a maximum in the

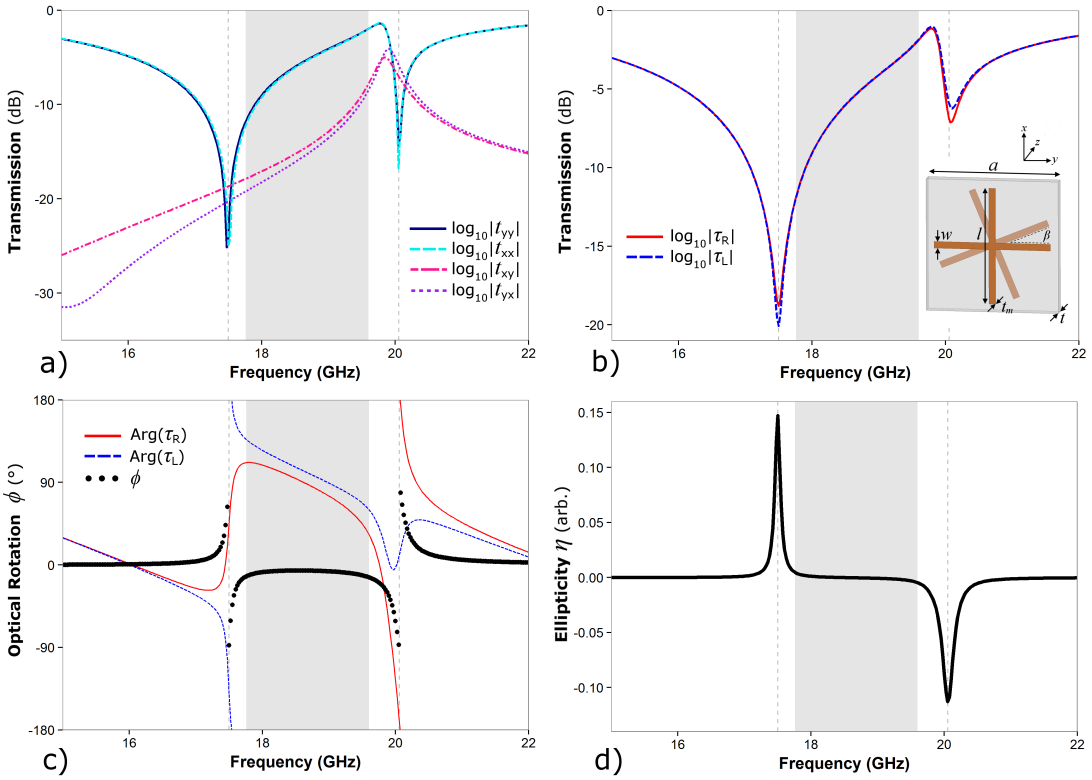

Figure 5.2: The linear (a) and circular (b) polarised transmission coefficients for the D-cross structure overs a frequency band from 14 to 22 GHz. The transmission is represented on a logarithmic (dB) scale. c) The optical rotation, ϕ (black points), calculated from the phase of RCP (red line) and LCP (blue line) transmitted radiation, according to equation 5.3. d) The ellipticity, η of transmitted radiation calculated from the magnitude of circularly polarised transmitted radiation in (b), according to equation 5.4. Two resonant frequencies are highlighted by grey dashed lines. The frequency band of interest, where non-zero optical rotation is accompanied by negligible ellipticity, is shaded grey.

cross-polarised signals ($t_{\mathrm{xy}}, t_{\mathrm{yx}}$). The four linear transmission parameters are converted into the circular polarisation transmission parameters ($\tau_{\mathrm{R}}, \tau_{\mathrm{L}}$) and the logarithmic magnitudes of these are shown in Fig. 5.2b. The chirality of the structure is manifested in to the differential transmission magnitude for the two circular polarisations. The phase of RCP/LCP transmission is presented in Fig. 5.2c as red and blue lines respectively. On resonance, the phase for each polarisation undergoes a discontinuous change, leading to a phase difference between the right and left handed components. This differential phase (circular birefringence) means the structure is optically active and will rotate the plane of linear polarised transmitted radiation by an angle given by the optical rotation formula (equation 5.3). This optical rotation is plotted as points in Fig. 5.2c, and is limited to angles between $-\pi/2$ and $\pi/2$. This shows that on resonance the plane of

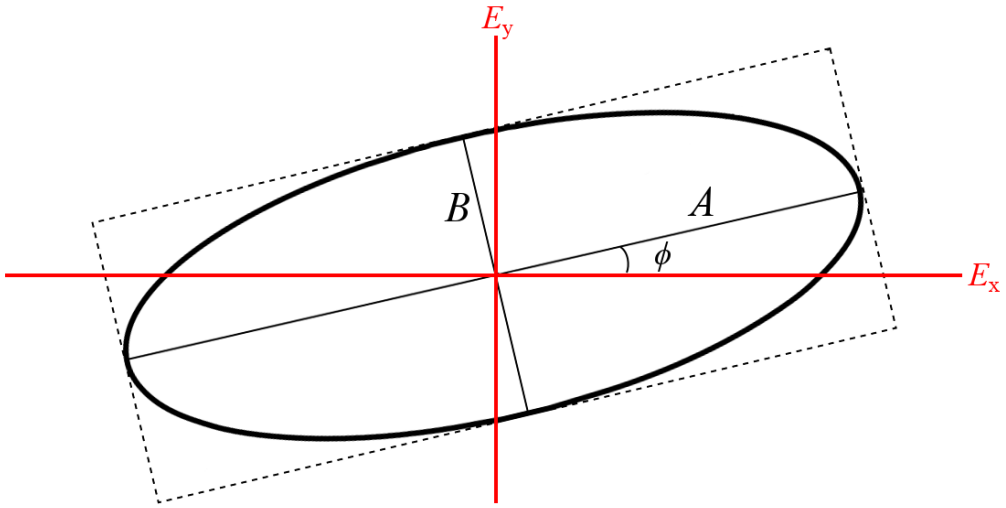

Figure 5.3: A polarisation ellipse. The electric field vector of elliptically polarised radiation traces the ellipse as the phase of the field advances. The ellipse is defined by its major (A) and minor (B) axes and orientation ϕ with respect to the x-axis.

polarisation undergoes a full rotation; in a clockwise(anticlockwise) direction for the lower(upper) frequency resonance. In between these resonances, the competing rotary effects result in a small residual rotation. This effect has been discussed in previous works where the approximately constant optical rotation across a certain frequency band is described as 'dispersionless'. In order to fully understand the polarisation state of transmitted radiation, the ellipticity is also required. In this situation, this is a measure of the differential absorption (circular dichroism) of RCP and LCP radiation. Optical rotation does not imply that the polarisation has remained linear, only that the axis of the polarisation ellipse has rotated. The polarisation ellipse is an ellipse traced by the electric field vector as a wave propagates through space. An example polarisation ellipse is portrayed in Fig. 5.3 where the major axis is rotated by ϕ with respect to the incident polarisation (assumed to be along the x-axis). The magnitude of ellipticity η is proportional to the ratio of the minor and major axis, B and A. Note that if $\eta = 1$, the polarisation is circular and the rotation angle ϕ is not defined. Further, ellipticity and optical rotation are not independent quantities; they are linked by Kramers-Kronig relations[81]. Equation 5.4 defines the ellipticity, η, instead in terms of the transmitted RCP and LCP signals and also defines the handedness of the transmitted field (negative:LH, positive:RH). The ellipticity, plotted as function of frequency in Fig. 5.2d, is greatest at the resonant frequencies due to the fact that absorption occurs on resonance. The large optical rotation at these resonances is therefore accompanied by significant ellipticity. However, the residual optical rotation between the resonances

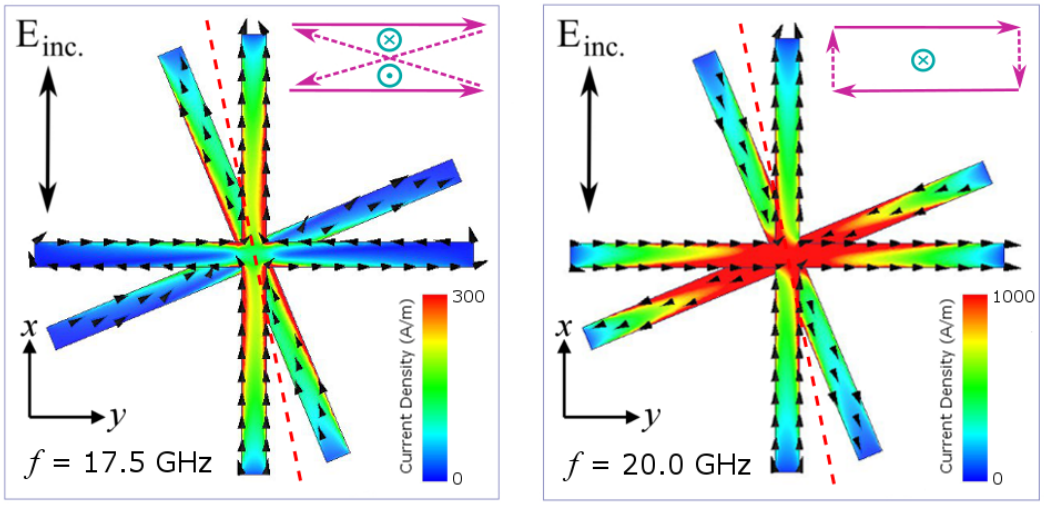

Figure 5.4: Direction of current flow (arrows) and surface current density (colour) in the upper and lower elements of one unit cell of the D-cross structure at (a) $f = 17.5$ GHz and (b) $f = 20.0$ GHz, corresponding to resonant dips in transmission. Inset: electric dipole orientation (purple arrows) and magnetic dipoles (blue arrows) in a cross-section through the dielectric in the mid-rotation plane, marked by the dashed red line. Displacement currents (dashed purple lines) link electric dipoles.

corresponds to a region of negligible ellipticity (here defined as less than 0.005). In this band, shaded grey in Fig. 5.2, the structure is acting as a linear polarisation rotator, with an average optical rotation across the band of 8°.

The region of dispersionless, pure, optical activity is caused by the differential phase shift for LCP and RCP incident radiation at the two resonances. Fig. 5.4 depicts the current flow on each of the layers for these resonances, both of which correspond to minima in transmission for both polarisations. At the lower resonant frequency of 17.5 GHz, Fig. 5.4a shows that incident field excites dipolar modes of cross arms aligned with the incident electric field. This occurs in both of the closely spaced ($\ll \lambda$) layers of the structure, such that the current in the vertical arms are in-phase with each other. This mode is referred to as the 'symmetric dipole' due to the mirror symmetry of the currents with respect to the mid-rotation plane (red dashed line).

At the upper resonant frequency, the dipolar modes of the arms are again excited by the incident field. However, the vertical arms of the two layers are out of phase (Fig. 5.4b). This mode is hence referred to as the 'antisymmetric dipole' mode. The incident field excites the antisymmetric mode in both the vertical and horizontal pair of arms. A projection of the currents onto the mid-rotation plane (red dashed line) is shown inset.

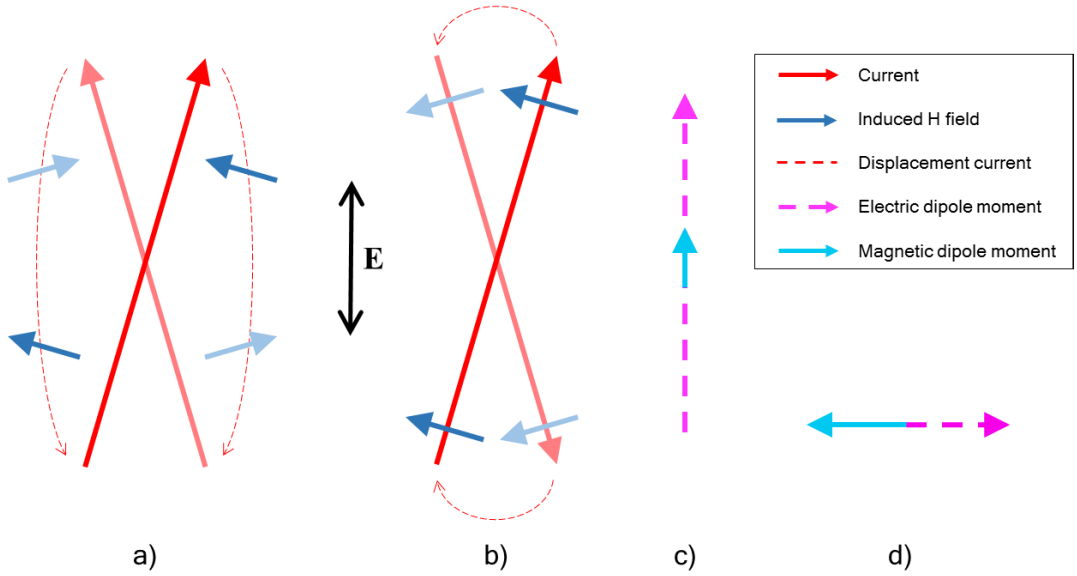

Figure 5.5: Schematic of the currents (red arrows) in a two-rod (i.e. stacked cut-wire pair) structure with rotation ϕ between them. a) symmetric currents b) antisymmetric currents. The upper and lower rod are indicated by darker and lighter colour rendering. Displacement currents (dashed red lines) link the rods and result in magnetic fields (blue arrows) due to current loops. The net electric (magenta arrows) and magnetic (cyan arrows) dipole moments for the symmetric (c) and antisymmetric (d) modes are shown to be aligned.

For the antisymmetric dipole mode, displacement currents (dashed magenta arrows) between the upper and lower arms complete a single current loop that generates a large magnetic field (blue arrow) normal to the plane. In the symmetric mode, (inset in (a)), displacement currents are weak and form a figure-of-8 loop, which can be thought of as two counter-rotating current loops. The normal component to the magnetic field in this case is small and in opposite directions in the upper and lower loops, with the net component summing to zero. However the twist in the structure creates a small, net in-plane component discussed below.

Optical activity requires *parallel* electric and magnetic dipole moments. In order to determine the origin of these, it is convenient to consider instead a simpler twisted rod structure, i.e. a stacked cut wire pair. In other words, the horizontal cross arms are neglected. Exciting these rods with an electric field polarised along the mid-rotation plane ensures the field component in the direction of both rods is equal, assisting the following qualitative analysis. The currents excited by the incident field are shown schematically in Fig. 5.5a-b (red arrows) for the symmetric and antisymmetric modes respectively. In this figure, darker (lighter) rendering indicates the upper (lower) layer. Currents within arms separate charges, resulting in the formation of electric dipoles,

whereas current loops (completed by displacement currents, dashed red lines) generate magnetic dipoles in a direction perpendicular to the plane of the loop, as seen inset in Fig. 5.4. Fig. 5.5a-b also illustrates the induced in-plane magnetic dipoles (blue arrows). The sum of electric (magenta) and magnetic (cyan) dipoles within the unit cell are shown in Figs. 5.5c-d for the symmetric and antisymmetric mode respectively. In both, μ_e and μ_m are aligned, with μ_e dominant for the symmetric mode and μ_m for the antisymmetric mode. The electric dipoles are advanced in phase by $\pi/2$. For the symmetric mode (c), μ_m leads μ_e by $\pi/2$ radians, whereas the reverse is true for the antisymmetric mode (d). This explains why the direction of optical rotation is switched for the two resonances (b in Fig. 5.2). The inclusion of a second set of orthogonal rods (resulting in the cross geometry) results in a polarisation independent response of the structure (assuming linear polarisation).

In this section, the origin of optical rotation in the double cross (D-cross) twisted cross metamaterial has been demonstrated. Two resonant excitations of the cross elements, one with currents in-phase (symmetric) and one out-of-phase (antisymmetric), lead to alignment of magnetic and electric dipole moments; the condition required for optical rotation. As the two resonances result in opposite rotations, a residual rotation exists for a frequency band between the two resonant frequencies. As there is negligible loss away from these resonant frequencies, the optical rotation band is also accompanied by negligible ellipticity. The following section extends the discussion to the complementary pair (C-cross) structure.

5.2.2 C-cross Structure

In this section, a similar analysis of the complementary pair (C-cross) array is undertaken. The structure is different to the D-cross only in that the lower layer has been inverted such that there is a continuous PEC sheet with a cross-shaped void. This structure is known to exhibit similar, more broadband, dispersionless optical activity[82]. In the following analysis it will be shown that the pair of resonances involved are of a fundamentally different nature.

Fig. 5.6a-b shows the linear and circular transmission magnitudes on a logarithmic scale. The minima in circular transmission are now accompanied by two maxima. This is due to the coupling between the disconnected layer (crosses) and the connected layer (cross holes). The maxima correspond to resonant excitations of the cross-shaped holes with the antennas above enhancing the transmission, in a similar way that metasurfaces have shown to enhance transmission through thin resistive metal films[83]. The minima correspond to a phase condition where radiation from the two layers interferes constructively in the reflected direction (-z) and destructively in transmission (+z).

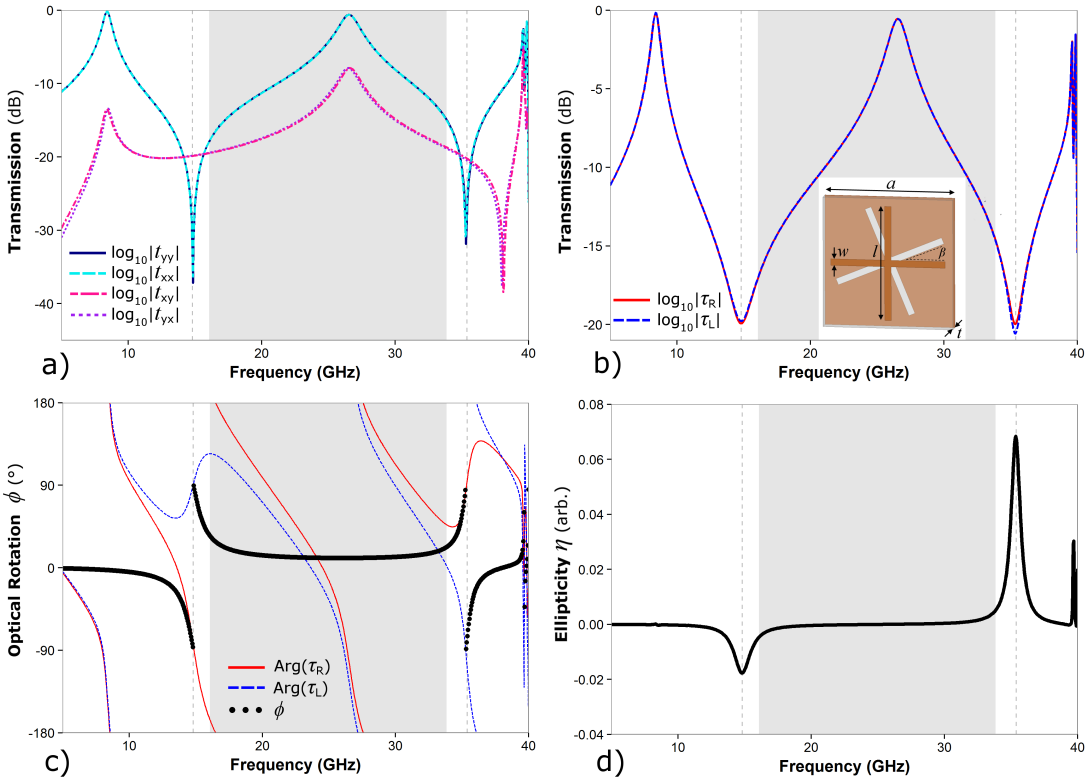

Figure 5.6: The linear (a) and circular (b) polarised transmission coefficients for the C-cross structure across a frequency band of 5 to 40 GHz. The transmission is represented on a logarithmic (dB) scale. c) The optical rotation, ϕ (black points), calculated from the phase of RCP (red line) and LCP (blue line) transmitted radiation, according to equation 5.3. d) The ellipticity, η, of transmitted radiation calculated from the magnitude of circularly polarised transmitted radiation in (b), according to equation 5.4. Two resonant frequencies are highlighted by grey dashed lines. The frequency band of interest, where non-zero optical rotation is accompanied by negligible ellipticity, is shaded grey.

Fig. 5.6c shows that the phase of both RCP (red) and LCP (blue) radiation undergoes a phase change at each of the four resonant conditions (two maxima, two minima). However, only for the minima are these phase changes of opposite sign, which leads to prominent features in the optical rotation, ϕ, (black points) at 14.8 GHz and 35.4 GHz. Strong optical activity at transmission minima has been reported in other studies of chiral metamaterials[84]. Similarly to the D-cross structure, these rotations are in opposite directions and a region of dispersionless rotation exists between them. However, the direction of rotation is swapped for the lower and upper resonance; the change in optical rotation at the lower frequency resonance resembles that of the higher frequency resonance in the D-cross structure. The explanation for this requires studying the currents in the two layers on resonance.

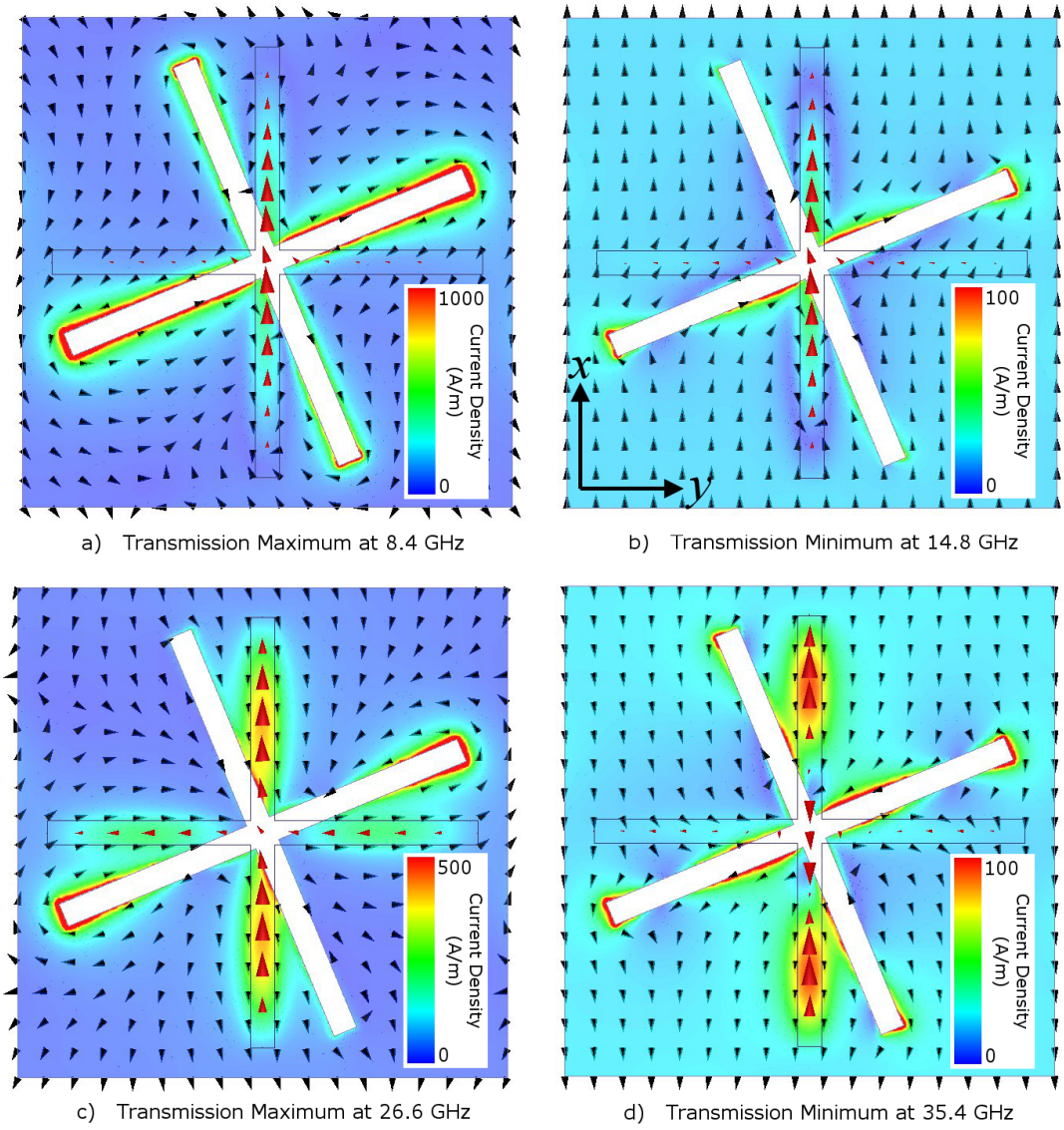

Figure 5.7: One unit cell of the C-cross structure showing the direction and magnitude of surface current density in the cross layer (red arrows) where the magnitude is proportional to the arrow size and is normalised for each plot. This cross, aligned along x and y, is closest to the source of radiation, and is marked by a black outline. The surface current density on the complementary cross layer beneath is illustrated by black arrows (direction) and colour scale (magnitude). (a) $f = 8.4$ GHz (b) $f = 14.8$ GHz (c) $f = 26.6$ GHz and (d) $f = 35.4$ GHz. (a) and (c) correspond to transmission maxima whereas (b) and (d) result in transmission minima due to dipolar and quadrapolar modes of the vertical arm of the cross element. Normally-incident electric field is polarised vertically.

Figs. 5.7a-d depict the current density on the cross (red arrows) and complementary cross (black arrows and colour scale) layers at the four resonant frequencies. The

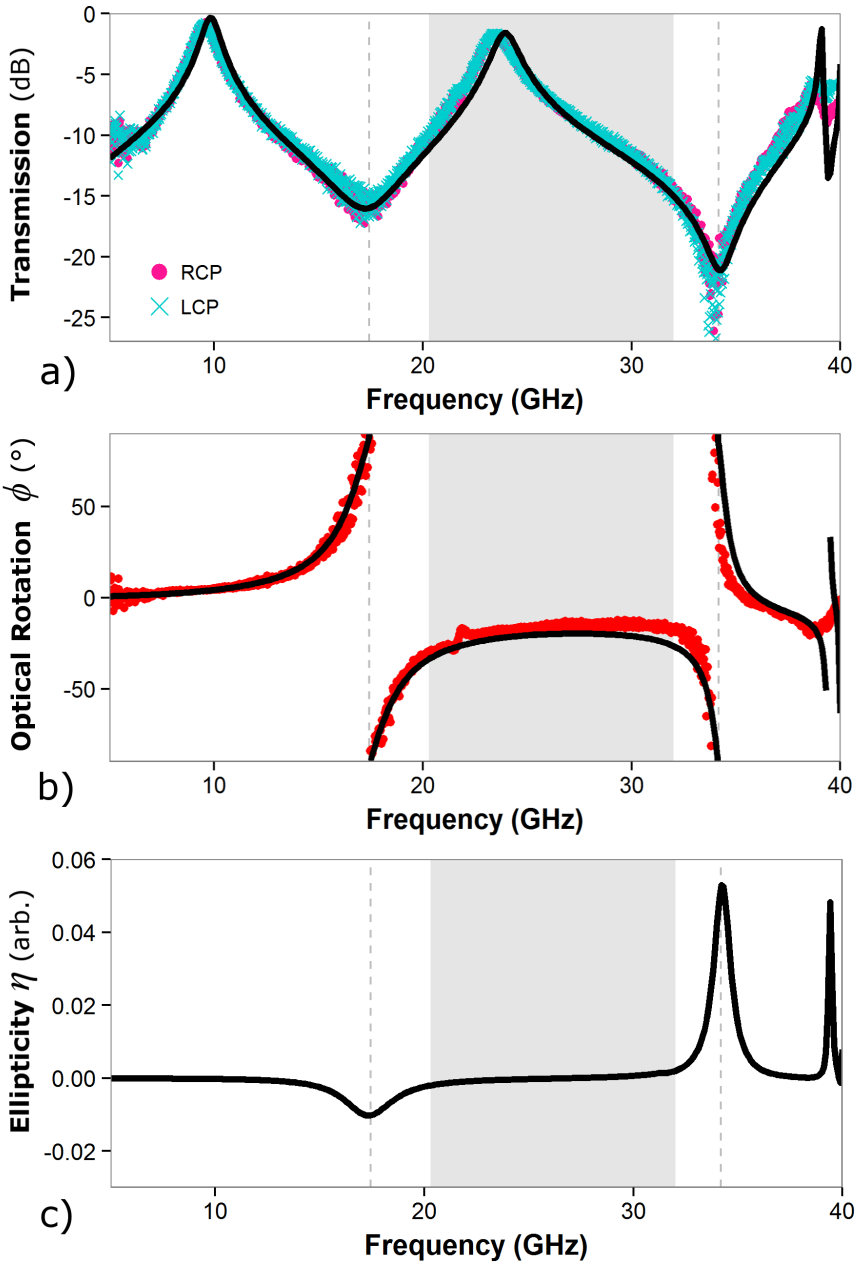

Figure 5.8: Experimental measurements of transmission through the C-cross sample. a) The RCP (pink circles) and LCP (blue cross) transmission amplitudes, $\tau_{R/L}$, on a logarithmic (dB) scale. b) The optical rotation, ϕ (red circles). Results from numerical modelling are overlaid as black lines. c) The modelled ellipticity of transmitted radiation.

size of the red arrows on the cross layer indicates the current density magnitude, which is normalised to unity in each plot. The two transmission maxima (Figs. 5.7a and

c) occur due a coupling between the resonance of the cross-shaped hole (excited by incident magnetic field) and the dipolar mode of the vertical cross arm. The resonant frequency is largely dictated by the geometry of the complementary cross layer, on which the maximum current density is large relative to the transmission minima resonances (Figs. 5.7b). At the lower frequency minimum (Fig. 5.7b), the dipolar mode of the vertical cross is excited by the vertically polarised electric field at normal incidence. The complementary cross layer is non-resonant, with current excited across the entire metallic sheet. This is in phase with the incident field except for beneath the cross element, where image currents flow in the opposite direction. It is these image currents that give the mode an 'antisymmetric' character, similar to the higher frequency resonance for the D-cross structure, while no mode exists that is analogous to the symmetric mode. The higher frequency resonance (Fig. 5.7d) corresponds to a higher order mode of charge distribution within the cross arm, specifically the quadrapolar mode. The current in the centre of the vertical arm is in the opposite direction to that at the arm ends, but in phase with the current on the continuous sheet. Again, the image currents beneath the cross arms are driven out of phase and this mode is referred to as 'antisymmetric quadrapolar'. The resonant frequency of these transmission minima modes is largely dictated by the geometry of the cross element and its separation from the lower ground plane. The presence of the hole in the conducting sheet perturbs the current and allows for induced magnetic dipoles aligned with the electric dipole/quadrapole of the vertical arm of the cross.

5.2.3 Experimental Results

Experimental verification of optical activity in the C-cross array is obtained by measuring the four complex linear transmission parameters ($t_{xx}, t_{yy}, t_{xy}, t_{yx}$) at normal incidence using the radiative experimental setup described in section 3.4.1. Broadband (5-40 GHz) horn antennas are used that can be rotated through 90° to obtain the required linear polarisations. From the four linear parameters the circular transmission parameters are derived, along with optical rotation and ellipticity according to equations 5.2-5.4. The right (pink circles) and left (cyan crosses) handed circular transmission results are presented in Fig. 5.8a, with the simulated result overlaid. The experimental sample dimensions match that from the previous section and it is produced using commercial printed circuit board techniques using an Isola Tachyon board with thickness $t = 0.406$ mm and permittivity $\epsilon = 3.02(1 + 0.002\text{i})$. The sample is formed of 50 unit cells in the x- and y- directions and alignment of the upper and lower layers is accurate to within 10 μm. Over-etching of the two metallic layers means that the cross dimensions are adjusted by $\delta = 0.05$ mm. This value is estimated via

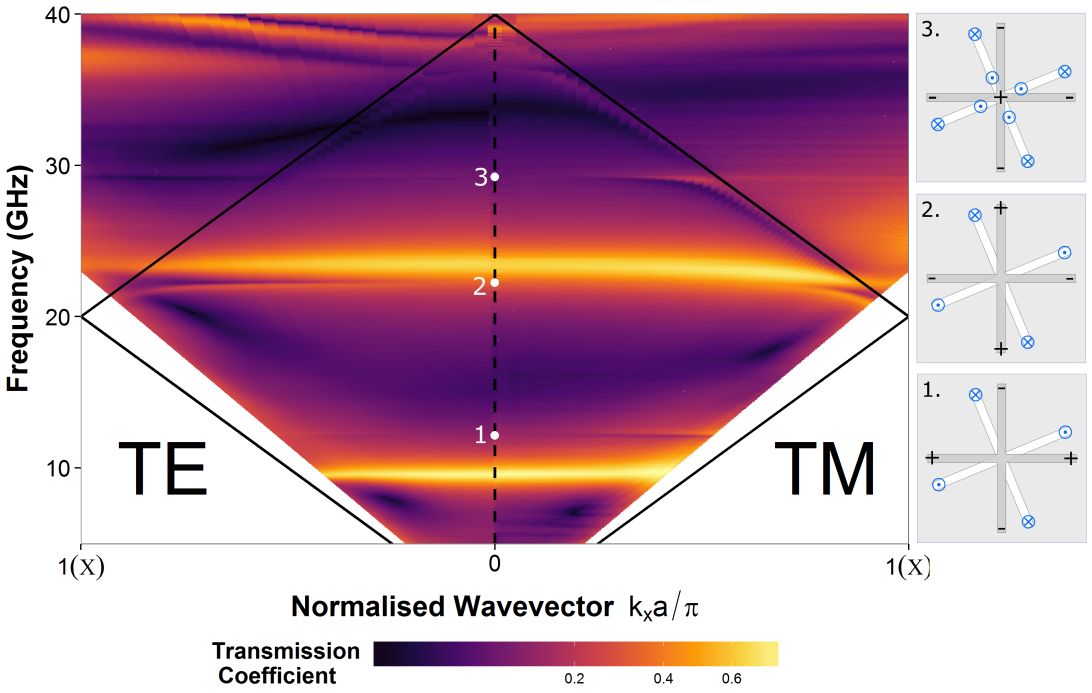

Figure 5.9: The experimentally obtained, linearly polarised transmission coefficient, t_{xx} as a function of in-plane wavevector (incident angle). Left-hand-side: transverse electric (TE) radiation, right-hand-side: transverse magnetic (TM). Quadrapolar cross modes are seen away from normal incidence. Inset: The charge configurations on the cross layer (black) and out of plane magnetic field direction within the hole (blue) for modes marked 1-3.

measurement of 5 unit cell dimensions using a microscope. The cross layer has larger arms of length $l = 6.6\ \text{mm} + \delta$ and width $w = 0.375\ \text{mm} + \delta$, whereas the cross-shaped hole in the complementary layer is smaller, $l = 6.6\ \text{mm} - \delta$ and $w = 0.375\ \text{mm} - \delta$. The simulated results (black lines in Fig. 5.8) account for this alteration. Good agreement is found between experiment and simulation for the transmission magnitude as well as the optical rotation (Fig. 5.8b), with a small shift in resonant frequencies attributed to etching inaccuracy. An additional feature of small amplitude at ≈ 22 GHz is due to the sample not being aligned exactly at normal incidence relative to the incident beam as well as an inherent angle spread in the incident beam. This extra feature is a quadrapolar mode of the cross element that cannot be excited without a phase change of the incident field across the surface of the sample (i.e. cannot be excited at normal incidence). Experimental determination of ellipticity (Fig. 5.8c) was not possible due to experimental noise in the data when the transmission magnitude is small.

Additional resonances exist that are not excited by normal incident radiation. These can be seen in Fig. 5.9, which shows the experimentally obtained transmission intensity

as a function of frequency, f, and in-plane wavevector, $k_\mathrm{p} = k_0 \sin(\theta)$, for both transverse electric (left hand side) and transverse magnetic (right hand side) radiation. Here, $k_0 = 2\pi f/c$ is the free-space wavevector and θ the angle of incidence. The additional modes have a high quality factor, due to their radiative losses being very small. This is because the field configuration of the mode does not match that of an incident plane wave. In this instance, the modes correspond to quadrapolar modes of the entire cross element (as opposed to the quadrapolar mode of just one arm in Fig. 5.7d). The first three of these modes are depicted in Fig. 5.9, with the charge distribution represented on the upper cross layer (black), and the direction of magnetic field represented within the cross-shaped hole (blue). These schematics are derived from eigenmode simulations using COMSOL Multiphysics. These sharp quadrapolar resonances also lead to optical rotatory effects and hence the band of dispersionless rotation is destroyed by the presence of modes 2 and 3 in Fig. 5.9 for incident angles $>\approx 10^\circ$.

5.2.4 Varying Dielectric Thickness

In the previous sections, optical rotation bands in the D-cross and C-cross structure have been distinguished by the resonances at either end of the band. In the cross structure, these resonances are coupled dipole modes of the upper and lower layer, whereas in the C-cross system they are the dipolar and quadrapolar modes of the cross arms with image currents formed on the complementary cross layer beneath.

The distinct nature of resonances for the two systems means that the effect of changes to the unit cell geometry is different for each of them. Fig. 5.10a and b shows the optical rotation of the cross and C-cross systems respectively, for a variety of dielectric thicknesses, t, according to driven modal simulations in HFSS. The arm length, l is shortened to 6.25 mm for these simulations in order to keep the resonances within the frequency range of study (5-40 GHz). This modelling was carried out by Lauren Barr (PhD student, Exeter).

Fig. 5.10c demonstrates the frequency of the two resonances (where the optical rotation is $\pm\pi/2$) for the D-cross (unfilled circles) and C-cross (filled circles), extracted from Figs. 5.10a-b. The mode positions of the D-cross structure are more sensitive to change in the dielectric thickness due to the coupled nature of the resonances. As $t \to \infty$ the resonant frequencies converge onto the single cross layer eigenfrequency ($\approx$ 24 GHz). For the C-cross system, the frequency gap between the resonances also reduces. However the change is small compared to the D-cross structure because the two modes converge onto *separate* eigenfrequencies (i.e. different modes) of a single cross layer as the thickness approaches infinity.

Fig. 5.10d shows the optical rotation in the centre of the band between the two

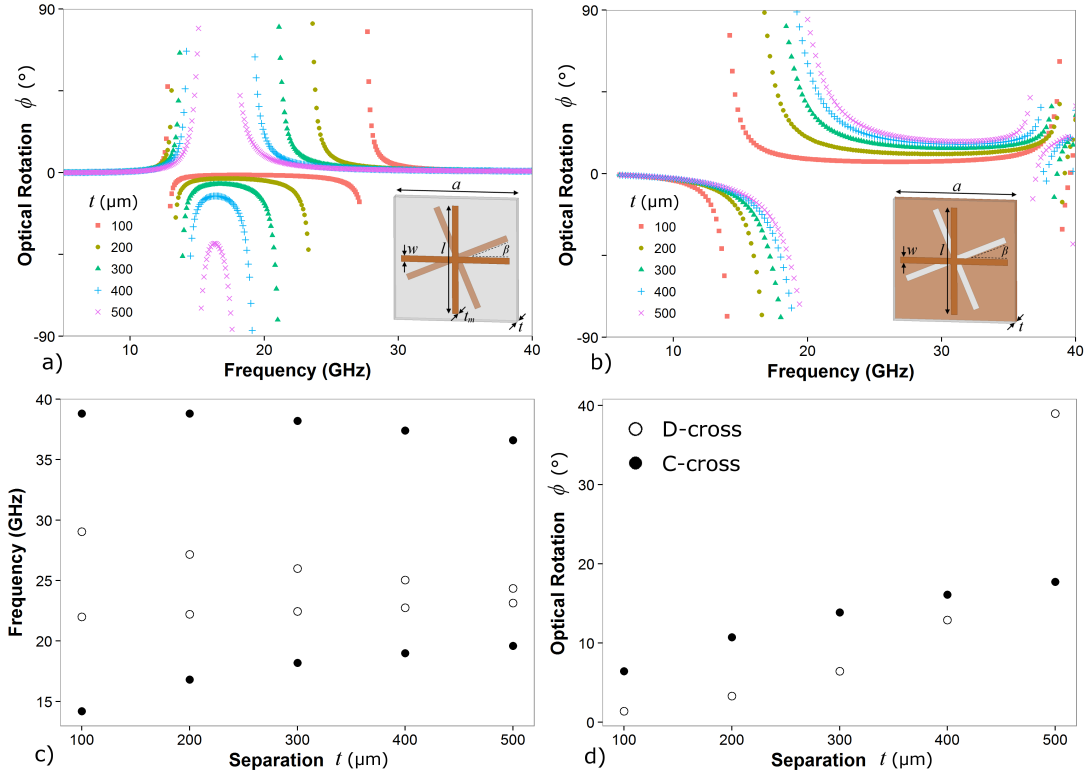

Figure 5.10: Simulated demonstration of the change in optical rotation on increasing the separation, t, between upper and lower layers. (a) Modelled optical rotation for (a) D-cross structure and (b) C-cross structure with dielectric thicknesses of 100 μm to 500 μm. (c) Upper and lower resonant frequencies (where $\phi = \pm\pi/2$) for the D-cross (unfilled) and C-cross (filled) structures for a range of separations; (d) Optical rotation midway between the two resonances. Simulations were carried out by Lauren Barr.

resonances as the dielectric thickness t is increased. For both structures there is an increase in optical rotation with t, and hence a trade-off between the degree of rotation attainable and the bandwidth. For all but the largest thickness studied, the C-cross structure provides both a wider bandwidth and greater optical rotation than the cross structure, making it the better candidate for polarisation rotating applications.

5.2.5 Multilayer

In the final section of this chapter, two C-cross structures are stacked in order to enhance the width of the transmission band. The two identical structures have the same dimensions as the experimental sample from earlier in this chapter, and are separated by a 1.5 mm expanded polystyrene spacer (with refractive index $n \approx 1$).

The experimental transmission magnitude is illustrated in Fig. 5.11 for RCP (ma-

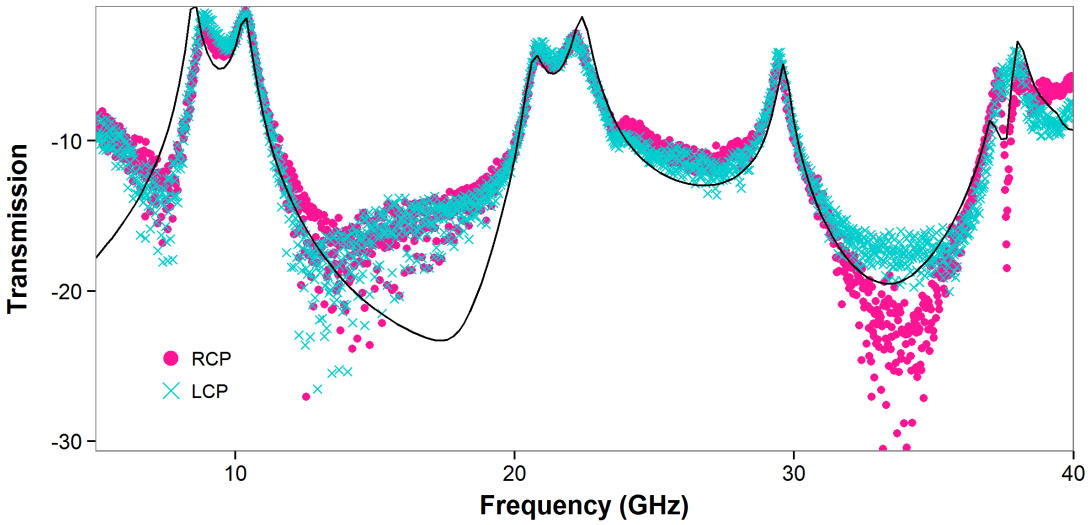

Figure 5.11: Experimental measurements of transmission through the Double-C-cross sample. a) The RCP (pink circles) and LCP (blue cross) transmission amplitudes, $\tau_{R/L}$, on a logarithmic (dB) scale. The simulated result for LCP is shown as a solid black line, with negligible difference for RCP radiation on this scale.

genta circles) and LCP (cyan crosses) radiation. Each of the single transmission peaks in Fig. 5.8a have now split into two peaks, corresponding to symmetric and antisymmetric currents with respect to the central plane between the two structures.

Numerically modelled results for LCP radiation are shown as a black line in Fig. 5.11. This simulation is fitted to the transmission peaks by adjusting the dielectric constant of the material separating the two structures. The RCP simulated transmission differs from LCP at the tranmission minima, however this difference is insignificant on this scale. Whilst good agreement is obtained for the frequency and magnitude of transmission peaks, the model fails to represent the data at lower frequency minima. This discrepancy is attributed to inconsistencies in the sample. In particular, the spacing between the two C-cross structures varies across the sample. For this reason, experimental determination of optical rotation was not possible, as the phase change of transmitted radiation is significantly different for different regions of the sample.

5.3 Conclusions

In this chapter, the origin of optical rotatory effects in twisted cross chiral metamaterials has been determined.

The double cross structure (D-cross), a bilayer consisting of a two square arrays of metallic crosses with those of one layer rotated by 22.5°, exhibits a pair of cou-

pled resonances in its transmission spectrum, corresponding to dipolar currents in the arms of the cross elements. The two resonances cause opposite rotations of linearly polarised radiation as it transmits through the structure, and between them a region of dispersionless, pure optical rotation exists[73].

The complementary pair structure (C-cross), where the second layer is replaced by its complement (i.e. a cross-shaped hole in a metallic film) is known to exhibit a similar band of optical rotation that coincides with a peak in transmission[77]. In this work, the two resonances that give rise to this effect have been shown to be the dipolar and a higher order (quadrapolar) mode of the cross arms, with image currents formed in the continuous metal layer beneath. Transmission maxima resonances also exist on this structure, which are primarily attributed to the dipolar mode of the cross-shaped hole coupling with the dipolar mode of the cross element above. An excellent agreement between experimental results and simulation was presented. Future work in this topic would focus on effective parameter retrieval, such as that performed in [80].

The coupled nature of the two resonances in the D-cross system means that the width of the band between them is more sensitive to changes in the layer separation than the C-cross structure. However the latter provides improved performance; a larger bandwidth and larger optical rotation for separations below 500 μm. Finally, an experimental study of a multilayer C-cross structure demonstrated that the single peak pass band in transmission can be broadened to a double peak with reduced transmission magnitude.

Chapter 6

Compound Checkerboard Array

In this chapter, checkerboard metasurfaces comprising a single patterned metallic layer supported on a substrate are studied. The propagation of bound surface waves on these structures is experimentally investigated, as well as their use as frequency selective screens. Compound (two elements per unit cell) arrays of holes within a metallic sheet are shown to enhance isotropy of surface mode propagation as well as provide sharp resonances in transmission.

6.1 Background

Patterned metallic sheets have been used as filters for electromagnetic radiation since the birth of the diffraction grating in the late 18th century. Such patterned sheets implemented as frequency selective surfaces (FSSs) in the microwave and radio frequency regimes have found use in the telecommunications industry, where the transmission and reflection spectra are dictated by the periodicity, size and shape of the individual elements comprising the patterned array. These features in the transmitted or reflected signal may be attributed to the excitation of surface waves (a resonant phenomenon associated with the geometry of the array) which then re-radiate and interfere with the non-resonant radiation (see Sec. 2.4). Much prominence has been given to selective transmission in the optical regime as a consequence of the excitation of surface waves due to the work of Ebbesen et al. that demonstrated extraordinary optical transmission through an array of subwavelength holes in a metallic film[85]. This enhanced transmission has been attributed to the excitation of coupled surface waves (Sec. 2.5.2) on either side of the film[86].

In electromagnetism the applications of metamaterials can be broadly split into radiative and non-radiative categories. In the radiative regime, structures may be tailored to provide desired scattering parameters. These include pass (or stop) bands

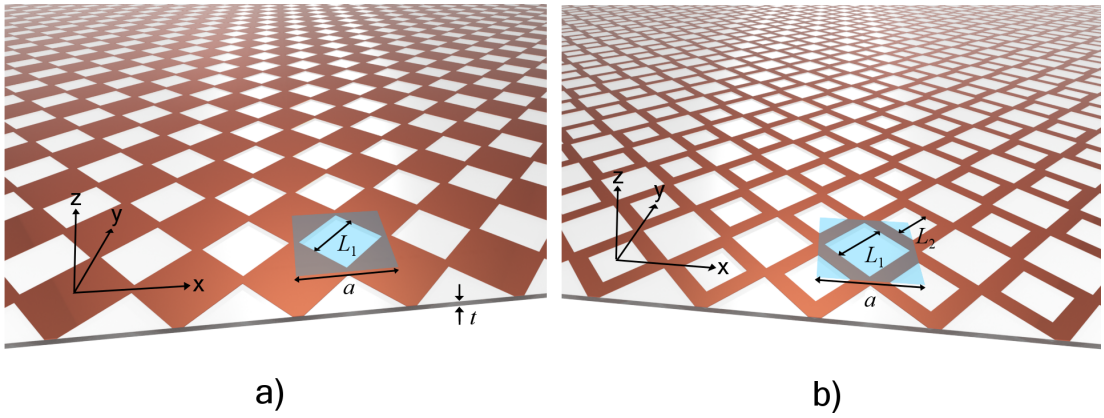

Figure 6.1: Sample illustration for a) the connected ordinary checkerboard array (CA) with square hole size L_1 b) the compound checkerboard array (CCA) with two different sized square holes per unit cell, L_1 and L_2. The CA is the CCA with $L_2 = 0$. The samples consist of a patterned metallic layer above a 25 μm Mylar substrate.

in transmission, perfect absorption[87], enhanced scattering into diffractive orders[88] and improved directivity[89]. In some cases a sharp resonance in transmission or reflection may be desired, in order to pass or block only a very narrow range of frequencies. Such sharp resonances (high quality factor) with FSSs have been achieved using arrays of asymmetric[90] and compound[91][92] ring resonators in the microwave regime, and pairs of coupled nanoparticle 'dimers' at optical frequencies[93][94]. Often the functionality relies on multiple elements per unit cell whose resonant frequencies are detuned from one another by varying their relative size. Similarly, sharp 'phase resonances' have been observed in transmission through compound gratings of one-dimensional slits in a metallic sheet, comprising identical slits in a compound array[95][96][97][98][99][100][101], different sized slits[102][103], and cavities within slits of a regular array[104][105]. Reflection gratings have also demonstrated a similar phenomenon[106]. These additional resonances arise from the increased degrees of freedom when the unit cell contains multiple elements, and generally correspond to the fields associated with different elements being driven out of phase with one another. In the non-radiative regime, where the surface waves are localised to the surface, enhanced control of their in-plane propagation may be desired. For example lensing of surface waves[107] has been demonstrated, as well as unidirectional propagation[108] and negative mode index[109]. If the constituent elements are deeply subwavelength, the material is truly a metamaterial and can be described by effective properties. Provided the elements possess the symmetry groups of a square (group D4[110]) or greater, the propagation will be isotropic. However when the element size and wavelength have the same order of magnitude, the material no longer acts isotropically and the sur-

face wave propagation differs for different in-plane directions. In some circumstances it may be helpful to enhance this anisotropy, in others it may be beneficial to improve the isotropy of surface propagation in this barely-subwavelength regime. This work demonstrates how isotropy may be improved for the non-radiative surface waves while at the same time demonstrating a very sharp resonant feature in the radiative regime. In this study we focus on the metallic checkerboard array (CA, shown in Fig. 6.1a), a FSS that has received interest due to its change from an inductive to a capacitive filter as the square hole size, L_1, increases beyond a critical value and the connected array becomes instead an array of disconnected patches. For frequencies below the onset of diffracted orders, the response of the connected structure to normal incidence microwave radiation is an extremely broad resonant feature in transmission[111]. Adding a second square hole element into the unit cell of the checkerboard array (resulting in the compound checkerboard array, or CCA, illustrated in Fig. 6.1b) significantly sharpens this feature in the transmission spectrum while also acting to produce near isotropy in the propagation of the localised surface wave across the array. The thin structure supports a surface wave on both the top and bottom surfaces, resulting in a symmetric/antisymmetric pair (Sec. 2.5.2). For this analysis we only consider the symmetric mode, with the antisymmetric effectively propagating as a surface current.

The experimental samples consist of a patterned metallic laminate (18 μm Copper on 25 μm Mylar). The design is printed directly onto the laminate and void regions are removed using an etchant, as described in section 3.2.1. The checkerboard array (Fig. 6.1a) has a periodicity, $a = 6$ mm, and the square holes have side length $L_1 = 4.6$ mm. The compound checkerboard array has periodicity $a = 8$ mm and contains two holes per unit cell (shown in blue in Fig. 6.1) of side lengths $L_1 = 5.1$ mm and $L_2 = 3.7$ mm. The CCA periodicity is larger so that resonances in the transmission spectrum exist within the frequency range of the experimental setup (18 - 40 GHz). In order to compare the response of the two samples, frequencies are normalised to $f_\mathrm{n} = (a/\lambda)$, where λ is the free-space wavelength. Both samples have a size of 400 mm $\times$ 280 mm and the elements comprising each array are electrically connected; supporting a transverse magnetic fundamental surface wave (see Sec. 2.5). Bound surface waves are excited and detected using stripped coaxial antennas placed in the near field, attached to a Vector Network Analyser (Sec. 3.3.1). One antenna is scanned across the surface to produce a 2D map of the near-surface electric field distribution. A 2D Fourier transform of this map is used to extract the in-plane wavenumbers, $k_\mathrm{p}(k_\mathrm{x}, k_\mathrm{y})$, present. From this information reciprocal space dispersion diagrams and isofrequency contours can be plotted. In the radiative region, modes of the structure can couple to free-space radiation and hence are no longer bound surface waves. Radiation from these modes interferes with non-resonant transmitted radiation to produce features in the transmission spectrum. This

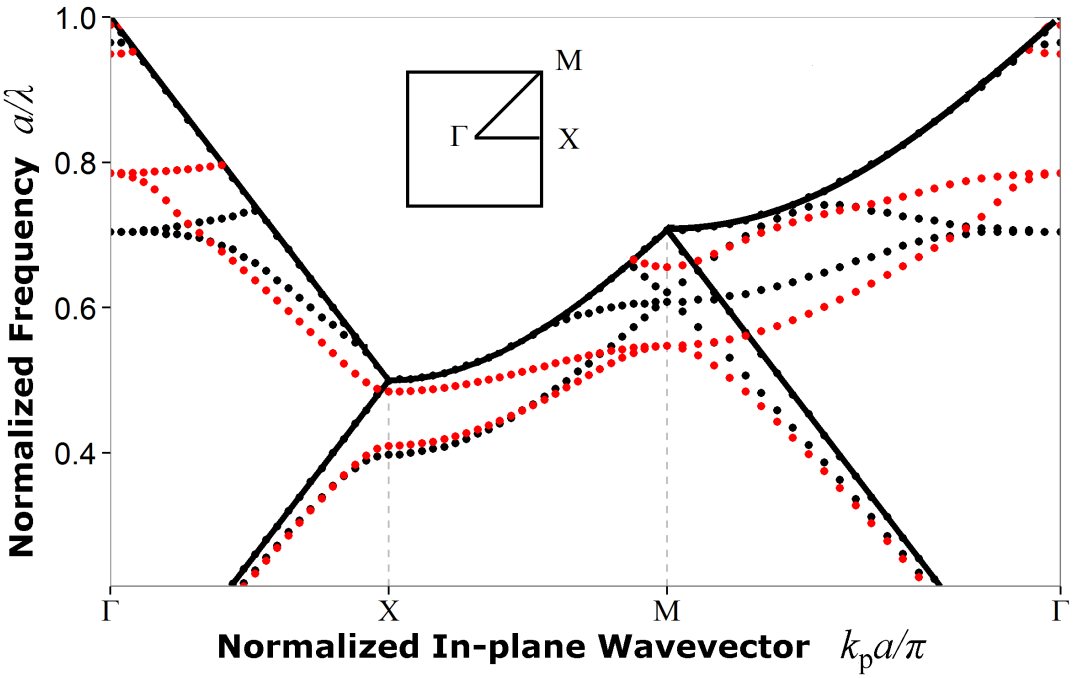

Figure 6.2: Modelled band structure for an ordinary (black points) and compound (red points) checkerboard array, representing the mode propagation around the irreducible Brillouin zone (see inset). Eigenfrequencies are obtained via COMSOL Multiphysics. Solid black lines represent light lines (grazing radiation).

is measured in a second experiment (Sec. 3.4.1) by illuminating the sample with an approximately planar, collimated, linearly polarized microwave beam at an incident angle, θ, polarised along specific symmetry planes of the sample and measuring the transmitted intensity as a function of frequency.

6.2 Band Structure Simulation

The simulated surface wave band structure for both the ordinary (black points) and compound (red points) checkerboard arrays are presented in Fig. 6.2, which covers the irreducible Brillouin zone given by the points of high symmetry in reciprocal space, Γ, X and M (see inset). Of particular significance are the Γ to X and Γ to M sections which correspond to surface wave propagation along the x-direction (also y-direction due to symmetry) and diagonally respectively. Adding a second square hole into each unit cell has a significant effect on the band structure as outlined below. First, the mode characteristics in the non-radiative region will be discussed and the modelled band structure compared to experimental data. Secondly, the effect these modes have on the transmission coefficients of the structures in the radiative region will be explored,

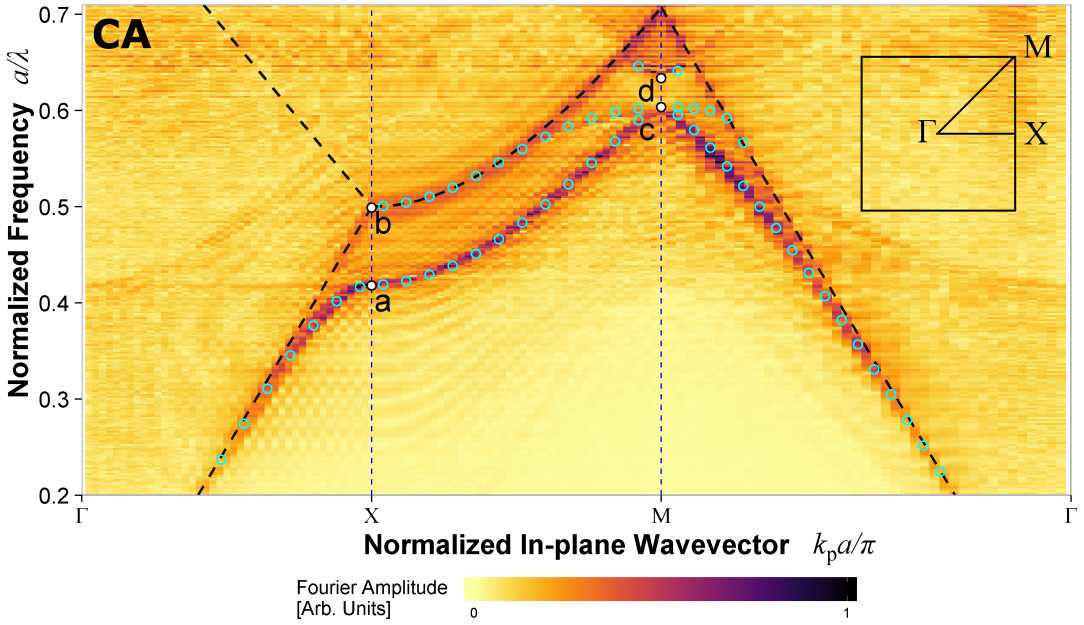

Figure 6.3: Experimental band structure for the ordinary checkerboard array (CA), obtained via near field excitation and detection of surface modes. The points a-d correspond to standing wave solutions of lower and upper band edges at the X and M points. Light lines are represented as dashed lines and eigenmode positions from numerical modelling are shown as blue circles.

again by comparison to experimental data and by studying the field configurations at the Γ point.

6.3 Non-Radiative Measurements

From Γ to X, and Γ to M a localised surface wave with greater momentum than grazing radiation is supported on both the CA and CCA. Due to the periodicity of the structure, this surface wave interacts with its back-scattered counterpart resulting in two standing wave solutions at both the X and M point with the same momentum (wavevector) but different energies (frequency), each with zero group velocity.

6.3.1 Ordinary Checkerboard Array ($L_2 = 0$)

The experimentally obtained dispersion relation for surface waves on the ordinary checkerboard array is presented in Fig. 6.3, with overlaid eigenfrequencies calculated from numerical simulation. Fig. 6.4 shows the electric field configuration in the x-y plane of the band-split modes. Fig. 6.4a-b show the fields of the split modes at the X

point, and Fig. 6.4c-d the two sets of fields at the M point. The electric field magnitude within the hole is represented by the colour scale, and the greyscale signifies charge density on the metallic regions (i.e. charge accumulates in white regions). The white and orange arrows show the electric field vector and current density respectively, at a phase where they are maximum. These quantities are used to infer the instantaneous charge distribution shown on the surface. As a guide for visualization, a sinusoidal approximation of this charge distribution is shown overlaid as a white/black line to distinguish the typical $\lambda/4$ shift of charges for band-split pairs.

At the X point, where the direction of propagation is along the x-direction and the wavelength $\lambda = 2a$, the two transverse magnetic modes (a and b in Fig. 6.3) are separated by a gap in energy. The lower band edge (Fig. 6.4a) corresponds to charge concentrated between the rows of holes, causing enhanced electric field within the holes on resonance. The upper band edge exists on the light line at b in Fig 6.3. This mode corresponds to charges offset by $a/2$ with respect to the lower band edge mode. This charge configuration cannot hybridise with a resonance of the individual hole elements, instead the mode resembles a surface current on a planar metallic sheet. At higher frequencies, this upper band edge disperses into the radiative region. From X to M, as the momentum vector along the surface of the structure rotates from the x-direction by 45°, these two modes (a and b) converge and become degenerate at M. This behaviour is typical of four-fold symmetric elements on a square lattice[110]. At M, this degenerate pair form the lower band edge (c in Fig. 6.3). The fields of one of the solutions is presented in Fig. 6.4c, with the other simply being the same field profile, rotated by 90°. The lower band edge mode again corresponds to charge accumulation on either side of the hole. The mode has dispersed away from the light line as it asymptotes towards the dipolar resonant frequency of the individual hole element (the spoof surface plasma frequency)[16]. Again, the difference between the lower and upper band edges (c and d in Fig. 6.3) is an offset of charge, this time by $\sqrt{2}a/4$ in the diagonal direction (see black line approximation in Fig. 6.4c-d). Both of these charge configurations excite a resonance of the holes; the lower one being dipolar (Fig. 6.4c) and the upper one quadrapolar (Fig. 6.4d).

Coupling to a mode of the hole localises the wave to the surface. The exponentially decaying fields away from the surface enhance the in-plane momentum, k_{p}, of the mode such that it is much greater than that of grazing radiation (light line). This occurs for the band edges at a,c and d in Fig. 6.3 but not b, where the mode exists close to the light line and propagates as a surface current.

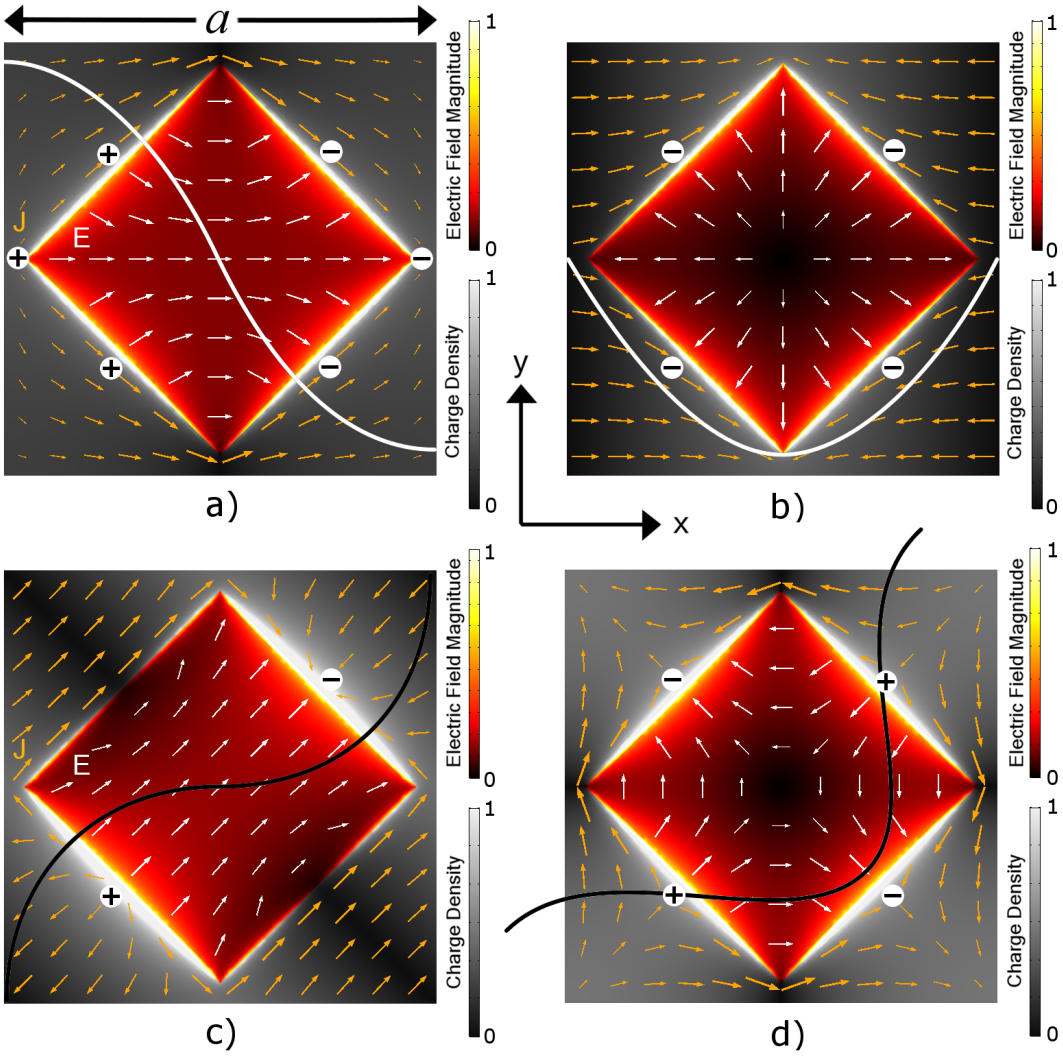

Figure 6.4: FEM predictions of electric field profiles of the CA standing wave eigenmode at the points a-d in Fig. 6.3, shown in the x-y plane at a height corresponding to the top-plane of the metallic layer. Within the holes the electric field magnitude is plotted as a colour scale (arb. units), with the instantaneous electric vector as white arrows. On the metal surface, the charge density is shown as a greyscale (arb. units), and corresponding charges labelled. The current density is plotted as orange arrows. Overlaid is an approximation to the charge modulation across the surface (black/white lines).

6.3.2 Compound Checkerboard Array ($L_2 \neq 0$)

The experimentally obtained dispersion for the compound checkerboard array is presented in Fig. 6.5a, with the four standing wave solutions marked e-h. Eigenmode modelling (blue circles) is overlaid and shows excellent agreement with the experimental data, although the upper band around the M point is not apparent in the experi-

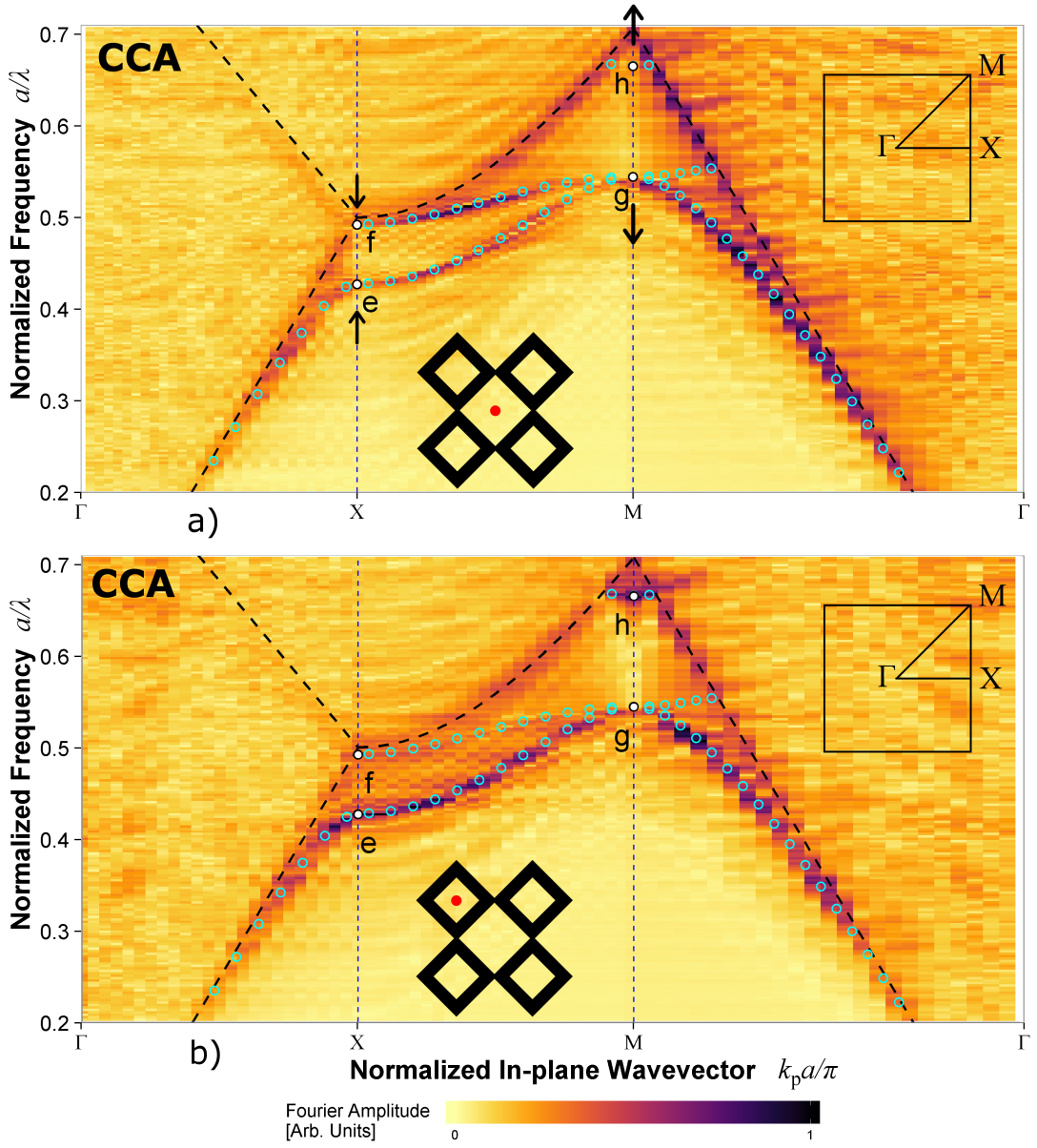

Figure 6.5: Experimental band structure for the compound checkerboard array, obtained via near field excitation and detection of surface modes. The points e-h correspond to standing wave solutions of lower and upper band edges at the X and M points. Light lines are represented as dashed lines and eigenmode positions from numerical modelling are shown as blue circles. The source antenna is positioned above (a) the larger square hole and (b) the smaller square hole.

mental data. This is due to the placement of the near field antenna, which is oriented normal to the surface, directly above the centre of the larger square (as shown by the red dot inset). The eigenmode of the upper band edge at M contains no z-component

of electric field at this position and hence coupling to this mode is very weak. The result of a second near-field scan, this time with the source above the smaller hole (inset), is shown in Fig. 6.5b. The mode around the upper band edge at M can now effectively provide a coupling mechanism between the source and detector antennas, however the higher frequency band between X and M is missing, again due to the lack of z-component of the electric field profile for the mode. Excitation of all modes of the system would therefore require some asymmetry in the antenna orientation with respect to the z-axis and/or asymmetry in its position with respect to the unit cell. Again, the fields of the four modes (e-h) are studied using eigenmode simulations of the structure and are shown in Fig. 6.6. The band-splitting is reduced at the X point, as the upper band edge lowers in frequency. Conversely, the band splitting at the M point is increased compared to the CA as a result of adding a second square hole into the unit cell. The change in frequency of all 4 band edges relative to those of the CA structure is represented by arrows in Fig. 6.5a, and can also be seen in the simulated dispersion diagrams in Fig. 6.2. The addition of the second hole element into the unit cell perturbs the current flow around the surface and charge accumulation occurs at the edges of both holes. For the upper band edge at X (f in Fig. 6.5) and the lower band edge at M (g in Fig. 6.5), the smaller square hole has replaced a region of maximum current flow in the CA structure (see arrows in Figs. 6.3b and c). For the CCA, the current instead flows around the smaller hole, exciting its dipolar resonance (see corners of Fig. 6.6b and c). This increases the confinement of the mode to the surface, hence increasing the imaginary component of k_z and thereby its in-plane momentum, resulting in a band edge at a lower frequency than for the CA structure in Fig. 6.3. For the other two modes, the lower band edge at X and the upper at M (e and h in Fig. 6.5 respectively, fields in Fig. 6.6a and d), the additional hole has replaced a region of charge accumulation in the CA (see corners of Fig. 6.4a and d). This second hole, surrounded by charges of the same sign, does not localise the field to the surface. Instead, confinement is reduced and the eigenmode frequency is increased relative to the position in Fig. 6.3 for the CA structure.

The dispersion of surface waves in all directions is represented by isofrequency contours (Sec. 3.5.3), slices through the full 3D dispersion as a function of frequency. The decreased (increased) band splitting of the compound checkerboard array at the X (M) point compared to the regular checkerboard array results in improved isotropy of wave propagation. This can be seen by comparing the isofrequency contours for the checkerboard (Fig. 6.7a) and compound checkerboard arrays (Fig. 6.7b), at a frequency just below the lower band edge at X for the CA. In both cases the surface wave has dispersed away from the light circle (black dotted line) with a difference in wavevector δk which depends upon the direction of in-plane propagation. The CCA

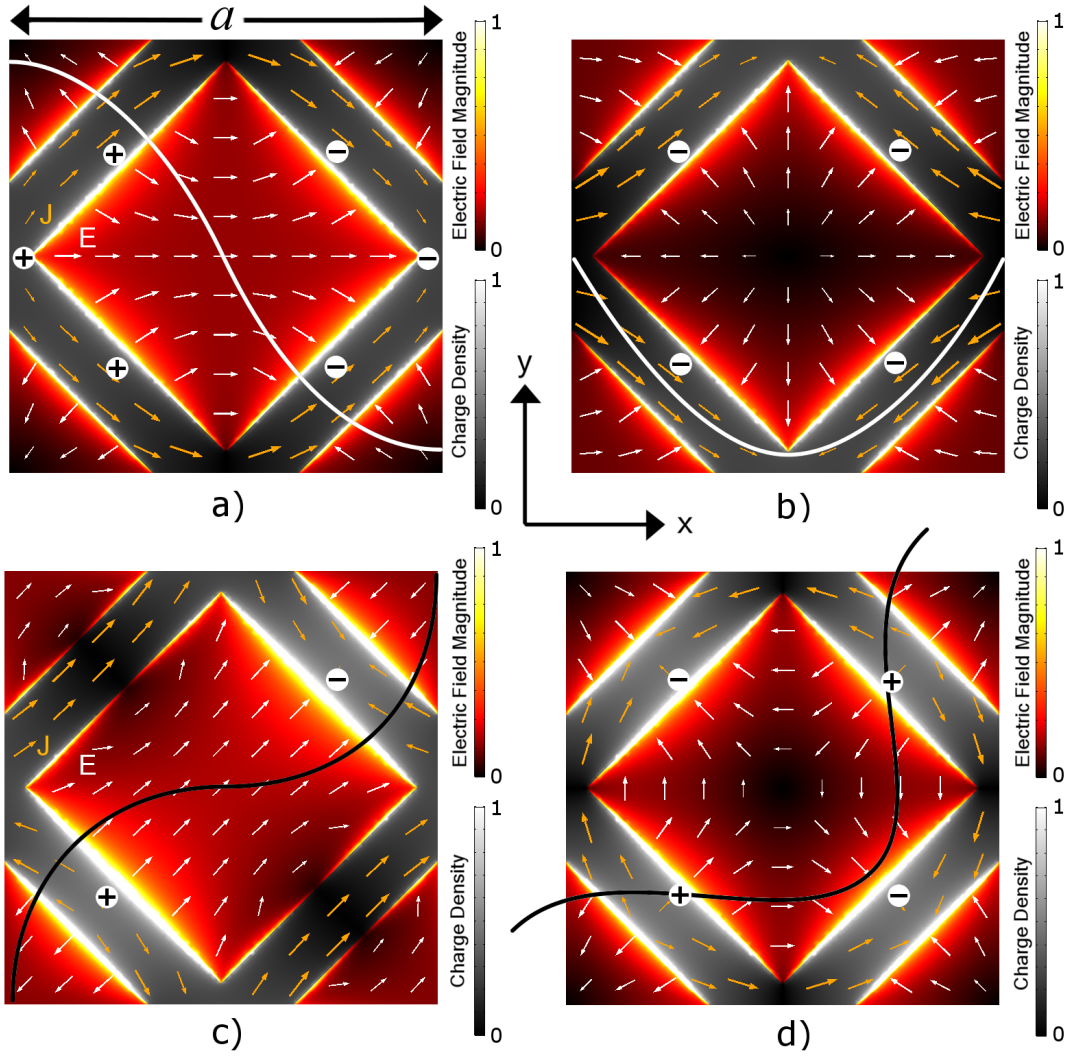

Figure 6.6: Electric field profiles of the CCA standing wave eigenmode at the points e-h in Fig. 6.6, shown in the x-y plane at a height corresponding to the top-plane of the metallic layer. Within the holes the electric field magnitude is plotted as a colour scale (arb. units), with the instantaneous electric vector as white arrows. On the metal surface, the charge density is shown as a colour scale (arb. units), and corresponding charges labelled. The current density is plotted as orange arrows. Overlaid is an approximation to the charge modulation across the surface (black/white lines).

contour is approximately circular, meaning the mode propagates with approximately circular phase fronts with an approximately even distribution of power radially. A comparison of isotropy for the two structures can be made by comparing the differences of wavevector δk along ΓX and ΓM, which are equal if the contour is circular. These δk values, obtained via eigenmode modelling and shown inset in Fig. 6.7, confirm that mode propagation on the CCA is far more isotropic ($\delta k_{\mathrm{M}} = 0.072$ and $\delta k_{\mathrm{X}} = 0.083$) than on the CA structure ($\delta k_{\mathrm{M}}= 0.038$ and $\delta k_{\mathrm{X}} = 0.128$).

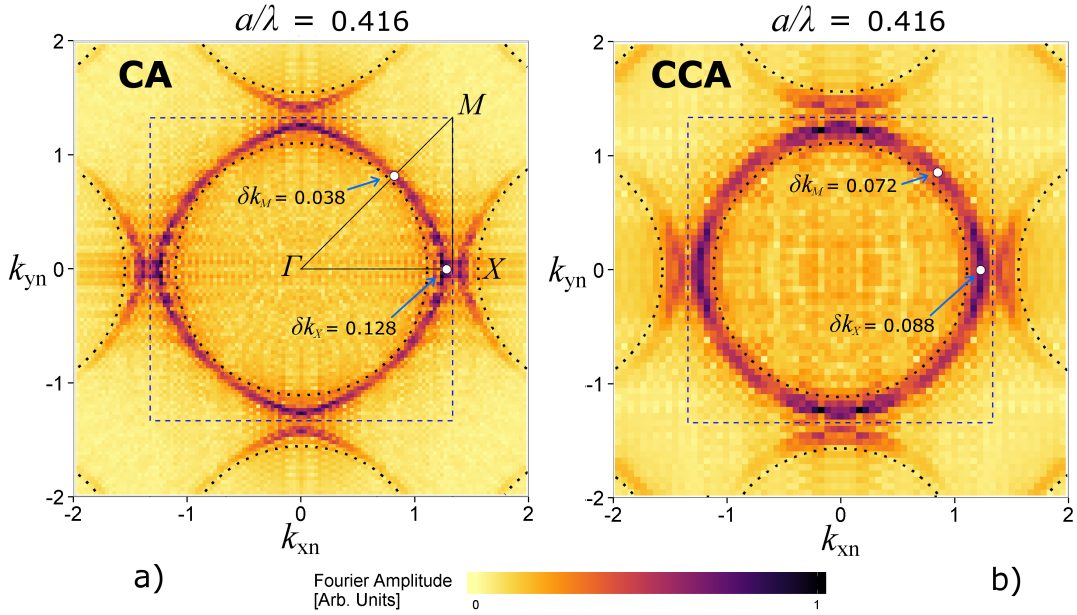

Figure 6.7: Experimentally obtained isofrequency contours demonstrating the in-plane wavevector of a surface wave on the regular checkerboard (a) and the compound checkerboard (b) at the same reduced frequency, $a/\lambda = 0.416$. The first Brillouin zone boundary is shown as a dashed blue line, and light circles as red and black dotted lines. The mode positions along ΓX and ΓM according to eigenmode modelling are shown as white points, and their difference in wavevector from the light line (δk_{M} and δk_{X}) is labelled

Although the increase and decrease in band gap size at the X and M positions is sufficient to explain the enhanced isotropy of the isofrequency contour for the CCA shown in Fig. 6.7b, another qualitative reasoning is obtained by considering the periodicity of the structure. As the second square hole size increases, and L_2 approaches L_1, the period of the structure becomes increasingly ambiguous, and is equal to $a/\sqrt{2}$ for $L_2 = L_1$. At this point the Brillouin zone in reciprocal space is larger. It is therefore unsurprising that the isofrequency is more circular for increasing L_2; because the contour is smaller relative to the Brillouin zone. Only when the contour approaches the edge of the Brillouin zone does interaction with scattered modes occur, resulting in band gaps and anisotropic contours.

6.4 Radiative Measurements

6.4.1 Compound Checkerboard Array

Within the radiative region the dispersion of modes for the CCA is experimentally observed by studying the transmission spectrum of the arrays as a function of incident

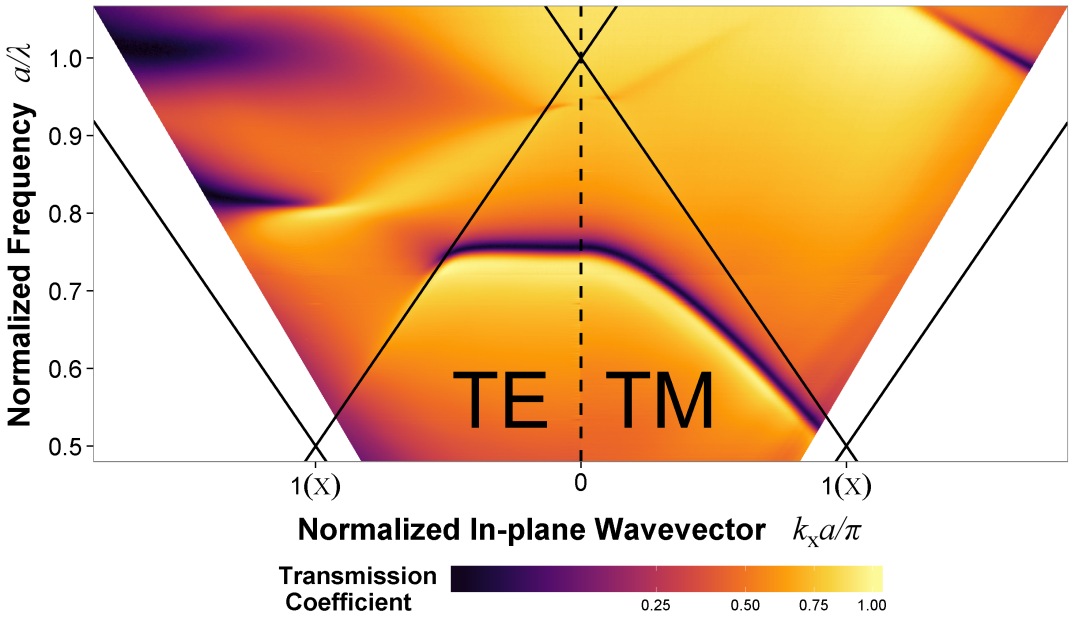

Figure 6.8: Experimental dispersion of radiative modes on the CCA structure for TE (left hand side) and TM (right hand side) incident polarization. The colour scale represents the transmission coefficient obtained for incident angles up to 60° and light lines are plotted as solid black lines.

angle, θ. Increasing this angle increases the normalised in-plane wavevector, $k_n = k_p a/\pi$, of the incident plane wave according to

$$k_n = 2 f_n \sin\theta \tag{6.1}$$

where f_n is the normalised frequency (a/λ) and c the speed of light in vacuum. The polarisation of the incident radiation can be either transverse electric (TE) or magnetic (TM). For each polarization, θ was varied between 0° and 60°, with a step size of 0.2°. We limit the radiative study to the ΓX direction. Fig. 6.8 shows the transmission coefficient as a function of both frequency and wavevector for TE (left hand side) and TM (right hand side) radiation. A comprehensive study of the radiative modes for the CA can be found in [111].

A sharp Fano shape resonance (maximum followed by a minimum) occurs in transmission at a reduced frequency of 0.75 at normal incidence (Γ point). This is due to interference between the resonant and non-resonant transmission which is constructive below the resonant frequency and destructive above it. As the in-plane momentum (and incident angle) increases, this mode splits in two. A TM mode reduces in frequency as it tends towards the diffracted light line whereas a TE mode remains at a

constant frequency as the wavevector increases. This is because the in-plane electric field remains constant for TE radiation as θ increases, but reduces for TM. The normal incidence transmission spectrum for the CCA is presented in Fig. 6.9. Along with the experimental data, the simulated spectra for a variety of second square hole side lengths, L_2, are shown. Good agreement is observed between model and experiment. The width of the resonant feature can be controlled by varying L_2. As L_2 tends towards zero (and the CCA tends towards the CA) the feature broadens and the resonant frequency increases. For small L_2 the feature is so broad that it is terminated by the diffraction edge at a reduced frequency of 1. This transmission response is typical of the CA structure[111]. As L_2 tends towards L_1, the feature sharpens and eventually disappears as the periodicity of the structure reduces to $a/\sqrt{2}$. This feature is sharp due to the lack of radiative losses associated with this resonance, which corresponds to the fields within the larger and smaller hole elements oscillating out of phase with each other. This is in contrast to the CA in which fields within all elements oscillate in phase. The sharp transmission feature of the experimentally studied CCA structure, which exhibits no losses, may make it a useful notch filter for microwave communications applications, and demonstrates how two-dimensional arrays with a near-identical two-element basis can provide sharp features in reflection and transmission for any region of the electromagnetic spectrum.

6.5 Conclusion

In conclusion, the inclusion of a second square hole into the unit cell of a thin, metallic checkerboard array has been shown, both in simulation and experiment, to enhance the isotropy of surface mode propagation compared to the ordinary checkerboard. This is due to the narrowing and widening of band gaps formed at the X and M points in reciprocal space respectively, which has been explained by studying the field configurations of the standing wave solutions on the band edges. In the radiative regime, the compound checkerboard array exhibits a very sharp, high quality factor, Fano resonance in transmission, with very little loss. The width of this resonance is shown to be controlled by the ratio of the two square hole sizes.

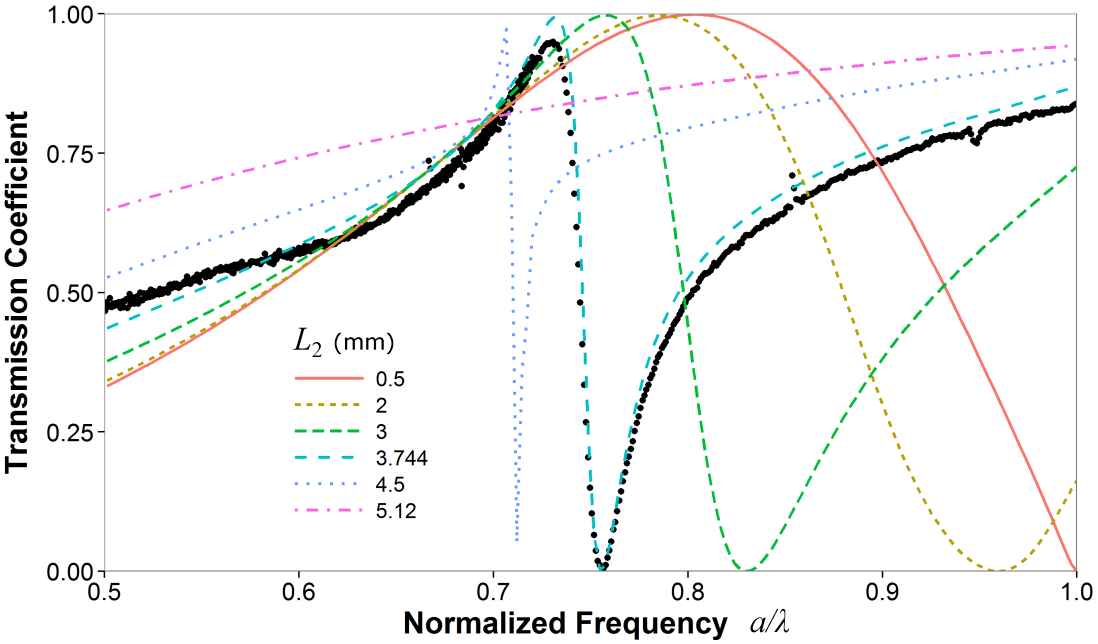

Figure 6.9: Normal incidence transmission coefficient (logarithmic scale) as a function of frequency for the CCA structure. Experimental data is shown as a black line for L_2 =3.744 mm. Simulated transmission spectra are shown for a variety of square hole sizes, L_2. The data is terminated at the onset of diffracted orders at a normalised frequency of 1.

Chapter 7

Non-Periodic Checkerboard Arrays

In this chapter the effect of disorder on the transmission through the metallic checkerboard array studied in Chapter 4 is explored. First, disorder is introduced by a rotational perturbation to each element comprising the array, causing changes to the connectivity between neighbouring elements. Secondly, a non-periodic yet deterministic Fibonacci checkerboard geometry is studied.

7.1 Rotational Disorder

7.1.1 Background

The previous chapter introduced the electrically connected checkerboard array (shown in Fig. 7.1c), consisting of a 2D square array (periodicity a) of perfect electric conducting (PEC) patches of side length L, each rotated by 45°. Surface waves were shown to propagate on this 2D photonic crystal, whilst it also showed a broad resonant feature in its normal incidence transmission spectrum[111].

The perfect checkerboard (Fig. 7.1b) is a non-physical geometry where the corners of the squares meet at a point ($L = a/\sqrt{2}$). Two neighbouring patches are neither electrically connected nor disconnected and the system is at the percolation threshold. According to Babinets principle[112], the transmitted intensity, T, through any non-diffracting patterned perfect electric conductor (PEC) sheet with no loss mechanism, is equal to the reflected intensity, $R_c = 1 - T_c$, from its complementary structure (PEC areas and voids exchanged). For the self-complementary perfect checkerboard, $T = T_c$ (transmission through both the original and complimentary structure is the same), and therefore the transmitted and reflected intensity must both be equal to 1/2 for all

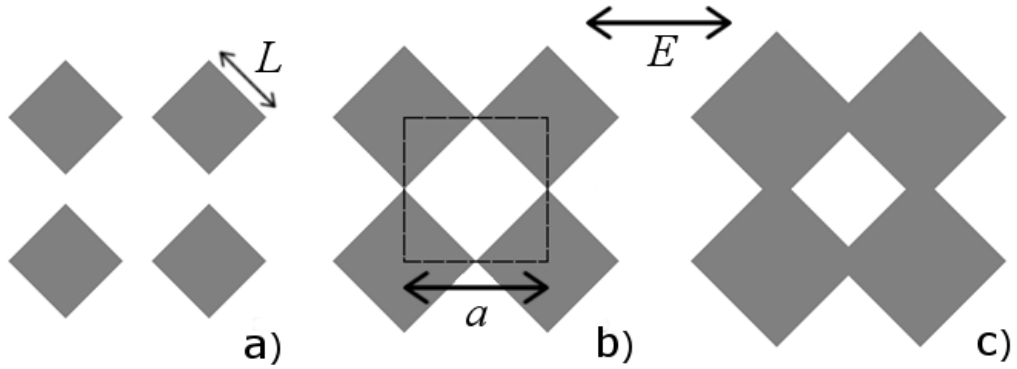

Figure 7.1: Illustration of square metallic patches of side length L rotated at 45° to a square lattice of pitch $a = 5.95$ mm. Orientation of the incident electric field vector E is also illustrated. a) disconnected patches, where metallic occupancy X = 40% b) threshold connection, X = 50% c) connected patches, X = 60%

frequencies below the onset of diffraction, resulting in an ideal beamsplitter[113][114]. Due to this fundamental concept, the checkerboard array has received much attention. Transmission features associated with connected and disconnected checkerboard arrays have been studied experimentally in the microwave[111], terahertz[115], and optical[116] regimes. Frequency-independent transmission has been observed in disordered systems where the square size is varied[115], and by using resistive sheets to join the metallic elements[117][118]. In addition, a checkerboard transmission line has been used to study surface modes[119] and layers of checkerboard arrays have resulted in a zero-index metamaterial[120].

Strong resonant microwave transmission (reflection), similar to enhanced optical transmission (EOT), has been observed through periodic checkerboard square hole (patch) arrays both above and below the percolation threshold[111]. This is attributed to bound surface waves (or so-called 'spoof' surface plasmons) on both sides of the structure acting as a coupling mechanism to free-space radiation, as in Ebbesen et al.[85]. In hole arrays (i.e. connected structures) electric current can pass throughout the entire structure, and coupled transverse magnetic (TM) surface waves are supported[111]. Patch arrays (disconnected) support transverse electric (TE) surface waves, with neighbouring patches interacting via displacement currents. In both cases, these surface waves can reradiate into free space (see Sec. 2.4.1). This radiation can combine constructively (or destructively) with non-resonant transmission through the holes resulting in enhanced (or reduced) transmission.

The behaviour of arrays of metallic elements close to the connectivity threshold, defined here as the critical occupancy at which metallic elements begin to overlap,

is of particular importance to this study due to the fundamental difference between the nature of the bound surface waves supported by electrically connected and disconnected structures. Many authors have studied connectivity threshold of a variety of metamaterials by applying disorder to the arrangement of the elements comprising the array. For example, Edmunds et al. explored the transmission of randomly distributed circular elements over a series of filling fractions[121]. The disruption of the array's periodicity disrupted the resonant transmission, and the arrays showed a rather featureless behaviour, reminiscent of short pitch metallic mesh filters. The region between the periodic and the fully random has been explored by Nishijima et al.[122] who illustrated the effect on plasmonic resonances of a gradual increase in the spatial disorder of gold nano-disks, and reported a broadening and lowering of the transmission extinction peak. In contrast, it has been shown that strong transmission is maintained through a random array of strongly asymmetric rectangular holes[123][124] and that positional disorder of a 2D array of metal-dielectric-metal stack nanoparticles has little effect on the magnetic dipole resonance[125]. Similarly, the effect of random distribution on an array of split ring resonators was shown to depend on whether the elements interact coherently or incoherently[126]. Rockstuhl et al. studied random arrays of circular apertures and concluded that enhanced transmission due to the resonance of a single hole acting as a waveguide was not suppressed by the presence of disorder provided a minimum hole separation was enforced such that the elements do not overlap[127]. Enhanced transmission has also been reported in quasiperiodic arrays of elements. This is because whilst the reciprocal space structure does not contain discrete points (like that of a periodic structure) it does have well-defined peaks in its Fourier spectrum[127][128].

In this study a similar approach is taken to Takano et al.[115] by randomly perturbing the perfect checkerboard geometry. However in this case the square size is fixed and a Gaussian random rotation is applied to each element. This allows connections between the metallic squares to be broken (or made) whilst keeping the lattice spacing constant. As the system retains this underlying periodicity, diffractive effects such as the excitation of surface waves and the onset of diffracted orders above frequency $f = c/a$ are expected to remain. Disorder in element rotation of the checkerboard patch and hole arrays is shown to affect the enhanced transmission resonance below this onset of diffraction. The initial structure is the checkerboard array studied in Chapter 6; a square array of square metallic patches of side length L rotated by 45° with respect to the square lattice vectors, as shown in Fig. 7.1. Varying the side length of the squares changes the metal occupancy (X) of the array and allows transmission both below and above the connectivity threshold ($X = 50\%$) to be studied. As mentioned previously, for samples of metal occupancy $X\%$ the transmission T_X of their inverse (or complementary) structures of metal occupancy $(100 - X)\%$ is $1 - T_X$, assuming

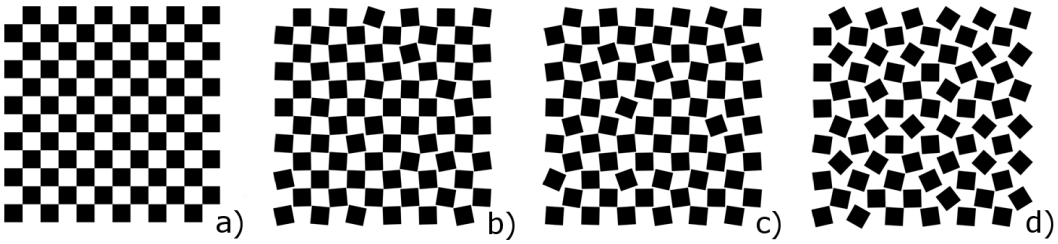

Figure 7.2: 50% metal occupancy arrays with increasing rotational disorder in square orientation defined by an increase in the standard deviation (σ) of a Gaussian distributed rotation: a) $\sigma = 0°$ b) $\sigma = 6°$ c) $\sigma = 10°$ d) uniform distribution corresponding to $\sigma = 26.5°$

that the only loss channels are specular reflection or transmission. This accords with the description of Babinet's principle[112]. Disorder in the orientation of the patches is introduced by increasing the standard deviation about a mean rotation μ of 0° of a Gaussian rotation distribution

$$f_x = \frac{1}{\sigma\sqrt{2\pi}}\exp(\frac{-(x-\mu)^2}{2\sigma^2}) \tag{7.1}$$

as demonstrated in Fig. 7.2. The standard deviation, σ, has an upper limit of approximately 26.5° due to the fact that the rotation angle is a cyclic quantity. In addition, we also study an array with a uniform distribution which has the same standard deviation as this upper limit (26.5°).

Samples are fabricated using the print and etch technique outlined in Section 3.2.2. A first set of samples consists of 300 nm thick patterned aluminium on a 50 μm thick polyester substrate. The lattice spacing a = 6 mm and the overall sample size is 200 × 300 mm. Although the thickness of the aluminium layer is less than the skin depth ($\approx$ 1 μm) in the frequency range studied, it is largely opaque to microwaves due to the large impedance mismatch caused by its Drude-like dielectric function (Sec. 2.3.1). However, on resonance some electromagnetic loss to Joule heating is expected, particularly as in the thin aluminium layer there is significantly enhanced probability of collisions between free electrons and the two surfaces of the metal. Patch arrays were created with metal occupancies X = 40%, 51% (just above the connectivity threshold) and 60%, and 8 different standard deviations, σ (24 samples in total). In this chapter we refer to each patch array by its original occupancy and the standard deviation of the patches, however note that this occupancy will change as patches begin to overlap. 24 complementary hole arrays were created by simply inverting the exposure mask thus switching the areas of metal and voids on the sample. For these complementary structures the occupancy refers to that of the voids, not the metal. Hence, without disorder ($\sigma = 0°$), a 40% patch array is identical to a 60% hole array. A second set of

patch samples with metal occupancy X = 51% and standard deviations $\sigma = 0°$, 4°, 18° were produced using a much thicker laminate of 18 μm copper. This change is made in order to minimize absorption loss and it is the greater thickness, not the change of metal, that achieves this. By obtaining transmission and reflection measurements from these samples, the scatter loss can be better established.

7.1.2 Transmission Measurements

Normal incidence transmission measurements for the thinner aluminium samples, taken in the frequency range $26.5 \leq f \leq 60$ GHz, are shown in Fig. 7.3. The measurements are obtained using the collimated beam transmission setup as described in Section 3.4.1. Radiation is emitted and collected by standard gain horn antennas fed by coaxial cables connected to a Vector Network Analyser (Sec 3.3).

When $\sigma = 0°$ (solid black lines) all arrays exhibit a broad resonance just below the 50 GHz onset of diffraction, manifesting as a transmission minimum for electrically disconnected arrays and a maximum for connected ones. This behaviour is much the same as the Fano-type resonant transmission observed in similar studies[16][17][18]. These features are due to diffractive coupling between the bound surface mode resonance of each patch/hole array and the incident radiation. For disconnected arrays near field interactions between isolated patches are supported by displacement currents and the surface supports a TE polarised surface mode. Similarly, for connected arrays a TM mode exists, however in this case fields are linked via propagating currents[111] (Sec.2.5). Interference between the resonant and non-resonant (straight through) transmission channels leads to the characteristic Fano-type response. A diffraction edge is present at 50 GHz, corresponding to the 6 mm periodicity, above which some power is lost to the first diffracted order. We restrict our discussion to lower frequencies in the non-diffractive regime. The results show that these structures do not obey Babinet's principle, with the transmission of each patch and hole pair (left and right columns respectively) summing to approximately 80%. This violation is due to Joule losses within the metal as mentioned earlier. Another loss channel: scatter loss, can be assumed to be zero below the onset of diffraction at 50 GHz for this periodic structure, but will be a significant for disordered arrays. Despite the absorption loss, the patch and hole array pairs clearly show the inverse behaviour expected. We therefore restrict our discussion to the patch array results, with the complementary hole array results being inferred from Babinet's theory.

The effect of element rotation without change in the array connectivity is illustrated by the 40% occupancy arrays in Fig. 7.3a-b. Below the connectivity threshold (X = 50%) no amount of disorder can change the array connectivity. The transmission

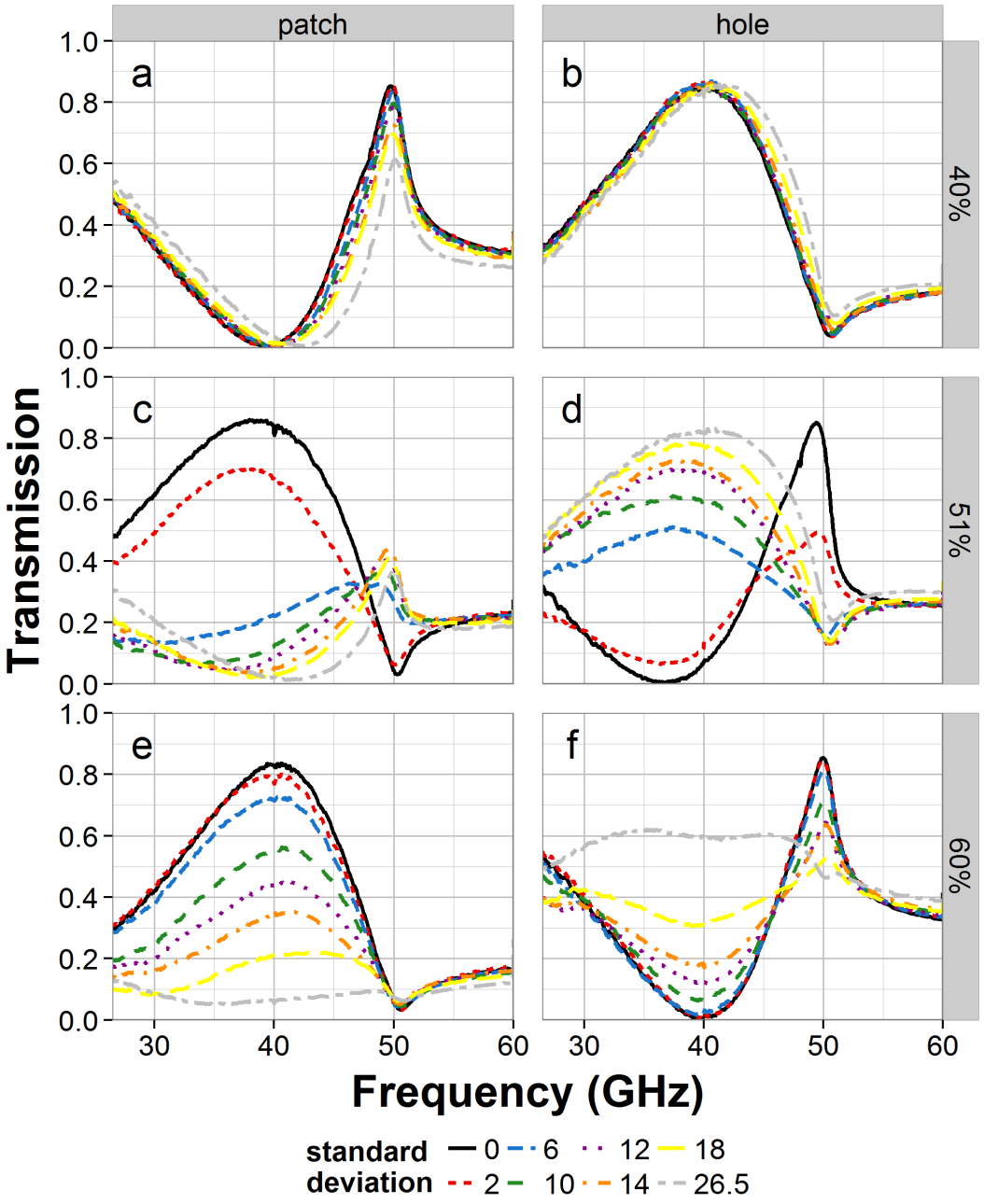

Figure 7.3: Normal incidence microwave transmission of an aluminium square checkerboard array of periodicity $a = 5.95$ mm, with increasing standard deviation, σ, in square orientation. i.e. $\sigma = 0$ corresponds to an ordered checkerboard array, with every square rotated by 45° with respect to the square lattice. a) 40% patch array b) 40% hole array c) 51% patch array d) 51% hole array e) 60% patch array f) 60% hole array. Data obtained with Chris Durrant (PhD student, Exeter).

spectra vary little with increasing disorder, highlighting that element rotation alone has little effect when it does not make or break connections between elements. These arrays show a small increase in resonant frequency with increasing σ which is attributed to a decrease in the electromagnetic coupling between neighbouring elements as the distance between them decreases on average across the array.

The most interesting behaviour is observed just above the connectivity threshold in the 51% occupancy arrays. In this region the connectivity of the arrays is at its most sensitive to rotation. Fig. 7.3c-d demonstrates strong transmission dependence on rotational disorder. For $0 \leq \sigma \leq 2^\circ$ the majority of patches remain connected and so the strong resonant transmission associated with connected arrays is observed. Above this level of disorder the transmission inverts (i.e. switches from a resonant maximum to a minimum) suggesting a critical change in the connectivity of the array. In order to clarify this, Fig. 7.4 shows the percentage of square elements that are connected to at least one neighbour as a function of standard deviation. This plot was produced by analyzing fifty 20×20 arrays each with a different standard deviation. For X = 51%, between $\sigma = 2^\circ$ and $\sigma = 6^\circ$, Fig. 7.4 shows that the array abruptly changes from a connected to a primarily disconnected array. This change in connectivity inverts the transmission shape as the large clusters of connected metal patches have become disconnected and so propagating currents no longer support transverse magnetic surface modes. Regions of metal patches are now linked by displacement currents, supporting a transverse electric mode and the overall transmission behaviour is that of a disconnected array. (For the 51% hole arrays which are initially disconnected, Fig. 7.3d, the opposite of this argument is then true as metallic regions surrounding the holes begin to connect with the introduction of disorder.) The rate of decrease of the peak transmission value with standard deviation qualitatively corresponds to the gradient of the red points within Fig. 7.4. The large change in peak intensity between $\sigma = 2^\circ$ and $\sigma = 6^\circ$ in Fig. 7.3c coincides with a large number of squares becoming isolated from their neighbours, as shown by the steep gradient in Fig. 7.4. The large difference in connectivity between these two arrays is demonstrated more clearly in Fig. 7.5. Connections between squares are shown by lines connecting the lattice points of the array with isolated squares shown as dots.

The amplitude of the resonant feature is strongly dependent on the connectivity of the structure. Before applying rotations ($\sigma = 0^\circ$), Fig. 7.3c. shows a large peak due to the excited TM surface mode. This mode will propagate many wavelengths (losing some energy to absorption) before reradiating into the specular transmission beam where it interferes with radiation that passes straight through the structure and produces a transmission peak (high-pass filter). When the square patches are rotated such that almost all the squares are isolated from one another ($\sigma = 18^\circ$), a TE mode is supported

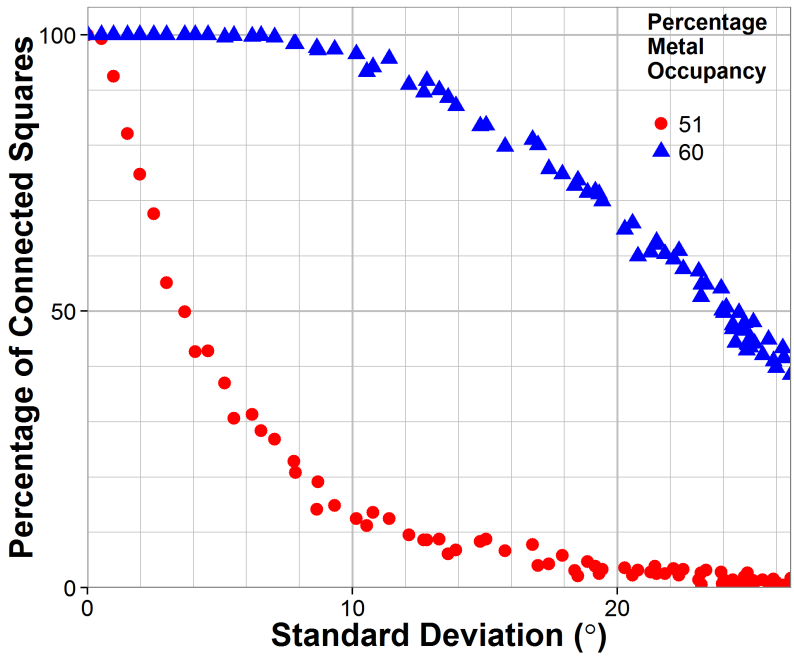

Figure 7.4: Percentage of patches that are connected to at least one neighbouring square as a function of standard deviation of the rotation for both 51% and 60% patch arrays, based on a 20 × 20 array. There is a limiting standard deviation of approximately 26.5°, which corresponds to the standard deviation of the uniformly distributed sample.

leading to a minimum in transmission (i.e. it is now a low-pass filter). In between these two situations (between $\sigma = 2°$ and $\sigma = 6°$), there exists a mix of connected and disconnected regions that leads to a feature with small amplitude. To understand this it is necessary to look at the reflected signal, as well as the transmission, which is discussed in the next section. The blue shift of the transmission feature arises from the fact that the longer length chains of connected squares are broken more readily by disorder than the shorter ones; hence the higher frequency connected response survives better with increasing disorder.

The 60% array is similar in that its connectivity is affected by increasing rotational disorder. However, the larger element size means low levels of disorder have a smaller effect on the transmission. The patch array shown in Fig. 7.3e shows a gradual decrease in resonant transmission as the standard deviation is increased. At $\sigma = 26.5°$, the resonance is almost completely suppressed to give a relatively uniform, approx. 5-10%, transmission for all frequencies studied. Again, the rate of decrease in transmitted intensity correlates qualitatively with the gradient of Fig. 7.4 (blue points). The percentage of connected squares decreases approximately linearly above

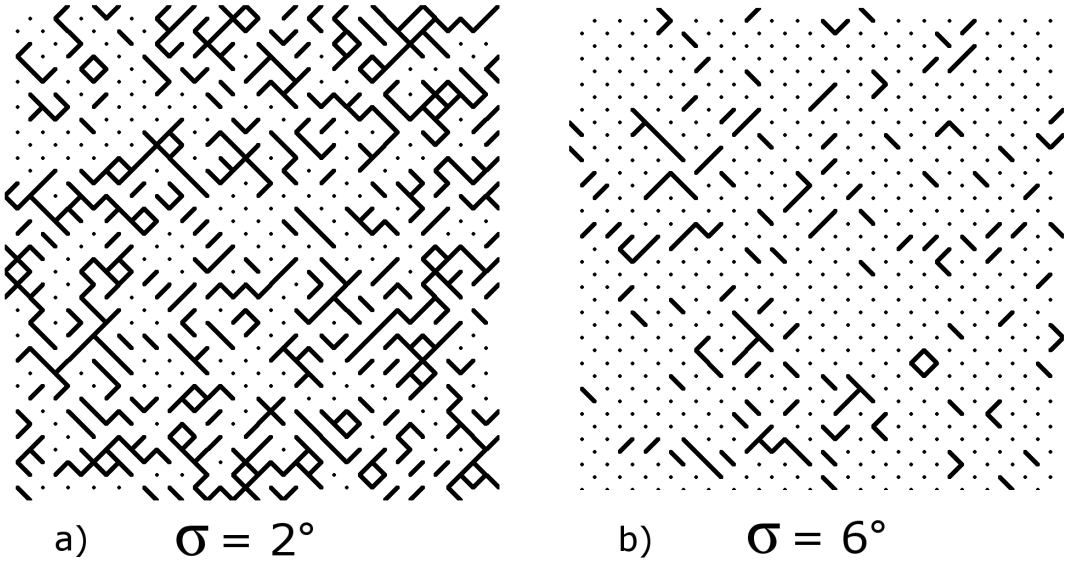

Figure 7.5: Schematics representing the difference in connectivity of the 51% patch arrays with a standard deviation of a) 2° and b) 6°. Rather than the squares themselves, connections between them are depicted as lines between the lattice points. Disconnected squares are shown as dots. At 2° disorder ≈ 30% of squares are isolated, whereas at 6°, ≈ 70% are isolated.

a standard deviation of 8°, as does the peak intensity in Fig. 7.3e. Only at $\sigma = 26.5°$ does the transmission show an inversion of the resonant feature, which corresponds to approximately half of the squares being disconnected (Fig. 7.4). The result shows a tuneable transmission peak at 40 GHz which varies from 80% to 5% depending on the chosen standard deviation (Fig. 7.3e). The uniform distribution of square rotation ($\sigma = 26.5°$), produces a flattened band of transmission between 30 and 47.5 GHz across which the transmission varies by less than 5%. For the patch array, (grey dash-dotted line in Fig. 7.3e) the transmission intensity is small at 5 - 10%. For the complimentary hole array (grey dash-dotted line in Fig. 7.3f), the transmission is approximately 60%. This sample acts as a broadband beamsplitter or attenuator for microwave radiation and may have an application in long wavelength communications.

7.1.3 Scatter Measurements

A qualitative measure of the amount of power lost to scatter from the 51% occupancy patch arrays is obtained by adding the reflection and transmission coefficients of the thicker copper samples. Three different standard deviations are used, $\sigma = 0°, 4°, 18°$. The specular reflection and transmission coefficients are related to the scatter loss and absorption loss by $R + T = 1 - (S + A)$. Hence, a change in the sum of reflection and

transmission requires a change in either power lost to scatter (not detected in the specular transmission or reflection beam) or power lost to Joule heating in the structure. As mentioned before, thicker copper samples are used at this stage to minimise absorption within the metal, which was significant for the aluminium samples. On resonance, some absorption also occurs in the dielectric substrate and the total absorption can be approximated by recording the reflection and transmission coefficients of a periodic array (which exhibits no scatter loss, $S = 0$), and comparing their sum to a lossless simulation (for which $R + T = 1$ at 40 GHz). Fig. 7.6a shows that, for the $\sigma = 0°$ structure, the absorption on resonance (40 GHz) is less than 4%. This is assumed to be the maximum possible absorption for this set of samples and we therefore use the addition of the transmission and reflection coefficients as a qualitative measure of scatter loss $(1 - S)$. Experimental constraints mean that reflection measurements exactly at normal incidence are not possible (see Sec.3.4.2) and so we approximate with results at 2° to the surface normal. Whilst this small angle change will affect the shape and position of the resonant feature in reflection, the difference is negligible.

Fig. 7.6b-c shows the reflection and transmission coefficients, as well as their sum, for square patches with 51% occupancy and standard deviations of $\sigma = 4°$ and 18° respectively. The connections diagrams for these are shown in Fig. 7.7, which demonstrates that approximately half of the elements of the $\sigma = 4°$ distribution are disconnected, whilst the $\sigma = 18°$ distribution is largely disconnected, except for a small amount (<3%) of 2-element chains. For these results new samples were made using the same method but with thicker metal (18 μm copper) and larger panel size (400 × 280 mm). These changes result in much less electromagnetic loss due to absorption in the metal and scatter from the sample edges respectively. In order to verify that the incident beam is sampling a sufficiently large area of the sample to provide reproducible results, 6 different regions with $\sigma = 4°$ have been fabricated and tested. The transmitted intensity shown in Fig. 7.6b (blue squares) is an average of these 6 measurements and their standard deviation is represented by the grey region. The standard deviation in the transmitted intensity is always less than 4%, sufficiently small that our qualitative analysis is valid. As the transmission through the $\sigma = 4°$ sample is most sensitive to disorder, verifying the validity of this result is sufficient to validate the entire data set. Therefore the other results shown are based on just a single sample.

Fig. 7.6b shows that when there is a mix of disconnected and connected patches this total loss is greater than 40% of the incident power on average across the frequency range studied. This is significantly larger than the loss of 5% for $\sigma = 0°$ and 20% for $\sigma = 18°$ (Fig. 7.6a & c). This shows that, rather than propagating along the surface and reradiating into the specular reflection and transmission beams, the power coupled into the surface modes is scattered as it is unable to pass from a connected region to a

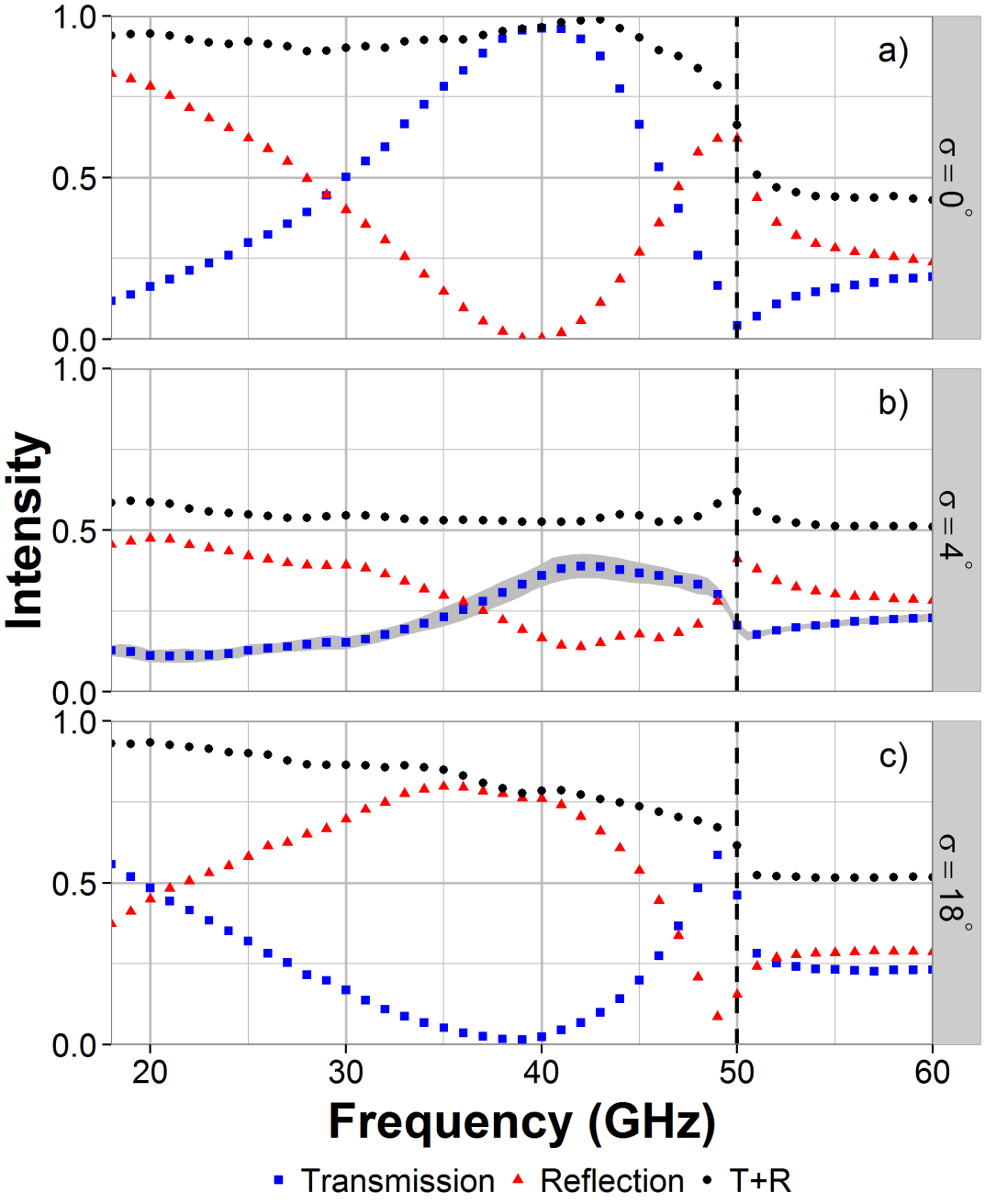

Figure 7.6: Reflected intensity (red triangles), transmitted intensity (blue squares) and their sum (black circles) for 51% occupancy copper patch arrays with standard deviations of a) 0° b) 4° and c) 18°. The transmission in b) is an average of 6 measurements with the standard deviation represented by the grey region.

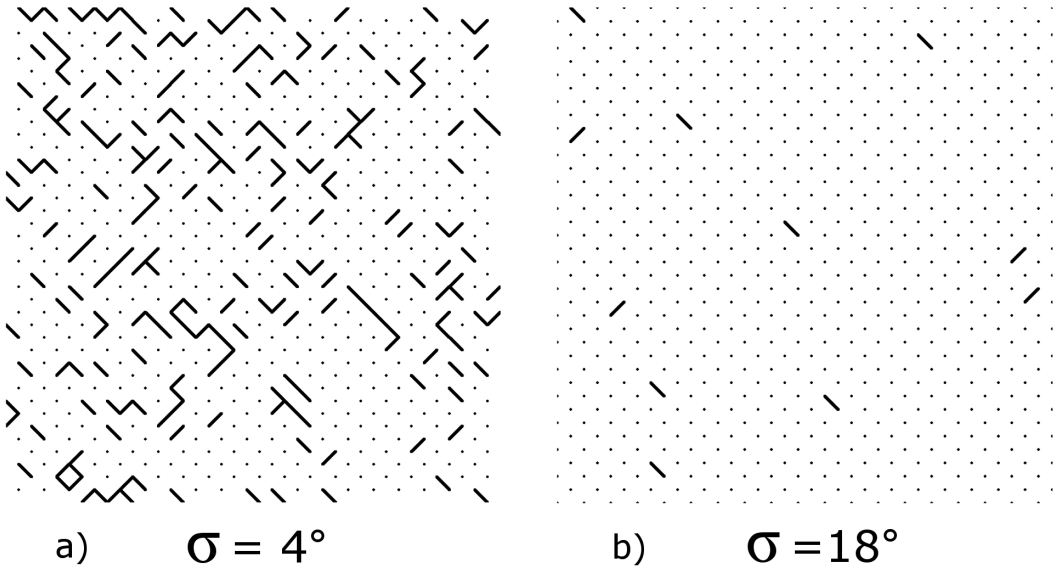

Figure 7.7: Schematics representing the difference in connectivity of the 51% patch arrays with a standard deviation of a) 4° and b) 18°. Connections between patches are depicted as lines between the lattice points. Disconnected squares are shown as dots.

disconnected one (or vice-versa) due to the mismatch in eigenmode polarization. The decrease in $R + T$ with increasing frequency for $\sigma = 18°$ is attributed to the fact that there are still some small length chains of connected patches causing increased scatter at higher frequencies.

7.2 Fibonacci Checkerboard

In this section, the connected checkerboard array is again modified, this time by replacing the periodic lattice with a non-periodic yet deterministic Fibonacci lattice. This 'quasiperiodic' structure consists of two periods (a_1 and a_2) but contains no repeating unit cell. The propagation of tightly bound surface waves (which rely upon structuring at microwave frequencies) on such a lattice is studied experimentally in this section.

7.2.1 Background

In the previous section the propagation of surface waves on the 2D checkerboard array was shown to be heavily reliant on the electrical connectivity of the elements. It is therefore important to maintain the arrays connectivity when studying the introduction of quasiperiodicity.

A bi-periodic system is chosen with periods $a_1 = 4.8$ mm and $a_2 = 6$ mm. Placing

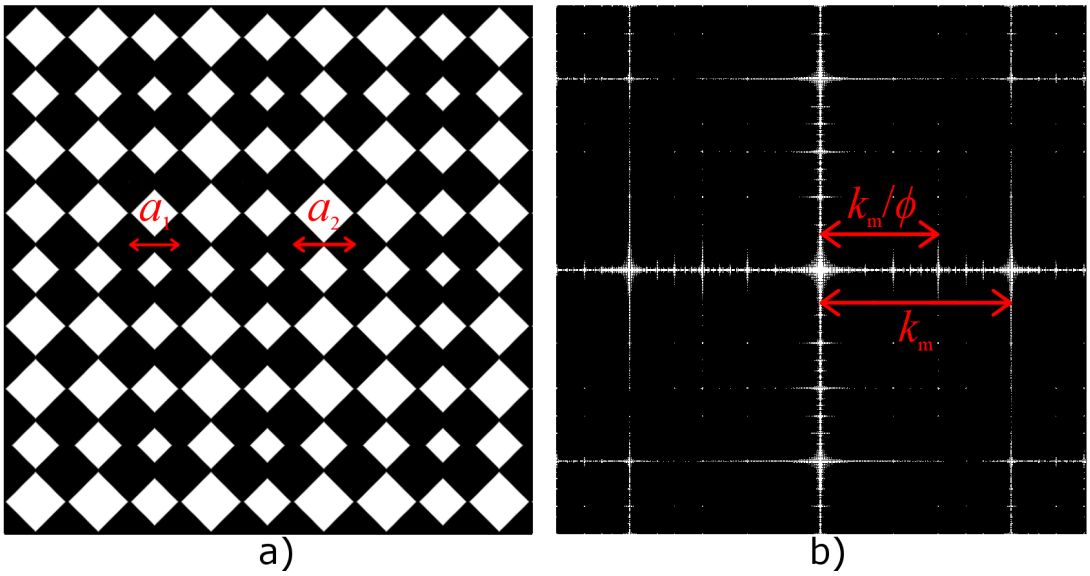

Figure 7.8: a) A section of the Fibonacci checkerboard array (black corresponds to metallic regions) comprising two periods a_1 and a_2. b) A fast fourier transform of a larger sample image.

metallic patches of side length $L = 4.5$ mm in the lattice ensures that they all remain electrically connected regardless of the lattice distribution. The binary sequence given by the 'Golden string' is chosen in order to distribute the elements in a deterministic, yet non-periodic manner. This string is obtained by applying the following recursive rules[129]:

$$A \rightarrow AB$$
$$B \rightarrow A$$

to the initial sequence, A. Hence, the first 5 iterations are

$$AB$$
$$ABA$$
$$ABAAB$$
$$ABAABABA$$
$$ABAABABAABAAB$$

The ratio of As to Bs follows the Fibonacci sequence and the ratio as the iteration

number $n \to \infty$ is equal to the golden ratio, ϕ given by

$$\phi = \frac{1+\sqrt{5}}{2} = 1.61803.... \tag{7.2}$$

The binary 'Golden string' represents the distribution of elements in both the x and y directions, with A corresponding to a patch separation of a_1 and B corresponding to a_2. A section of the resulting 'Fibonacci Checkerboard' array (FCA) is shown in Fig. 7.8a. The sample that is studied experimentally is 40 $\times$ 60 elements in size, and is produced using the print and etch technique described in Section 3.2.2. The metallic layer has a thickness of 18 μm and is supported on a substrate of Mylar with thickness 25 μm. A Fast Fourier transform (FFT) of a much larger sample region than that shown in (a) is shown in Fig. 7.8b, which is produced using the image processing software ImageJ. The FFT indicates the relative strength of wavevector components in the sample image. This corresponds to wavevectors from which scattered modes should appear in the dispersion diagram of modes supported by the surface, with the strength of scattering proportional to the amplitude of the FFT.

Quasiperiodic arrays obeying the Fibonacci recursive rules have been studied in great detail in the context of one-dimensional photonic crystals (PCs). These often comprise layers of two different materials (either dielectrics with different refractive index[130], or a metal/dielectric pair[131]) which are stacked according to the Fibonacci sequence above. The result is the formation of band gaps for radiation propagating perpendicular to the layers[132][133][134] often referred to as $< n >= 0$ gaps due to the fact that there is no propagating radiation[135][136]. It has been shown that localised states can exist within these band gaps[137][138]. Similar phenomena have been demonstrated for surface plasmon polaritons on a quasiperiodic grating[139] and for phononic crystals[140]. 1D quasiperiodic PCs can exhibit omnidirectional reflection maxima[141], perfect transmission when the sequence used is symmetric[142], and topological edge modes[143].

Two-dimensional quasicrystals have also been studied[144], particularly in the context of nanoparticle arrays[145][146]. A two dimensional golden-ratio spiral hole array has been shown to support localised modes[147] and a high impedance surface comprising a quasiperiodic array has demonstrated enhanced directivity when utilised as an antenna reflector[148]. Existing studies of Fibonacci-based quasiperiodic arrays have focussed largely on radiative modes suuported, which lead to features in the transmitted and reflected spectra. In this section, non-radiative modes supported by the Fibonacci checkerboard array are measured directly using the near field scanning technique outlined in Sec. 3.5.

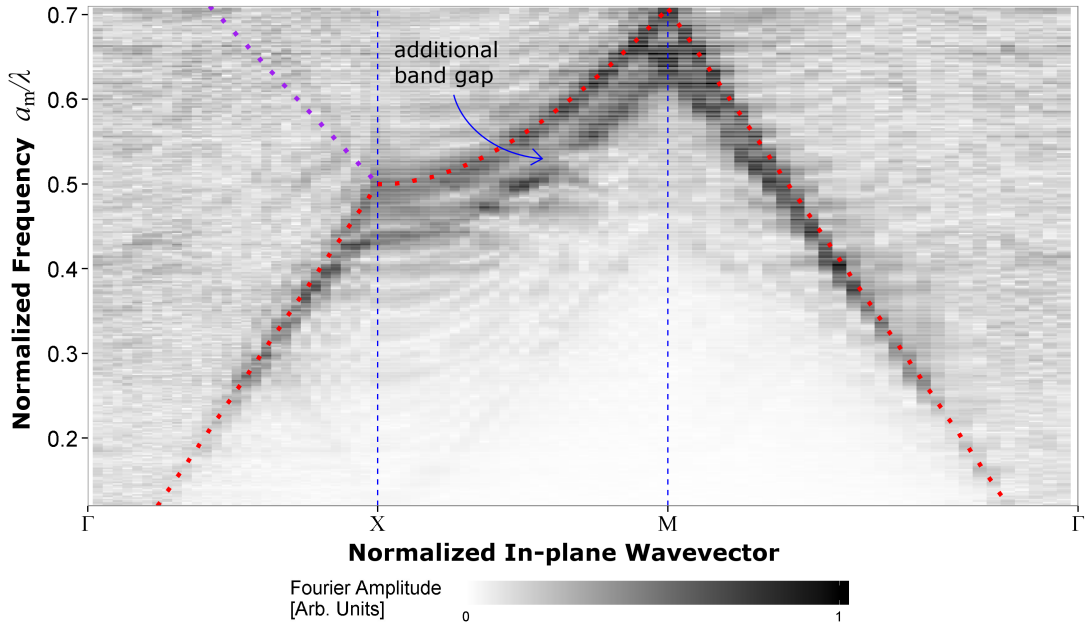

Figure 7.9: The dispersion of modes supported by the 'Fibonacci Checkerboard' array, represented along the irreducible Brillouin zone in reciprocal space.

7.2.2 Surface Modes

Near field antennas are used to excite and detect surface waves and a square region of the surface is scanned (with the probe positioned $\approx$ 1 mm away) and the source positioned in one corner of the sample. The spatial Fourier transform of the single frequency electric field maps give the isofrequency contours in reciprocal space, and the frequency variation of these provides the full dispersion diagram. Fig. 7.9 shows this dispersion along the irreducible Brillouin zone planes, given by the point of symmetry in k-space, Γ, X and M. For this non-periodic system, those points are dictated by a mean periodicity of the structure given by

$$a_{\mathrm{m}} = \frac{(1+\sqrt{5})a_1 + 2a_2}{1+\sqrt{5}+2} \approx 5.26\mathrm{mm} \tag{7.3}$$

which is derived from the fact that the ratio of patches separated by a_1 to those separated by a_2 approaches the Golden ratio (ϕ, equation 7.2) as the sample size tends to infinity. This mean periodicity defines an effective Brillouin zone and the dominant in-plane scattering is by $k_{\mathrm{m}} = 2\pi/a_{\mathrm{m}}$ in the x and y directions. These scattering points in reciprocal space correspond to points of large amplitude in the Fourier transform of the sample image in Fig. 7.8b, in which the magnitude of k_{m} is shown. The experimen-

tally obtained dispersion curve is shown in Fig. 7.9. The surface mode disperses much like that of the regular checkerboard array discussed in the previous chapter, however the band structure is interrupted by additional weakly-scattered radiation, causing additional band gaps to appear in the dispersion curve. This is because, as can be seen in Fig. 7.8b, there are additional scattering planes of the quasi-periodic structure from which the scattering amplitude is weaker, such as that from $k = k_{\mathrm{m}}/\phi$. This can be seen more clearly in the isofrequency contours.

Fig. 7.10 shows the isofrequency contours at various positions in the dispersion. At a normalised frequency of 0.10 (Fig. 7.10a), where all modes exist close to the light circle and propagate as surface currents. Scattering centres corresponding to the mean periodicity a_{m} appear at wavevectors of $k_{\mathrm{m}} = 2N\pi/a_{\mathrm{m}}$, where N is an integer, similar to the regular checkerboard studied in Chapter 6. Light circles centred at these wavevectors are shown as red dashed lines and are referred to as modes scattered from k_{m}. For each of these there are additional light circles, scattered by $k = k_{\mathrm{m}}/\phi = k_{\phi}$ due to the quasi-periodicity. These are highlighted (purple lines) in Fig. 7.10a, with only a subset shown in b-d for clarity. Additional weak scattering from other points in k space occurs due to the spectrum of k values with a smaller Fourier amplitude in Fig. 7.8b. However these are sufficiently weak that only scattering by k_{m} and k_{ϕ} is considered. At a_{m}/λ =0.3 (Fig 7.10b), modes on the zeroth order light cone interact with those scattered from $(k_{\mathrm{x}}, k_{\mathrm{y}}) = (k_{\phi}, 0), (-k_{\phi}, 0), (0, k_{\phi}), (0, -k_{\phi})$. The k_{ϕ} scattered mode can be seen at low frequency across the dispersion curve in Fig. 7.9.

At a_{m}/λ =0.45 (Fig 7.10c)the interaction with the zeroth order modes and those from k_{m} causes a band gap to appear at the X point of the dispersion curve in Fig. 7.9. This is very similar to that seen for the regular and compound checkerboard arrays in the previous chapter. In Fig. 7.10d, interaction between the $(k_{\phi}, 0)$ and $(k_{\phi}, k_{\mathrm{m}})$ modes (magenta dotted lines) results in an additional band split in the X - M region of Fig. 7.9 (labelled in the figure). This band gap can be seen in the isofrequency contour at a_{m}/λ =0.52 (Fig 7.10d) and can be seen more prominently in the k_{y} direction due to a bias in the excitation of the modes and interference effects caused by imperfect orientation of the dipole antenna and the rectangular sample respectively. At higher frequencies the mode continues to disperse as expected for a connected checkerboard array, with a band gap forming at the M point and both the lower and upper band edge visible in Fig. 7.9.

7.3 Conclusion

In this chapter, results from the studies of two distinct non-periodic variations of the metallic checkerboard array presented in Chapter 4, have been reported. In the first

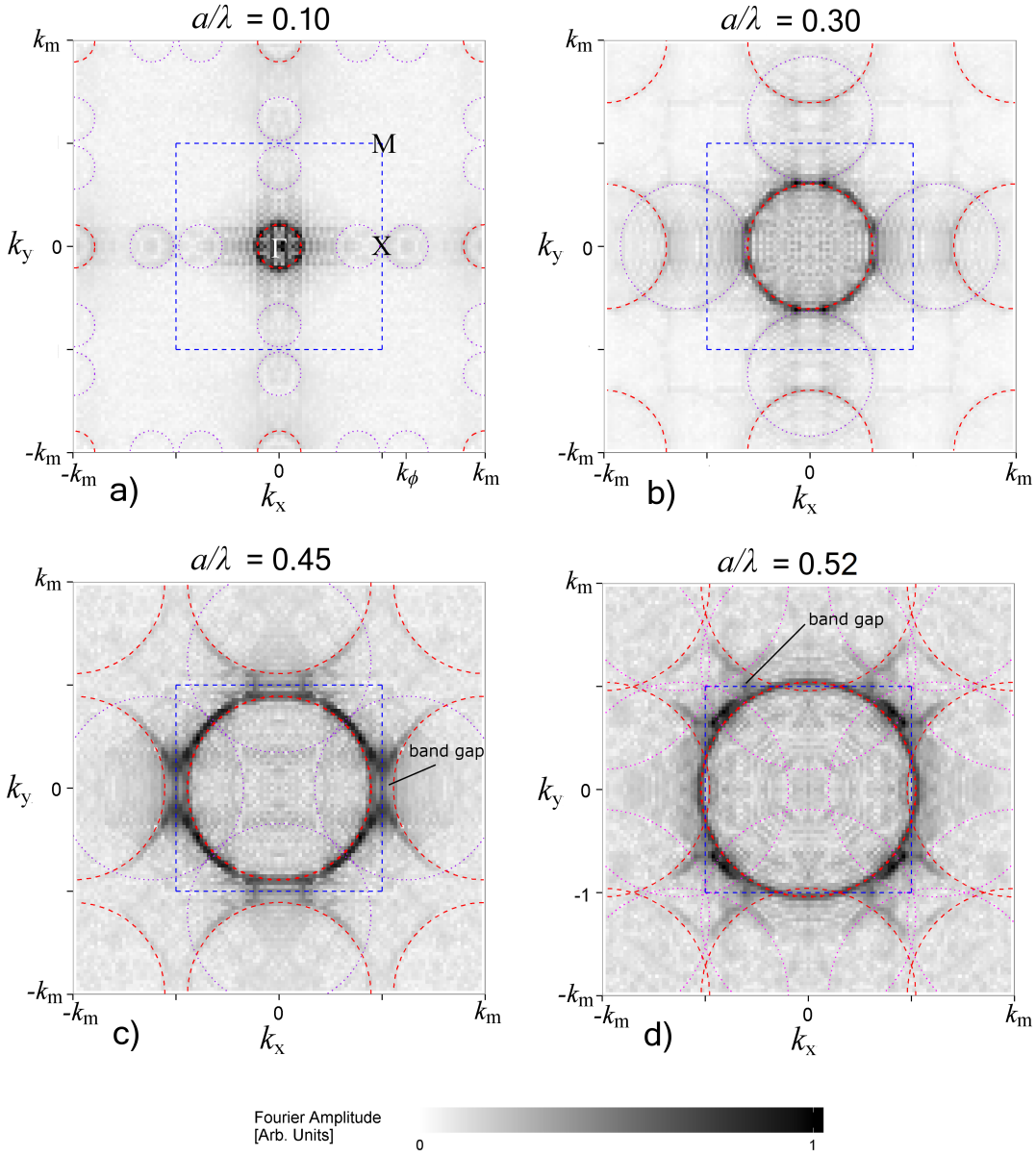

Figure 7.10: Isofrequency contours showing the Fourier transform of experimentally obtained electric field maps at various frequencies. Zeroth order and diffracted light circles associated with the average pitch, a_m, are shown as red dashed lines. Additional light circles due to the quasi-periodicity are shown in purple.

section, the effects of increasing rotational disorder on the microwave transmission response of a checkerboard square array of metallic patches and their complementary hole arrays has been presented for a range of metal occupancies significantly above and below, as well as close to, the 50% metal occupancy connectivity threshold.

It was found that disorder in the rotation of the patches had negligible effect on the

transmission if it did not change the connectivity between elements of the array. However for patches (or holes) just above 50% occupancy the increase in disorder changes the connectivity of the squares and substantially weakens the strength of the resonant transmission maximum (or minimum). This is because connected and disconnected regions of the structure support surface modes with different polarizations. If the sample is not predominantly connected or disconnected, the amplitude of re-radiation from surface modes is low. Measurement of the reflected intensity, combined with the transmission measurements, showed that the power must be instead scattered away from the specular beam. Further disorder results in an inversion of the transmission feature, now a minimum, as the array becomes predominantly disconnected. This is accompanied by a reduction in scatter loss despite the array containing more disorder in element rotation. The introduction of rotational disorder allows for control of the microwave frequency response over a wide spectral window, opening up fresh potential for Frequency Selective Surfaces. Of particular note is the ability to scatter 40% of the incident radiation away from the specular reflection and transmission beams over a 30 GHz frequency band. Secondly, by increasing the square size (an occupancy of 60%) and applying a uniform distribution to the rotation angle, a 17.5 GHz band of flat (5% variation) transmission intensity was achieved. The type of disorder chosen maintains some periodicity in the structure and hence the diffraction edge at 50 GHz is still visible even for large standard deviations in the rotation distribution.

In the second section of the chapter, the Fibonacci checkerboard was studied. The propagation of surface waves on a such a planar photonic quasi-crystal is dictated primarily by scattering from k_{m}, an average grating wavevector corresponding to the average periodicity of the structure. Additional scattering centres exist from which scattering is weaker. The positions of these are shown to correspond to maxima in the Fourier Transform of the sample image. This additional scattering introduces additional band splitting in the dispersion of surface waves. This work opens up the potential for tailored dispersion curves using quasi-crystal designs with the desired reciprocal space components.

Chapter 8

Edge Waves on Checkerboard Arrays

The previous chapters have focussed on surface waves supported on metallic checkerboard metasurfaces. Whilst finite element method modelling of these structures simulates an infinitely large sample, finite-sized experimental structures can support one-dimensional modes (edge waves) that are localised at the termination of the sample to free space. This chapter investigates the properties of these edge modes and compares them with modes of the surface. The coupling of two edge modes is investigated and mode conversion between surface and edge waves is proposed.

8.1 Background

An electrically connected metallic checkerboard array is known to support a bound transverse magnetic (TM) surface wave, which propagates in the plane of the sample with greater momentum than that available to planar incident radiation. Currents within the continuous metal sheet create charge separation either side of the square-shaped holes, which can resonantly excite the dipolar fields within the holes (See Sec. 2.5 and Chapter 6).

At the termination of the sample to free space, a corrugated 'zigzag' edge is formed (Fig. 8.1a), which can support a similar bound mode that decays in both the y and z directions, whilst propagating along the edge in x. In this chapter, this edge mode is experimentally observed and compared with the surface wave. This comparison leads to the proposal of mode conversion between the two waves.

Previous studies of modes supported on a narrow edge have focussed primarily on one-dimensional chains of connected metallic elements, such as an array of 'domino' protrusions from a thin metallic wire[149][150]. It was shown that changing the thick-

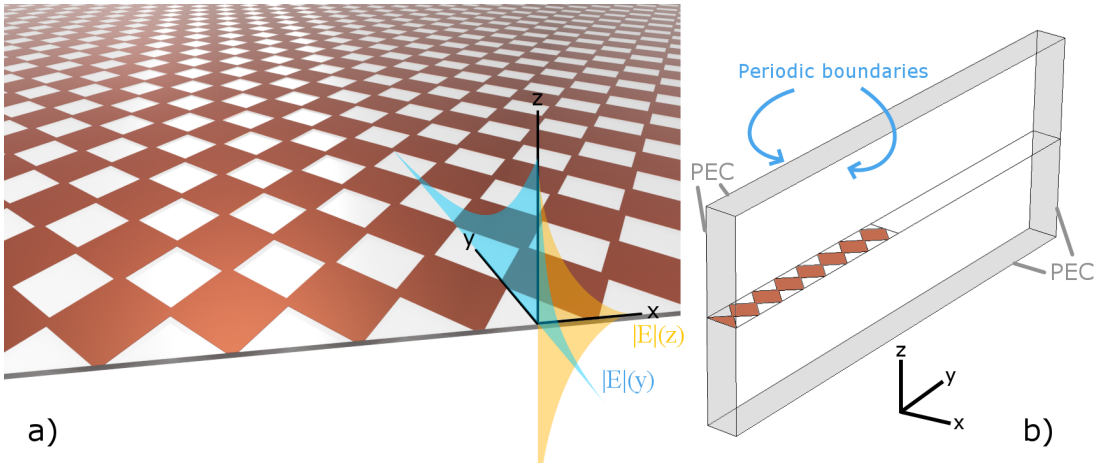

Figure 8.1: a) The edge of a metallic checkerboard array. The array supports a mode bound to its surface, as discussed in previous chapters, and also a mode on its edge. This edge mode decays into the y and z directions and only propagates in the x direction, along the edge. b) The unit cell used in eigenmode modelling with COMSOL. The boundaries are periodic in the x direction and PEC in the y and z directions.

ness of the structure has little effect on the dispersion of the supported mode, which is primarily dictated by the length, width and periodicity of the protrusions[149][151], i.e. the in-plane geometry. Similar waveguides have shown promise in creating photonic devices, such as a power divider and directional coupler[152][153]. Much research has focussed on 'wedge' plasmons[154], which are localised to the tip of a triangular-shaped wedge corrugation in a metallic surface. The mode supported has a lower asymptotic frequency than that associated with the planar interface surface plasmon polariton, and at a given frequency the wedge plasmon has dispersed further from the light line. The limit frequency can be lowered further by adding periodic variation along the wedge[155][156]. Whilst the existing literature contains many studies of bound modes on corrugated edges, none examines the termination of a 2D array metasurface to free space.

8.2 Results and Discussion

The checkerboard edge is modelled using the unit cell shown in Fig. 8.1b. This is similar to the unit cell geometry discussed in Sec. 3.7.1 in that there are periodic boundaries in the x-direction and the model is surrounded by a region of air in the z-direction and bounded by perfect electric conductor (PEC) sheets. However for this system the unit cell is finite also in the y direction, with the checkerboard region on the negative side, and air on the positive side. This unit cell is suitable for finding

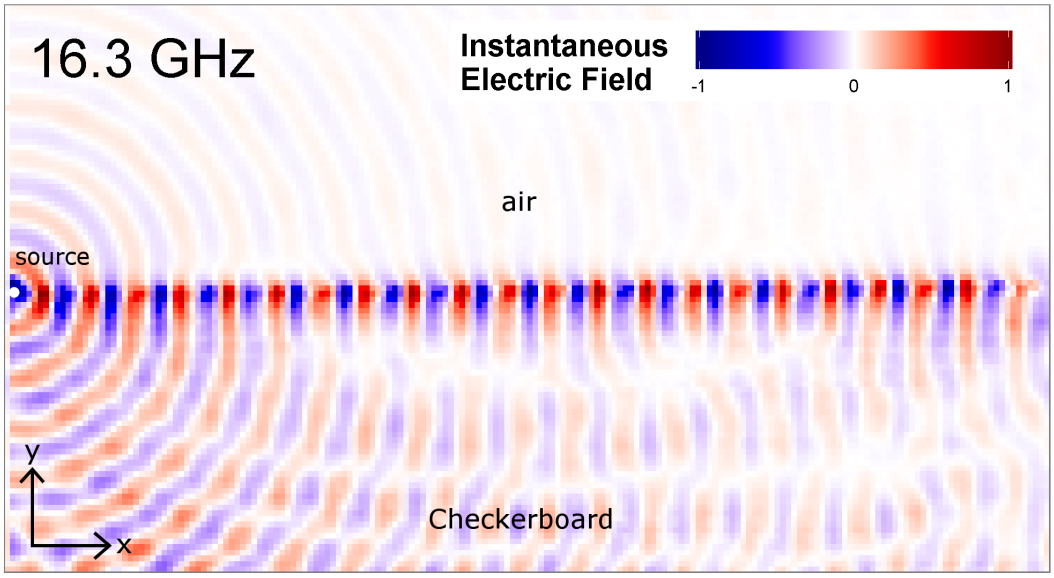

Figure 8.2: Experimentally obtained map of the z-component of electric field, recorded using a pair of stripped coaxial antennas. The source is positioned at the edge, on the left of the image. In the lower half-space a surface wave is excited on the checkerboard structure, whereas in the upper half-space, free-space radiation is observed with weaker amplitude. Along the edge a mode is supported that propagates from left to right and decays in the y-direction.

eigenmodes localised on the edge provided that the fields of those modes fall to zero at each of the four PEC boundaries. Experimental data is acquired using two stripped coaxial antennas, oriented in the z-direction, and positioned close to the structure so as to couple to the mode via near fields. The source antenna is fixed at the edge of the checkerboard, whilst the other scans a rectangular region in the positive x-space relative to the source (see Fig. 8.2). More detail on this technique is outlined in Sec. 3.5.

8.2.1 Single Edge

Fig. 8.2 shows the experimentally obtained z-component (out of plane) of the instantaneous electric field on an xy plane 1 mm above the sample at 16.3 GHz. The checkerboard is located in the lower half of the image, with the edge running horizontally along the centre. The field amplitude is greatest along the edge, corresponding to an edge mode that decays into both the air and checkerboard either side. In the checkerboard 'surface' region, a surface wave is also excited with an amplitude that falls with distance between the two antennas. Interference occurs between the surface and edge modes resulting in nulls in the field where the two are out of phase. In the

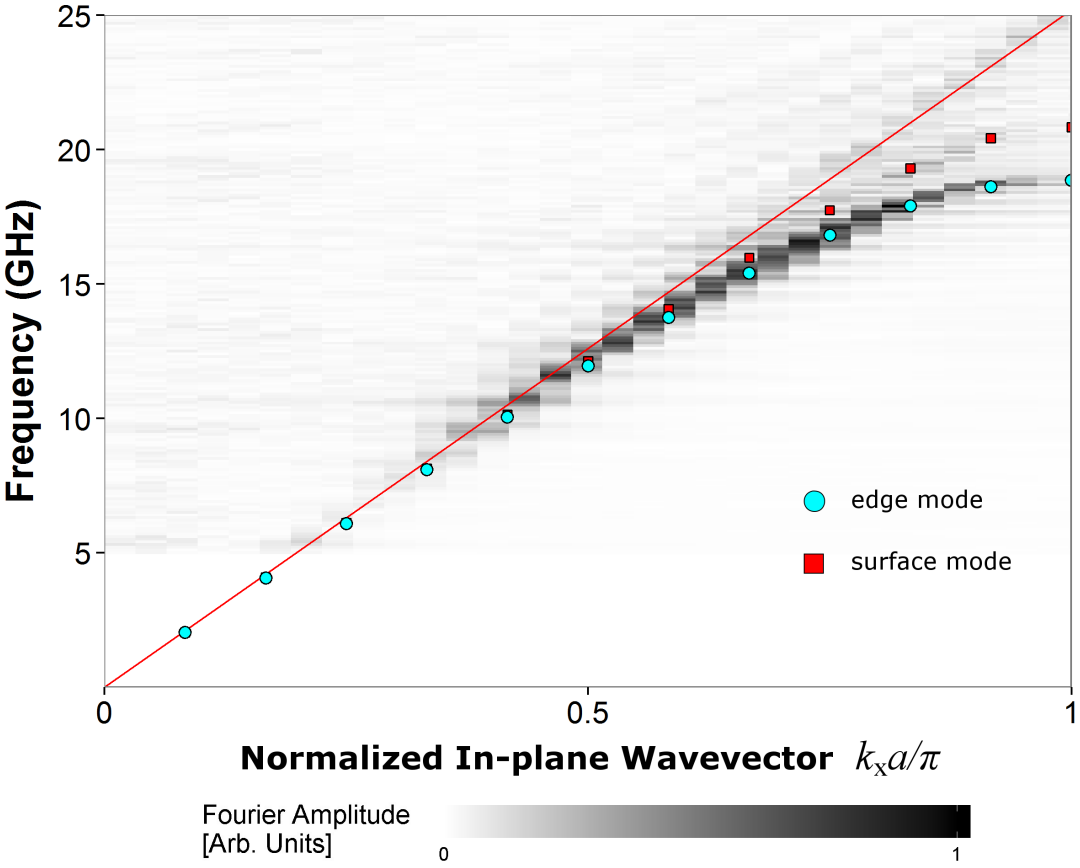

Figure 8.3: The dispersion of modes obtained via a Fast Fourier Transform of the image in Fig. 8.2 for a range of frequencies. The x-axis corresponds to the wavevector component in the x-direction. The dispersion of the edge mode is clear, with large Fourier amplitude due to strong coupling to the mode in the experiment. A surface mode is also supported with weaker Fourier amplitude and smaller k_x for all frequencies. Eigenmode positions according to numerical simulations are overlaid for both the surface (red squares) and edge (blue circles) modes.

air region a free space wave (which disperses along the light line) is apparent, albeit with smaller field amplitude. This is due to the near-field source acting as an inefficient radiating dipole antenna.

Fig. 8.3 shows the dispersion of modes in the x-direction, extracted via Fourier Transforms of the field maps (such as that in Fig. 8.2) for a range of frequencies. This represents a plane in reciprocal space corresponding to $k_y = 0$, i.e. only modes that have momentum in the x-direction are considered. A surface-wave-like mode is present with large Fourier amplitudes that matches eigenmode modelling of a mode on the edge of the checkerboard (blue circles). A second mode is also present that corresponds to

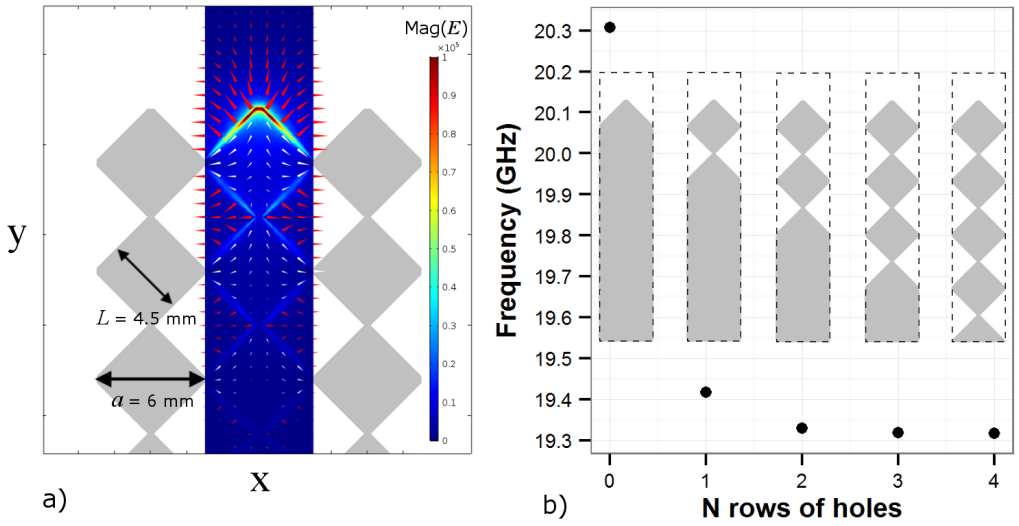

Figure 8.4: a) The electric field magnitude (colour plot), vector (red arrows) and current density (white arrows) for the standing wave solution at $k_x = \pi/a$. Like the surface wave, the edge wave has transverse magnetic polarisation. Additional unit cells either side are shown as a guide. b) The edge mode frequency at the edge of the Brillouin zone ($k_x = \pi/a$) for increasing rows of checkerboard holes in a metallic sheet. The unit cell for each is shown inset.

the surface mode from simulation (red squares). The Fourier amplitude of this surface mode is weaker due to it having weaker electric field amplitude compared to the edge mode (see Fig. 8.2). The edge mode disperses like the surface wave but with greater momentum for a given frequency and therefore a greater mode index, $n = c/v_p$. This is due to the increased localisation of the mode. The wavevector $k_0 = 2\pi f/c$ of a plane wave with frequency f can be expressed as a sum of its cartesian components as:

$$k_0^2 = k_x^2 + k_y^2 + k_z^2 \tag{8.1}$$

The in-plane wavevector for a surface wave, k_{surf}, corresponds to the x- and y-components only and can be expressed by rearranging the equation above. As the surface wave exponentially decays in the z-direction, k_z is purely imaginary which leads to the surface wave having a greater wavevector (momentum) than the free space wavevector ($k_{surf} > k_0$) as shown below:

$$k_{surf}^2 = k_x^2 + k_y^2 = k_0^2 - k_z^2 \tag{8.2}$$

$$k_{surf}^2 = k_0^2 - (i|k_z|)^2 = k_0^2 + |k_z|^2. \tag{8.3}$$

For the edge mode, exponential decay is in both the y- and z- directions, whilst the in-plane wavevector is only the x-component

$$k_{\mathrm{edge}}^2 = k_{\mathrm{x}}^2 = k_0^2 - k_{\mathrm{y}}^2 - k_{\mathrm{z}}^2 \tag{8.4}$$

$$k_{\mathrm{edge}}^2 = k_0^2 - (i|k_{\mathrm{y}}|)^2 - (i|k_{\mathrm{z}}|)^2 = k_0^2 + |k_{\mathrm{y}}|^2 + |k_{\mathrm{z}}|^2. \tag{8.5}$$

This leads to the edge mode having even greater wavevector (momentum) than the surface wave for a given frequency such that $k_{\mathrm{edge}} > k_{\mathrm{surf}} > k_0$, as seen in Fig. 8.3.

The dispersion of the edge mode supported by a thin checkerboard array is quite different to topologically protected edge modes reported in other structures that exist in the band gap of bulk states of a photonic metamaterial[157]. In this case, the edge mode is best described as a surface wave supported by the very narrow zig-zag surface in the xz-plane. This view is confirmed by a somewhat similar study of modes supported by a very thin corrugated metallic strip waveguide by other authors. For example, Shen et al. found that mode dispersion was relatively insensitive to changes in the waveguide thickness compared to other geometrical parameters[149].

Fig. 8.4a shows the simulated electric field magnitude (colour plot) and instantaneous electric field vector (red arrows) for the edge mode at the Brillouin zone boundary ($k_{\mathrm{x}} = \pi/a$), on the xy-plane containing the metallic sheet. The mode resembles that of the transverse magnetic (TM) surface wave studied in Chapter 6; the current (white arrows) passes between connected patches in the x-direction and charge accumulation either side of the hole excites a dipolar mode of the hole. The magnetic field loops around the connections between patches in the transverse yz-plane (the mode propagates in x) giving the mode its TM character. The magnitude of the field weakens as it penetrates the checkerboard structure in the y direction, with the field maximum on the edge where charge accumulates. Fig. 8.4b shows the effect of reducing the number of checkerboard holes, plotting the eigenmode frequency at the edge of the Brillouin zone against the integer number of rows of holes in the surface (see inset). It is clear that these holes beyond the edge are not required in order to support the edge mode; the edge mode is supported by a simple zig-zag corrugation on the edge of a metal sheet ($N = 0$). The effect of the checkerboard holes is to reduce the limit frequency of the mode by approximately 1 GHz. Above $N = 3$ levels of holes, the frequency does not change, indicating that this is the maximum penetration depth of the field. This is qualitatively confirmed by the field distribution in Fig. 8.4a. In the next section, coupled modes supported between two edges are investigated.

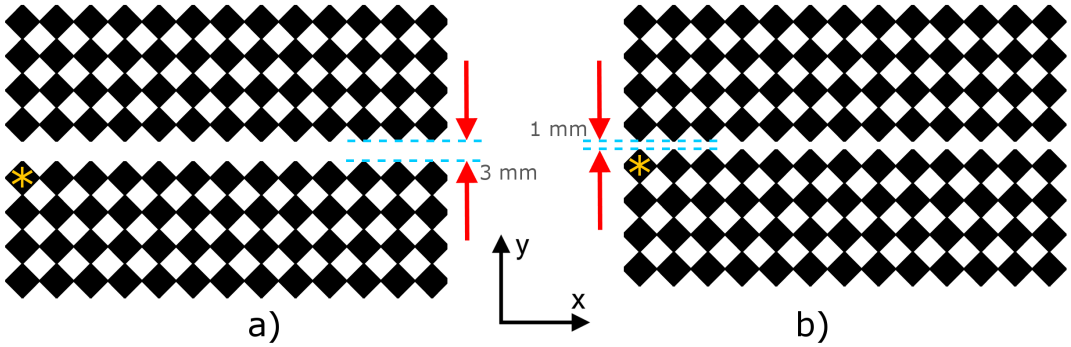

Figure 8.5: Schematic of the coupled edge samples with separation of a) 3 mm and b) 1 mm. Orange asterix represents the position of near field antenna.

8.2.2 Coupled Edges

This section explores the coupling together of two identical edge modes on a metallic checkerboard array. Surface waves on either side of a thin patterned metallic layer are known to couple together, resulting in a symmetric/antisymmetric pair that are distinguished by the symmetry of a given field component, or of the charge configuration. The two solutions are usually separated in energy, which increases as the surfaces are brought closer together. This is often because the field reversal over a short distance for the antisymmetric-in-charge mode requires a higher energy than the symmetric mode in which the E field does not reverse.

Fig. 8.5 shows a section of the samples studied; comprising a checkerboard array cut along the x-axis and the two sections separated by a distance $s = 1$ mm and 3mm. In the experiment, the source antenna is placed at one end of this channel directly above a metallic square on one edge. This asymmetry in the antenna position with respect to the y-axis allows excitation of both the symmetric and antisymmetric modes. The second antenna scans the same region as for the single edge in Fig. 8.2. Fig. 8.6 shows the dispersion for the $s = 3$ mm case; two modes are present with an energy gap of 1 GHz at the edge of the Brillouin zone. Reducing the separation to 1 mm results in the dispersion shown in Fig. 8.7 where the energy gap has increased to 2.5 GHz. For both cases the eigenmode positions according to numerical modelling are overlaid and agree well with observation.

The difference between the two modes supported by the coupled-edge waveguide is made clear by studying the experimentally obtained field profiles at frequencies (marked by horizontal lines in Fig. 8.7) below and above the limit-frequency of the lowest frequency mode ($\approx$ 17.5 GHz). At 12 GHz (below limit) both modes are excited, however coupling to the lower frequency mode is much greater as shown by the increased Fourier amplitude in the dispersion curve compared to the higher frequency mode. Fig.

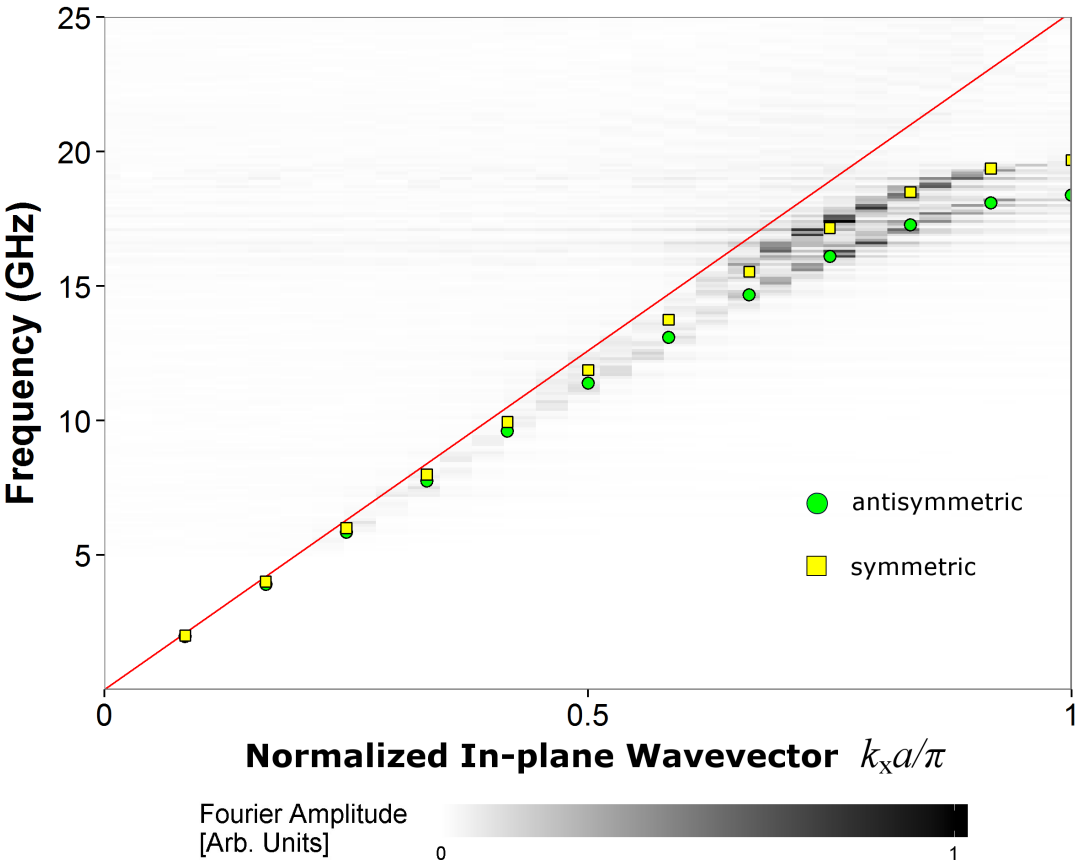

Figure 8.6: The dispersion of modes supported on the coupled edge sample with edge separation $s = 3$ mm, with results from eigenmode modelling overlaid. Two modes are excited, corresponding to antisymmetric (green circles) and symmetric (yellow squares) E_z field with respect to a line midway between the two edges. The frequency splitting of the standing wave solutions at the Brillouin zone is ≈ 1 GHz.

8.8 shows that the E_z field reverses sign either side of the channel between the edges, and hence this mode is referred to as the antisymmetric E_z mode.

In contrast, above the first limit frequency, only the higher frequency mode is present in the field map. Fig. 8.9 shows that at 19.1 GHz the E_z field is symmetric about the centre of the channel and hence the higher frequency mode is referred to as symmetric E_z. This could alternatively be defined as symmetric/antisymmetric in charge. This symmetric E_z mode has a smaller in-plane wavevector for a given frequency. Conservation of total momentum results in the mode having a smaller purely imaginary k_y component, and therefore the field penetration depth into the checkerboard region either side of the interface in Fig. 8.9 is greater than in the asymmetric case. There is also a periodic variation of the E_z field along the x direction due to the edge wave reflecting from the end of the sample and setting up a standing wave. Unlike surface

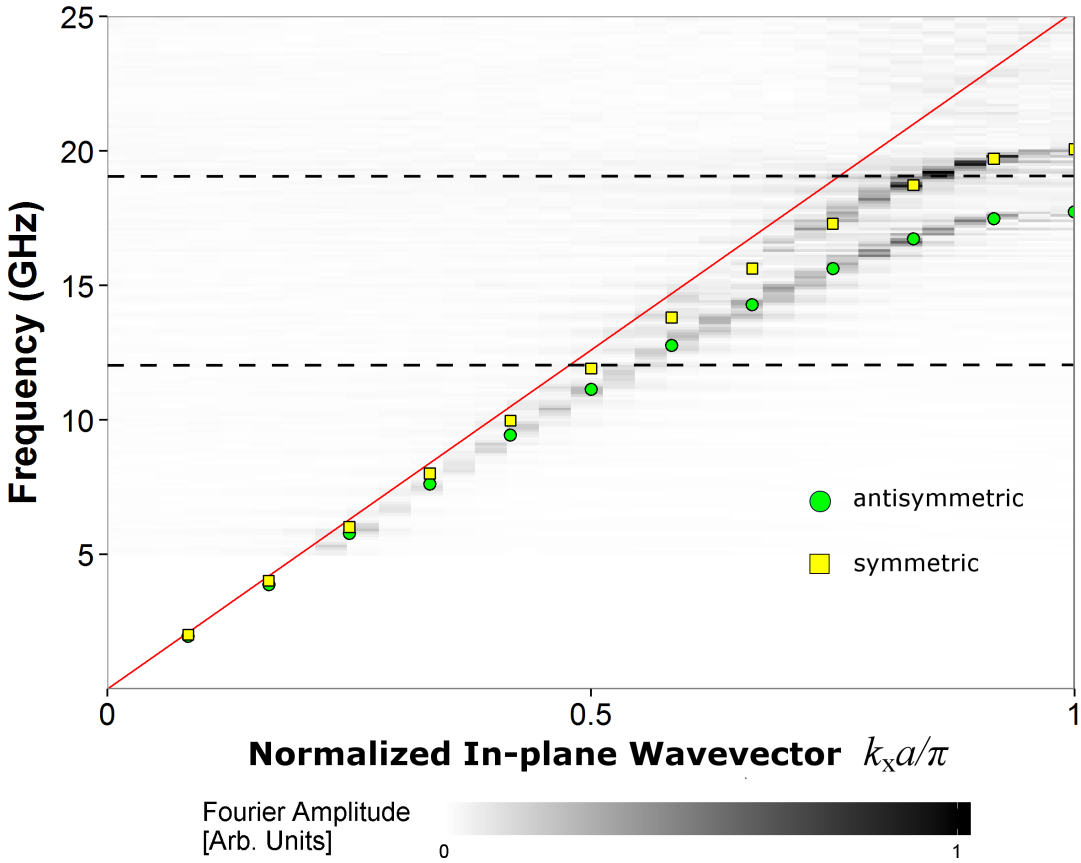

Figure 8.7: The dispersion of modes supported on the coupled-edge sample with edge separation $s = 1$ mm, with results from eigenmode modelling overlaid. Two modes are excited, corresponding to antisymmetric (green circles) and symmetric (yellow squares) E_z field with respect to a line midway between the two edges. The frequency splitting of the standing wave solutions at the Brillouin zone is ≈ 3 GHz.

waves, multiple (>2) edges can be coupled together in this way to create a multi-mode waveguide.

8.2.3 Surface to Edge Conversion

The checkerboard geometry supports a bound surface wave both across its surface and an edge mode along the zigzag edge where the sample terminates to free-space. Whilst it was shown in Fig. 8.4b that the same edge on a non-patterned metallic sheet supports an edge mode, the checkerboard geometry allows the transfer of power between the surface and edge modes. This could be useful in plasmonic devices which suffer from power loss when a bound surface mode is scattered into free-space by a boundary.

In the same way that an incident plane wave can couple to a diffracted surface mode at a particular angle θ (see Sec. 2.4), a surface wave impinging on an edge can match

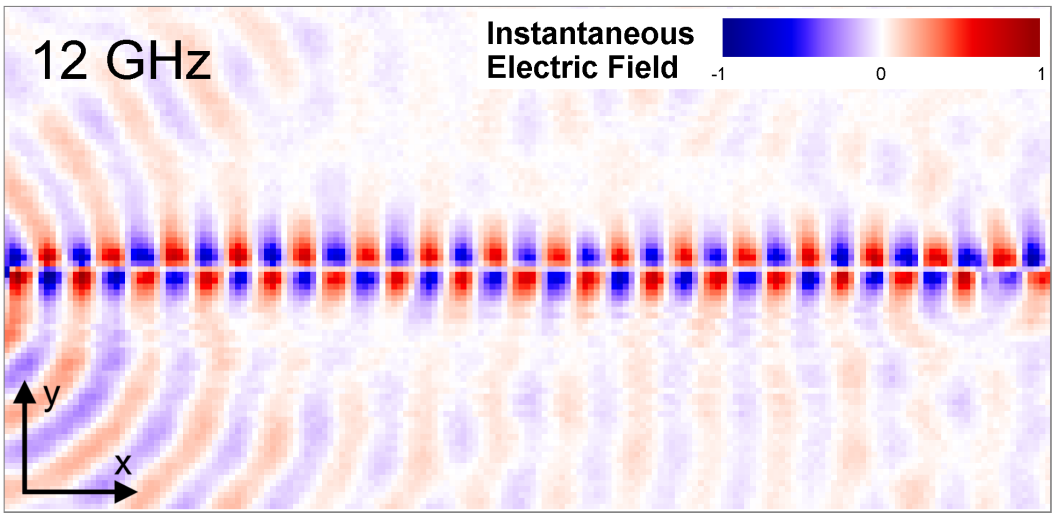

Figure 8.8: The E_z field (out of plane component) measured at 12 GHz and separation $s = 1$ mm. The source is positioned on the left hand edge of the image. The field shows that the E_z field of the lower frequency mode has asymmetric character.

both the frequency and wavevector of an edge mode. Mode conversion can take place provided there is some overlap in the field configurations of the two modes. Due to the similarity in the fields of the surface and edge modes on the checkerboard array (both are TM polarised) conversion should be possible provided that

$$k_{\mathrm{surf}}(\mathrm{x},\mathrm{y})\sin(\theta) = k_{\mathrm{edge}}(\mathrm{x}) \tag{8.6}$$

This requires that the surface mode has greater momentum than the edge mode; which as seen in Fig. 8.3 is not the case. However, sufficiently increasing the frequency (energy) of the edge mode alone would allow equation 8.6 to be satisfied. This may be achieved by making the zigzag protrusions of the edge mode shallower. This effectively increases the limit-frequency (frequency of the mode at the BZ boundary) of the edge by making the resonant cavity length shorter (the cavity length given by the depth of the groove, between the peak and trough of the zigzag edge). This geometry is shown in Fig. 8.10a.

A preliminary simulation of a radial surface wave (originating from a point dipole source) impinging on the modified edge in Fig. 8.10a is shown in Fig. 8.10b. This represents the E_z field on a plane 0.5 mm above the surface. An edge mode is seen along a horizontal line through the centre of the image, in addition to the surface wave in the lower half-space. Further modelling, experimental verification and optimisation of this mode conversion are required and are included with the Future Work section at

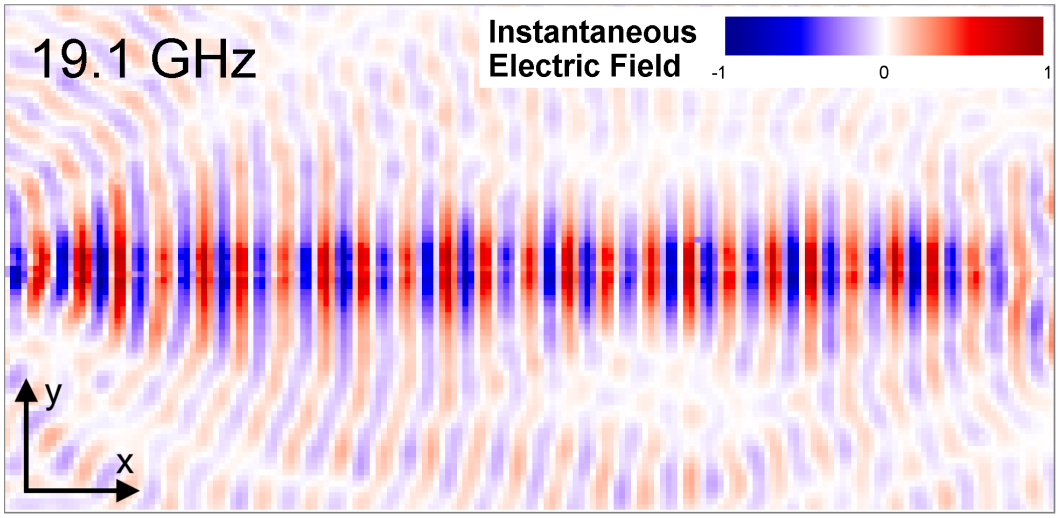

Figure 8.9: The E_z field (out of plane component) measured at 19.1 GHz and separation $s = 1$ mm. The source is positioned on the left hand edge of the image. The field shows that the E_z field of the higher frequency mode has symmetric character.

the end of this thesis.

8.3 Conclusion

In this chapter, the propagation of a mode along the edge of a metallic checkerboard hole array has been studied. Numerical modelling predicts that a finite sized sample supports a bound edge wave in addition to the surface wave discussed in Chapter 6. This edge wave exponentially decays in both transverse directions and propagates along the edge with in-plane momentum greater than that of the surface wave. Eigenmode modelling showed that the field configuration is similar to that of the transverse magnetic surface wave and that the field penetration depth into the checkerboard structure is approximately 3 times the periodicity.

Placing two edges together and separated by a distance s resulted in coupled edge modes, whose difference in energy is approximately inversely proportional to the size of s. The dispersion of these coupled modes was experimentally determined for two separations by mapping the electric field of an area surrounding the interface. The electric field profile verified that the two coupled modes are a symmetric/antisymmetric pair.

Finally, the possibility of power conversion from a surface wave into an edge wave was introduced, and the result of preliminary modelling presented. Large coupling efficiency between the two requires momentum-matching. This can be achieved by

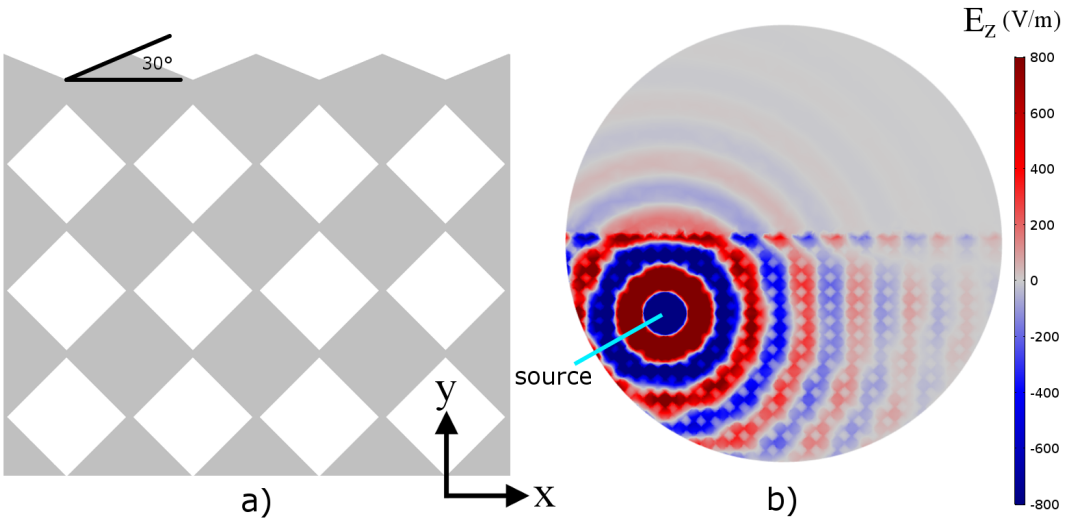

Figure 8.10: a) The proposed modified geometry for conversion between surface and edge modes. The depth of the zigzag groove is reduced to $a\tan(30)/2$ in order to increase the frequency of the edge mode. b) Preliminary modelling results showing a surface wave impinging on the boundary to free space. An edge wave is seen propagating from left to right.

modifying the geometry of the edge in order to increase the energy of the edge mode without affecting the surface mode.

Chapter 9

Planar Metallic Waveguides with Negative Mode Index

In 1968 Veselago postulated that a material with simultaneously negative values of permittivity, ϵ, and permeability, μ, must have an index of refraction given by the *negative* root of the product of the two[158]. In such a material Snell's law of refraction would be reversed, with incident rays from a positive index medium (PIM) refracting into the same side of the surface normal inside the negative index material (NIM), as depicted in Fig. 9.1a. Within the NIM, a wave has anti-parallel phase and group velocities, $\mathbf{v}_\mathrm{p}$ and $\mathbf{v}_\mathrm{g}$ (Fig. 9.1a), meaning the direction of phase propagation (momentum) is opposite that of power flow. These materials are also known as backward wave media (BWM) or left-handed media (LHM) due to the left-hand rule associating the momentum vector with the electric and magnetic field vectors of a propagating wave, as opposed to the right-hand relationship of waves in positive index media.

In this chapter, the principles of negative index materials are studied in the context of bound surface waves, where the *mode* index, defined as the ratio of the speed of light in vacuum to the phase velocity of the surface mode, can be negative. In this case, the region of negative mode index exists outside of the light cone in the non-radiative region of the dispersion curve (Sec. 2.4.1). Initially, various one-dimensional, planar, surface waveguides are investigated both numerically and experimentally. Secondly, this idea is extended to a planar two-dimensional sheet demonstrating negative mode index which could be used as a surface-wave 'superlens'.

9.1 Background

Simultaneously negative permittivity and permeability does not occur in nature due to the fact that naturally occuring materials with negative permeability, μ, do not

exist. Many metals act as metallic plasmas with negative permittivity at frequencies below the material plasma frequency which often occurs in the optical/UV regimes (Sec. 2.3.1). The real part of relative permeability ($\mu_r = \mu/\mu_0$) of permanent magnetic materials such as Iron is positive and increasingly large with decreasing frequency. In non-permanent magnetic materials an external magnetic field induces a magnetic field within the material which can oppose the external field (diamagnetism), resulting in a permeability less than 1. Superconductors can be described as perfect diamagnets as they completely screen the external magnetic field at temperatures close to absolute zero and hence have relative permeability equal to 0. In 1999, Pendry et al.[159] demonstrated that an array of non-magnetic, conducting sheets curled into cylinders has a resonant condition at which it behaves as an artificial magnetic medium, with negative effective permeability for a band of frequencies above the resonant frequency. A metamaterial that supports opposing currents (i.e. a cut wire pair[160][161][162], split-ring resonators[163][164][165]) or 'staple'-like protrusions from a metallic layer[166] will couple strongly to an external magnetic field, similarly giving the material an effective negative permeability providing the resonance is strong enough (i.e it has a high quality factor and electromagnetic losses are sufficiently small). Unlike natural magnetic materials, these magnetic effects are not caused by the spin of unpaired electrons and are therefore not isolated to microwave frequencies and below.

In 2000, Smith et al[167] proposed a composite metamaterial which could provide both negative permittivity and permeability over a narrow frequency range. The material consisted of a 3-dimensional array of split ring resonators (SRRs) to provide the necessary magnetic resonance, interlocked with an array of thin metallic wires mimicking an electric plasma with negative epsilon. Experimental verification of negative refraction in this metamaterial in the microwave regime shortly followed[168], and it was later shown that simultaneous negative ϵ and μ occurs at the higher frequency 'antisymmetric' resonance of the SRR, without the need for the metallic wires[169]. More recently, SRRs with embedded diodes acting as an effective gain medium have compensated for electromagnetic loss inherent in many NIMs[170]. Remarkably, it was postulated that a finite slab of NIM could overcome the diffraction limit and act as a 'superlens'[171] due to the reversal of Snell's Law (negative refraction). This concept is shown schematically in Fig. 9.1b. Rays are refracted negatively and come to a focus within the NIM layer. After refracting again at the second interface an image is formed at a second focus in the positive index medium (PIM). Since this realisation much focus has been on negative index in the terahertz, infrared and visible regimes, where subwavelength imaging is valuable. Comprehensive reviews of the achievements in the field of negative index materials are provided in [21][172].

In addition to the SRR geometry, negative refraction at optical frequencies has

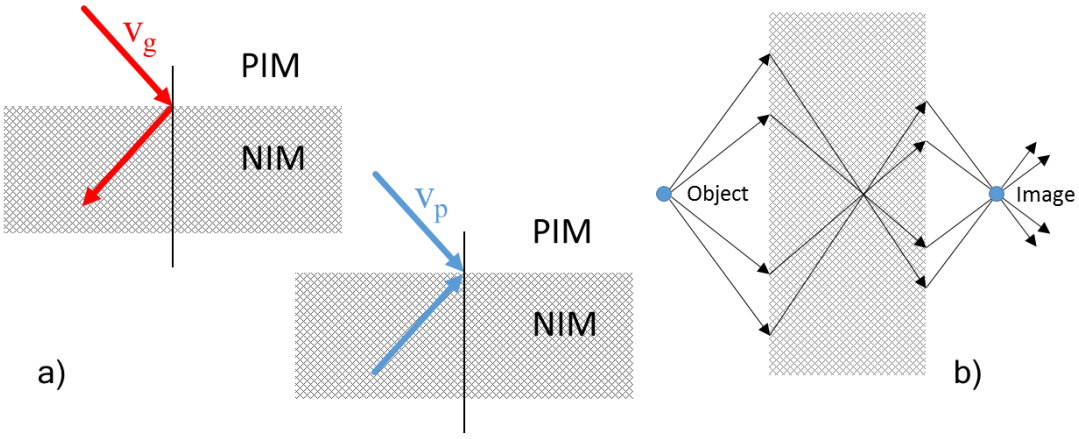

Figure 9.1: a) Direction of group velocity (red arrows) and phase velocity (blue arrows) as a wave passes from a positive index material (PIM) into a negative index material (NIM). Negative refraction occurs and the transmitted ray appears on the same side of the normal as the incident ray. Inside the NIM, group and phase velocities are in opposite directions. b) A NIM acting as a superlens. Rays emitted from an object focus within the NIM and again on the opposite side, forming an image.

been reported using other structures[173]. One of these is the stacked 'fishnet' structure, where magnetic polarisability arises due to opposing currents on neighbouring layers[174][175]. Negative refraction has been demonstrated experimentally by creating a prism from this structure and observing the angle at which a beam emerges[176]. Similarly, structured metal-insulator-metal (MIM) waveguides have exhibited all-angle negative refraction of visible light in a frequency band between the surface and bulk plasma frequencies[177]. Chiral structures have also been shown to exhibit negative index for a particular handedness of radiation both theoretically[178][179] and experimentally in the terahertz regime[180].

Negative refraction can arise without a material acting as an effective homogenised medium. This has been demonstrated in photonic crystals (PCs), where negative refraction is possible due to diffraction phenomena; modes that are back-scattered due to the periodicity[181][182]. The operating wavelength within these materials is often not sufficiently larger than the periodicity for the material to be considered an effective medium. Despite the inappropriateness of describing an effective permittivity and permeability, superlensing using PCs has been demonstrated at microwave[183][184] and infrared[185] frequencies, and even using acoustic waves[186][187]. In the optical regime, PCs are advantageous as they can be made entirely from dielectrics, minimising electromagnetic loss (which is significant in metals at optical frequencies).

Bound modes, such as surface plasmons on the interface between metallic and dielectric media at optical frequencies and surface waves on patterned metamaterials at

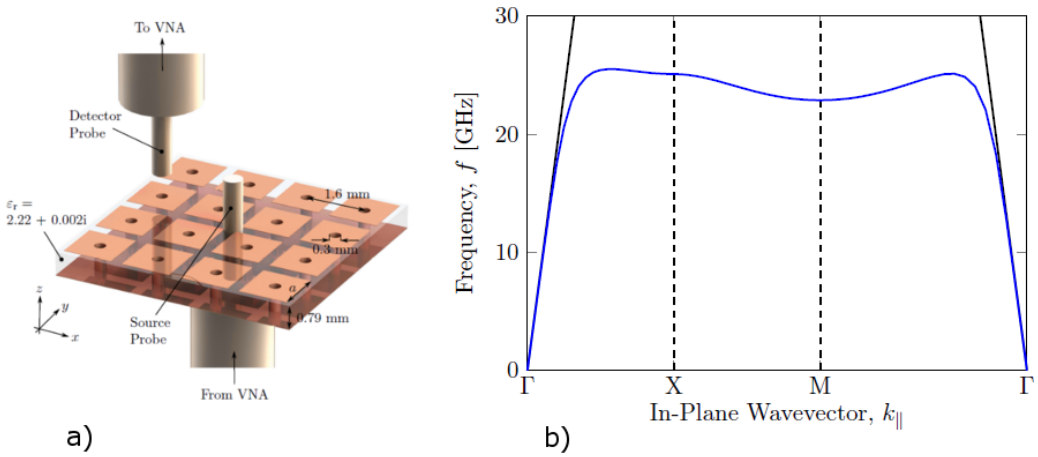

Figure 9.2: Figure published in [2]. a) A section of the Sievenpiper mushroom array b) The simulated dispersion curve covering the irreducible Brillouin zone. ΓX and ΓM correspond to propagation along the x direction and 45° in-plane direction respectively. Both of these sections of the dispersion contain a region of negative mode index.

lower frequencies, can be described as having a *mode* index. This is described as the ratio of the speed of light in vacuum c to the phase velocity $\mathbf{v}_\mathrm{p}$ of the wave, and is an effective property of the interface and not the media either side. Much like negative effective index bulk media for plane propagating waves, negative mode index for inhomogenous surface waves implies opposite signs of the group and phase velocity. This means power flows 'forwards' away from the source whilst the phase fronts travel 'backwards'. Negative mode index generally occurs where the dispersion curve has negative gradient (negative $\mathbf{v}_\mathrm{g}$) and positive wavevector (positive $\mathbf{v}_\mathrm{p}$), or vice-versa. A surface that supports a mode with isotropic negative mode index could be used to create a superlens for surface waves in a similar way to other surface wave analogies of lenses, e.g. the Luneburg lens[188]. Negative mode index has been demonstrated for a range of surface-plasmon-supporting structures[189], whilst all-angle negative mode index at microwave frequencies has recently been reported using the Sievenpiper mushroom geometry[109], and a modified 'comb' planar waveguide geometry[190]. Fig. 9.2 shows the dispersion curve of the former along with the unit cell of the Sievenpiper mushroom, taken from [2]. The dispersion shows that a region of negative mode index is present for surface wave propagation along both the x direction (ΓX) and 45° (ΓM) direction. The aim of the present work is to replicate this dispersion using a single layer structure, which has the benefits of flexibility, ease and cost of fabrication, and can easily be scaled to higher frequencies due to the simplicity of the geometry.

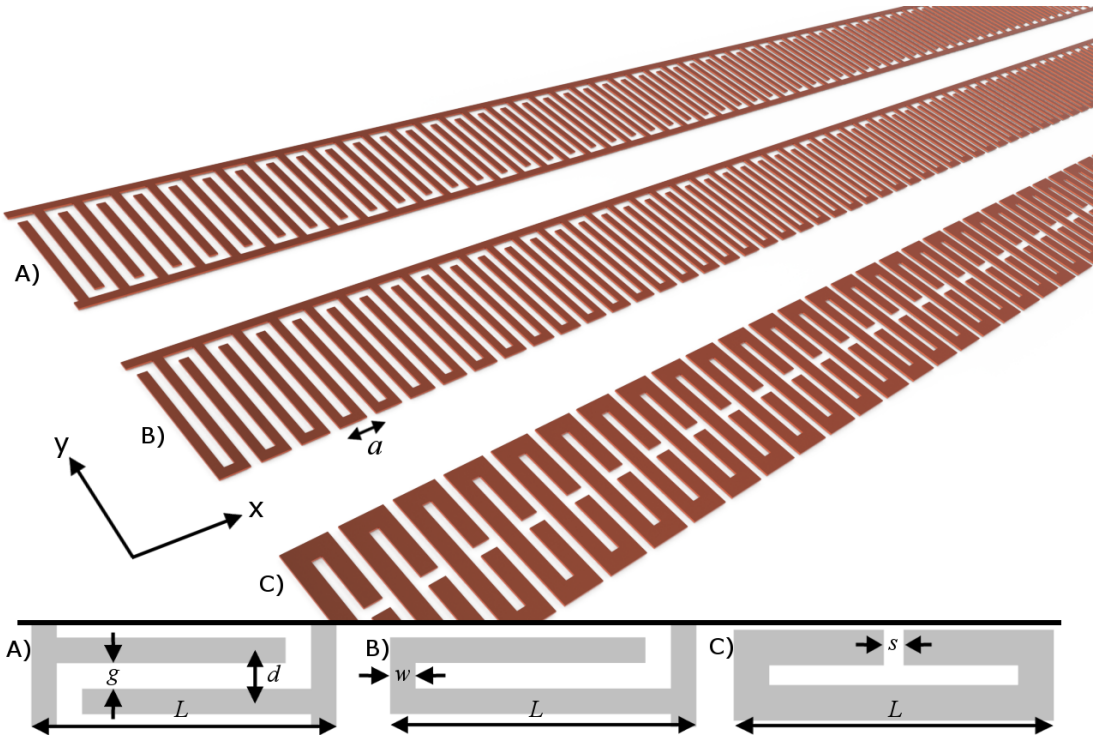

Figure 9.3: Sections of the three metallic waveguides studied. A) the coupled domino waveguide B) the hook or 'J' waveguide and C) the rectangular split ring resonator chain. The experimental samples (B and C) were attached to a Mylar substrate and the chains contained approximately 100 and 200 unit cells respectively.

9.2 One-Dimensional Planar Waveguides

Recently, studies of thin single-layer metallic waveguides have shown a negative gradient region within the first Brillouin zone of the guided mode's dispersion curve[151]. As discussed above, the use of the term 'negative index' to describe modes supported on a barely subwavelength structure is a matter of ongoing discussion[181]. In this section, we discuss this issue and investigate other planar geometries that can provide negative mode index waveguiding along a one-dimensional chain of elements at wavelengths greater than 20 times the periodicity.

The three geometries considered are shown in Fig. 9.3. The first (A) is a pair of coupled 'domino' guides; narrow protrusions from a continuous metallic strip which are very thin (18 μm). The two guides are separated by a distance, $L = 8$ mm, and are shifted with respect to each other in the direction of propagation (x) by $d = a/2$, where a is the periodicity. This structure bears resemblance to that discussed in Quesada et al.[151]. The second geometry (B) is a single structure consisting of hook or 'J' shaped protrusions from the metallic strip with length, $L = 8$ mm. In both cases, the periodicity $a = 2$ mm, metal width $w = 0.5$ mm and gap $g = 0.5$ mm. The third

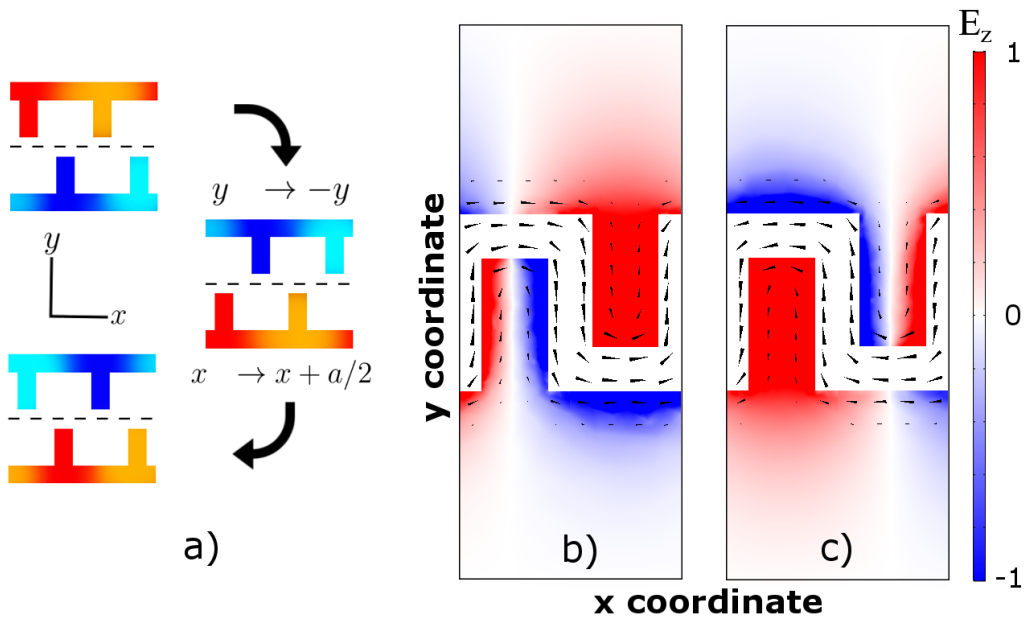

Figure 9.4: a) Schematic demonstrating the glide operation on a coupled domino waveguide. Colours are used to highlight different regions of the geometry and do not correspond to any physical quantity. b-c) The two degenerate field solutions at the Brillouin zone of the waveguide's dispersion diagram, where the wavelength $\lambda = 2a$. The colour plot and black arrows represent the z component of the electric field and the Poynting vector, S, respectively. The two modes have the same energy (and frequency) but propagate in opposite directions.

structure (C) is a chain of rectangular split ring resonators, with $a = 2.8$ mm, $L = 8.1$ mm, $w = 0.9$ mm and $g = 0.5$ mm. The split s is also 0.5 mm wide. These planar waveguides support bound surface waves[149] which propagate along the waveguide in the x direction (i.e. $\mathbf{k} = k_{\mathrm{x}}\hat{\mathbf{x}}$). The fields of these modes decay exponentially in the y and z direction, and must be coupled to via the near field of an antenna, as the momentum of the mode is greater than that available to incident plane wave radiation. The experimental setup used in outlined in Sec. 3.5. The phase ($\mathbf{v}_{\mathrm{p}} = \hat{\mathbf{x}}v_{\mathrm{p}} = \hat{\mathbf{x}}\omega/k_{\mathrm{x}}$) and group ($\mathbf{v}_{\mathrm{g}} = \hat{\mathbf{x}}v_{\mathrm{g}} = \hat{\mathbf{x}}d\omega/dk_{\mathrm{x}}$) velocities of the modes are directed along the guide in the x direction and their magnitude and sign can be determined by studying the dispersion curves for each structure within the first Brillouin zone, and also the field profiles obtained from numerical modelling.

9.2.1 Coupled Domino Waveguide

The coupled domino structure shown in Fig. 9.3A is an example of a one-dimensional waveguide that possesses 'glide' symmetry (Sec. 2.6). This means that the structure is invariant under a combination of a mirror inversion in the y direction and a translation

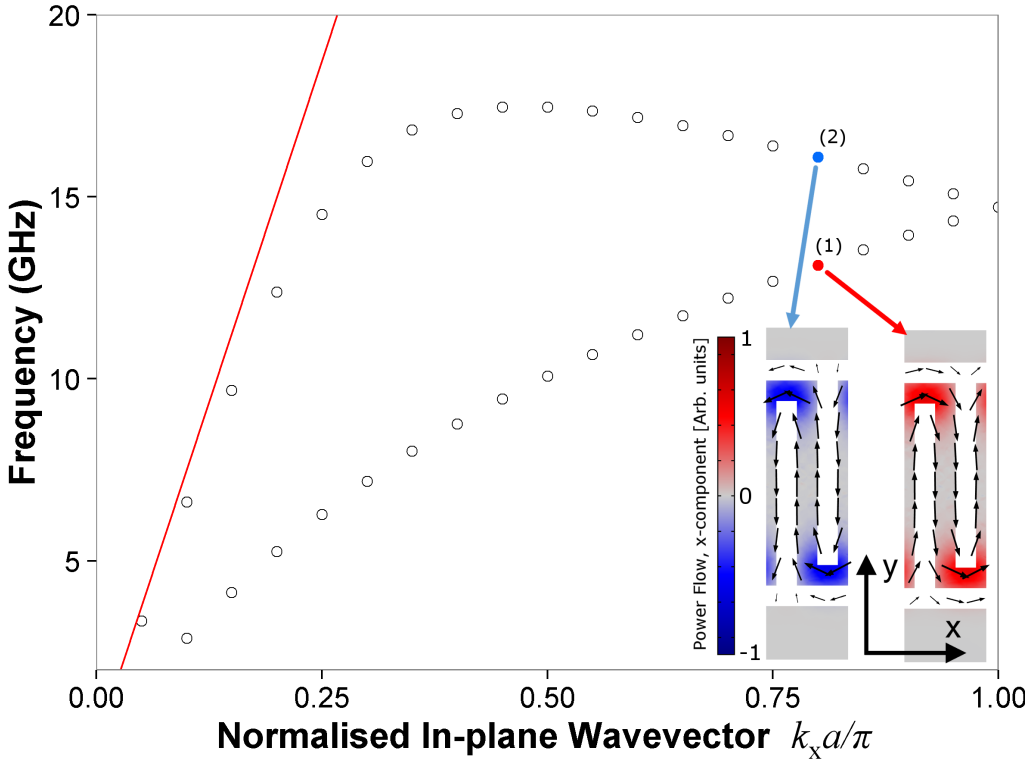

Figure 9.5: The simulated dispersion diagram for the glide domino structure in Fig. 9.3A which supports two coupled bound modes. Points indicate eigenmode solutions according to COMSOL. The wavevector axis spans from zero to the edge of the first Brillouin zone. Inset: The x component of time-averaged power flow 0.5 mm above the metal surface (colour scale) and the Poynting vector (arrows) for the two eigenmodes at a normalised in-plane wavevector of 0.8 (marked (1) and (2)). The modes have opposing power flow and hence opposite group velocity (also evident by the gradient of the dispersion curve). The light line is shown in red. The origin of this dispersion relation is discussed in Sec. 2.6 and Fig. 2.14 in particular.

of half the period in the x direction. This glide operator is demonstrated in Fig. 9.4a and can be formally written as

$$G \equiv \begin{cases} x & \to x + a/2 \\ y & \to -y \\ z & \to z \end{cases} \tag{9.1}$$

This symmetry operation is only satisfied if the lateral shift d between the two individual domino arrays is precisely $a/2$. The plane of reflection normal to the y direction is known as the glide plane. A recent study of this structure demonstrated that the existence of glide symmetry resulted in a dispersion relation which is gapless at the Brillouin zone boundary[151][191], i.e. $k_x a/\pi = 1$ (similar to that shown in

Fig. 9.5). The non-radiative guided mode does not form a standing wave with its counterpart scattered from $k_x a/\pi = 2$ as would be expected in a periodic medium, instead the two modes pass through each other with non-zero group velocity. At the Brillouin zone boundary the two modes are degenerate and their field configurations are energetically identical, glide symmetric pairs, as shown in Fig. 9.4b-c. The black arrows demonstrate the time-averaged Poynting vector (Power flow), **S**, on a plane containing the upper metallic surface, whereas the colour plot shows the out-of-plane (z direction) electric field component. The local power flow 'meanders' around the waveguide and its integrated value over the whole geometry provides the direction of the mode's group velocity, v_g. For the two degenerate modes in Fig. 9.4b, the net y component of the power flow is zero, whereas the net x component is non-zero and the two cases have counter-propagating power flow and hence antiparallel group velocities. As discussed in earlier chapters (and Sec. 2.5.2 in particular), a pair of coupled modes at the first Brillouin zone boundary of a periodic structure (where $d = 0$ i.e. no glide symmetry) are standing wave solutions with a half wavelength ($\lambda/2$) within the unit cell. The difference in energy of the two modes is due to a shift of $a/2$ of the nodes/antinodes (one mode looks sinusoidal, the other cosinusoidal) which gives each mode a different field configuration, one of which is more energically favourable than the other (see Sec. 2.4.3). In a *glide* symmetric structure, the $a/2$ shift of the standing wave results in the same field configuration with the same energy, and hence the two modes are degenerate. An in-depth discussion of the origin of modes in a glide-symmetric structure is given in Sec. 2.6 and in [26][192].

Fig. 9.5 shows the dispersion for the glide domino waveguide depicted in Fig. 9.3A. Studying the power flow just above the metallic surface for a wavevector, $k_x a/\pi = 0.8$, within the first Brillouin zone shows that the two modes are counterpropagating (see inset). The only net component of the Poynting vector (black arrows) across the surface is in the x direction, and the direction of this component is given by the colour scale. The group velocity for each highlighted mode is given by the gradient of the dispersion curve ($v_g = d\omega/dk_x$) and the direction is also evident from the direction of net power flow. Fig. 9.6 shows the x component of the power flow S_x integrated over the entire unit cell volume as a function of in-plane wavevector k_x. The green points correspond to the two modes of the glide symmetric domino waveguide from which an interpolation using a spline fitting function in R yields the green curves. The values at $k_x a/\pi = 1$ (edge of first BZ) have been determined from this interpolation as the eigenmode solver in COMSOL can not accurately predict the field configurations where two eigenmodes are degenerate (black lines). The net power flow of the higher frequency mode (dashed green line) is zero at $k_x a/\pi = 0.45$, the point at which the gradient of the dispersion falls to zero. Crucially, at the Brillouin zone boundary ($k_x a/\pi = 1$) both modes have equal

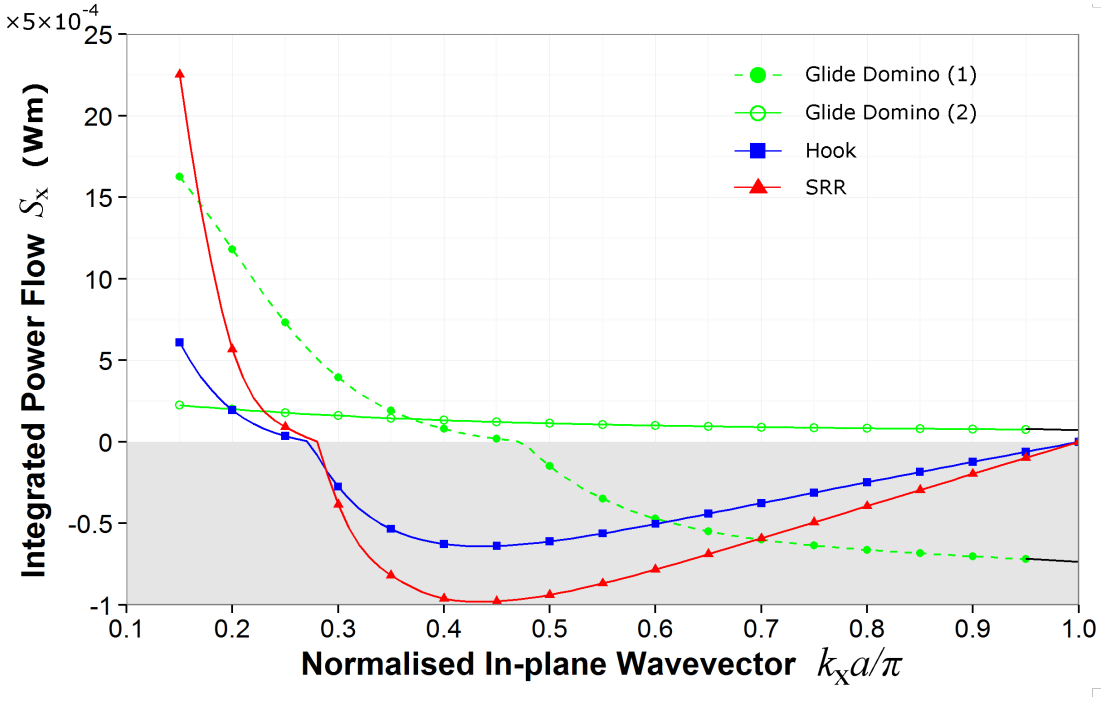

Figure 9.6: The x component of the power flow, integrated over the entire unit cell volume, S_x, as a function of normalised in-plane wavevector. These values are obtained from eigenmode simulations using COMSOL for each of the one-dimensional waveguides studied: lower frequency mode of the glide domino (hollow green circles/solid line), higher frequency mode of the glide domino (filled green circles/dashed line), the hook waveguide (blue squares) and the split ring resonator waveguide (red triangles). The negative region of the y axis (grey area) has been scaled by a factor of 10 for clarity. The S_x values at $k_x a/\pi = 1$ have been interpolated (black lines) from the preceding points due to the inability to distinguish degenerate modes at the Brillouin zone boundary using the eigenmode model.

and opposite non-zero power flow (The negative S_x region (grey) is scaled by a factor of 10 for clarity). Whilst the direction of group velocity for modes on this structure is very well defined, the same can not be said for the phase velocity in a periodic medium. This is due to an ambiguity in wavevector; the dispersion is periodic and hence any wavevector k_x can also be expressed as $k_x \pm nk_g$ for any integer n, where $k_g = 2\pi/a$ is the magnitude of the periodic or 'grating' wavevector. The spatial component of the wavefunction for a mode in such a system is given by the sum

$$\Psi_n = \sum_{n=-\infty}^{\infty} A_n \exp(i(k_x - nk_g)x) \tag{9.2}$$

where A_n are a set of weighting factors which correspond to Fourier amplitudes from each diffracted order. For a truly subwavelength metamaterial structure which can be considered an effective medium, only A_0 is sufficiently large to contribute to

the wavefunction. In such structures, the phase velocity is unambiguous and is given by ω/k_{x}. As the periodicity of the medium approaches the operating wavelength, the magnitude of A_1 increases, such that the wavefunction can be approximated as

$$\Psi = \underbrace{A_0 \exp(ik_{\mathrm{x}}x)}_{\text{forward going wave}} + \underbrace{A_1 \exp(i(k_{\mathrm{x}} - k_{\mathrm{g}})x)}_{\text{backward going wave}} \tag{9.3}$$

For $0 \leq k_{\mathrm{x}} \leq k_{\mathrm{g}}$, the wavefunction is a sum of a forward-going, non-diffracted wave with wavevector k_{x} and a backward going, diffracted wave with wavevector $k_{\mathrm{x}} - k_{\mathrm{g}}$. This results in an ambiguity in the phase velocity, as phase fronts appear to be travelling in opposite directions, at different speeds, in different regions of the sample. In order to determine the sign of v_{p}, a chosen instantaneous field component can be advanced in phase and the progression of phase fronts observed. Fig. 9.7 shows the z component of the magnetic field corresponding to the higher frequency eigenmode solution at $k_{\mathrm{x}}a/\pi = 0.8$ (blue point in Fig. 9.5, where the gradient and therefore the group velocity is negative). Each image covers 7 unit cells (the first of which is outlined in grey) and net power flow is from right to left. A mode with negative index would therefore have phase fronts moving in the opposite (forward) direction, from left to right. The second and third field profiles have been advanced in phase by 45° and 90° with respect to the first. The dashed cyan line demonstrates that the phase front propagation is forward along the white solid line through the waveguide centre. However, along a line (solid black) outside the waveguide the phase fronts are shown to move backwards (pink dashed line). This result is unsurprising given that the mode in this negative gradient region is the hybridisation of a forward going wave and a back-scattered wave due to the periodicity. In order to usefully assign an index to the waveguide, it must be homogenised and therefore approximate an effective medium. This requires that the structuring be very subwavelength. The following section aims to achieve this via a different variation on the domino waveguide.

9.2.2 Planar Hook Waveguide

The negative gradient region of the dispersion of the mode supported by the glide symmetric coupled domino array arises due to the existence of diffractive band folding (more in Sec. 2.4.1). As a result, the validity of effective parameters such as index of refraction are limited. This section considers a very subwavelength ($a \ll \lambda$) negative mode index planar waveguide such as the 'hook' or 'J' planar waveguide depicted in Fig. 9.3B.

The dimensions used are the same as that for the glide domino waveguide in the previous section, the periodicity $a = 2$ mm, the length in the y direction $L = 8$ mm

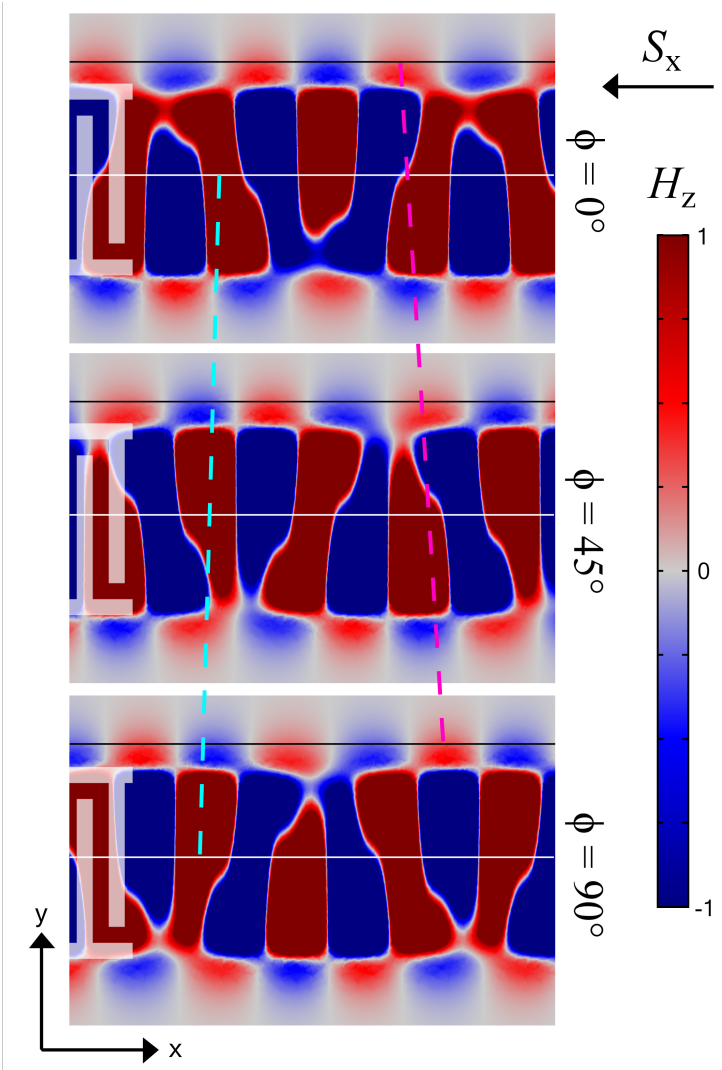

Figure 9.7: The z component of magnetic field, H_z, 1 mm above the glide domino structure. Power propagation is from right to left, as is the direction of group velocity, v_g. Each successive image shows an advance in phase by 45°. Along the central plane of the waveguide (white line), the phase fronts appear to flow forwards (dashed magenta line), i.e. phase velocity in the same direction to group velocity. However on the outside of the guide (black line), where the mode decays in the ± y direction, the phase fronts advance backwards (dashed cyan line), suggesting v_p, v_g are in the opposite direction. This is a typical shortcoming of defining phase velocity in a photonic crystal, where the structuring is not significantly subwavelength in size. Despite this, such materials are often deemed to have 'negative index'.

and the metal width w and gap g are both 0.5 mm. Fig. 9.8a shows the simulated electric field profile of a unit cell according to eigenmode modelling using COMSOL (Sec. 3.7). The momentum in the direction of the guide, $k_x = \pi/a$, is chosen in order to study the field profile of the mode on the edge of the first Brillouin zone.

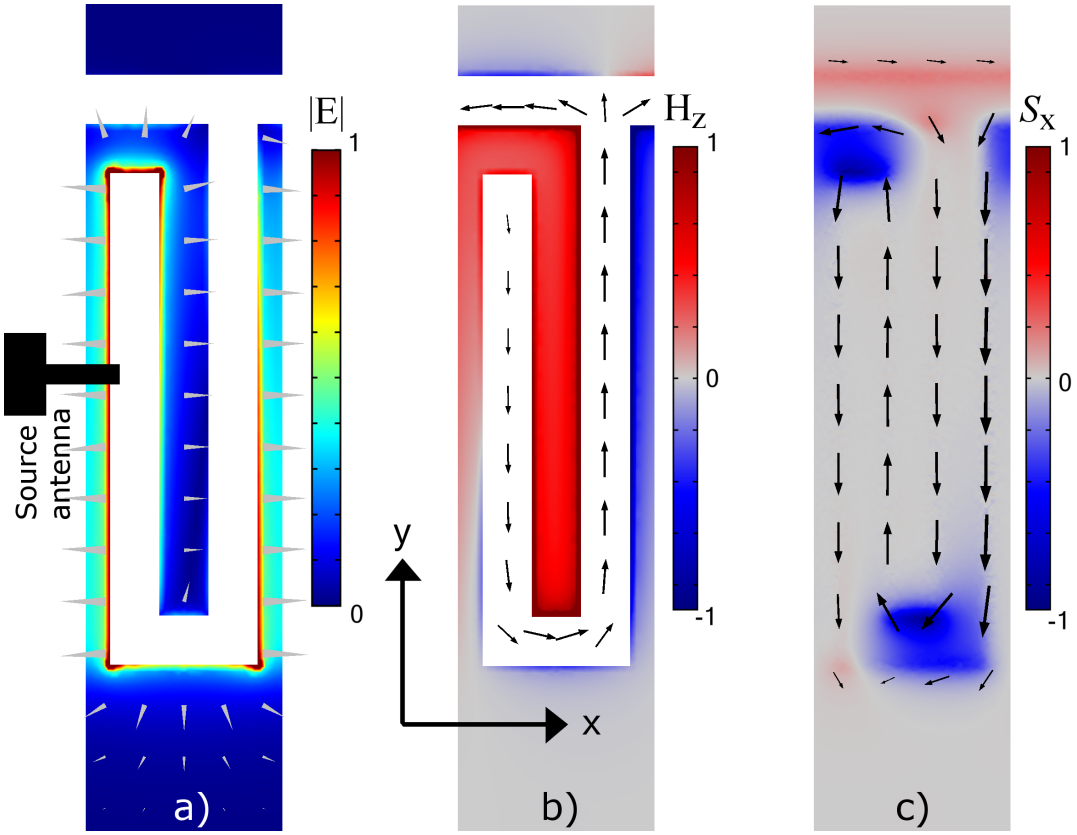

Figure 9.8: a) The normalised electric field magnitude on the top face of the waveguide for $k_x a/\pi = 1$ (edge of first BZ). Arrows represent instantaneous electric field magnitude and direction. The source antenna (see Fig. 3.11) is positioned in order to couple to the mode where the electric field strength is largest. b) The normalised instantaneous normal (z) component of the magnetic field and the current density on the metal surface (arrows). Both have the phase advanced by $\pi/2$ relative to (a). c) The normalised time averaged power flow (colour scale) in the x direction at $k_x a/\pi = 0.8$, along with the Poynting vector (arrows) 0.4 mm above the top face of the waveguide for . White regions represent metal in a) and b).

In experiment, the guided wave is excited and detected using the near-field scanning system described in Sec. 3.5, with the source probe (Fig. 3.11) oriented in an xy plane 1 mm above the sample, positioned between the first and second hooks of the chain as shown in Fig. 9.8a. This placement maximises coupling to the mode via the large electric field amplitude in the x direction where neighbouring elements are capacitively coupled. Like the glide symmetric waveguide in the previous section, this geometry is also based on the 'domino' or 'comb' waveguide; periodically spaced protrusions from a continuous metallic strip. However in this case the system is not based on two coupled arrays but rather a single line of connected elements. The protrusions are bent back on themselves, creating a current loop (arrows in Fig. 9.8b), which when driven at

the resonant frequency induces a large magnetic dipole in the z direction. Fig. 9.8b shows this H_z field of the mode on the Brillouin zone boundary, in the plane of the metallic surface. It is this resonant magnetic polarisability of the array that leads to a negative effective μ_z, whilst the wires, polarisable in the y direction, provide a negative component of permittivity, ε_y. This leads to a negative mode index for a range of frequencies where these two effects exist simultaneously, where the group and phase velocities of the guided mode are antiparallel.

Fig. 9.9 shows the experimental dispersion, with the results from eigenmode simulation overlaid. The frequency range is chosen as to only show the fundamental surface wave, the only mode which exhibits negative mode index. This mode corresponds to a dipolar charge distribution within each protrusion, as seen in Fig. 9.8a-b. Excellent agreement is found between experiment and numerical simulation. Higher order modes exist corresponding to increasing number of charge accumulation points within each hook element, and are discussed in depth in [193].

In the experiment, the source antenna is fixed at the start of the chain, and the second antenna, oriented in the z direction, 1 mm away from the surface, scans in the xy plane. The length of the scan in x covers 95 unit cells of the chain. Tapered graphite-loaded elastomer (Sec. 3.3.3) is placed on the surface at either end of the chain and absorbs electromagnetic radiation, minimising reflections from the end of the sample. The Fourier Transform of the instantaneous electric field profiles at each frequency provides the dispersion diagram in Fig. 9.9 (see Sec. 3.5.3). As the second antenna only scans on one side (positive x) of the source, provided there is no reflection from the sample end any transmitted radiation between the two antenna must have positive power flow (group velocity) and therefore only modes in regions of the dispersion curve with positive gradient are excited. This can be seen in Fig. 9.9 where the simulated dispersion curve (red points) for positive k_x is composed of a positive gradient section, which is detected in the experimental data, and a negative gradient section, which is not. The opposite is true for the negative k_x region. There is a band of frequencies (6.2 - 6.7 GHz) for which a solution exists with positive group velocity (the gradient of the curve $d\omega/dk_x$) and negative phase velocity (ω/k_x). This band of negative mode index does not arise due to the interaction between the light line and a diffracted positive index guided mode, but rather between the light line and a non-diffracted mode with negative index. In this sense, the dispersion of the mode somewhat resembles that of the long-range surface plasmon polariton (LRSPP) supported by a thin metallic sheet at optical frequencies[194]. This analogy can be seen by studying the power flow (Poynting vector) in the direction of propagation, integrated over various regions of the sample. Fig. 9.6 (blue squares) shows the x component of the Poynting vector, S_x, integrated over the entire volume of the unit cell used in simulation, as a function of

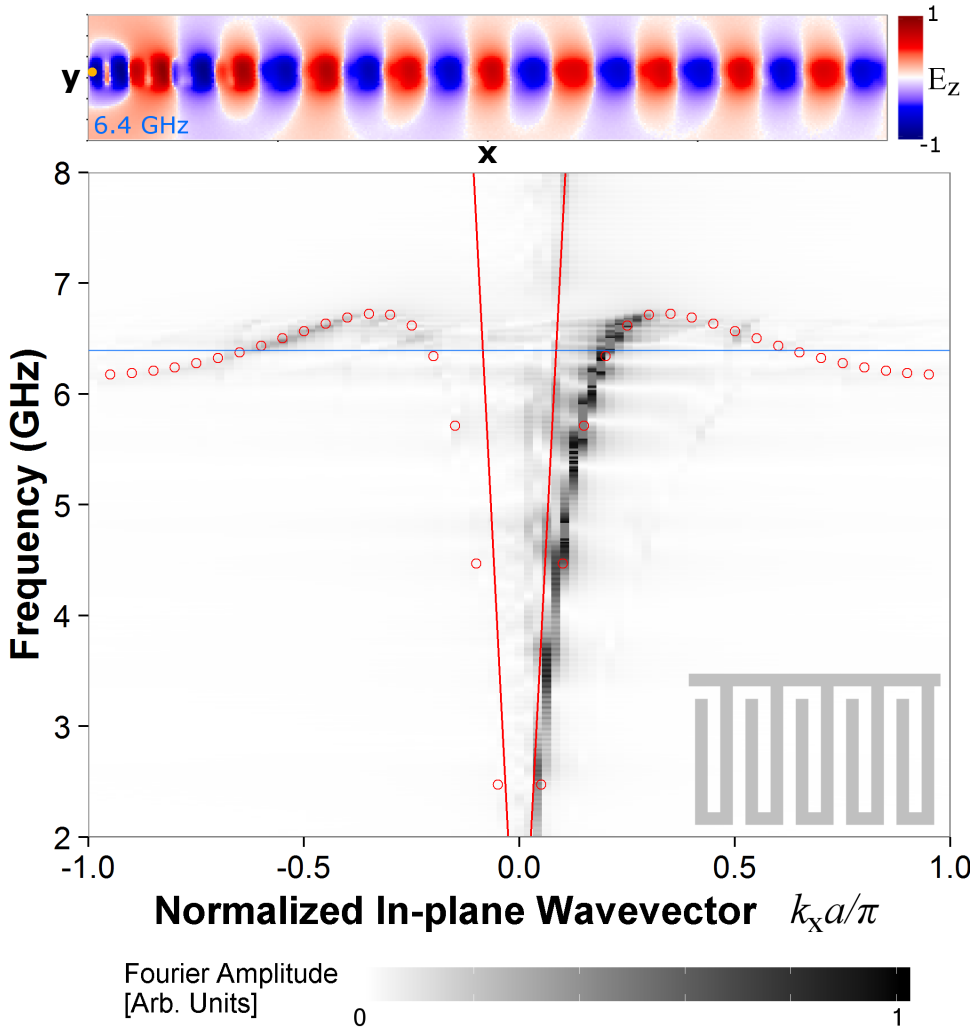

Figure 9.9: Experimentally obtained dispersion curve for the planar hook waveguide (shown inset). Eigenmodes of the system according to numerical modelling are shown as red circles, and the light line as a solid red line. The greyscale signifies the amplitude of Fourier components present in the measured instantaneous field image. The dispersion is obtained via a Fourier Transform of the instantaneous electric field profile across the surface of the sample, an example of which is shown above for a frequency of 6.4 GHz (blue line). The E_z scale has arbitrary units and is normalised to unity.

in-plane wavevector k_x. This volume equates to a box of size (2 mm, 21 mm, 21 mm) in (x,y,z) with the sample positioned in the box centre. The integral of S_x over this volume is proportional to the gradient of the dispersion curve (v_g) in Fig. 9.9 and it passes through zero at $k_x a/\pi = 0.27, 1$. This change in the direction of net power flow at $k_x a/\pi = 0.27$, which leads to the negative mode index region of the dispersion curve,

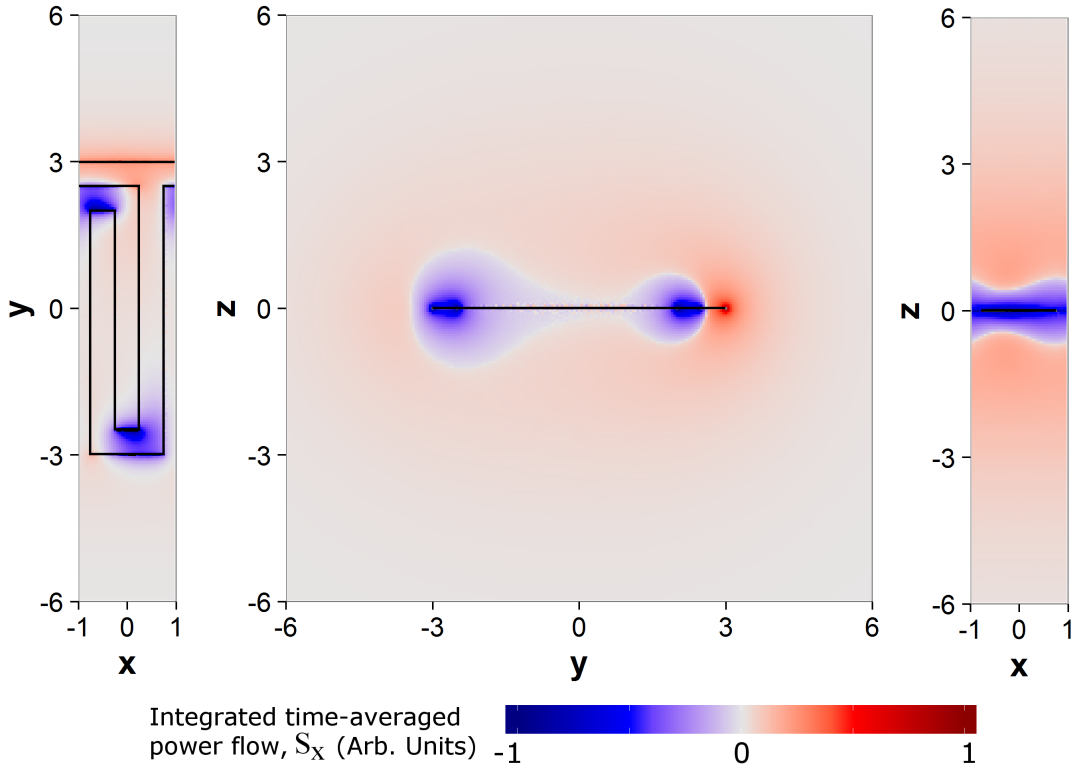

Figure 9.10: The time averaged power flow (given by the Poynting vector) in the direction of mode propagation (S_x) on three orthogonal planes about the unit cell centre. a) S_x in the plane of the waveguide (xy) integrated over the z direction. b) S_x in the yz plane integrated over the x direction. c) S_x in the xz plane integrated over the y direction. The position of the waveguide is shown as solid black lines.

is due to two regions of space with competing S_x. There is an envelope of negative S_x around the hook region of the surface (the protrusions from the continuous ground plane) that is surrounded by an envelope of positive S_x that eventually falls to $S_x = 0$ as the fields of the guided mode exponentially decay away form the structure. This is demonstrated in Fig. 9.10 which shows S_x on the three orthogonal planes (which pass through the unit cell centre) at $k_x a/\pi = 0.27$ where the net power flow is zero. In each figure, S_x has been integrated over the direction normal to the plane (i.e. (b) shows S_x in the yz plane, integrated along the x direction). The two regions described above can be clearly seen, with negative power flow (blue) close to the hook, surrounded by positive power flow (red) strongest near the continuous wire. This resembles the LRSPP which has negative power flow within the metal and positive power flow in the air either side, and is also similar to the negative power flow recently reported within the dielectric layer of the Sievenpiper mushroom array discussed earlier[109] and shown in Fig. 9.2.

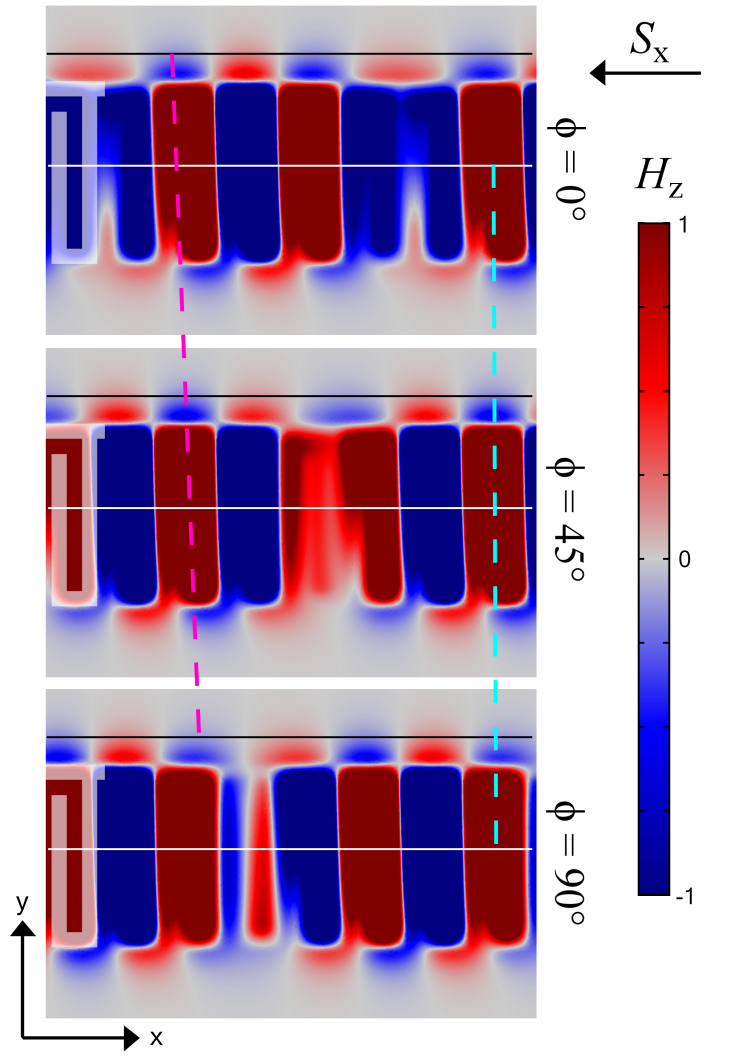

Figure 9.11: The numerically modelled z-component of magnetic field, H_z, 1 mm above the 'hook' waveguide structure. Power propagation along the guide is negative: from right to left, as is the direction of group velocity, v_g. Each successive image shows an advance in phase by 45°. Phase fronts move forwards both along the central plane of the waveguide (white line) outside of the guide (black line), where the mode decays in the ± y direction. The propagation of phase fronts in the same direction everywhere on the guide suggests that the guide is acting as an effective medium, with negative v_g and positive v_p and therefore negative mode index.

The hook geometry supports a mode at lower frequency than the glide domino structure occupying the same sized unit cell, primarily due to the increased resonant length of the elements. The result of this is that the waveguide is very subwavelength ($a < \lambda/25$) and can be described as having effective properties, such as mode index. This means that there is no ambiguity in the direction of phase velocity (as is the

case for the glide domino structure) and the phase fronts can be seen to propagate in the same direction everywhere. This can be seen by comparing Fig. 9.11, which shows the evolution in phase of the simulated instantaneous H_z field on an xy plane 0.5 mm away from the structure, to Fig. 9.7 - the equivalent for the glide domino waveguide. Both correspond to the mode at $k_x a/\pi = 0.8$, which lies in the negative gradient region of their respective dispersion diagrams. The fields are still broadly contained in two regions; an envelope close to the waveguide where the power flow is negative, and an outer envelope where it is positive. However for the hook waveguide, the phase fronts in both regions (traced by pink and cyan dashed lines) propagate in the positive x direction (opposite to v_g), albeit at different speeds. Overall, the group and phase velocities of the mode in the negative gradient section of the dispersion curve are antiparallel, and the mode has a negative mode index.

9.2.3 Split Ring Resonator Waveguide

The third one-dimensional planar waveguide studied is the split-ring resonator chain shown in Fig. 9.3C. This is an adaptation of the hook geometry that enhances the magnetic polarisability in the z direction by replacing each hook element with disconnected rectangular split rings. Arrays of SRRs have been subject to extensive research due to their ability to act as compact resonators, which has led to the design of artificial magnetic media[159]. In addition, arrays of SRRs within a waveguide have also been shown to demonstrate negative index[195][196][197][198]. These negative index waves supported by SRRs are often referred to as magneto-inductive waves[199], due to the fact that a resonant magnetic response is induced by circulating currents, as in the 'hook' elements studied in the previous section. In this section, the SRR is used to enhance the negative power flow (increase gradient of dispersion curve) in a one-dimensional chain by using rectangular SRRs to reduce the effective plasma frequency of the mode, and the dispersion showing this negative mode index region is experimentally determined.

The electromagnetic character of SRRs are often described using the equivalent circuit model as LC resonators[14]; with the current loop acting as an inductive element L and the charge separation across the split providing a capacitance C. The resonant frequency ω_0 of such a resonator is given by $\omega_0 = (LC)^{-\frac{1}{2}}$, and as such can be lowered by increasing L or C[200]. Comprehensive analytical studies of negative index modes on arrays of SRRs can be found in [201][202]. In the present study of a one-dimensional array, ω_0 is lowered by making the geometric path around the ring longer relative to the periodicity, compared to square or circular SRRs. The result is an array of rectangular SRRs as shown in Fig. 9.3C. The dispersion of the mode supported by the waveguide

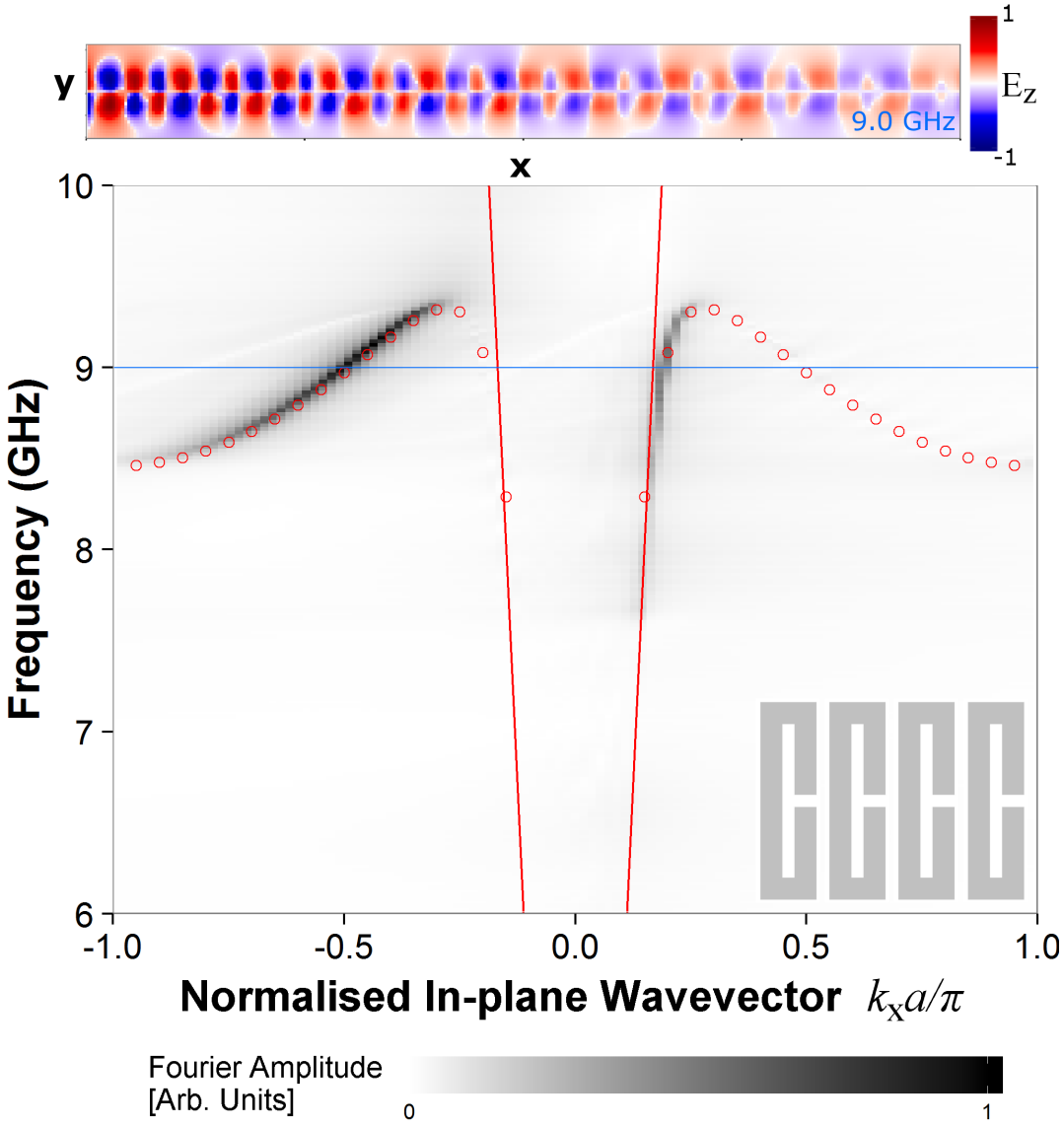

Figure 9.12: The experimentally obtained dispersion curve for the lowest order mode supported by the split-ring resonator chain. The x-axis spans from zero to the edge of the first Brillouin zone at $k_x a/\pi = 1$. The results from eigenmode modelling are shown as red circles and the light line is marked in red. For in-plane wavevector with magnitude above 0.26, the mode supported has counterpropagating group and phase velocities, and hence negative mode index.

is shown in Fig. 9.12. The mode was coupled to via the large capacitive electric field across the split in the first ring element, as shown in Fig. 9.13a, which shows the electric field magnitude and vector (arrows) of the eigenmode at the Brillouin zone, plotted on a plane containing the metallic surface. The Fourier amplitude of the negative

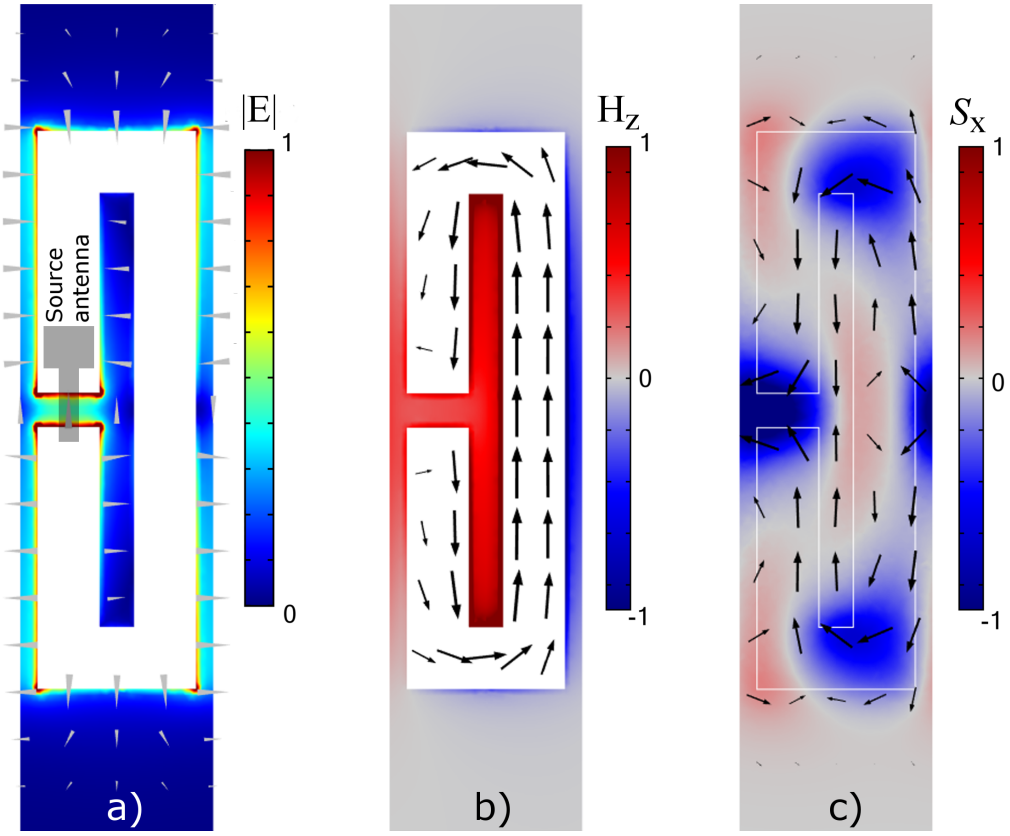

Figure 9.13: a) The normalised electric field magnitude on the top face of the waveguide for $k_x a/\pi = 1$ (edge of first BZ). Arrows represent instantaneous electric field. b) The normalised instantaneous normal (z) component of the magnetic field and the current density on the metal surface (arrows). Both with the phase advanced by $\pi/2$ relative to (a). c) The normalised time averaged power flow in the x-direction at $k_x a/\pi = 0.9$, along with the Poynting vector 0.4 mm above the top face of the waveguide.

mode index region relative to the positive mode index region in this configuration is enhanced compared to the 'hook' waveguide dispersion in Fig. 9.9. This is mostly due to an increased group velocity (gradient) of the mode resulting in greater power transfer between the two antennas than in the 'hook' array and may also be due to increased coupling strength (increased field overlap between the mode and the antenna's near-field). The eigenmode positions obtained via finite element method modelling are overlaid in Fig. 9.12 as red circles and agree well with experimental data. As the source antenna is positioned at one end of the SRR chain and the scanning area for the second antenna is only on one side of the source, only modes with positive power flow (positive group velocity) can couple the two antenna. For this reason, the region of positive mode index is seen on the right hand side of the dispersion curve ($v_p, k_x > 0$), whereas the negative mode index section is on the left ($v_p, k_x < 0$).

Similarly to the 'hook' waveguide, the current loop associated with the resonance creates a large magnetic field in the z-direction (Fig. 9.13b). This gives the waveguide a magnetic polarisability, and hence a negative effective permeability in the z-direction. Fig. 9.13c shows the time-averaged Poynting vector (arrows) of the eigenmode solution at $k_x a/\pi = 0.9$, along with the net x-component of the power flow (colour scale). This shows that the SRR is similar to two hook waveguides mirrored in the y direction, with two meandering paths of the Poynting vector evident.

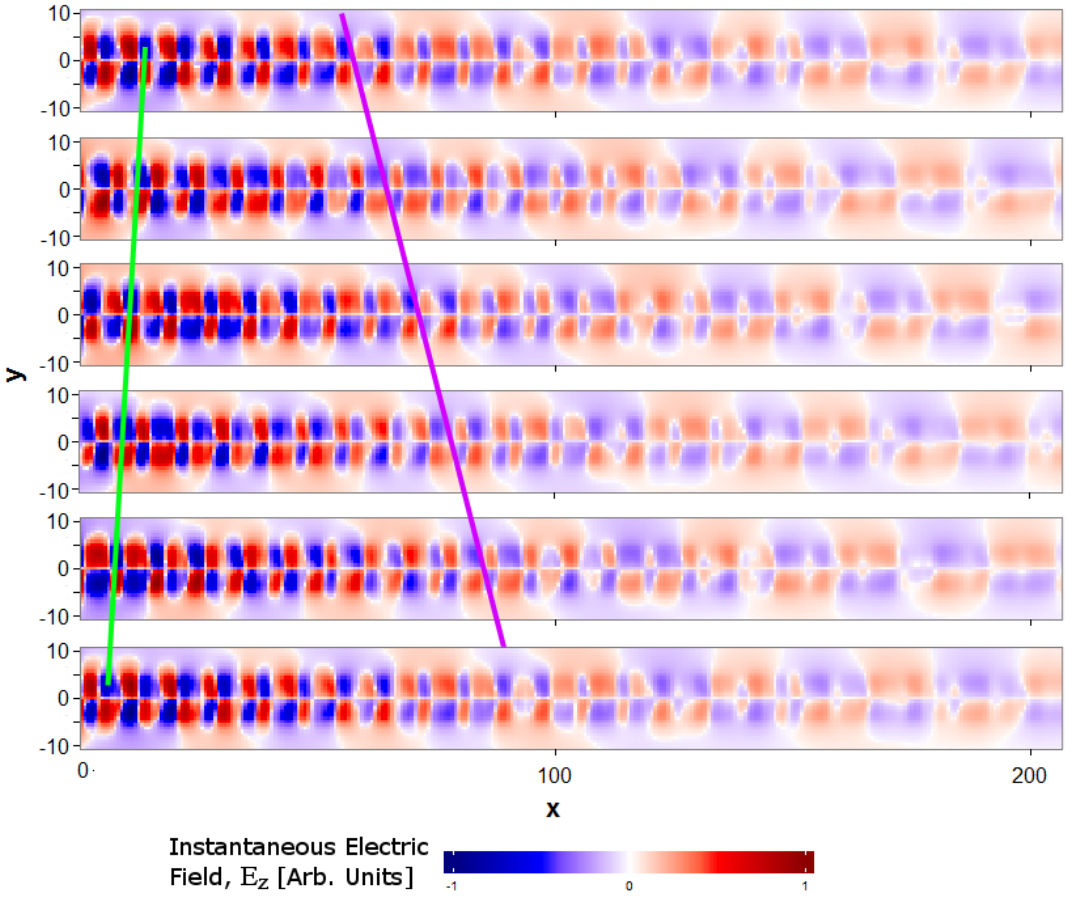

Figure 9.14: The experimentally measured z-component of the instantaneous electric field, on a plane 1 mm above the split-ring resonator waveguide. Each successive plot is advanced in phase by 60° and the phase fronts traced to observe the direction of phase velocity. A positive v_p wave can be seen by tracing the minimum in E_z along a line at $y = 10$ mm and a negative v_p wave (green line) along $y = 3$ mm, both with positive v_g.

At a frequency for which there are two solutions (i.e. in the range 8.5 - 9.4 GHz), the instantaneous electric field should show that their phase is counterpropagating. For instance, at 8.7 GHz (marked in Fig. 9.12), there exists two modes with positive

group velocity. The first has positive phase velocity, with a normalised wavevector of 0.18, whilst the second has negative phase velocity and a wavevector of -0.68. Fig. 9.14 shows the experimentally measured instantaneous electric field (z component) at 8.7 GHz, with sequential steps in phase of 60° from top to bottom. The positive v_p mode extends further into the air surrounding the guide (as it appears more grazing-radiation-like due to mode position being close to the light line) and its phase fronts trace the purple line in Fig. 9.14. The negative v_p mode has greater confinement in y and z directions and consequentially reduced propagation length along the guide (x direction). Its phase fronts (green line) are shown to move backwards, towards the source, as the phase is advanced.

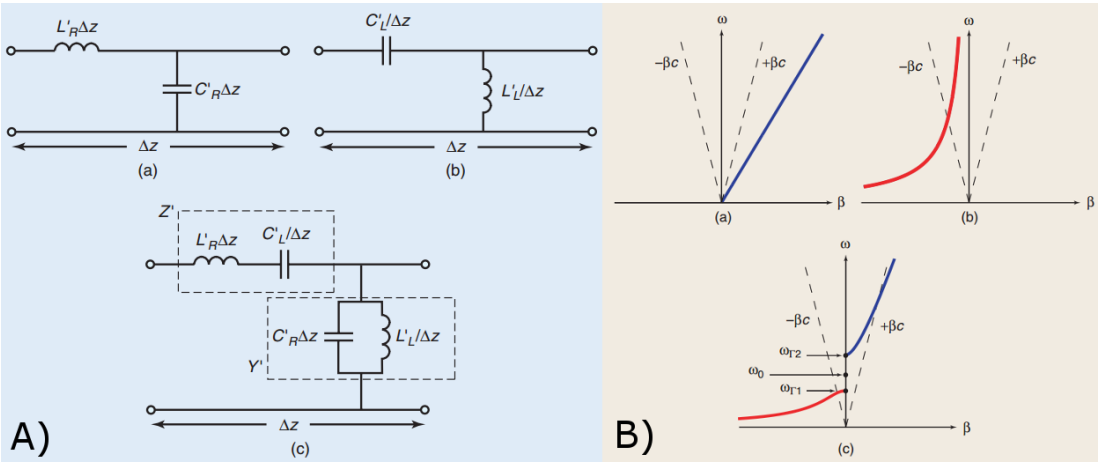

Figure 9.15: The equivalent circuit (A) and dispersion curves (B) for a transmission line that is right handed (a), left handed (b) and composite right/left handed (c).

As mentioned earlier, chains of elements such as those studied in this section can be described by equivalent circuits. The chains act as a combination of right and left handed transmission lines (TL). The equivalent circuit and dispersion of a typical right-handed TL is shown in Fig. 9.15A-a and B-a respectively. These figures are taken from [203]. The circuit consists of a series inductance L_R and shunt capacitance C_R. The reverse of this, a series capacitance C_L and shunt inductance L_L (Fig. 9.15A-b) describes a purely left-handed transmission line, which disperses according to Fig. 9.15B-b. A generalised transmission line is described as composite right/left handed (Figs. 9.15A-c and B-c). The propagation of the mode supported by this composite transmission line at low frequencies has left-handed behaviour, and its dispersion (shown as red line in Fig. 9.15B-c) is qualitatively similar to that of the hook and SRR waveguides. However, the modes supported by these two structures also hybridise with grazing electromagnetic radiation (dashed line in the figure). The dispersion of the mode in the composite

transmission line picture is described by

$$\beta(\omega) = -\sqrt{\omega^2 L_R C_R + \frac{1}{\omega^2 L_L C_L} - (\frac{L_R}{L_L} + \frac{C_R}{C_L})} \tag{9.4}$$

where $\beta = k_x$ is the propagation constant, and $\omega = 2\pi f$ is the angular frequency. Future work in this area would focus on describing one-dimensional planar waveguides in terms of inductance and capacitance in order to predict the dispersion of supported modes.

9.3 Two-Dimensional Planar Waveguide

Negative mode index for a one dimensional waveguide is achievable using a subwavelength array of anisotropic current loops, such as the 'hook' waveguide or chain of split ring resonators discussed thus far. Likewise, analytic modelling of a two-dimensional array of SRRs has shown negative mode index in one direction of propagation[204]. In this section, a 2D array of spiral elements are shown to exhibit negative mode index in all directions within the plane of the array, in a similar manner to the Sievenpiper mushroom array shown in Fig. 9.2. This work demonstrates potential for a surface wave superlens, a 2D analog to the superlensing phenomenon associated with negative index.

9.3.1 2D Quadrafilar Spiral Array

Fig. 9.16 depicts a section of the spiral array studied. The unit cell contains a single quadrafilar (four-armed) spiral hole within a continuous metallic sheet. Each arm contains five turns and revolves around an angle of 450°. The arm width, w, and gap, g, are both 200 μm; the smallest feature size that can be fabricated consistently across the experimental sample. The periodicity of the square array is $a = 4.4$ mm $(11w + 11g)$, and the entire rectangular sample contains approximately 90 × 60 unit cells. The separation between neighbouring resonators is minimised such that the spiral arm length can be maximised, reducing the resonant frequency and enhancing the bandwidth of negative mode index. The sample is produced using the print and etch method described in Sec 3.2.2 and comprises an 18 μm copper layer supported on a Mylar substrate of thickness $t = 0.05$ mm. The structure is modelled using an eigenmode simulation in COMSOL (Sec. 3.7.1), with the metallic region approximated as an infinitesimally thin sheet of perfect electric conductor (PEC).

Experimental data is obtained by measuring the transmission between two stripped coaxial antennas, both oriented normal to the spiral array surface, 1 mm away on either side. One antenna is fixed in the centre of the sample, whilst the other is scanned across

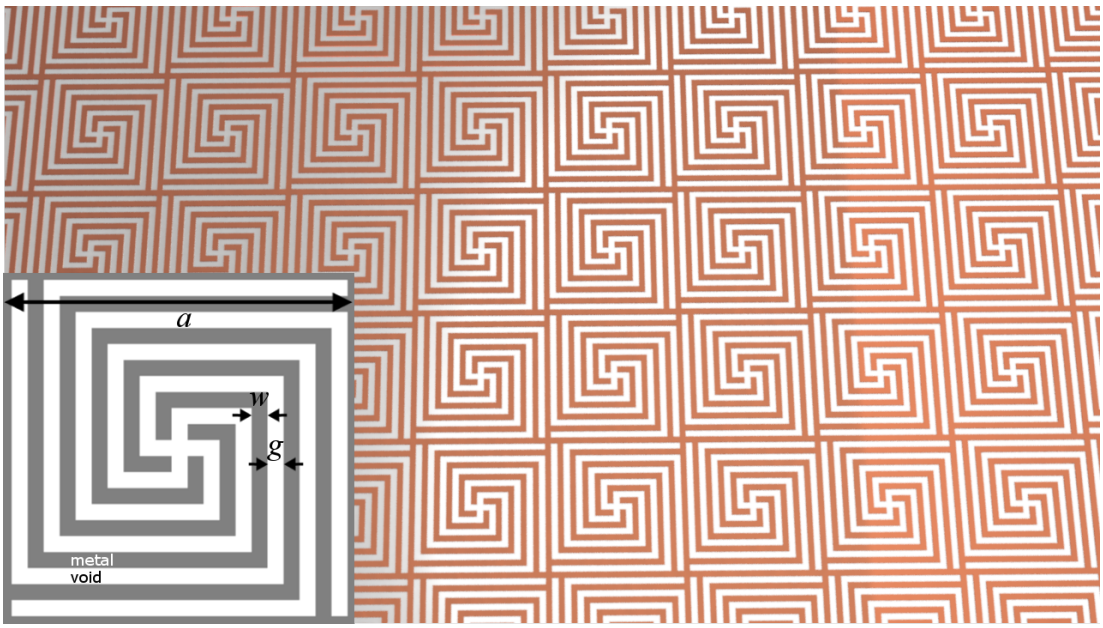

Figure 9.16: The quadrafilar spiral geometry. The unit cell (inset) consists of a single four-armed spiral shaped hole in a metal sheet. Each arm undergoes five 90° bends creating a square quadrafilar spiral with periodicity $a = 2.8$ mm. The arms have width $w = 200$ μm and the gap between them $g = 200$ μm.

a square region centred on the fixed antenna. This process builds an image of the normal component of the complex electric field (E_z) of any modes that can transfer power between the two antennas at a single frequency. This includes both bound surface waves and waves propagating through free space above the surface. A fast fourier transform (FFT) of the instantaneous field image, $E_z(x, y)$ produces a reciprocal space image $\mathcal{F}(k_x, k_y)$ containing maxima corresponding to in-plane wavevectors present in the real-space image. This reciprocal-space image, obtained for a single frequency, is known as an isofrequency (or equi-energy) contour. Repeating this process for a range of frequencies allows dispersion curves to be plotted along a given in-plane direction in the k_x, k_y plane. This process is detailed in Sec. 3.5 of Chapter 3.

Fig. 9.17 shows the result of this Fast Fourier Transform; the Fourier amplitude $\mathcal{F}$ as a function of frequency and in-plane wavevector. The x-axis traces a path in reciprocal space defined by the points of symmetry Γ, X and M (see inset), commonly known as the irreducible Brillouin zone (IBZ). Eigenmode modelling in COMSOL (Sec. 3.7.1) yields the frequency of modes supported by the surface for a given in-plane wavevector, the results of which are shown as red circles in Fig. 9.17. A good agreement is found between finite element method simulation and experiment, although a small shift in frequency (≈ 100 MHz) is seen due to inconsistencies in the sample, with an estimated spread Δw in spiral arm width of ± 50 μm. This spread is a combination of limitations

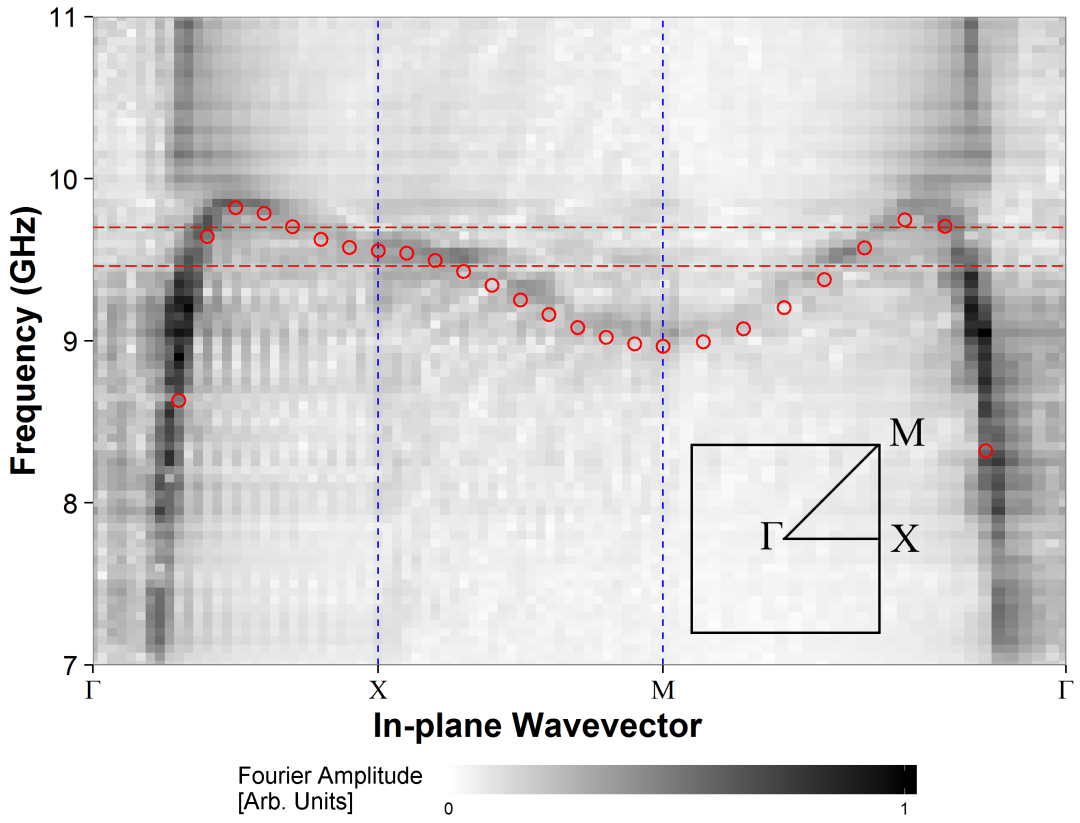

Figure 9.17: The 2D dispersion of the spiral array, covering the irreducible Brillouin zone defined by the points Γ, X and M in reciprocal space. Eigenmode positions according to numerical modelling are shown as red circles. The red dashed lines correspond to frequencies at which isofrequency contours are plotted in Fig. 9.18.

in printing resolution and variation in Ferric Chloride temperature during the etching process. The dispersion bears resemblance to that of the Sievenpiper mushroom shown in Fig. 9.2 and published in [2][109].

The dispersion diagram shows that there is a negative mode index solution for propagation in both ΓX and ΓM directions, although the positive index regions have much larger Fourier amplitude. Similarly to the 'hook' waveguide studied above, this indicates that power transfer between the antennas is much lower for the negative index mode than for the positive index mode. This could also be due to weaker coupling efficiency for the negative index mode. Nevertheless, there exists an inevitable limitation of negative index bound waves; as the momentum of the mode increases and the mode disperses away from the light line, its propagation length reduces as the group velocity slows. Therefore, a perfect lens for surface waves using a metasurface such as

the quadrafilar spiral array must consist of a slab of only a few elements long.

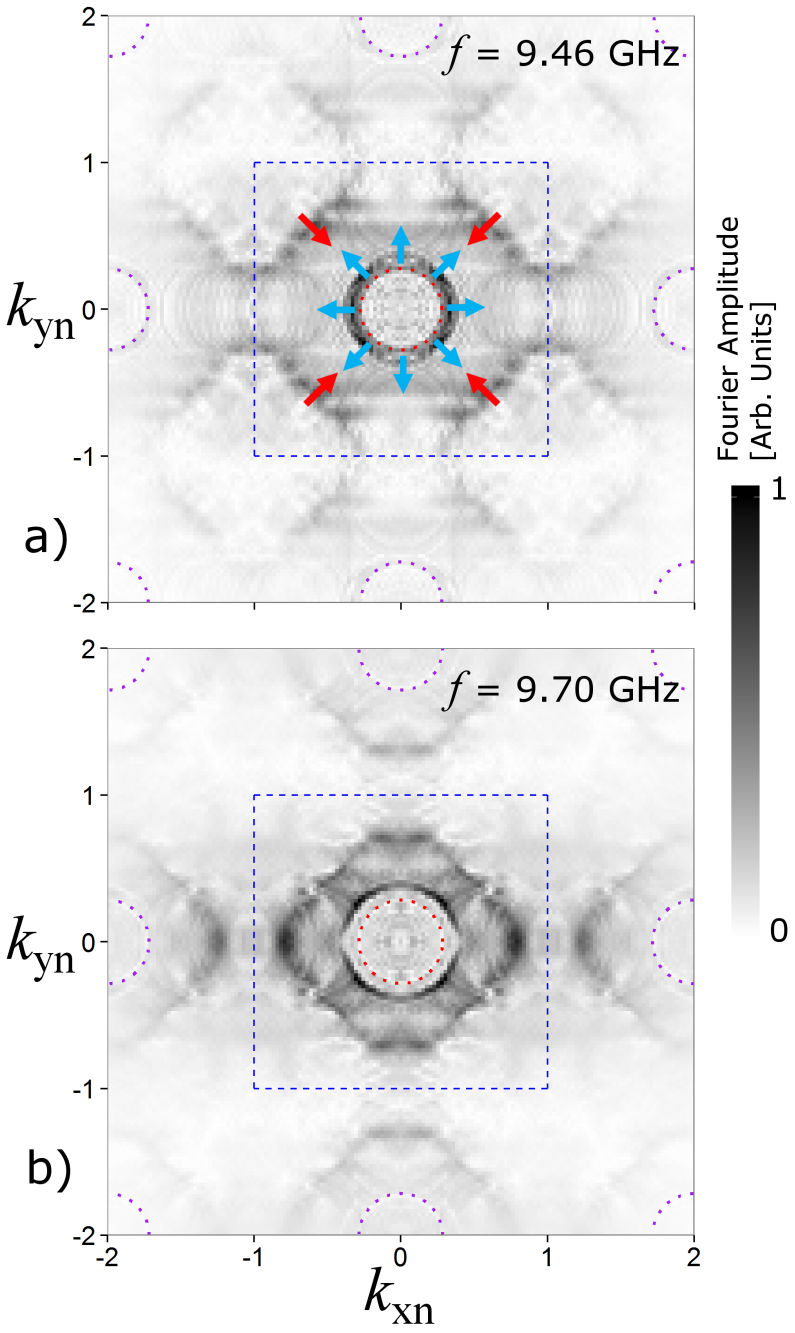

Figure 9.18: Isofrequency contours at a) 9.46 GHz b) 9.7 GHz (marked as red dashed lines in Fig. 9.17). In a) the direction of group velocity (power flow) is represented as arrows (Blue: v_g positive. Red: v_g negative)

In order to act as an isotropic effective index negative index surface, the negative

index mode must propagate isotropically and therefore its isofrequency contour must be approximately circular. Fig. 9.18 shows two isofrequency contour maps according to experimental data. The first, obtained at 9.46 GHz (red dashed line in Fig. 9.17), shows an isotropic forward propagating (blue arrows) mode with positive index, and a backward, negative index mode (red arrows) along ΓM. There is no negative index mode along ΓX at this frequency. At 9.7 GHz (Fig. 9.18b), a band gap has formed along XM, resulting in a closed contour around $k_x, k_y = (0, 0)$ with negative mode index. However, the index is greater along ΓM than ΓX and the contour is square. This presents a shortcoming in using this structure as a perfect lens for surface waves, however improved isotropy could be achieved by using a hexagonal lattice.

9.4 Conclusions

In this chapter, surfaces that support bound surface waves with negative mode index have been studied. Initially, numerical modelling of coupled domino arrays showed that the dispersion contains a region of negative gradient (negative group velocity) that has both a positive and negative contribution to the in-plane wavevector k_x (phase velocity). The mode appears as a superposition of a forward and a backward going wave and hence the sign of phase velocity is ambiguous. This is due to the fact that the periodicity of the structure is not sufficiently smaller than the operating wavelength that diffracted modes can be ignored. Despite this, the phenomenon of negative refraction is known to occur in photonic crystals, however effective properties such as permittivity, permeability and index should not be assigned as the material is not acting as an effective medium.

A single domino array was experimentally shown to exhibit negative mode index when each of the protrusions is lengthened and bent into a hook shape. This simultaneously lowers the resonant frequency of each element of the array (making the periodicity 1/25 of the resonant wavelength) and provides a magnetic polarisability due to the presence of a current loop (which gives the medium an effective negative permeability). Similarly, a one-dimensional array of split ring resonators, which has been shown in other studies to support a negative index mode within a metallic waveguide, was studied. The negative index mode was excited experimentally in the non-radiative region of the dispersion diagram and instantaneous electric field profiles demonstrated directly the phase fronts of the mode evolving 'backwards' towards the source. The SRR was elongated in the transverse dimension in order to reduce its resonant frequency and increase the bandwidth of negative mode index to 8.5 - 9.4 GHz.

Finally, a two-dimensional array of quadrafilar spiral elements was experimentally shown to support a negative index mode in all in-plane directions. This geometry contains the current loops necessary for negative effective permeability whilst maintaining

four-fold rotation symmetry of the unit cell. Isofrequency contours demonstrated that the mode propagation is not isotropic, limiting the use of this structure as a superlens. However, this is the first experimental demonstration of a negative mode index surface wave supported by a single metallic layer at microwave frequencies. Future work in this area will aim to create a surface wave superlens by using a hexagonal lattice in order to enhance the isotropy of the negative index mode.

Chapter 10

Future Work: Non-periodic Metasurfaces

In this chapter, two non-periodic metasurfaces composed of rhombus tilings are studied. It is known from the study of the Fibonacci checkerboard in Chapter 7, as well as other studies, that surface modes can be supported even in the absence of translational symmetry. The characteristics of these modes depend heavily on the reciprocal space wavevector components (the 2D Fourier spectrum) present in the surface geometry. A periodic array contains discrete delta function-like peaks in its Fourier spectrum. A quasiperiodic array also has well defined peaks yet in general the strength of scattering associated with them is weak.

The aim of this chapter is to verify the understanding above by measuring the isofrequency contours of modes supported on two non-periodic arrays; the Penrose tiling and a quasiperiodic diamond tiling. The symmetry of these contours is expected to mimic any symmetry in the tiling. Further, the discrete peaks in the Fourier spectrum of the surface should match the scattering wavevectors for any supported surface waves, as was seen for the Fibonacci checkerboard.

This chapter presents some preliminary results showing evidence of surface waves on quasiperiodic metasurfaces. Existing work on quasiperiodic tilings has focussed largely on their scattering parameters and diffraction patterns within the radiative regime[205][206], however its full band structure has also been calculated[206] revealing multiple energy gaps attributed to the quasiperiodicity[207] and the coupling to surface plasmons supported by quasiperiodic gratings has been experimentally studied[208]. A comprehensive review of the topic can be found in Ref.[209]. The topic of quasicrystals is an extensive one, and future work is required to sufficiently characterise surface wave propagation in the context of quasiperiodic arrays. This work will include enhancing the coupling strength to bound surface modes, and tailoring the Fourier spectrum to

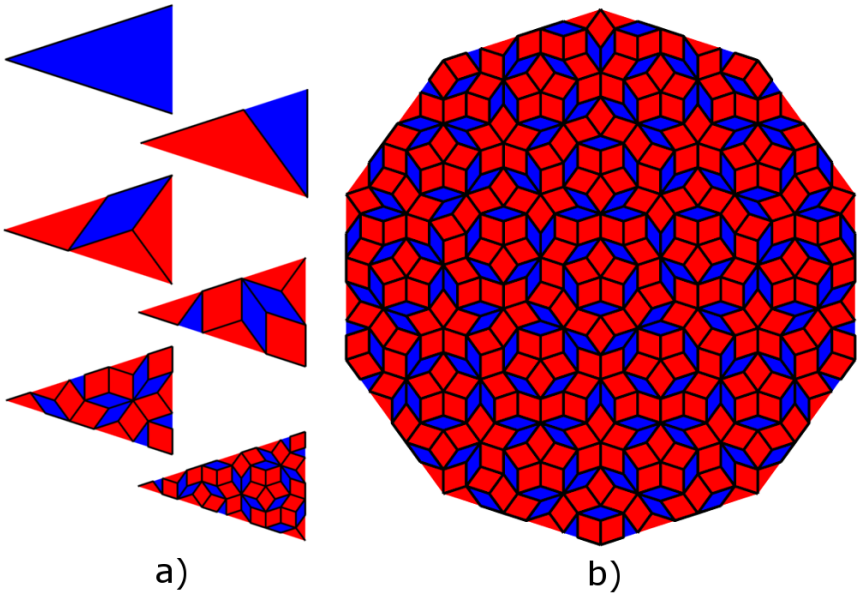

Figure 10.1: a) The substitution method for generating a segment of the aperiodic Penrose tiling shown in b). The tiling is composed of narrow (36°, blue) and wide (72°, red) rhombs and has 5-fold rotational symmetry about its centre.

give the desired surface wave band structure.

10.1 Generation of Non-periodic Tilings

The Penrose tiling geometry is an aperiodic tiling formed of a subset of two rhombs, with interior angles 36° (blue) and 72° (red) as depicted in Fig. 10.1b. This subset of tiles can not be used to produce a periodic tiling. The quasiperiodic Penrose tiling can be generated in a number of ways, one of which is by substitution in a manner similar to the Fibonacci sequence studied in Chapter. 7. The tiling has 5-fold rotational symmetry about its centre with the whole tiling forming a decagon. The substitution method shown in Fig. 10.1a shows one tenth of the tiling, and uses triangular tiles equivalent to half of the 36° and 72° rhombs. Initially, the 1/10 segment is simply a narrow triangle which is divided into a narrow and a wide triangle scaled by $1/\gamma$ where γ is the Golden Ratio. The same substitution is done for all subsequent narrow (blue) triangles, and each of the wide (red) triangles is replaced with two wide and a narrow. Five iterations of this process are shown in Fig. 10.1a after which the entire tiling resembles that shown in Fig. 10.1b.

The tiling contains no translation symmetry, and hence no translational periodicity. Despite this, finite-sized regions of the sample can be found at multiple positions in the sample. The size of any given region scales with the average distance to a matching

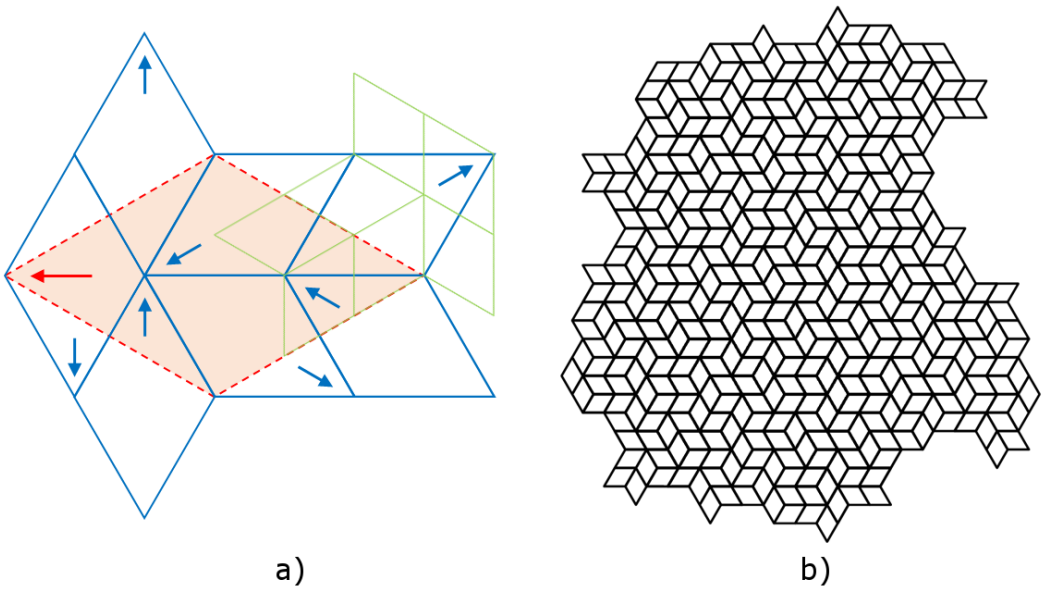

Figure 10.2: a) The substitution method for generating the quasiperiodic diamond tiling shown in b). Each diamond (red) is divided into 8 smaller diamonds in the shape of an arrow (blue). These are then divided again (green).

region elsewhere on the tiling, i.e. a smaller region will repeat over shorter distances than a large region. This is typical of quasiperiodic tilings and quasicrystals.

A diamond-shaped (60° rhombus) tile alone can also produce a quasiperiodic tiling using a substitution method. This tiling has no centre, and hence no rotational symmetry. Each diamond is assigned an orientation and is divided into 8 smaller diamonds forming an arrow-like shape as shown in Fig. 10.2a. The first iteration of this is shown in blue, with one arrow of the second iteration shown in green. After 10 iterations the tiling in Fig. 10.2b is produced.

Fig. 10.3a-c shows a section of two quasiperiodic tilings under study, along with a periodic 'box diamond' tiling for comparison. The underlying lattice for the box tiling is hexagonal, with a lattice vector of length $a = 2L\cos(30°)$, where L is the side length of each rhombus. The term 'box' is chosen as the unit cell of the structure resembles three sides of a cube viewed at an elevated angle. Image processing software 'ImageJ' is used to perform a Fast Fourier Transform (FFT) of each tiling, which are shown alongside the real-space images in Fig. 10.3d-f. The brightness and contrast of these FFTs has been decreased and increased respectively for print clarity. The FFT of the Penrose tiling (Fig. 10.3d) clearly shows the rotational symmetry of the structure; discrete points of large Fourier amplitude map the vertices of decagons around the centre which corresponds to $(k_x, k_y) = (0, 0)$. By definition, this quasicrystal contains many more peaks in its Fourier spectrum, however for this study only those with the

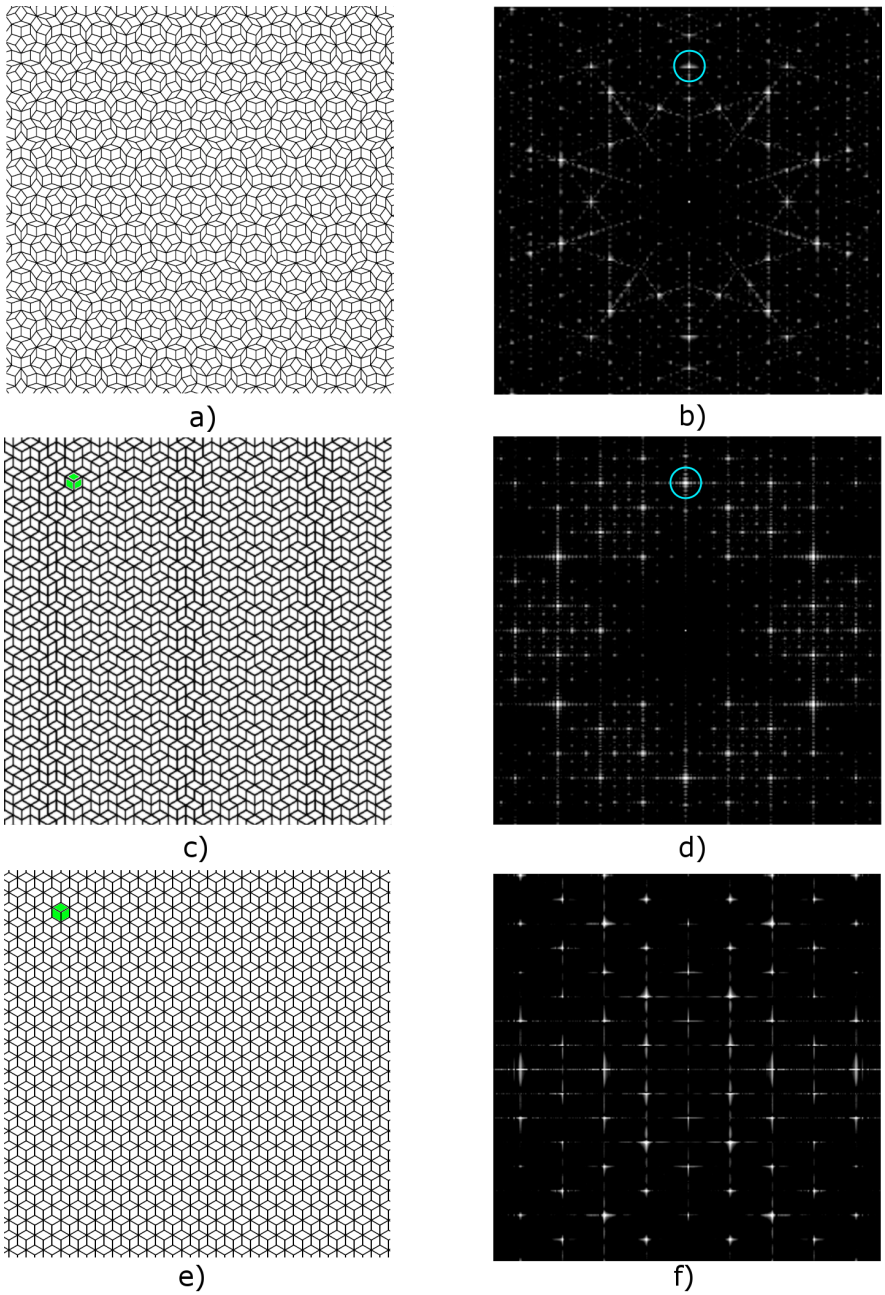

Figure 10.3: A section of the Penrose (a), quasiperiodic diamond (c) and box diamond (e) tilings. Black lines represent copper traces on the sample of width 0.5 mm. Each rhomb has side length $L = 5$ mm. The corresponding Fourier spectra for the images in a,c,e are shown in b,d,f.

largest Fourier amplitude are of interest, as it is these points which correspond to planes in the structure from which significant scattering of surface waves can occur. Fig. 10.3e shows the FFT for the quasiperiodic diamond tiling. The fourier spectrum

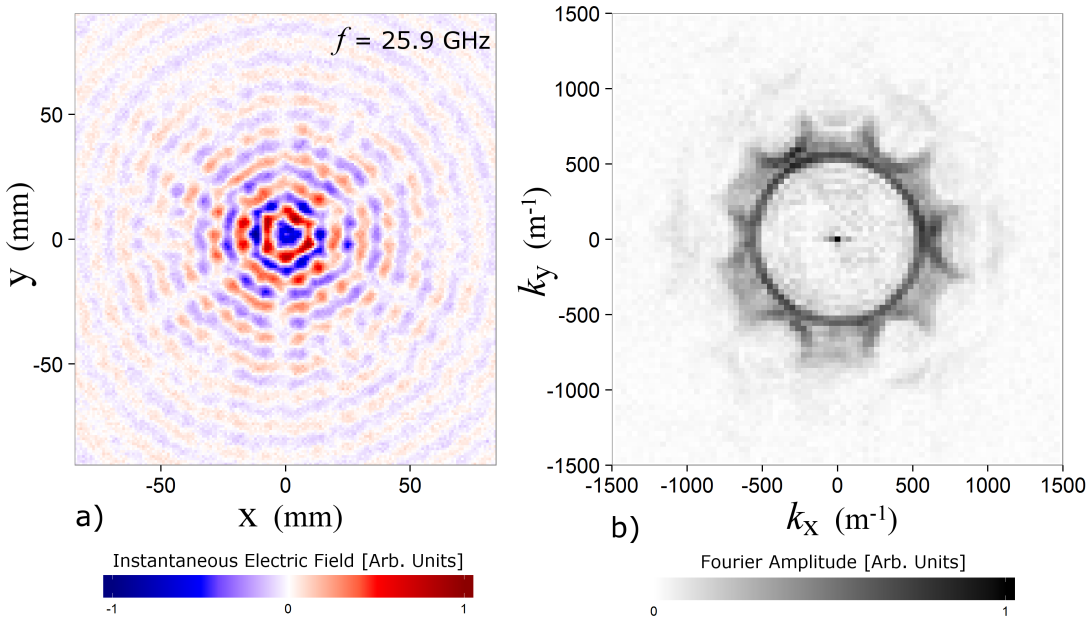

Figure 10.4: a) The normal component of the instantaneous electric field, measured on a plane 1 mm above the quasiperiodic diamond sample at 25.9 GHz. The source is positioned in the centre of the image. b) The FFT of the image in (a). Peaks in the Fourier amplitude map out the isofrequency contours of modes supported by the metasurface.

again contains multiple discrete peaks of varying amplitude. The symmetry however resembles that of the periodic 'box' diamond tiling (the FFT for which is shown in Fig. 10.3f). In fact, the two FFTs are very similar in terms of the positions of Fourier amplitude peaks, with additional peaks due to the quasiperiodicity apparent in Fig. 10.3e. This similarity is perhaps not surprising given that there is some short range order in the quasiperiodic diamond tiling; in some small regions the structure appears like the 'box' tiling, with the three-rhomb hexagon (highlighted in Fig. 10.3b and c) appearing many times.

Metallic hole arrays are fabricated using the print and etch method outlined in Section. 3.2.2. For the tilings described in this section, each rhombic element corresponds to a hole in the copper laminate. The laminate is formed of a 50 μm Mylar substrate, coated with 18 μm of copper. The side length of each rhomb is chosen as $L = 5$ mm, and each of the samples is 400 mm $\times$ 280 mm in size.

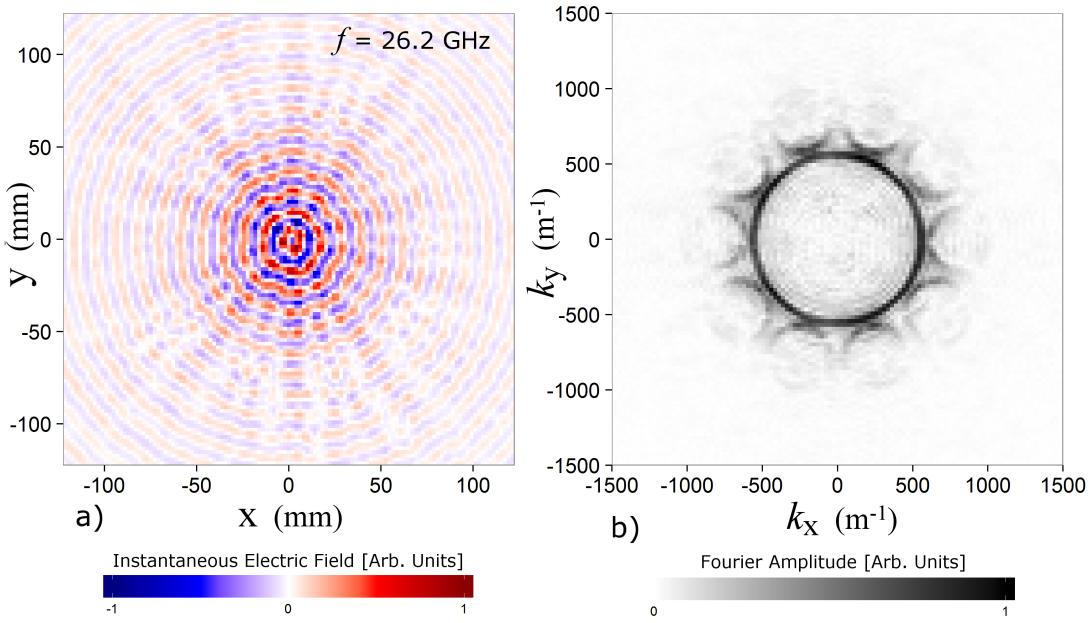

Figure 10.5: a) The normal component of the instantaneous electric field, measured on a plane 1 mm above the Penrose tiling sample at 26.2 GHz. The source is positioned in the centre of the image. b) The FFT of the image in (a). Peaks in the Fourier amplitude map out the isofrequency contours of modes supported by the metasurface.

10.2 Experimental Results

Near field excitation of surface waves is achieved using the method set out in Sec. 3.5. A map of the normal component of the electric field is obtained for a given frequency and the FFT of this image is the reciprocal space isofrequency contour.

10.2.1 Quasiperiodic Diamond

Fig. 10.4b shows an experimentally obtained isofrequency contour at 25.9 GHz for the quasiperiodic diamond metasurface. The zeroth order and diffracted light circles are marked as dashed lines. These diffracted orders correspond to 6 peaks in the Fourier spectrum of the sample image, one of which is marked in Fig. 10.3e. The contour shows that a bound surface wave, with momentum beyond that available to incident radiation, is supported by the structure. Six closed loops are formed, resulting in six directions in which a propagating mode is not supported. This can be seen in the real space field map in Fig. 10.4a.

10.2.2 Penrose Tiling

Fig. 10.5 shows the real and reciprocal space map of the electric field, 1 mm above the Penrose tiling sample, at a frequency of 26.2 GHz. Again, closed loop contours are formed which have greater momentum than zeroth order and diffracted radiation. Propagation of the surface wave is limited to ten directions (Fig 10.5a), and a variation in field amplitude is apparent. This result is intriguing as it demonstrates a symmetry in the field profile which can not be created by any periodic structure, due to the lack of five-fold rotationally symmetric regular tilings.

10.3 Conclusion

In this chapter, some preliminary experimental results have shown the presence of a bound surface mode supported by two non-periodic arrays; the Penrose tiling and a quasiperiodic diamond tiling. Despite the lack of translational symmetry, these metasurfaces can support bound modes due to the presence of peaks in the Fourier spectrum of the tilings. In other words, there still exists planes from which partial scattering of surface waves can occur. The Penrose tiling result shows that the propagation is limited to ten beams from the point source, a field profile which can not be excited on a periodic lattice.

Future work in this area will focus on this advantage of increased degrees of symmetry in quasicrystals, which can also have 8, 12, 16 fold rotational symmetry. An enhancement of the coupling strength to these modes is required, in order to enhance the field amplitude of the surface wave relative to free space radiation.

10.4 Other Future Work

In addition to the study of surface waves supported on quasiperiodic metasurfaces, there are other extensions of the work presented in this thesis that will be carried out in the future.

Surface wave propagation on the disordered checkerboard arrays studied in Chapter 7 was not studied directly in this thesis. Future work in this area would focus on mapping the near fields of a random structure, with the potential realisation of Anderson localisation; hot spots in the electric field which occur in random media.

Secondly, as discussed previously in Chapter 8, mode conversion from a surface wave to an edge wave could be explored. This requires matching the impedance of the surface to that of the edge, as well as ensuring there is some field overlap between the two, maximising the conversion of power. The intention of this is to minimise scatter

loss of the surface wave in systems where propagation length is greater than the size of the array. An edge wave that can be coupled to via a surface wave will also be 'leaky', i.e it will radiate into the surface at a particular angle. A study of an adiabatically graded edge would allow one to observe a transition from a bound edge wave to one which is leaky.

Finally, the planar negative mode index metasurface studied in Chapter 9 will be used in order to fabricate a surface wave superlens (see Fig. 9.1b). This requires a second metasurface with *positive* mode index in which can form the surrounding media either side of the quadrafilar spiral array. A good candidate for this metasurface would be an identical spiral array with shorter arm length. This would increase the asymptotic frequency of its surface mode without heavily distorting the field profile. A complete equivalent circuit model which describes the structures studied in Chapter 9 as composite left and right handed transmission lines could be formulated. Using this the geometry could be optimised to maximise the bandwidth of negative mode index.

Chapter 11

Conclusions

The initial study in this thesis focused on polarisation manipulation using 3 layer metasurfaces. In Chapter 4, a reflecting anisotropic microcavity array was presented, which converted linearly polarised incident radiation to its orthogonal polarisation state upon reflection due to linear birefringence. Absorption in the resonant cavities was minimised, resulting in 98% reflected intensity with converted polarisation over a 2.5 GHz band centred at 10 GHz. A modification of the geometry was shown to provide linear to circular conversion over a similar bandwidth. In Chapter 5, a chiral metasurface was used to provide a rotation of linearly polarised radiation upon transmission through the structure. This was possible due to circular birefringence; a differential phase change for left and right handed polarisation. The structure contains two metallic layers patterned with cross-shaped elements in a square array, with those of the bottom layer rotated by 22.5° with respect to the upper layer. The origin of optical rotation in such chiral metasurfaces was explained as a resonant effect. At frequencies between two resonances, a dispersionless band of non-zero rotation was observed. The sensitivity of this bandwidth to changes in the layer separation was shown to depend on the electrical connectivity of each of the two metallic layers and a multilayer system was proposed in order to enhance the bandwidth of transmission.

Chapters 6 and 7 focused on variations of a single layer metallic checkerboard metasurface. In Chapter 6, a compound checkerboard geometry was studied, which consisted of two arrays of different sized square holes offset from one another in both in-plane directions. Surface waves propagating in the plane of the metasurface were shown to have greater isotropy than in the ordinary checkerboard case. Further, the structure was shown to exhibit a sharp resonance in its transmission spectrum, the width of which is controlled by the ratio of square sizes. Chapter 7 presented two non-periodic variations. First, disorder was gradually introduced by rotating each patch about its lattice point. This perturbative approach allowed the transition from an electrically

connected (inductive) structure to a disconnected (capacitive) structure to be studied. An inversion of the transmission spectrum was observed as this transition occurs. The effect of disorder in the geometry was maximised when half of the metallic squares were isolated from their neighbours. At this level of disorder scatter loss is maximised, with only 60% of incident power detected in the speculation reflection and transmission paths.

In Chapter 8, modes localised at the edge of the metallic checkerboard samples were investigated. These modes exponentially decay in both transverse directions and propagate along the edge. They are distinct from the well studied topologically protected edge modes that occur in the band gap of bulk states; instead they exist as surface states supported on an extremely narrow region at the sample's edge. Much like surface waves, the edge waves were shown to couple together creating a symmetric/anti symmetric pair. Finally, the prospect of mode conversion between the surface and edge waves was discussed.

Chapter 9 focused on the phenomenon of negative mode index. First, one dimensional planar metallic waveguides that support a mode with negative mode index, i.e. opposite signs of group and phase velocity, were studied. To achieve this, current loops that provide the waveguide with a magnetic polarisability are required within each subwavelength element. The much-studied split ring resonator was shown experimentally to support such a mode, the frequency of which is reduced by lengthening the current loop in the transverse direction. The concept was extended to a two-dimensional surface mode that has negative mode index in all propagation directions in the plane of the structure. This was achieved using a four-armed spiral shape geometry and was experimentally verified. This presents the first observation of a surface wave with omnidirectional negative mode index supported on a single patterned metallic layer.

Finally, Chapter 10 presented a study of surface wave propagation on non-periodic rhombic tiling arrays. The metasurfaces studied consist of rhombic-shaped holes arranged in two tilings; the Penrose tiling, and a quasiperiodic diamond tiling, both of which are deterministic, yet non-periodic. Despite this, their Fourier spectra contain peaks corresponding to scattering planes of the structure, allowing surface waves to be supported. The isofrequency contours of these surface waves revealed the underlying symmetry of the array. This demonstrated the advantage of quasicrystalline surfaces; they can have symmetries that periodic geometries can not. For instance, the Penrose tiling supports a mode that, at a certain frequency, directs the majority of power into ten beams (due to five-fold rotational symmetry).

Chapter 12

Publications and Conferences

12.1 Publications

- Hooper, I. R., Tremain, B., Dockrey, J. A. & Hibbins, A. P. Massively sub-wavelength guiding of electromagnetic waves. *Sci. Rep.* **4**, 7495 (2014).

- Tremain, B., Rance, H. J., Hibbins, A. P. & Sambles, J. R. Polarization conversion from a thin cavity array in the microwave regime. *Sci. Rep.* **5**, 9366 (2015).

- Tremain, B., Durrant, C. J., Carter, I. E., Hibbins, A. P. & Sambles, J. R. The effect of rotational disorder on the microwave transmission of checkerboard metal square arrays. *Sci. Rep.* **5**, 16608 (2015).

- Barr, L. E., Díaz-Rubio, A., Tremain, B., Carbonell, J., Sánchez-Dehesa, J., Hendry, E. & Hibbins, A. P. On the origin of pure optical rotation in twisted-cross metamaterials. *Sci. Rep.* **6**, 30307 (2016).

- Tremain, B., Hibbins, A. P. & Sambles, J. R. Microwave surface waves on metal compound square-hole arrays. *Submitted June 2016, Sci. Rep.*

12.2 Conference Presentations

12.2.1 Oral Presentations

- Exeter Microwave Metamaterials Meeting (XM3) 2015, Tremain, B., Hooper, I. R., Hibbins, A. P. & Sambles, J. R. Edge waves on metallic checkerboard arrays. Exeter, UK. December 2015.

12.2.2 Poster Presentations

- Metamaterials 2014, Tremain, B., Rance, H. J., Hibbins, A. P. & Sambles, J. R. Polarization conversion from a thin cavity array in the microwave regime. Bordeaux, France. September 2013.
- Nanometa 2015, Tremain, B., Díaz-Rubio, A., Carbonell, J., Sánchez-Dehesa, J. & Hibbins, A. P. Experimental evidence of giant pure optical activity in a chiral metamaterial. Bordeaux, France. September 2013.
- Defence and Security Doctoral Symposium 2015, Tremain, B., Hooper, I. R., Hibbins, A. P. & Sambles, J. R. Edge waves on metallic checkerboard arrays. Seefeld, Austria. January 2015.

References

[1] Barnes, W., Preist, T., Kitson, S., and Sambles, J. Physical origin of photonic energy gaps in the propagation of surface plasmons on gratings. *Phys. Rev. B*, **54**, 6227 (1996). v, 6

[2] Dockrey, J. *Manipulation of microwave surface waves supported on metamaterials.* Ph.D. thesis (2015). xix, 136, 156

[3] Zenneck, J. Uber die Fortpanzung ebener elektromagnetischer Wellen langseiner ebenen Leiterache und ihre Beziehung zur drahtlosen Telegraphie. *Annalen der Physik*, **328**, 846 (1907). 5, 8

[4] Sommerfeld, A. The broadening of the waves and the wireless telegraph. *Annalen der Physik*, **28** (1909). 5

[5] Elliott, R. On the theory of corrugated plane surfaces. *Trans. IRE Prof. Gr. Antennas Propag.*, **2**, 169 (1954). 5

[6] Barlow, H. and Cullen, A. Surface waves. *Proc. IEE-Part III Radio Commun. Eng.*, **100**, 329 (1953). 5

[7] Rotman, W. A study of single-surface corrugated guides. *Proc. IRE*, **39**, 952 (1951). 5

[8] Cutler, C. Genesis of the corrugated electromagnetic surface. *Proc. IEEE Antennas Propag. Soc. Int. Symp. URSI Natl. Radio Sci. Meet.*, **3**, 1456 (1994). 5

[9] Ulrich, R. and Tacke, M. Submillimeter waveguiding on periodic metal structure. *Appl. Phys. Lett.*, **22**, 251 (1973). 5

[10] Stratton, J.A. *Electromagnetic theory.* McGraw-Hill Book Company (1941). ISBN 9780470131534. 6, 22

[11] Collin, R.E. *Field Theory of Guided Waves*. IEEE Press (1991). ISBN 0-87942-237-8. 6, 14, 27

[12] Fano, U. The Theory of Anomalous Diffraction Gratings and of Quasi-Stationary Waves on Metallic Surfaces (Sommerfelds Waves). *J. Opt. Soc. Am.*, **31**, 213 (1941). 6

[13] Drude, P. Zur elektronentheorie der metalle. *Annalen der Physik*, **306**, 566 (1900). 6, 13

[14] Baena, J.D., Bonache, J., Martin, F., Marqués, R., Falcone, F., Lopetegi, T., Laso, M.A.G., Garcia-Garcia, J., Gil, I., Portillo, M.F., and Sorolla, M. Equivalent circuit models for split ring resonators and complementary split ring resonators coupled to planar transmission lines. *IEEE Trans. Microw. Theory Tech.*, **53**, 1451 (2005). 16, 149

[15] Medina, F., Mesa, F., and Marqués, R. Extraordinary transmission through arrays of electrically small holes from a circuit theory perspective. *IEEE Trans. Microw. Theory Tech.*, **56**, 3108 (2008). 16

[16] Pendry, J.B., Martín-Moreno, L., and Garcia-Vidal, F.J. Mimicking surface plasmons with structured surfaces. *Science*, **305**, 847 (2004). 17, 94

[17] Hibbins, A.P., Evans, B.R., and Sambles, J. Experimental verification of designer surface plasmons. *Science*, **308**, 670 (2005). 17

[18] Hibbins, A.P., Lockyear, M.J., and Sambles, J.R. Otto coupling to a transverse-electric-polarized mode on a metamaterial surface. *Phys. Rev. B*, **84**, 115130 (2011). 17

[19] Brillouin, L. *Wave propagation in periodic structures*, volume 301 (1953). ISBN 0486495566. 19

[20] Enoch, S. and Bonod, N. *Plasmonics - From basics to advanced topics*, volume 167 (2012). ISBN 978-3-642-28078-8. 19

[21] Soukoulis, C.M., Kafesaki, M., and Economou, E.N. Negative-index materials: New frontiers in optics. *Adv. Mater.*, **18**, 1941 (2006). 21, 134

[22] Joannopoulos, J.J.D., Johnson, S., Winn, J.N.J., and Meade, R.R.D. *Photonic crystals: molding the flow of light* (2008). ISBN 9780691124568. 21

[23] Kittel, C. *Introduction to solid state physics* (2005). ISBN 0-471-11181-3. 22

[24] Brown, J. *Electromagnetic Wave Theory: Proceedings of a Symposium Held at Delft, The Netherlands, September 1965*. Pergamon Press (1967). ISBN 66-17928. 27

[25] Constant, T.J., Taphouse, T.S., Rance, H.J., Kitson, S.C., Hibbins, A.P., and Sambles, J.R. Surface plasmons on zig-zag gratings. *Opt. Express*, **20**, 23921 (2012). 27

[26] Hessel, A., Oliner, A.A., Chen, M.H., and Li, R.C.M. Propagation in periodically loaded waveguides with higher symmetries. *Proc. IEEE*, **61**, 183 (1973). 27, 140

[27] Bloch, F. Uber die Quantenmechanik der Elekronen in Kristallgittern. *Zeitschrift für Phys. A*, **52**, 555 (1929). 30

[28] Agilent. Network analyzer basics (2004). 36

[29] Anritsu. Understanding vna calibration (2012). 37

[30] Emerson and Cuming. Eccosorb cv data sheet (2010). 39

[31] Emerson and Cuming. Eccosorb vhp-nrl data sheet (2010). 39

[32] Gogoi, J.P., Bhattacharyya, N.S., and James Raju, K.C. Synthesis and microwave characterization of expanded graphite/novolac phenolic resin composite for microwave absorber applications. *Compos. Part B Eng.*, **42**, 1291 (2011). 39

[33] Inchaussandague, M.E. and Depine, R.A. Polarization conversion from diffraction gratings made of uniaxial crystals. *Phys. Rev. E*, **54**, 2899 (1996). 55

[34] Depine, R.A. and Gigli, M.L. Conversion between polarization states at the sinusoidal boundary of a uniaxial crystal. *Phys. Rev. B*, **49**, 8437 (1994). 55

[35] Tsai, C.C. and Wu, S.T. Study of broadband polarization conversion with metallic surface-relief gratings by rigorous coupled-wave analysis. *J. Opt. Soc. Am. A*, **25**, 1339 (2008). 55

[36] Elston, S., Bryan-Brown, G., and Sambles, J. Polarization conversion from diffraction gratings. *Phys. Rev. B*, **44**, 6393 (1991). 55

[37] Feng, L., Mizrahi, A., Zamek, S., Liu, Z., Lomakin, V., and Fainman, Y. Metamaterials for enhanced polarization conversion in plasmonic excitation. *ACS Nano*, **5**, 5100 (2011). 55

[38] Hallam, B.T., Lawrence, C.R., Hooper, I.R., and Sambles, J.R. Broadband polarization conversion from a finite periodic structure in the microwave regime. *Appl. Phys. Lett.*, **84**, 849 (2004). 55

[39] Watts, R.A. and Sambles, J.R. Polarization conversion from blazed diffraction gratings. *J. Mod. Opt.*, **44**, 1231 (1997). 55

[40] Hooper, I.R. and Sambles, J.R. Broadband polarization-converting mirror for the visible region of the spectrum. *Opt. Lett.*, **27**, 2152 (2002). 55

[41] Seshadri, S.R. Polarization conversion by reflection in a thin-film grating. *J. Opt. Soc. Am. A*, **18**, 1765 (2001). 55

[42] Passilly, N., Karvinen, P., Ventola, K., Laakkonen, P., Turunen, J., and Tervo, J. Polarization conversion by dielectric sub-wavelength gratings in conical mounting. *J. Eur. Opt. Soc. Rapid Publ.*, **3**, 08009 (2008). 55

[43] Wang, F., Chakrabarty, A., Minkowski, F., Sun, K., and Wei, Q.H. Polarization conversion with elliptical patch nanoantennas. *Appl. Phys. Lett.*, **101** (2012). 56, 68

[44] Yang, Y., Wang, W., Moitra, P., Kravchenko, I.I., Briggs, D.P., and Valentine, J. Dielectric meta-reflectarray for broadband linear polarization conversion and optical vortex generation. *Nano Lett.*, **14**, 1394 (2014). 56, 68

[45] Li, T., Wang, S.M., Cao, J.X., Liu, H., and Zhu, S.N. Cavity-involved plasmonic metamaterial for optical polarization conversion. *Appl. Phys. Lett.*, **97**, 261113 (2010). 56, 68

[46] Grady, N.K., Heyes, J.E., Chowdhury, D.R., Zeng, Y., Reiten, M.T., Azad, A.K., Taylor, A.J., Dalvit, D.a.R., and Chen, H.T. Terahertz metamaterials for linear polarization conversion and anomalous refraction. *Science*, **340**, 1304 (2013). 56, 68

[47] Zheng, H.Y., Yoo, Y.J., Kim, Y.J., Lee, Y.P., Kang, J.H., Kim, K.W., and Nikitov, S.a. Reflective metamaterial polarization converter in a broad frequency range. *J. Korean Phys. Soc.*, **64**, 822 (2014). 56, 68

[48] Chin, J.Y., Lu, M., and Cui, T.J. Metamaterial polarizers by electric-field-coupled resonators. *Appl. Phys. Lett.*, **93**, 251903 (2008). 56

[49] Hao, J., Yuan, Y., Ran, L., Jiang, T., Kong, J., Chan, C., and Zhou, L. Manipulating electromagnetic wave polarizations by anisotropic metamaterials. *Phys. Rev. Lett.*, **99**, 063908 (2007). 56, 68

[50] Ma, H.F., Wang, G.Z., Kong, G.S., and Cui, T.J. Broadband circular and linear polarization conversions realized by thin birefringent reflective metasurfaces. *Opt. Mater. Express*, **4**, 1717 (2014). 56, 68

[51] Hibbins, A., Sambles, J.R., Lawrence, C., and Brown, J. Squeezing millimeter waves into microns. *Phys. Rev. Lett.*, **92**, 90 (2004). 57

[52] Lockyear, M.J., Hibbins, A.P., and Sambles, J.R. Transmission of microwaves through a stepped subwavelength slit. *Appl. Phys. Lett.*, **91**, 251106 (2007). 57, 65

[53] Wu, C., Neuner, B., Shvets, G., John, J., Milder, A., Zollars, B., and Savoy, S. Large-area wide-angle spectrally selective plasmonic absorber. *Phys. Rev. B*, **84**, 1 (2011). 61

[54] Pan, W., Huang, C., Pu, M., Ma, X., Cui, J., Zhao, B., and Luo, X. Combining the absorptive and radiative loss in metasurfaces for multi-spectral shaping of the electromagnetic scattering. *Sci. Rep.*, **6**, 21462 (2016). 61

[55] Brown, J.R., Hibbins, A.P., Lockyear, M.J., Lawrence, C.R., and Sambles, J.R. Angle-independent microwave absorption by ultrathin microcavity arrays. *J. Appl. Phys.*, **104**, 043105 (2008). 63

[56] Li, Z., Mutlu, M., and Ozbay, E. Chiral metamaterials: from optical activity and negative refractive index to asymmetric transmission. *J. Opt.*, **15**, 023001 (2013). 71

[57] Wang, B., Zhou, J., Koschny, T., Kafesaki, M., and Soukoulis, C.M. Chiral metamaterials: simulations and experiments. *J. Opt. A Pure Appl. Opt.*, **11**, 114003 (2009). 71

[58] Schäferling, M., Dregely, D., Hentschel, M., and Giessen, H. Tailoring enhanced optical chirality: design principles for chiral plasmonic nanostructures. *Phys. Rev. X*, **2**, 031010 (2012). 71

[59] Gansel, J.K., Thiel, M., Rill, M.S., Decker, M., Bade, K., Saile, V., von Freymann, G., Linden, S., and Wegener, M. Gold helix photonic metamaterial as broadband circular polarizer. *Science*, **325**, 1513 (2009). 72

[60] Brewitt-Taylor, C., Lederer, P., Smith, F., and Haq, S. Measurement and prediction of helix-loaded chiral composites. *IEEE Trans. Antennas Propag.*, **47**, 692 (1999). 72

[61] Helgert, C., Pshenay-Severin, E., Falkner, M., Menzel, C., Rockstuhl, C., Kley, E.B., Tünnermann, A., Lederer, F., and Pertsch, T. Chiral metamaterial composed of three-dimensional plasmonic nanostructures. *Nano Lett.*, **11**, 4400 (2011). 72

[62] Menzel, C., Rockstuhl, C., Paul, T., and Lederer, F. Retrieving effective parameters for quasiplanar chiral metamaterials. *Appl. Phys. Lett.*, **93**, 233106 (2008). 72

[63] Kuwata-Gonokami, M., Saito, N., Ino, Y., Kauranen, M., Jefimovs, K., Vallius, T., Turunen, J., and Svirko, Y. Giant optical activity in quasi-two-dimensional planar nanostructures. *Phys. Rev. Lett.*, **95**, 227401 (2005). 72

[64] Bai, B., Svirko, Y., Turunen, J., and Vallius, T. Optical activity in planar chiral metamaterials: Theoretical study. *Phys. Rev. A*, **76**, 023811 (2007). 72

[65] Jia, Y.P., Zhang, Y.L., Dong, X.Z., Zheng, M.L., Li, J., Liu, J., Zhao, Z.S., and Duan, X.M. Complementary chiral metasurface with strong broadband optical activity and enhanced transmission. *Appl. Phys. Lett.*, **104**, 011108 (2014). 72

[66] Prosvirnin, S.L. and Zheludev, N.I. Analysis of polarization transformations by a planar chiral array of complex-shaped particles. *J. Opt. A Pure Appl. Opt.*, **11**, 074002 (2009). 72

[67] Decker, M., Klein, M.W., Wegener, M., and Linden, S. Circular dichroism of planar chiral magnetic metamaterials. *Opt. Lett.*, **32**, 856 (2007). 72

[68] Plum, E., Fedotov, V.A., Schwanecke, A.S., Zheludev, N.I., and Chen, Y. Giant optical gyrotropy due to electromagnetic coupling. *Appl. Phys. Lett.*, **90**, 223113 (2007). 72

[69] Plum, E., Zhou, J., Dong, J., Fedotov, V., Koschny, T., Soukoulis, C., and Zheludev, N. Metamaterial with negative index due to chirality. *Phys. Rev. B*, **79**, 035407 (2009). 72

[70] Ye, Y. and He, S. 90 polarization rotator using a bilayered chiral metamaterial with giant optical activity. *Appl. Phys. Lett.*, **96**, 203501 (2010). 72

[71] Kwon, D.H., Werner, P.L., and Werner, D.H. Optical planar chiral metamaterial designs for strong circular dichroism and polarization rotation. *Opt. Express*, **16**, 11802 (2008). 72

[72] Rogacheva, b.V., Fedotov, V.A., Schwanecke, A.S., and Zheludev, N.I. Giant gyrotropy due to electromagnetic-field coupling in a bilayered chiral structure. *Phys. Rev. Lett.*, **97**, 177401 (2006). 72

[73] Decker, M., Ruther, M., Kriegler, C.E., Zhou, J., Soukoulis, C.M., Linden, S., and Wegener, M. Strong optical activity from twisted-cross photonic metamaterials. *Opt. Lett.*, **34**, 2501 (2009). 72, 73, 88

[74] Decker, M., Zhao, R., Soukoulis, C.M., Linden, S., and Wegener, M. Twisted split-ring-resonator photonic metamaterial with huge optical activity. *Opt. Lett.*, **35**, 1593 (2010). 72

[75] Xiong, X., Sun, W.H., Bao, Y.J., Wang, M., Peng, R.W., Sun, C., Lu, X., Shao, J., Li, Z.F., and Ming, N.B. Construction of a chiral metamaterial with a U-shaped resonator assembly. *Phys. Rev. B*, **81**, 075119 (2010). 72

[76] Shi, J., Liu, X., Yu, S., Lv, T., Zhu, Z., Feng Ma, H., and Jun Cui, T. Dual-band asymmetric transmission of linear polarization in bilayered chiral metamaterial. *Appl. Phys. Lett.*, **102**, 191905 (2013). 72

[77] Hannam, K., Powell, D.A., Shadrivov, I.V., and Kivshar, Y.S. Dispersionless optical activity in metamaterials. *Appl. Phys. Lett.*, **102**, 201121 (2013). 72, 73, 88

[78] Liu, N., Liu, H., Zhu, S., and Giessen, H. Stereometamaterials. *Nat. Photonics*, **3**, 157 (2009). 72

[79] Plum, E., Fedotov, V.A., and Zheludev, N.I. Optical activity in extrinsically chiral metamaterial. *Appl. Phys. Lett.*, **93**, 191911 (2008). 72

[80] Feng, T., Liu, F., Tam, W.Y., and Li, J. Effective parameters retrieval for complex metamaterials with low symmetries. *EPL (Europhysics Lett.*, **102**, 18003 (2013). 72, 88

[81] Engheta, N. and Zablocky, P. A step towards determining transient response of chiral materials: Kramers - Kronig relations for chiral parameters. *Electron. Lett.*, **26**, 2132 (1990). 76

[82] Hannam, K., Powell, D.A., Shadrivov, I.V., and Kivshar, Y.S. Dispersionless optical activity in metamaterials. *Appl. Phys. Lett.*, **102** (2013). 79

[83] Edmunds, J.D., Lockyear, M.J., Hibbins, A.P., Sambles, J.R., and Youngs, I.J. Resonantly overcoming metal opacity. *Appl. Phys. Lett.*, **102**, 011120 (2013). 79

[84] Gorkunov, M.V., Dmitrienko, V.E., Ezhov, A.A., Artemov, V.V., and Rogov, O.Y. Implications of the causality principle for ultra chiral metamaterials. *Sci. Rep.*, **5**, 9273 (2015). 80

[85] Ebbesen, T., Lezec, H.J., Ghaemi, H.F., Thio, T., and Wolff, P.A. Extraordinary optical transmission through sub-wavelength hole arrays. *Nature*, **86**, 1114 (1998). 89, 104

[86] Martín-Moreno, L., García-Vidal, F., Lezec, H., Pellerin, K., Thio, T., Pendry, J., and Ebbesen, T. Theory of extraordinary optical transmission through subwavelength hole arrays. *Phys. Rev. Lett.*, **86**, 1114 (2001). 89

[87] Landy, N.I., Sajuyigbe, S., Mock, J.J., Smith, D.R., and Padilla, W.J. Perfect metamaterial absorber. *Phys. Rev. Lett.*, **100**, 207402 (2008). 90

[88] Tremain, B., Durrant, C.J., Carter, I.E., Hibbins, A.P., and Sambles, J.R. The effect of rotational disorder on the microwave transmission of checkerboard metal square arrays. *Sci. Rep.*, **5**, 16608 (2015). 90

[89] Pfeiffer, C. and Grbic, A. Metamaterial Huygens' surfaces: Tailoring wave fronts with reflectionless sheets. *Phys. Rev. Lett.*, **110**, 197401 (2013). 90

[90] Fedotov, V.A., Rose, M., Prosvirnin, S.L., Papasimakis, N., and Zheludev, N.I. Sharp trapped-mode resonances in planar metamaterials with a broken structural symmetry. *Phys. Rev. Lett.*, **99**, 5 (2007). 90

[91] Wu, L., Yang, Z., Zhao, M., Zheng, Y., Duan, J., and Yuan, X. Polarization-insensitive resonances with high quality-factors in meta-molecule metamaterials. *Opt. Express*, **22**, 14588 (2014). 90

[92] Bai, Z., Zhang, Q., Ju, Y., Tao, G., Jiang, X., Kang, N., Liu, C., and Zhang, L. Flexible metamaterial narrow-band-pass filter based on magnetic resonance coupling between ultra-thin bilayer frequency selective surfaces. *J. Phys. D. Appl. Phys.*, **49**, 065002 (2016). 90

[93] Humphrey, A.D., Meinzer, N., Starkey, T.A., and Barnes, W.L. Surface lattice resonances in plasmonic arrays of asymmetric disc dimers. *ACS Photonics*, **3**, 634 (2016). 90

[94] Kravets, V.G., Schedin, F., and Grigorenko, A.N. Extremely narrow plasmon resonances based on diffraction coupling of localized plasmons in arrays of metallic nanoparticles. *Phys. Rev. Lett.*, **101**, 087403 (2008). 90

[95] Skigin, D.C., Veremey, V.V., and Mittra, R. Superdirective radiation from finite gratings of rectangular grooves. *IEEE Trans. Antennas Propag.*, **47**, 376 (1999). 90

[96] Skigin, D.C. and Depine, R.A. Narrow gaps for transmission through metallic structured gratings with subwavelength slits. *Phys. Rev. E*, **74**, 046606 (2006). 90

[97] Skigin, D. and Depine, R. Transmission resonances of metallic compound gratings with subwavelength slits. *Phys. Rev. Lett.*, **95**, 217402 (2005). 90

[98] Grosz, S., Skigin, D., and Fantino, A. Resonant effects in compound diffraction gratings: Influence of the geometrical parameters of the surface. *Phys. Rev. E*, **65**, 056619 (2002). 90

[99] Depine, R.A., Fantino, A.N., Grosz, S.I., and Skigin, D.C. Phase resonances in obliquely illuminated compound gratings. *Optik (Stuttg).*, **118**, 42 (2007). 90

[100] Navarro-Cía, M., Skigin, D.C., Beruete, M., and Sorolla, M. Experimental demonstration of phase resonances in metallic compound gratings with subwavelength slits in the millimeter wave regime. *Appl. Phys. Lett.*, **94**, 091107 (2009). 90

[101] Mandel, I.M., Golovin, A.B., and Crouse, D.T. Fano phase resonances in multilayer metal-dielectric compound gratings. *Phys. Rev. A*, **87**, 053847 (2013). 90

[102] Hibbins, A.P., Hooper, I.R., Lockyear, M.J., and Sambles, J.R. Microwave transmission of a compound metal grating. *Phys. Rev. Lett.*, **96**, 1 (2006). 90

[103] Ma, Y., Rao, X., Zhang, G., and Ong, C. Microwave transmission modes in compound metallic gratings. *Phys. Rev. B*, **76**, 085413 (2007). 90

[104] Zhai, X., Liu, J.Q., He, M.D., Wang, L.L., Wen, S., and Fan, D. Adjustable phase resonances in a compound metallic grating with perpendicular cuts. *Opt. Express*, **18**, 6871 (2010). 90

[105] Liu, Z., Li, H., Xie, S., Xu, H., Fu, S., Zhou, X., and Wu, C. Tunable phase resonances in a compound metallic grating with perpendicular bumps and cuts. *Opt. Express*, **19**, 4217 (2011). 90

[106] Fantino, A.N., Grosz, S.I., and Skigin, D.C. Resonant effects in periodic gratings comprising a finite number of grooves in each period. *Phys. Rev. E*, **64**, 016605 (2001). 90

[107] Zentgraf, T., Liu, Y., Mikkelsen, M.H., Valentine, J., and Zhang, X. Plasmonic luneburg and eaton lenses. *Nat. Nanotechnol.*, **6**, 151 (2011). 90

[108] López-Tejeira, F., Rodrigo, S.G., Martín-Moreno, L., García-Vidal, F.J., Devaux, E., Ebbesen, T.W., Krenn, J.R., Radko, I.P., Bozhevolnyi, S.I., González, M.U., Weeber, J.C., and Dereux, A. Efficient unidirectional nanoslit couplers for surface plasmons. *Nat. Phys.*, **3**, 324 (2007). 90

[109] Dockrey, J.A., Horsley, S.A.R., Hooper, I.R., Sambles, J.R., and Hibbins, A.P. Direct observation of negative-index microwave surface waves. *Sci. Rep.*, **6**, 22018 (2016). 90, 136, 147, 156

[110] Miller, W. *Symmetry groups and their applications.* Academic Press (1972). ISBN 72-82628. 90, 94

[111] Edmunds, J.D., Taylor, M.C., Hibbins, A.P., Sambles, J.R., and Youngs, I.J. Babinets principle and the band structure of surface waves on patterned metal arrays. *J. Appl. Phys.*, **107**, 103108 (2010). 91, 100, 101, 103, 104, 107

[112] Booker, H.G. Slot aerials and their relation to complementary wire aerials (Babinet's principle). *J. Inst. Electr. Eng. - Part IIIA Radiolocation*, **93**, 620 (1946). 103, 106

[113] Compton, R.C. Babinet's principle applied to ideal beam-splitters for submillimetre waves. *Opt. Acta Int. J. Opt.*, **31**, 515 (1984). 104

[114] Kempa, K. Percolation effects in the checkerboard Babinet series of metamaterial structures. *Phys. Status Solidi - Rapid Res. Lett.*, **4**, 218 (2010). 104

[115] Takano, K., Miyamaru, F., Akiyama, K., Chiyoda, Y., Miyazaki, H., Takeda, M.W., Abe, Y., Tokuda, Y., and Ito, H. Crossover from capacitive to inductive electromagnetic responses in near self- complementary metallic checkerboard patterns. *Sci. Technol.*, **515**, 1222 (2010). 104, 105

[116] Ramakrishna, S.A., Mandal, P., Jeyadheepan, K., Shukla, N., Chakrabarti, S., Kadic, M., Enoch, S., and Guenneau, S. Plasmonic

interaction of visible light with gold nanoscale checkerboards. *Phys. Rev. B*, **84**, 245424 (2011). 104

[117] Nakata, Y., Urade, Y., Nakanishi, T., and Kitano, M. Plane-wave scattering by self-complementary metasurfaces in terms of electromagnetic duality and Babinet's principle. *Phys. Rev. B*, **88**, 205138 (2013). 104

[118] Urade, Y., Nakata, Y., Nakanishi, T., and Kitano, M. Frequency-independent response of self-complementary checkerboard screens. *Phys. Rev. Lett.*, **114**, 237401 (2015). 104

[119] Gonzalez-Ovejero, D., Martini, E., Loiseaux, B., Tripon-Canseliet, C., Mencagli, M., Chazelas, J., and Maci, S. Basic properties of checkerboard metasurfaces. *IEEE Antennas Wirel. Propag. Lett.*, **14**, 406 (2015). 104

[120] Kwon, D.H., Li, L., Bossard, J., Bray, M., and Werner, D. Zero index metamaterials with checkerboard structure. *Electron. Lett.*, **43**, 319 (2007). 104

[121] Edmunds, J.D. *Microwave transmissivity of sub-wavelength metallic structures.* Ph.D. thesis, University of Exeter (2011). 105

[122] Nishijima, Y., Rosa, L., and Juodkazis, S. Surface plasmon resonances in periodic and random patterns of gold nano-disks for broadband light harvesting. *Opt. Express*, **20**, 11466 (2012). 105

[123] Lee, J., Seo, M., Kang, D., Khim, K., Jeoung, S., and Kim, D. Terahertz electromagnetic wave transmission through random arrays of single rectangular holes and slits in thin metallic sheets. *Phys. Rev. Lett.*, **99**, 137401 (2007). 105

[124] Ruan, Z. and Qiu, M. Enhanced transmission through periodic arrays of subwavelength holes: The role of localized waveguide resonances. *Phys. Rev. Lett.*, **96**, 233901 (2006). 105

[125] Albooyeh, M., Kruk, S., Menzel, C., Helgert, C., Kroll, M., Krysinski, A., Decker, M., Neshev, D.N., Pertsch, T., Etrich, C., Rockstuhl, C., Tretyakov, S.A., Simovski, C.R., and Kivshar, Y.S. Resonant metasurfaces at oblique incidence: interplay of order and disorder. *Sci. Rep.*, **4**, 4484 (2014). 105

[126] Singh, R., Lu, X., Gu, J., Tian, Z., and Zhang, W. Random terahertz metamaterials. *J. Opt.*, **12**, 015101 (2010). 105

[127] Rockstuhl, C., Lederer, F., Zentgraf, T., and Giessen, H. Enhanced transmission of periodic, quasiperiodic, and random nanoaperture arrays. *Appl. Phys. Lett.*, **91**, 151109 (2007). 105

[128] Przybilla, F., Genet, C., and Ebbesen, T.W. Enhanced transmission through Penrose subwavelength hole arrays. *Appl. Phys. Lett.*, **89**, 121115 (2006). 105

[129] Janot, C. *Quasicrystals: a primer. 2nd ed.*, volume 31. Cryst. Res. Technol. (1994). ISBN 0198565518. 115

[130] Vasconcelos, M.S., Albuquerque, E.L., and Mariz, A.M. Optical localization in quasi-periodic multilayers. *J. Phys. Condens. Matter*, **10**, 5839 (1998). 116

[131] Sibilia, C., Scalora, M., Centini, M., Bertolotti, M., Bloemer, M.J., and Bowden, C.M. Electromagnetic properties of periodic and quasi-periodic one-dimensional, metallo-dielectric photonic band gap structures. *J. Opt. A Pure Appl. Opt.*, **1**, 490 (1999). 116

[132] Kohmoto, M., Sutherland, B., and Iguchi, K. Localization of optics: Quasiperiodic media. *Phys. Rev. Lett.*, **58**, 2436 (1987). 116

[133] Aissaoui, M., Zaghdoudi, J., Kanzari, M., and Rezig, B. Optical properties of the quasi-periodic one-dimensional generalized multilayer fibonacci structures. *Prog. Electromagn. Res.*, **59**, 69 (2006). 116

[134] Chakraborty, S., Parker, M.C., and Mears, R.J. A Fourier (k-) space design approach for controllable photonic band and localization states in aperiodic lattices. *Photonics Nanostructures - Fundam. Appl.*, **3**, 139 (2005). 116

[135] Bruno-Alfonso, A., Reyes-Gómez, E., Cavalcanti, S.B., and Oliveira, L.E. Band edge states of the n=0 gap of Fibonacci photonic lattices. *Phys. Rev. A*, **78**, 035801 (2008). 116

[136] Zhang, L., Fang, K., Du, G., Jiang, H., and Zhao, J. Transmission properties of Fibonacci quasi-periodic one-dimensional photonic crystals containing indefinite metamaterials. *Opt. Commun.*, **284**, 703 (2011). 116

[137] Peng, R.W., Wang, M., Hu, A., Jiang, S.S., Jin, G.J., and Feng, D. Photonic localization in one-dimensional k-component Fibonacci structures. *Phys. Rev. B*, **57**, 1544 (1998). 116

[138] El Hassouani, Y., Aynaou, H., El Boudouti, E.H., Djafari-Rouhani, B., Akjouj, A., and Velasco, V.R. Surface electromagnetic waves in Fibonacci superlattices: Theoretical and experimental results. *Phys. Rev. B*, **74**, 035314 (2006). 116

[139] Reyes-Gomez, E., Raigoza, N., Cavalcanti, S.B., De Carvalho, C.a.a., and Oliveira, L.E. Plasmon polaritons in photonic metamaterial Fibonacci superlattices. *Phys. Rev. B*, **81**, 153101 (2010). 116

[140] Chen, A.L., Wang, Y.S., Guo, Y.F., and Wang, Z.D. Band structures of Fibonacci phononic quasicrystals. *Solid State Commun.*, **145**, 103 (2008). 116

[141] Lusk, D., Abdulhalim, I., and Placido, F. Omnidirectional reflection from Fibonacci quasi-periodic one-dimensional photonic crystal. *Opt. Commun.*, **198**, 273 (2001). 116

[142] Peng, R.W., Huang, X.Q., Qiu, F., Wang, M., Hu, a., Jiang, S.S., and Mazzer, M. Symmetry-induced perfect transmission of light waves in quasiperiodic dielectric multilayers. *Appl. Phys. Lett.*, **80**, 3063 (2002). 116

[143] Kraus, Y.E., Lahini, Y., Ringel, Z., Verbin, M., and Zilberberg, O. Topological states and adiabatic pumping in quasicrystals. *Phys. Rev. Lett.*, **109**, 106402 (2012). 116

[144] Dal Negro, L. and Boriskina, S.V. Deterministic aperiodic nanostructures for photonics and plasmonics applications. *Laser Photonics Rev.*, **6**, 178 (2012). 116

[145] Dallapiccola, R., Gopinath, A., Stellacci, F., and Dal Negro, L. Quasi-periodic distribution of plasmon modes in two-dimensional Fibonacci arrays of metal nanoparticles. *Opt. Express*, **16**, 5544 (2008). 116

[146] Gopinath, A., Boriskina, S.V., Feng, N.N., Reinhard, B.M., and Dal Negro, L. Photonic-plasmonic scattering resonances in deterministic aperiodic structures. *Nano Lett.*, **8**, 2423 (2008). 116

[147] Liew, S.F., Noh, H., Trevino, J., Negro, L.D., and Cao, H. Localized photonic band edge modes and orbital angular momenta of light in a golden-angle spiral. *Opt. Express*, **19**, 23631 (2011). 116

[148] Gallina, I., Villa, A.D., and Galdi, V. Aperiodic-tiling-based mushroom-type high-impedance surfaces. *IEEE Antennas Wirel. Propag. Lett.*, **7**, 54 (2008). 116

[149] Shen, X., Cui, T.J., Martin-Cano, D., and García-Vidal, F.J. Conformal surface plasmons propagating on ultrathin and flexible films. *PNAS*, **110**, 40 (2013). 121, 122, 126, 138

[150] Brock, E.M.G., Hendry, E., and Hibbins, A.P. Subwavelength lateral confinement of microwave surface waves. *Appl. Phys. Lett.*, **99**, 051108 (2011). 121

[151] Quesada, R., Martín-Cano, D., García-Vidal, F.J., and Bravo-Abad, J. Deep-subwavelength negative-index waveguiding enabled by coupled conformal surface plasmons. *Opt. Lett.*, **39**, 2990 (2014). 122, 137, 139

[152] Martin-Cano, D., Nesterov, M.L., Fernandez-Dominguez, A.I., Garcia-Vidal, F.J., Martin-Moreno, L., and Moreno, E. Domino plasmons for subwavelength terahertz circuitry. *Opt. Express*, **18**, 754 (2010). 122

[153] Ma, Y.G., Lan, L., Zhong, S.M., and Ong, C.K. Experimental demonstration of subwavelength domino plasmon devices for compact high- frequency circuit. *Opt. Express*, **19**, 21189 (2011). 122

[154] Moreno, E., Rodrigo, S.G., Bozhevolnyi, S.I., Martín-Moreno, L., and García-Vidal, F.J. Guiding and focusing of electromagnetic fields with wedge plasmon polaritons. *Phys. Rev. Lett.*, **100**, 1 (2008). 122

[155] Fernández-Domínguez, A.I., Moreno, E., Martín-Moreno, L., and García-Vidal, F.J. Terahertz wedge plasmon polaritons. *Opt. Lett.*, **34**, 2063 (2009). 122

[156] Gao, Z., Zhang, X., and Shen, L. Wedge mode of spoof surface plasmon polaritons at terahertz frequencies. *J. Appl. Phys.*, **108**, 113104 (2010). 122

[157] Khanikaev, A.B., Mousavi, S.H., Tse, W.K., Kargarian, M., MacDonald, A.H., and Shvets, G. Photonic topological insulators. *Nat. Mater.*, **12**, 233 (2013). 126

[158] Veselago, V. The electrodynamics of substances with simultaneously negative values of epsilon and mu. *Physics-Uspekhi*, **509**, 509 (1968). 133

[159] Pendry, J.B., Holden, A.J., Robbins, D.J., and Stewart, W.J. Magnetism from conductors and enhanced nonlinear phenomena. *IEEE Trans. Microw. Theory Tech.*, **47**, 2075 (1999). 134, 149

[160] Dolling, G., Enkrich, C., Wegener, M., Zhou, J.F., Soukoulis, C.M., and Linden, S. Cut-wire pairs and plate pairs as magnetic atoms for optical metamaterials. *Opt. Lett.*, **30**, 3198 (2005). 134

[161] Shvets, G. and Urzhumov, Y.A. Negative index meta-materials based on two-dimensional metallic structures. *J. Opt. A Pure Appl. Opt.*, **8**, 122 (2006). 134

[162] Zhou, J., Zhang, L., Tuttle, G., Koschny, T., and Soukoulis, C.M. Negative index materials using simple short wire pairs. *Phys. Rev. B*, **73**, 041101 (2006). 134

[163] Katsarakis, N., Konstantinidis, G., Kostopoulos, A., Penciu, R.S., Gundogdu, T.F., Kafesaki, M., Economou, E.N., Koschny, T., and Soukoulis, C.M. Magnetic response of split-ring resonators in the far-infrared frequency regime. *Opt. Lett.*, **30**, 1348 (2005). 134

[164] Yen, T.J., Padilla, W.J., Fang, N., Vier, D.C., Smith, D.R., Pendry, J.B., Basov, D.N., and Zhang, X. Terahertz magnetic response from artifical materials. *Science*, **303**, 1494 (2004). 134

[165] Linden, S., Enkrich, C., Wegener, M., Zhou, J., Koschny, T., and Soukoulis, C.M. Magnetic response of metamaterials at 100 terahertz. *Science*, **306**, 1351 (2004). 134

[166] Zhang, S., Fan, W., Minhas, B.K., Frauenglass, A., Malloy, K.J., and Brueck, S.R.J. Midinfrared resonant magnetic nanostructures exhibiting a negative permeability. *Phys. Rev. Lett.*, **94**, 037402 (2005). 134

[167] Smith, D.R., Smith, D.R., Padilla, W.J., Padilla, W.J., Vier, D.C., Vier, D.C., Nemat-Nasser, S.C., Nemat-Nasser, S.C., Schultz, S., and Schultz, S. Composite medium with simultaneously negative permeability and permittivity. *Phys. Rev. Lett.*, **84**, 4184 (2000). 134

[168] Shelby, R.A., Smith, D.R., and Schultz, S. Experimental verification of a negative index of refraction. *Science*, **292**, 77 (2001). 134

[169] Dong, Z.G., Lei, S.Y., Xu, M.X., Liu, H., Li, T., Wang, F.M., and Zhu, S.N. Negative index of refraction in metallic metamaterial comprising split-ring resonators. *Phys. Rev. E*, **77**, 056609 (2008). 134

[170] Ye, D., Chang, K., Ran, L., and Xin, H. Microwave gain medium with negative refractive index. *Nat. Commun.*, **5**, 5841 (2014). 134

[171] Pendry, J.B. Negative refraction makes a perfect lens. *Phys. Rev. Lett.*, **85**, 3966 (2000). 134

[172] Smith, D.R., Pendry, J.B., and Wiltshire, M.C.K. Metamaterials and negative refractive index. *Science*, **305**, 788 (2004). 134

[173] Shalaev, V.M. Optical negative-index metamaterials. *Nat. Photonics*, **1**, 41 (2007). 135

[174] Zhang, S., Fan, W., Panoiu, N.C., Malloy, K.J., Osgood, R.M., and Brueck, S.R. Optical negative-index bulk metamaterials consisting of 2D perforated metal-dielectric stacks. *Opt. Express*, **14**, 6778 (2006). 135

[175] Dolling, G., Enkrich, C., Wegener, M., Soukoulis, C.M., and Linden, S. Simultaneous negative phase and group velocity of light in a metamaterial. *Science*, **312**, 892 (2006). 135

[176] Valentine, J., Zhang, S., Zentgraf, T., Ulin-Avila, E., Genov, D.A., Bartal, G., and Zhang, X. Three-dimensional optical metamaterial with a negative refractive index. *Nature*, **455**, 376 (2008). 135

[177] Lezec, H.J., Dionne, J.A., and Atwater, H.A. Negative refraction at visible frequencies. *Science*, **316**, 430 (2007). 135

[178] Tretyakov, S., Nefedov, I., Sihvola, A., Maslovski, S., and Simovski, C. Waves and energy in chiral nihility. *J. Electromagn. Waves Appl.*, **17**, 695 (2003). 135

[179] Pendry, J.B. A chiral route to negative refraction. *Science*, **306**, 1353 (2004). 135

[180] Zhang, S., Park, Y.S., Li, J., Lu, X., Zhang, W., and Zhang, X. Negative refractive index in chiral metamaterials. *Phys. Rev. Lett.*, **102**, 023901 (2009). 135

[181] Luo, C., Johnson, S.G., Joannopoulos, J.D., and Pendry, J.B. All-angle negative refraction without negative effective index. *Phys. Rev. B*, **65**, 201104 (2002). 135, 137

[182] Notomi, M. Theory of light propagation in strongly modulated photonic crystals: Reflectionlike behavior in the vicinity of the photonic band gap. *Phys. Rev. B*, **62**, 10696 (2000). 135

[183] Parimi, P.V., Lu, W.T., Vodo, P., and Sridhar, S. Photonic crystals: imaging by flat lens using negative refraction. *Nature*, **426**, 404 (2003). 135

[184] Cubukcu, E., Aydin, K., Ozbay, E., Foteinopoulou, S., and Soukoulis, C.M. Electromagnetic waves: Negative refraction by photonic crystals. *Nature*, **423**, 604 (2003). 135

[185] Berrier, A., Mulot, M., Swillo, M., Qiu, M., Thylen, L., Talneau, A., and Anand, S. Negative refraction at infrared wavelengths in a two-dimensional photonic crystal. *Phys. Rev. Lett.*, **93**, 073902 (2004). 135

[186] Addouche, M., Al-Lethawe, M.A., Choujaa, A., and Khelif, A. Superlensing effect for surface acoustic waves in a pillar-based phononic crystal with negative refractive index. *Appl. Phys. Lett.*, **105**, 023501 (2014). 135

[187] Kaina, N., Lemoult, F., Fink, M., and Lerosey, G. Negative refractive index and acoustic superlens from multiple scattering in single negative metamaterials. *Nature*, **525**, 77 (2015). 135

[188] Dockrey, J.A., Lockyear, M.J., Berry, S.J., Horsley, S.A.R., Sambles, J.R., and Hibbins, A.P. Thin metamaterial Luneburg lens for surface waves. *Phys. Rev. B*, **87**, 125137 (2013). 136

[189] Dionne, J.A., Verhagen, E., Polman, A., and Atwater, H.A. Are negative index materials achievable with surface plasmon waveguides? A case study of three plasmonic geometries. *Opt. Express*, **16**, 19001 (2008). 136

[190] Liu, X., Feng, Y., Zhu, B., Zhao, J., and Jiang, T. Backward spoof surface wave in plasmonic metamaterial of ultrathin metallic structure. *Sci. Rep.*, **6**, 20448 (2016). 136

[191] Mock, A., Lu, L., and OBrien, J. Space group theory and Fourier space analysis of two-dimensional photonic crystal waveguides. *Phys. Rev. B*, **81**, 155115 (2010). 139

[192] Crepeau, P. and McIsaac, P. Consequences of symmetry in periodic structures. *Proc. IEEE*, **52**, 33 (1964). 140

[193] Hooper, I.R., Tremain, B., Dockrey, J.A., and Hibbins, A.P. Massively sub-wavelength guiding of electromagnetic waves. *Sci. Rep.*, **4**, 7495 (2014). 145

[194] Berini, P., Charbonneau, R., and Lahoud, N. Long-range surface plasmons on ultrathin membranes. *Nano Lett.*, **7**, 1376 (2007). 145

[195] Esteban, J., Camacho-Peñalosa, C., Page, J.E., Martín-Guerrero, T.M., and Márquez-Segura, E. Simulation of negative permittivity and

negative permeability by means of evanescent waveguide modes - Theory and experiment. *IEEE Trans. Microw. Theory Tech.*, **53**, 1506 (2005). 149

[196] Marqués, R., Medina, F., and Rafii-El-Idrissi, R. Role of bianisotropy in negative permeability and left-handed metamaterials. *Phys. Rev. B*, **65**, 144440 (2002). 149

[197] Martín, F., Bonache, J., Falcone, F., Sorolla, M., and Marqués, R. Split ring resonator-based left-handed coplanar waveguide. *Appl. Phys. Lett.*, **83**, 4652 (2003). 149

[198] Estep, N.A., Askarpour, A.N., and Alu, A. Experimental demonstration of negative-index propagation in a rectangular waveguide loaded with complementary split-ring resonators. *IEEE Antennas Wirel. Propag. Lett.*, **14**, 119 (2015). 149

[199] Shamonina, E. Magnetoinductive polaritons: Hybrid modes of metamaterials with interelement coupling. *Phys. Rev. B*, **85**, 155146 (2012). 149

[200] Sydoruk, O., Tatartschuk, E., Shamonina, E., and Solymar, L. Analytical formulation for the resonant frequency of split rings. *J. Appl. Phys.*, **105**, 014903 (2009). 149

[201] Eleftheriades, G.V., Iyer, A.K., and Kremer, P.C. Planar negative refractive index media using periodically L-C loaded transmission lines. *IEEE Trans. Microw. Theory Tech.*, **50**, 2702 (2002). 149

[202] Shadrivov, I.V., Sukhorukov, A.A., and Kivshar, Y.S. Guided modes in negative-refractive-index waveguides. *Phys. Rev. E*, **67**, 057602 (2003). 149

[203] Lai, A., Caloz, C., and Itoh, T. Composite right/left-handed transmission line metamaterials. *IEEE Microw. Mag.*, **5**, 34 (2004). 153

[204] Lunnemann, P. and Koenderink, A.F. Dispersion of guided modes in two-dimensional split ring lattices. *Phys. Rev. B*, **90**, 245416 (2014). 154

[205] Kaliteevski, M.A., Brand, S., and Abram, R.A. Directionality of light transmission and reflection in two-dimensional Penrose tiled photonic quasicrystals. *J. Phys. Cond. Mat.*, **16**, 1269 (2004). 161

[206] Kaliteevski, M.A. Two-dimensional Penrose-tiled photonic quasicrystals: from diffraction pattern to band structure. *Nanotechnology*, **11**, 274 (2000). 161

[207] Vignolo, P., Bellec, M., Böhm, J., Camara, A., Gambaudo, J.M., Kuhl, U., and Mortessagne, F. Energy landscape in a Penrose tiling. *Phys. Rev. B*, **93**, 1 (2016). 161

[208] Dolev, I., Volodarsky, M., Porat, G., and Arie, A. Multiple coupling of surface plasmons in quasiperiodic gratings. *Opt. Lett.*, **36**, 1584 (2011). 161

[209] Steurer, W. and Sutter-Widmer, D. Photonic and phononic quasicrystals. *J. Phys. D. Appl. Phys.*, **40**, 229 (2007). 161